Technische Universität München
TUM School of Natural Sciences

Transverse-Field Ising Transition under Tilted Magnetic Field

Andreas Wendl

Vollständiger Abdruck der von der TUM School of Natural Sciences der Technischen Universität München zur Erlangung des akademischen Grades eines

Doktors der Naturwissenschaften (Dr. rer. nat.)

genehmigten Dissertation.

Vorsitz: Prof. Dr. Frank Pollmann

Prüfer*innen der Dissertation:

1. Prof. Dr. Christian Pfleiderer
2. Priv.-Doz. Dr. Hans-Gregor Hübl

Die Dissertation wurde am 21.09.2022 bei der Technischen Universität München eingereicht und durch die TUM School of Natural Sciences am 27.04.2023 angenommen.

Abstract

In this thesis LiHoF$_4$ is investigated experimentally, which shows a quantum phase transition (QPT) at $T = 0$, when an external magnetic field of $B_c \approx 5.1\,\text{T}$ is applied perpendicular to the easy axis. The central question of this study is the evolution of this phase transition under tilting the magnetic field away from this perfect transverse orientation. The magnetic and caloric properties are determined by measuring the AC susceptibility, heat capacity and magnetocaloric effect using a dilution fridge and a vector magnet. From these data, a detailed evolution of the phase diagram is obtained. The established microscopic Landau theory expects a crossover under tilted magnetic field, since the longitudinal field component breaks the symmetry. In stark contrast however, the main result of this thesis shows a well-defined phase transition under tilted field and a strong angular dependence of the critical field. Therefore, a model is developed in collaboration with colleagues from the TU Dresden, which takes magnetic domains and the volume fraction of the minority domains into account and allows to explain the experimental results quantitatively.

All experiments require a very precise orientation of the sample with respect to the vector magnet. Therefore, a procedure is presented which allows alignment with precision better than one tenth of a degree. For the measurements of the heat capacity and magnetocaloric effect a special experimental setup is developed and constructed, which withstands the magnetic torque resulting from applying the magnetic field perpendicular to the easy axis.

Kurzzusammenfassung

Im Rahmen dieser Arbeit wird der Quantenphasenübergang in LiHoF$_4$ experimentell untersucht, der selbst bei $T = 0\,\mathrm{K}$ auftritt, wenn man ein externes Magnetfeld senkrecht zur magnetisch leichten Achse anlegt und dieses ein kritisches Feld B_c überschreitet. Die zentrale Fragestellung lautet, wie sich der Phasenübergang entwickelt, wenn man das Magnetfeld gegenüber dieser perfekt senkrechten Ausrichtung verkippt. Mithilfe eines Entmischungskryostaten und Vektormagneten wird das magnetische Phasendiagramm unter verschiedenen Kippwinkeln in den Messgrößen der AC Suszeptibilität, der Wärmekapazität und des magnetokalorischen Effektes vermessen. In der mikroskopischen Theorie erwartet man wegen der Symmetriebrechung beim Anlegen des Feldes unter einem Winkel einen Crossover-Übergang. Im Gegensatz dazu zeigen die Messergebnisse einen klaren Phasenübergang und eine starke Abhängigkeit des kritischen Feldes vom Feldwinkel, was das Hauptergebnis dieser Arbeit darstellt. Deshalb wird in Kooperation mit Kollegen der TU Dresden ein Modell entwickelt, das die ferromagnetischen Up- und Down-Domänen und deren Verhältnis berücksichtigt und es erlaubt die Messdaten quantitativ zu beschreiben.

Alle Experimente setzen eine sehr präzise Orientierung der Probe im Bezugssystem des Vektormagneten voraus, weshalb eine Vorgehensweise beschrieben wird, mit der man eine Präzision genauer als ein zehntel Grad erreichen kann. Für die Messungen der Wärmekapazität und des magnetokalorischen Effekts werden Messaufbauten entwickelt, die dem magnetischen Drehmoment widerstehen können, welches entsteht, wenn das Magnetfeld senkrecht zur leichten Achse angelegt wird.

Contents

1. Introduction

1.1. Quantum Phase Transitions

Following the definitions by Sachdev [1] and Vojta [2], a *quantum phase transition* (QPT) occurs at absolute zero temperature. This transition takes place at a *quantum critical* value of a non-thermal parameter such as pressure, magnetic field or chemical composition. There, quantum fluctuations originating from Heisenbergs uncertainty principle destroy the order.

Various review articles were published over the last decades, which discuss this class of phase transitions [1–3] and provide a thorough overview of the topic. The introduction to the topic relevant to this thesis follows Refs. [2, 4, 5].

In order to discuss the differences between classical *thermal* phase transitions, driven by the reduction of entropy and thermal fluctuations, and *quantum* phase transitions, driven by quantum fluctuations, we will in the following address general aspects of phase transitions. Three cases are commonly differentiated, namely the first and second order phase transition as well as the crossover. These are displayed in Fig. 1.1.1 (A), (B) as well as (C), respectively.

Classification of Phase Transitions Phase transitions can be described using Landau theory using a local order parameter, in the following M. This order parameter can be found by minimizing the Landau free energy, which is a function determined from Taylor expansion, only including terms allowed by symmetry [6]. The Landau free energy for a first order phase transition is shown in Fig. 1.1.1 (A1). Within the ordered phase, the system has two global minima at the order parameter $\pm M$ and a local minimum at $M = 0$. When an external parameter g, such as the temperature for a thermal transition, or

magnetic field, pressure or chemical composition for a QPT, is varied the energy landscape changes. At the first order phase transition, the minima at finite $\pm M$ and $M = 0$ coexist. Accordingly, the coexistence of the ordered and disordered phases at this point is a defining feature of first order phase transitions. By increasing the external parameter further, the minimum at $M = 0$ evolves from a local to global minimum and the order parameter jumps to $M = 0$. The order parameter as a function of the external parameter is shown in (A2). The values of M in the minimum are displayed as dots both in (A1) and (A2) for comparison.

A second order phase transition is shown in Fig. 1.1.1 (B). An example for a system displaying such a *continuous phase transition* is the easy-axis ferromagnet (as LiHoF$_4$), where M is the magnetization along the easy-axis per site. For symmetry reasons, only even terms are included in the Landau free energy

$$F(M) = \frac{a}{2}M^2 + \frac{b}{4}M^4.$$

(1.1.1)

The coefficients a and b are functions of the external control parameter g. In this case, $b > 0$ across the phase transition and $a > 0$ only in the disordered phase. Then, the Landau free energy only has a single minimum at $M = 0$, cf. Fig. 1.1.1 (B1), and the order parameter vanishes in the disordered phase as expected. At the critical point $a = 0$, marking the second order phase transition. Within the ordered phase, $a < 0$ and two degenerate minima can be observed at $\pm M$. The system orders, as the degeneracy of both minima reflects the symmetry of the system. This symmetry is spontaneously broken, as one of the solutions is realized. Fig. 1.1.1 (B2) shows the order parameter M as a function of the external parameter g, which continuously decreases as g is increased, until it reaches $M = 0$ at the critical point.

In contrast to the above examples, a crossover is no phase transition, as the order parameter is always finite. A simple example for a crossover can be given by including an external magnetic field along the easy axis in the example given above. This leads to an additional linear term in the Landau free energy, which breaks the symmetry

$$F(M) = \frac{a}{2}M^2 + \frac{b}{4}M^4 + hM.$$

(1.1.2)

The Landau energy then has only one single minimum at a finite $M > 0$, cf. Fig. 1.1.1 (C1). The order only decreases across the crossover, but never reaches zero as shown in (C2).
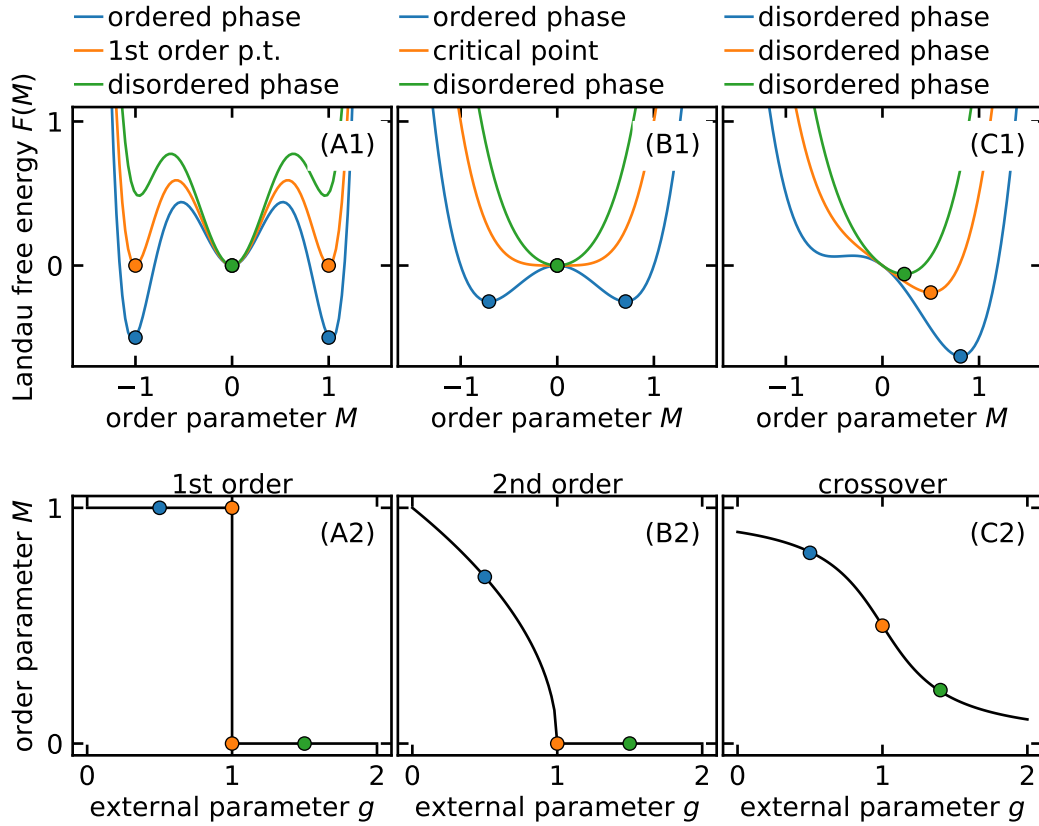
Figure 1.1.1.: Classifications of phase transitions in Landau theory. (A1, B1, C1) The Landau free energy $F(M)$ as a function of the order parameter M for three choices of an external parameter g. Within the ordered phase (blue), two symmetric minima are observed and the disordered phase only displays one minimum (green). (A1) At the first order phase transition, three global minima are observed simultaneously. (A2) Thus the order parameter jumps as a function of the external parameter g. (B1) At the critical point of the second order phase transition the two minima have merged into one minimum . (B2) Simultaneously, M goes to zero continuously at the critical point. (C1) For the crossover, independent of the external parameter g, only one minimum is observed. (C2) The order parameter M decreases continuously without reaching zero.

Critical Behavior For the discussion of QPTs, the case of the second order phase transition is most interesting. While the thermodynamic mean of the order parameter is zero in the disordered state, fluctuations around this value remain. These fluctuations can be described by a correlation length ξ and a correlation time τ. When approaching the critical point, the spatial correlation length of the order parameter diverges as

$$\xi \propto |g - g_c|^{-\nu}, \tag{1.1.3}$$

with ν being a so called *critical exponent*. Similarily, the lifetime of the fluctuation diverges as

$$\tau \propto \xi^z \propto |g - g_c|^{-\nu z}, \tag{1.1.4}$$

with z another critical exponent. These divergences lead to the so-called critical phenomena [2]. At the critical point of the phase transition, both ξ and τ are infinite. Thus fluctuations happen on all length- and timescales. The system becomes scale invariant, as the observables are described by power laws and their properties are qualitatively identical on both small and large scales. A set of so-called *critical exponents* corresponding to these power laws describe the behavior of many physical properties near a particular phase transition. The most commonly used definitions of critical exponents are shown in Tab. 1.1.1.

Table 1.1.1.: Important critical exponents at second order phase transitions [2] relevant to this work.

	Exponent	Definition
Specific heat	α	$C \propto |g - g_c|^{-\alpha}$
Order parameter	β	$m \propto (g_c - g)^{\beta}$
Susceptibility	γ	$\chi \propto |g - g_c|^{-\gamma}$
Correlation length	ν	$\xi \propto |g - g_c|^{-\nu}$
Dynamic	z	$\tau \propto \xi^z$

Mean-Field Theory   The *mean-field* ansatz is probably the simplest approximation used in the context of phase transitions. This ansatz replaces all individual degrees of freedom within the systems by their average. For example, in a magnetic system, the influence of every individual spin on one local moment is replaced by the mean magnetic field generated by all spins in the sample. For this approach to be reasonable, the mean-field must be calculated self-consistently, which is often done by iteration [5]. A drawback of the mean field method is that by replacing the individual degrees of freedom with a model for its mean only descriptions consistent with this model will be found.

At this point it needs to be noted, that the mean field approximation neglects fluctuations [2, 5]. Since fluctuations around this mean value become increasingly important when the dimensionality of the system is reduced, mean-field theory is only accurate in systems with a dimension greater than the upper critical dimension $d \geq d_c^+$. In this case, every site has a large number of neighbors, thus fluctuations average out. For systems with short range interactions and scalar order parameters, the upper critical dimension is $d_c^+ = 4$. At $d = d_c^+$ logarithmic corrections to the power laws discussed above need to be taken into account.

In this context, an important difference between thermal and quantum phase transitions needs to be highlighted. In the classical case of a thermal transition, the kinetic and potential energies commute in the Hamiltonian and thus static and dynamic can be decoupled. This means, that the singularities at the phase transition are only caused by the potential energy terms and such transition can be described by a static theory in d dimensions. In contrast, a theory of a QPT must include dynamics, since kinetic and potential energy are linked by the laws of quantum mechanics. Therefore the necessary dimensionality increases, since both time and space need to be included. It can be shown, that a QPT in d dimensions is related to a classical transition in $d + z$ dimensions, where z is the critical exponent of the lifetime fluctuations as shown in Tab. 1.1.1 [2]. Therefore the QPT of the 3d transverse field Ising model of $LiHoF_4$ can be described with mean field theory including logarithmic corrections due to the dynamic critical exponent $z = 1$ and thus $D = d + z = 3 + 1 = d_c^+ = 4$.

While the QPT can be described using the scaling laws above, this description is only valid for ground states and thus at $T = 0$. The quantum critical point (QCP) however still influences the physical properties in its proximity. At finite temperature these properties
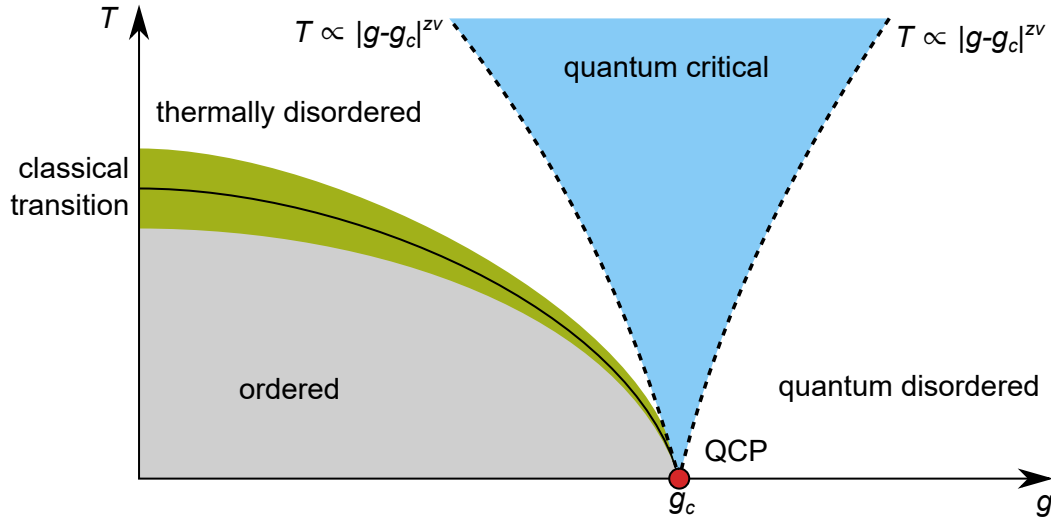
Figure 1.1.2.: Phase diagram of a typical quantum phase transition with dimensionality $d \geq 2$. The transition is controlled by a non-thermal control parameter g. At low temperature and order parameter, the system shows an ordered phase. With increasing $g > g_c$ above the quantum critical point (QCP) where $g = g_c$, the system becomes quantum disordered. Above the QCP, a quantum critical regime evolves, where thermal fluctuations can couple to quantum entangled states. Figure adapted from Refs. [2, 4].

are dominated by two relevant energy scales, the thermal energy $k_B T$ and long-range order parameter fluctuations $\hbar \omega_c$, which vanish at the QCP

$$\hbar \omega_c \propto |g - g_c|^{\nu z}. \tag{1.1.5}$$

From this we will discuss the phase diagram for a QPT depicted in Fig. 1.1.2. Three different regions can be distinguished, which are separated by the dashed lines corresponding to $T \propto |g - g_c|^{\nu z}$. In the regime of $g \ll g_c$ thermal disorder dominates as order is destroyed by classical thermal fluctuations of the order parameter. Here, an ordered phase can arise, when the temperature is low enough. The corresponding transition line of this ordered phase is entirely classical down to lowest temperatures. For $g \gg g_c$, a quantum disordered regime is observed, where quantum fluctuations dominate the physics [2]. In between is the so-called quantum critical region, where both types of fluctuations are important. This regime is the blue region between the dashed lines in Fig. 1.1.2, determined by the condition $k_B T > \hbar \omega_c \propto |g - g_c|^{\nu z}$. Here, the system appears critical with respect to the external parameter g, but is driven away from criticality by thermal fluctuations. In this quantum critical region, the physics is governed by thermal excitations of the quantum critical ground state, whose main characteristic is the absence of conventional excitations

with quasi-particle behavior. This regime therefore often displays unusual behavior, such as unconventional power laws and non-Fermi liquid behavior. Interestingly, this quantum critical nature is sometimes enhanced with increasing temperature [3, 7] and in this case accessible for experiments. The quantum critical behavior however is cut of at high temperatures as soon as $k_B T$ exceeds the microscopic energy scales of the problem, such as the exchange energy for typical magnets.

1.2. State of the Art: LiHoF$_4$

The conceptually simplest example of a quantum phase transition [8] arises from the response of an insulating easy-axis ferromagnet to a magnetic field applied transverse to the preferred magnetization axis. This transverse-field quantum magnetism is of broad interest, as it allows to benchmark, among other things, the quantum entanglement of complex spin systems, the tunneling of single magnetic moments and domain walls, quantum annealing, and Rabi oscillations [9–11]. The most extensively studied material featuring such transverse-field phenomena is LiHoF$_4$, in which AC susceptibility and inelastic neutron-scattering measurements have long identified Ising ferromagnetism that vanishes in a QCP at $B_c = 5.1$ T [12–14].

Outside of the interest in basic research outlined below, LiHoF$_4$ recently caught attention due to its magnetocaloric properties as a possible medium for adiabatic demagnetization cooling [15]. Additionally, LiHoF$_4$ is structurally very similar to LiYF$_4$, which doped with Neodymium finds large scale application as a lasing medium in solid state lasers. Therefore, high quality crystals of LiHoF$_4$ are commercially available nowadays[1]. For information about the typical growth procedure using the Bridgman-Stockbarger and Czochralski methods refer to Ref. [16].

In the following the crystalline structure and its effect on the energetic landscape of the magnetic ions will be described. This will be followed by a summary of the important magnetic properties of LiHoF$_4$. Based on this knowledge previous work on the ferromagnetic phase will be summarized, including the search for logarithmic corrections around the thermal phase transition as well as magnetic domain formation and dynamics. Following that, the transverse field Ising model will be presented in the context of LiHoF$_4$, discussing the developments in the description of the magnetic phase boundaries and quantum criticality.

---

[1]The samples used in this thesis were purchased at Altechna / AcalBFI Germany.

1.2.1. Crystal Structure and Magnetic Properties

LiHoF$_4$ is a paramagnetic insulator at room temperature. It crystallizes in a tetragonal scheelite structure visualized in Fig. 1.2.1 (A) with lattice constants $a = b = 5.175$ Å, $c = 10.75$ Å and in the space group C_{4h}^6 ($I4_1/a$) [17]. The Ho^{3+} ions in $4f^{10}$ [18] configuration occupy positions with S_4 point symmetry. Their electronic spin is $J = 8$ and nuclear spin is $I = 7/2$ [12]. The large local magnetic moments of the Ho-ions ($\approx 7\mu_B$ per Ho-ion) order ferromagnetically below the Curie temperature of $T_c = 1.53$ K [19]. Within this ordered state the spins align parallel to the easy axis due to the Ising-like magnetic anisotropy ($g_\parallel \approx 14$, $g_\perp \approx 0$ [20]). While the crystalline c-axis represents the easy axis, no magnetic anisotropy is observed in the ab-plane [19, 20]. The ferromagnetic order is driven by dominant long-ranged dipolar interactions between the magnetic ions as well as weak short-ranged exchange interactions.
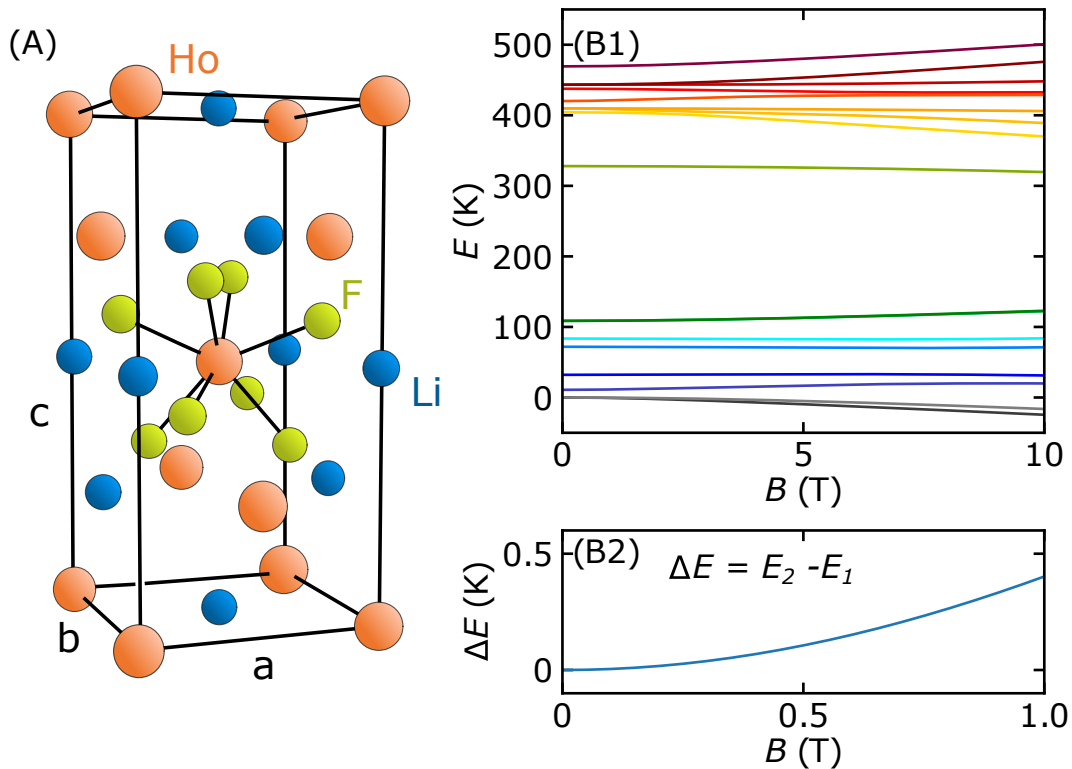
Figure 1.2.1.: Crystal structure and crystalline electric fields of LiHoF$_4$. (A) Crystallographic unit cell of LiHoF$_4$ with a four-fold symmetry along the c-axis, which represents the magnetic easy axis. (B1) Crystal field spectrum of the Ho^{3+} ions as a function of a magnetic field applied within the ab-plane. (B2) The splitting of the to lowest-lying CEF levels show a quadratic field dependence characteristic of the non-Kramers nature of the Ho ions. Figure adapted from Ref. [21].

LiHoF$_4$ is part of a larger family of compounds LiREF$_4$ where RE is a trivalent rare earth ion such as Ho, Tb, Yb or Er [20, 22–26]. This class of materials offers the advantage that it is relatively easy to replace the magnetic RE ions with Y to dilute and disorder the system to create and discover interesting physics like (anti)glass states, quantum annealing, domain wall tunneling, coherent spin oscillations and quantum entanglement [27–38].

The crystalline electric field (CEF) at the location of the Ho^{3+} ions exhibits an S_4 symmetry originating from the surrounding F^- ions. It lifts the 17-fold degeneracy of the $^5I_8$ configuration, such that the ground state is a non-Kramers doublet. Applying a magnetic field transverse to the easy c-axis ($\Phi = 0$) changes the energies of the CEF levels as shown in Fig. 1.2.1 (B1). Due to the non-Kramers nature of the Ho^{3+} ions, the ground state doubletsplits with a quadratic field dependence, cf. Fig. 1.2.1 (B2). The CEF levels were studied in various works with neutron spectroscopy, electron paramagnetic resonance (EPR) and optical spectroscopy [14, 20, 22, 39, 40] which report similar values for the parameters. The theoretical model presented in Sec. 2.4 uses the parameters published in Ref. [41].

As it will be shown later in Sec. 2.4.1 this non-Kramers nature of the Ho-ions has important implications on the model of domain driven phase transitions in LiHoF$_4$. Earlier studies [12, 14, 41, 42] neglected all higher levels due to their large separation from the ground state doublet and treated this doublet as an effective spin 1/2. Since the ground state doublet are not Kramers partners, they are not related by time reversal symmetry and a polarization along the x-direction as a reaction to transverse field cannot be achieved by a simple superposition of up- and down states but must involve higher excited states [5].

Due to the large nuclear spin ($I = 7/2$), a large hyperfine interaction of the nuclear spin and electronic states via a core polarization effect arises [12, 43], which influences the static and dynamic properties of LiHoF$_4$ at low temperatures ($< 800\,\text{mK}$). From early specific heat [43] and EPR [22] measurements the hyperfine constant was determined as $A = (A_\parallel)g/g_\parallel = 0.039\,\text{K}$ with $A_\parallel = 0.43\,\text{K}$, the Landé factor $g = 1.25$ and the ground state longitudinal g-factor $g_\parallel = 13.8$ [12].

1.2.2. Ferromagnetic Phase

First investigations of LiHoF$_4$ in the 1970s and 1980s focused on the classic ferromagnetic phase transition at the Curie temperature of $T_c = 1.53$ K in zero field. Critical phenomena and logarithmic corrections to classic Landau theory were topic of theoretical and experimental investigations [44]. LiHoF$_4$ caught special attention since for an uniaxial dipolar ferromagnet the spatial and marginal dimension are equal $d = d^* = 3$ and thus are a perfect system for testing theoretical predictions [45–48].

Logarithmic Corrections In this context, first measurements of the specific heat in LiREF$_4$ compounds, namely LiTbF4, were performed in the 1970s by Holmes *et al.* [49] and Ahlers *et al.* [50]. They claimed to have found logarithmic corrections to the specific heat from Landau theory. When Mennenga *et al.* [43] investigated the specific heat of LiHoF$_4$ in the temperature range of $T = 0.06 - 7$ K almost one decade later, they did not search for such logarithmic corrections, since this requires a very good temperature resolution around the phase transition. Only when approaching the phase transition as close as $\epsilon = |T - T_c|/T_c \approx 10^{-5} - 10^{-6}$, these effects could be distinguished from normal specific heat behavior. Lattice defects, impurities, etc. reduced the approachable distance to the transition to $\epsilon \approx 10^{-3}$ [43].

In 2001, Nikkel *et al.* [51] performed additional specific heat measurements and confirmed renormalization group predictions at the critical dimension of LiHoF$_4$ in the proximity of the thermal phase transition ($T_c \pm 4\%$). By combining their measurements with existing data from magnetization and susceptibility they were able to confirm logarithmic corrections $C_p \propto \log^{1/3}(\epsilon)$ akin to Ref. [50]. The properties of the temperature driven, classical phase transition was again investigated by Biltmo *et al.* [52] using Monte-Carlo simulations providing further evidence for logarithmic corrections. Furthermore, the authors emphasized that magnetic domains and sample shape play an important role in the ordered state due to the long-range and angular dependence of the dipolar interaction.

Magnetic Domains In the study by Biltmo *et al.* [52] domains appeared naturally in Monte-Carlo simulations and the authors predicted a ground state domain pattern of thin parallel sheets for cylindrical LiHoF$_4$ samples. Since the domain walls showed no width, the authors recommended LiHoF$_4$ as an ideal testing ground for domain physics. Magnetic
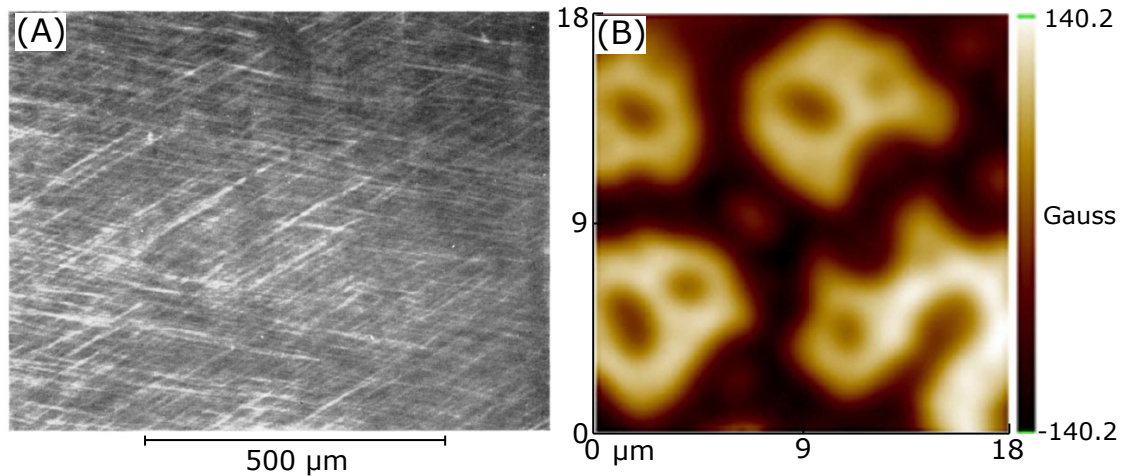
Figure 1.2.2.: Experimental observations of domain structure in the ferromagnetic phase of LiHoF$_4$. (A) Image taken by Battison *et al.* [53] via light scattering at the domain walls at 1.4 K. The white stripes are the domain walls perpendicular to the *c*-axis. The two stripe patterns are a result of two crystal layers being observed at the same time. (B) Scanning hall probe microscope image of LiHoF$_4$ at 40 mK by Karci *et al.* [54]. Both images show domains of a few micrometer in size. Both pictures taken from their respective Refs..

domains in LiHoF$_4$ were part of several studies with their first mention in Refs. [19, 53] which provided a first image of the domains at 1.4 K, shown in Fig. 1.2.2 (A). They found domain walls perpendicular to the *c*-axis with domain sizes in the μm-regime.

Pommier *et al.* [55] and Meyer *et al.* [56] investigated the magnetic phase diagram of LiHoF$_4$ with field applied to along the easy *c*-axis in the vicinity of the thermal phase transition. Using Faraday rotation, they found stripe like domains at low fields and bubble like domains at larger fields. In low fields, up- and down-domains are populated equally. With increasing field, the volume ratio of the domains changes until at large fields the volume fraction of the down domain gets so small that they collaps into bubbles. Furthermore the authors discussed the effects of domain nucleation near the surface from spike like domains.

Later, Karci *et al.* [54] observed bubble-like domain structures with μm-size at a much lower temperature of 40 mK, cf. Fig. 1.2.2 (B). The authors utilized scanning Hall probe microscopy [57], which is only sensitive to the surface. They conclude that the ground state domains in LiHoF$_4$ are needle shaped cylinders and explain their formation - and the differences to the study of Biltmo *et al.* [52] - with branching effects at the surface. Pau
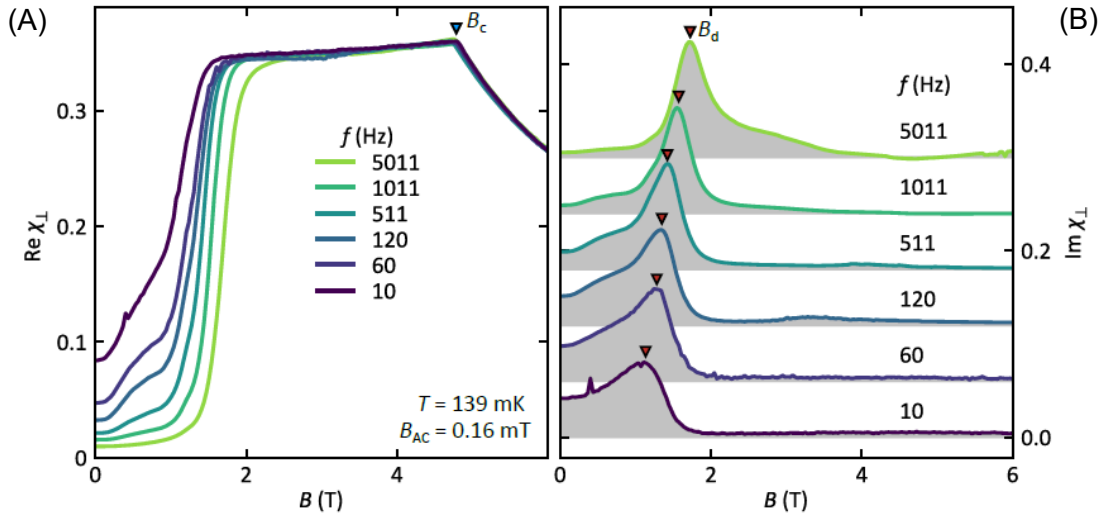
Figure 1.2.3.: Frequency dependence of the real and imaginary parts of the susceptibility of LiHoF$_4$ in the low temperature region. (A) Re $\chi_\perp$ as a function of the magnetic field at $T = 139\,\text{mK}$ for excitation frequencies between $f_{AC} = 10\,\text{Hz}$ and $501\,\text{Hz}$. (B) Im $\chi_\perp$ as a function of the magnetic field at $T = 139\,\text{mK}$ for various frequencies. Im $\chi_\perp$ shows a strong peak-shaped contribution at low magnetic fields for all measured frequencies, indicated by red triangles. Figure taken from Ref. [4].

Jorba [57] also conducted studies varying the transverse magnetic field and temperature as part of his master thesis with the same setup. He observed denser domains at higher temperatures, which are consistent with the predictions about branching effects in dipolar magnets by Gabay *et al.* [58], which were also investigated in greater detail for the example of LiTbF$_4$ [59, 60]. At $T \approx 30\,\text{mK}$ Jorba observed significant changes of the domain structure even at small transverse fields, with some domains shrinking rapidly. Their measurements were limited to the regime below $3\,\text{T}$ due to instrument resolution and and the domain size growing larger than their field of view. Furthermore, the authors directly observed domain freezing at very low temperatures, when comparing the field cooled and zero-field cooled states.

Evidence for such a reduction of domain-wall mobility was also observed in the studies by Bitko *et al.* [61] and Rucker *et al.* [4] using AC susceptibility in a transverse magnetic field. This domain wall freezing was expressed in several observations. First, with the magnetic field applied perpendicular to the c-axis, the real part of the AC susceptibility at low temperatures ($< 500\,\text{mK}$) and fields ($< 2\,\text{T}$) was suppressed and this effect was more pronounced for larger excitation frequencies as shown in Fig. 1.2.3 (A). Second, the reduction of the real part was complemented by a peak in the imaginary part indicating

dissipation, cf. Fig. 1.2.3 (B). The authors discussed that the domain wall freezing was better visible for higher frequencies as their mobility was reduced such that the domain walls cannot follow the AC field. Furthermore Ref. [4] attributed the recovery of the plateau value at higher fields to quantum fluctuations facilitating tunneling of the domain walls akin to the observations of Brooke *et al.* in the diluted compound $LiHo_{0.44}Y_{0.56}F_4$ [28].

1.2.3. Phase Boundaries and Quantum Criticality

In the previous subsection we covered the developments in the ferromagnetic phase, its dipolar interactions and domains as well as the thermal phase transition. However, $LiHoF_4$ caught an even bigger attention in the study of quantum criticality and quantum phase transitions.

Transverse Field Ising Transition $LiHoF_4$ is described by the transverse field Ising model as a textbook example for a quantum field transition driven by magnetic field [1]. The Hamiltonian reads

$$H = -J \sum_{\langle i,j \rangle} S_{iz} S_{jz} - g_e \vec{H} \cdot \sum_i \vec{S}_i, \tag{1.2.1}$$

where the electronic spins $\vec{S}_i$ sit on the lattice sites i, j and interact via the ferromagnetic Ising interaction $J > 0$ of the z-components. The first sum $\langle i,j \rangle$ runs over the nearest neighbors. This notation of the Hamiltonian considers a vectorial magnetic field $\vec{H}$ applied transverse to the Ising axis, which interacts with the spins. The vector description is a improvement of the model introduced by our collaborators from theory [5, 21] necessary to describe the effects of rotating the magnetic field. Earlier publications of the transverse field Ising model and $LiHoF_4$ ignore this facet [12, 13, 62].

For a vanishing transverse field $H \rightarrow 0$ ferromagnetic order along the z-direction develops. In strong external magnetic fields $H \rightarrow \infty$ the spins align parallel to the field direction x. Between both limits a second order phase transition from the ordered ferromagnetic to the disordered field polarized state occurs at a critical field H_0.

The first descriptions of such order-disorder transitions date back to the sixties, when de Gennes investigated ferroelectric materials [63]. In the seventies, it was established that
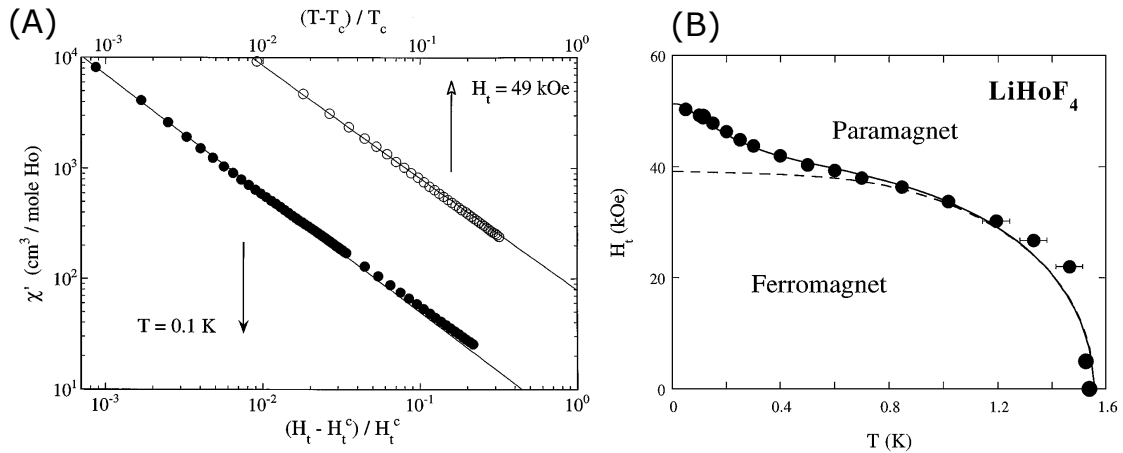
Figure 1.2.4.: Key results of the transverse susceptibility study of the transverse-field Ising transition in LiHoF$_4$ by Bitko *et al.* [12]. (A) Mean field critical behavior of the magnetic AC susceptibility as a function of temperature and field. The lines represent fits to the data corresponding to a critical exponent $\gamma = 1.07 \pm 0.11$ (solid circles) and $\gamma = 1.01 \pm 0.08$ (open circles). (B) The experimental phase boundary shown as circles is compared to the mean-field theory only incorporating electronic spins (dashed line) and also including the nuclear hyperfine interaction (solid line). Figure adapted from [12].

QPTs of Ising systems, such as in LiHoF$_4$, in d-dimensions can be mapped to the same universality class as the classical $(d + 1)$-dimensional Ising model [62, 64, 65], cf. Sec. 1.1. Bitko *et al.* [12, 61] found that the critical exponent $\gamma \approx 1$ has a mean field value both in the classical and quantum limit down to temperatures as low as 50 mK, cf. Fig. 1.2.4 (A). They describe the phase boundary above 0.6 K in terms of a classical mean-field model of a spin-$\frac{1}{2}$ magnet in transverse field. The corresponding phase boundary is shown in Fig. 1.2.4 (B) as a dashed line. Below $T = 0.6$ K this model clearly does not represent the experimental data. Hence, Bitko *et al.* attributed this feature with an additional hyperfine term. It arises from the interaction of the nuclear spins of the Ho-ions with the electronic states through a core polarization effect. Their effective mean-field Hamiltonian utilized the transverse g-factor $g_\perp$ and an effective dipole coupling strength J_0 as free parameters.

In 2004 Chakraborty *et al.* [41] described the magnetic phase diagram of LiHoF$_4$ theoretically by going beyond mean-field theory and employing a quantum Monte Carlo method. The influence of domains was incorporated into the model by considering an imaginary sphere deep within a single domain and clever utilization of the demagnetization factor in a partly mean-field approach. While pure mean-field treatment overestimates the size of the ferromagnetic regime, both in field and temperature, the authors were able to

reproduce the experimental phase diagram of Bitko *et al.* [12] qualitatively by tuning their parameters, see Fig. 1.2.5 (A). The authors emphasized the importance of hyperfine interactions for the low temperature physics and included an antiferromagnetic exchange interaction, which helped to reduce the critical temperature to the experimental value.

Electronic Mode Softening   The next big developments in the studies of the QPT in LiHoF$_4$ were brought by a series of works by Rønnov and coworkers, who studied the excitation spectrum using triple-axis neutron spectroscopy [13, 14, 66]. The excitations with lowest energy known at that time were magnons, at a QPT and $\vec{k} = 0$, the gap of such a lowest lying excitation should vanish according to Eq. (1.1.5). In contrast, the authors observed a incomplete softening with a remaining energy gap of $\Delta E = 0.24$ meV, cf. Fig. 1.2.5 (B). They attribute this to the hyperfine coupling, which shunts the electronic mode and raises the critical field. Additionally, the hyperfine interaction leads to a broadening of the peak $Q = (2, 0, 0)$ in reciprocal space, showing that it limits the electronic quantum coherence by coupling to the nuclear spin bath [13]. The features of the strong magnetic mode, which softens at the QPT highlight the impact of the hyperfine interaction. Lowering the field, coming from the field polarized paramagnetic phase, the mode follows the predictions from a ordinary transverse field Ising model. Once the energy of the mode becomes comparable to the hyperfine interaction strength, new modes appear, which are much lower energy. Therefore the ferromagnetic state emerges prematurely and the complete softening of the electronic mode is prevented.

Differences between theory and experiments were attributed to domain walls and magnetoelastic couplings [14]. Another glaring difference between these neutron spectroscopy studies and the AC susceptibility measurements by Bitko is that the "nose" at low temperatures and high fields, attributed to the hyperfine coupling is not visible in the neutron data, cf. Fig. 1.2.5 (A). Rønnow *et al.* explained this discrepancy with insufficient thermal coupling of the sample, meaning the sample temperature is never cooler than $T \approx 310$ mK, even when the temperature reading of the sensor at the cooling stage is lower [14]. In another study from the same group carried out by Krämer [66], a better thermalization was achieved and thus the feature observed. The maximum critical field at $T \approx 45$ mK however was only $H_c \approx 4.7$ T. As shown in this thesis, such a reduction of critical field can be explained by sample misalignment.
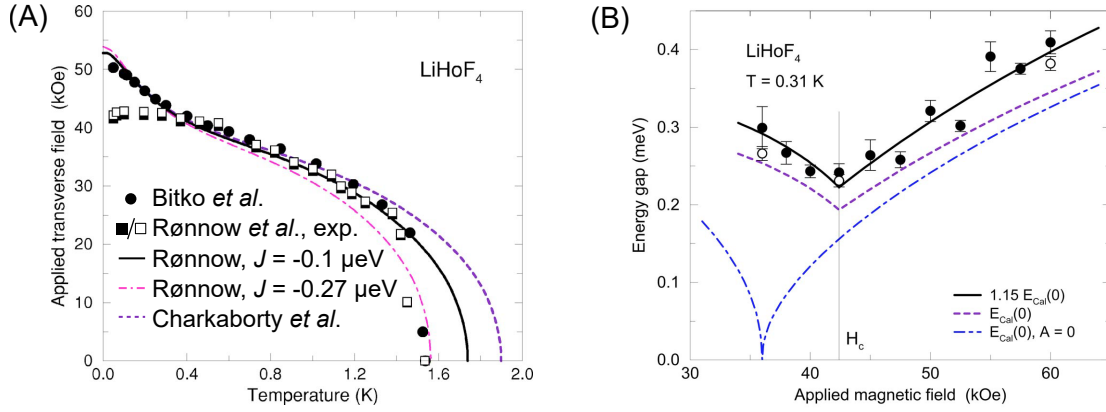
Figure 1.2.5.: Key results of Rønnow *et al.* [14]. (A) Direct comparison of experimental re-
sults and theoretical models. The experimental phase diagram of Bitko *et al.*
[12] is shown as solid circles. The experimental phase boundary determined
by Rønnow *et al.* [14] using neutron spectroscopy is shown as squares. Using
the additional free parameter J, an exchange coupling term, the phase diagram
could not be reproduced exactly. Adjusting it to the correct behavior at high
fields, leads to an overestimation of the Curie temperature in zero field. Also the
model by Chakraborty *et al.* overestimates the transition temperature, when the
same parameters are applied, that Rønnow used. (B) The energy gap of the low-
est excitation accessible to the triple-axis neutron spectroscopy measurements at
$T = 310\,\mathrm{mK}$. Neglecting the hyperfine interaction leads to the blue dotted-dashed
curve, whereas the model of Rønnov leads to the purple dashed line, which is a
factor of 1.15 lower than the experimental data. Figure taken from Ref. [14].

Electronuclear Mode Softening   The energy landscape and details of the mode soften-ing were analyzed in greater detail by McKenzie and Stamp [42]. Their work focused on incorporating both thermal and quantum fluctuations in the description of the quantum Ising system coupled to the spin bath. Their main finding was that quantum Ising sys-tems, like $LiHoF_4$, show a QPT, even if the system is coupled to a spin bath and quantum fluctuations are taken into account. Long-range dipolar interactions enhance fluctuations, but do not destroy the QPT. The QPT can be destroyed if the nuclear (bath) spins are frozen. As shown in Fig. 1.2.6 the electronic mode in blue was gaped, consistent with the observations by Rønnov *et al.*. Simultaneously, the electronuclear mode in red soft-ened at the QPT and developed a sharp peak in intensity, diverging at the QPT. Their model however did not include thermal fluctuation at this point, thus Fig. 1.2.6 is in the zero-temperature limit.

To verify their predictions, McKenzie and Stamp worked together with Libersky *et al.* [67], who studied the mode softening around the QPT using microwave spectroscopy very recently. The authors observed a variety of electronuclear modes at very low energies of only several μeV, inaccessible for neutron TAS. They observed (incomplete) mode softening of the lowest electronuclear mode at $1\,\text{GHz} \approx 4\,\mu\text{eV}$ and $B = 4.7\,\text{T}$, which is lower than the critical field predicted in theory and measured by AC susceptibility [4, 12]. After accounting for the experiment temperature of $T = 55\,\text{mK}$ in the calculations, they showed that this can be identified with the soft mode, which weakly interacts with the 14 other electronuclear modes. Additionally they were able to show that the soft mode can be quenched by applying a finite longitudinal magnetic field. Libersky *et al.* were able to describe this behavior only by incorporating magnetic domains with finite domain wall energies.

Taken together these studies of the mode softening in $LiHoF_4$ showed that the material is a good candidate for a QCP and sensitive to longitudinal magnetic fields. Simultaneously, other experimental work focused on the details of the magnetic phase diagram, which opens another perspective on the same topic.
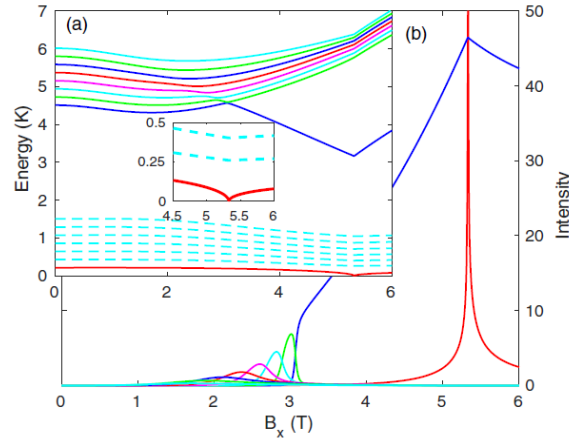
Figure 1.2.6.: Theoretical prediction of the modes in LiHoF$_4$ by McKenzie and Stamp [42]. (a) Energies of the zero-temperature modes at k = 0, as a function of transverse field B_x, obtained by RPA. The inset shows the electronuclear soft mode in the vicinity of the QCP. Dashed lines correspond to modes with negligible spectral weight. (b) Intensities of the modes. Figure taken from Ref. [42].

Phase Diagram   Since both Chakraborty and Rønnov could not present a complete theoretical model for the experimental observations without using free scaling parameters, Tabei *et al.* [68] revisited the microscopic Hamiltonian using pertubative quantum Monte Carlo to resolve the remaining issues. Although they excluded deficits of the theoretical tools, discussed in Ref. [41] as reasons for the incomplete picture, Tabei *et al.* were not able to modify the Hamiltonian to describe the complete phase diagram.

Legl *et al.* performed measurements of the magnetization in a vibrating coil magnetometer [44, 69], allowing measurements of the magnetization at mK-temperatures. Their key result was that the magnetization component perpendicular to the easy-axis shows a broadening at the phase transition down to the lowest temperatures, in contrast to the model proposed by Rønnow at this time. They interpreted this as a thermal broadening of the nuclear excitation spectrum within the picture of the coupled electronuclear system.

Simultaneously, Sarah Eisenhardt [70] investigated the magnetization of LiHoF$_4$ at mK-temperatures in her masters thesis using Cantilever magnetometry. In her experiments at the EPFL and University of Copenhagen she failed to observe the QPT due to a sample misalignment of 4°. She afterwards highlighted the complications by simple mean field calculations at finite misalignment angles.

C. Duvinage [71] continued the VCM studies of Legl *et al.* and investigated the impact of sample alignment on the hard axis magnetization under transverse magnetic field. It became obvious that such changes had a significant impact on the phase diagram in transverse fields as the critical field decreased for larger misalignment of the sample. The impact of the alignment angle, which was previously determined by X-ray Laue diffraction, however was difficult to quantize.

In order to investigate several inconsistencies in the theoretical modeling, like the broadening of the field driven phase transition at low temperatures observed by Legl and calculations typically predicting either the critical field or critical temperature too large, F. Rucker [4] continued to study the magnetic phase diagram of $LiHoF_4$ with great precision using AC susceptibility in transverse magnetic fields [72]. To achieve a better sample orientation he used a 2D vector magnet. His detailed description of the magnetic phase diagram highlighted the effects of domain wall freezing for $T < 500\,\mathrm{mK}$ and $B < 2\,\mathrm{T}$, an additional contribution to the AC susceptibility at $T < 500\,\mathrm{mK}$ and $B > 4\,\mathrm{T}$ originating from the hyperfine interaction and discovered a reentrant behavior of the phase boundary around the thermal phase transition at $T \approx 1.53\,\mathrm{K}$ and $B < 2\,\mathrm{T}$. Additionally these studies confirmed the critical behavior of the phase transitions in $LiHoF_4$ described earlier by Bitko *et al.* [12]. As part of the sample orientation Ref. [4] showed that the vector magnet is a good tool to investigate the angular dependence quantitatively, recommending detailed studies of the phase diagram at various angles.

1.3. Open Questions: Angular Dependence and Mesoscale Quantum Phase Transitions

Previous experimental and theoretical studies summarized above left several key questions unresolved. While several more recent studies acknowledge the importance of the sample orientation of the LiHoF$_4$ system, neither a quantitative experimental nor theoretical study of these effects was performed. Explicitly, the development of the magnetic phase diagram as a function of relative orientation of the crystalline c-axis and the magnetic field is unknown. Several experimental studies presented and discussed the formation and shape of magnetic domains in the ferromagnetic phase of LiHoF$_4$. In theoretical modeling however, the magnetic domains play only a minor role and their interaction with the microscopic system is often neglected. Apart from the early measurements of Mennenga *et al.*, no specific heat data are available at mK-temperatures. Furthermore, no data are available in transverse magnetic fields despite the heat capacity being one of the most important observables for the energy and entropy landscape of a magnetic system.

One special curiosity is the behavior of LiHoF$_4$ under a finite field angle Φ, thus with field components both perpendicular and parallel to the easy c-axis. As described earlier such a field parallel to the easy axis breaks the symmetry of the ground state as it forces a global minimum of the Landau free energy at a finite order parameter, cf. Eq. (1.1.2). Therefore, microscopic theory expected a crossover as a function of magnetic field in LiHoF$_4$ under finite field angles, cf. Fig. 1.1.1. As it will be shown in this thesis, this cannot be observed in our experiments, leading to the discovery and description of a new kind of QPT governed by magnetic domains.

Magnetic domains are a type of mesoscale pattern that forms in ferromagnets and hence can be observed in LiHoF$_4$, as seen in multiple studies described above. Mesoscale patterns reflect spatial variations of order parameters on length and timescales that may be described classically. Ferromagnets, ferroelectrics, superconductors, monomolecular films or block copolymers all fall in this category. The theory of quantum phase transitions, however, typically neglects such patterns in their microscopic description. As part of this thesis, it should be explored, how both length scales interact and what influence mesoscale patterns have on QPTs. Thus the possibility of mesoscale quantum phase transitions will be investigated.

1.4. Thesis Outline

The experimental studies presented in this thesis aim to resolve the questions stated above, thus the thesis is organized in the following way. This first chapter gives an overview of the the LiHoF$_4$ system and related research.

The second chapter presents the AC susceptibility studies of the magnetic phase diagram under varying magnetic field orientation and a theoretical model which describes the observations in the picture of a mesoscale quantum phase transition. The chapter starts with a introduction of the AC susceptibility technique and the experimental setup. Special focus is given to the sample alignment with the magnet, which is crucial for a precise measurement of the field angle relative to the crystalline c-axis. Then, the experimental results are presented, focusing on the magnetic phase diagram, its angular dependence and an analysis of the critical exponents around the field driven transition. Thereafter, the results are compared to previous studies by Bitko *et al.* and Rucker *et al.*. After a short remark about the discrepancy of experimental observations and expectations from microscopic models mentioned above, the chapter continues to explain a theoretical model which was developed by H. Eisenlohr and M. Vojta from TU Dresden after discussion of the new experimental observations in this thesis. Afterwards, this model of domain driven phase transitions is successfully compared with the results. The section concludes with a summary of the results and outlook about future research options.

In the third chapter, the caloric properties of LiHoF$_4$ under transverse magnetic fields are investigated. After a short introduction of the underlying principles, relaxation time specific heat and magnetocaloric measurements are explained in general. By discussing the challenges of such measurements at low temperatures, the design criteria for the experimental setup are developed. On this basis, the choice of the various components of the novel specific heat setup for measurements at mK-temperatures and under transverse magnetic fields are presented. Following this, the results of the specific heat measurements and magnetocaloric sweeps are presented and compared to other techniques and literature. Finally, these results are compared with the theoretical model developed in the second chapter and a summary of the results is provided.

2. AC Susceptibility in Transverse Magnetic Fields

This chapter covers the experimental and technical aspects of measurements of the AC susceptibility in transverse magnetic fields. The first section gives a definition of the magnetic susceptibility and describes the basic principles of the measurement technique. The technical details of the experimental setup used are discussed thereafter, followed by a presentation of the experimental results. The chapter concludes with a discussion of the theory of a domain driven transition in LiHoF$_4$.

2.1. The Magnetic Susceptibility

Modern condensed matter physics explores a variety of different magnetic structures, ranging from simple ferromagnets or antiferromagnets to more complex structures, like the skyrmion lattice [73] or spin ice [74, 75]. A simple way to describe different kinds of magnetism is to analyze the magnetization M, defined as the magnetic moment per unit cell [76]. Usually this quantity describes the material on a macroscopic scale, where $\mathbf{M}$ is described as a continuous pseudo-vector field up to the edges of the sample. It typically varies as a function of external parameters, such as magnetic field H or temperature T.

The magnetization may in general be described as a function of time and space $\mathbf{M}(\mathbf{r}, t)$ or momentum transfer and frequency $\mathbf{M}(\mathbf{q}, \omega)$. Each representation may be beneficial when describing different physical phenomena, e.g. reciprocal space is helpful when describing periodicity, long range order and spin waves. When the magnetization of a sample as a whole is measured, one investigates the uniform magnetization, corresponding to $\mathbf{M}(\mathbf{q} =$

0). The AC susceptibility measurements performed as part of this thesis measure the uniform susceptibility, thus $\chi(\mathbf{q} = 0)$.

Additional information about the magnetic structure can be derived from the response to time dependent fields. The response of the magnetization in a static magnetic field $\mathbf{H}$ to a small change in field $\delta\mathbf{H}_{\mathrm{AC}}(\omega)$ can be expressed by the magnetic susceptibility tensor χ_{ij}. It describes the change in the magnetization component along spatial direction i in response to a small change of magnetic field $\delta\mathbf{H}_{\mathrm{AC},j}(\omega)$ along direction j, i.e.

$$\chi_{ij}(\mathbf{H}, T, \omega) = \frac{\delta M_i(\mathbf{H}, T)}{\delta H_{\mathrm{AC},j}(\omega)} \tag{2.1.1}$$

where T is the sample temperature, ω is the frequency, and the indizes i and j denote the three spatial directions x, y, and z [4, 72].

The term magnetic susceptibility is widely used and often simplified in the literature for specific situations. In general two generic cases can be differentiated. First, the AC susceptibility χ, in which an oscillating field $\mathbf{H}_{\mathrm{AC}}(\omega)$ is used to probe the response of the magnetization in addition to an applied static field $\mathbf{H}$, stabilizing the magnetic order. Second, letting ω approach zero, the static case, χ^{stat}, in which a small change of the static field H is used to cause a change of the magnetization in the sample.

$$\chi_{ij}(H, T, \omega) \xrightarrow{i,j=x} \chi(H, T, \omega) \xrightarrow{\omega \to 0} \chi^{\mathrm{stat}}(H, T) \tag{2.1.2}$$

In many materials, the static susceptibility may be approximated by the ratio of the magnetization to the static field H [76]:

$$\chi^{\mathrm{stat}}(H, T) = \frac{\delta M(H, T)}{\delta H} \approx \frac{M(H, T)}{H} \tag{2.1.3}$$

To simplify these considerations, we restrict the susceptibility tensor χ_{ij} in Eq. (2.1.2) to diagonal elements only, assuming $i = j$. While the off-diagonal elements of the susceptibility tensor might be quantities of interest, in the context of the work presented in this thesis we expect the materials to show the largest response along the excitation axis and therefore keep this restriction.

The magnetic susceptibility χ is the defining response function of magnetic phase transitions. It diverges at the second order phase transition from a paramagnet to a ferromagnet. For experimental studies, additionally the demagnetization factor N needs to be included.
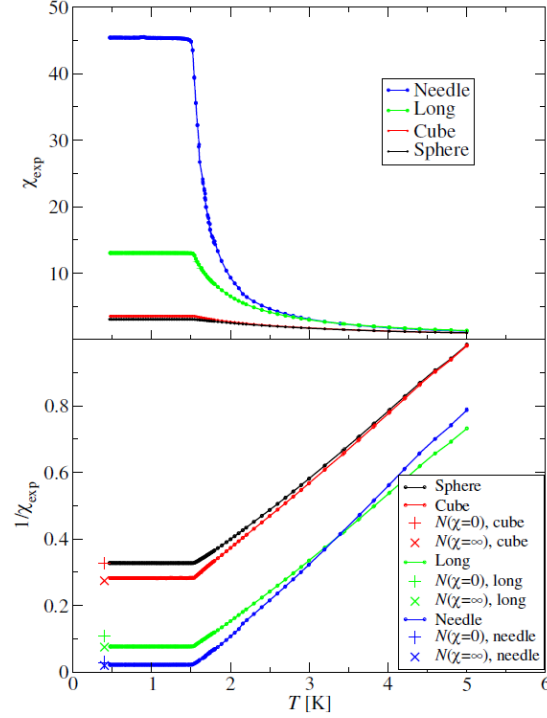
Figure 2.1.1.: Inverse susceptibility of LiHoF$_4$ as a function of temperature. Different sample shapes with different demagnetization factors N result in different susceptibilities. Figure taken from Ref. [78].

This factor describes the relation between the applied field H_a and the magnetization M, such that the internal field in a sample is $H_i = H_a - NM$. With it, the susceptibility measured in an experiment χ_{exp} relates to the microscopic susceptibility χ_{micro} via [19]

$$\frac{1}{\chi_{\mathrm{exp}}} = \frac{1}{\chi_{\mathrm{micro}}} + N. \tag{2.1.4}$$

Within the ferromagnetic phase and at the phase transition a diverging microscopic susceptibility $\chi_{\mathrm{micro}} \to \infty$ is expected. Therefore the experimentally observed susceptibility is limited by the demagnetization factor $\chi_{\mathrm{exp}} = 1/N$, cf. Fig. 2.1.1. The demagnetization factor depends on the sample shape and the direction of the applied field and magnetization [77]. A special case is the spherical sample, which has $N = 1/3$ independent of direction and is thus well suited for studies with varying field direction. Therefore, this sample geometry was chosen for the experiments presented in this thesis.

2.1.1. Longitudinal and Transverse Susceptibility

In general, the direction of the static magnetic field $\mathbf{H}$ and the oscillating excitation field $\mathbf{H}_{\mathrm{AC}}$ are independent of each other. We denote the direction of the static field with the index k, i.e. $\mathbf{H} = |\mathbf{H}| \cdot \hat{e}_k = H_k$ and keep the restriction to diagonal elements $i = j$.

Two configurations are of special interest, first the longitudinal susceptibility $\chi_\parallel$, where the oscillatory and static field are parallel. Second, the transverse susceptibility $\chi_\perp$, which corresponds to an AC excitation $\delta\mathbf{H}_{\mathrm{AC},j}(\omega)$ perpendicular to the static field H_k, i.e.

$$\chi_\perp = \chi_{ii}(H_{k\perp i}, T, \omega) = \frac{\delta M_i(H_{k\perp i}, T)}{\delta H_{\mathrm{AC},i}(\omega)}. \tag{2.1.5}$$

The latter was extensively studied as part of this thesis to determine the magnetic phase diagram of LiHoF$_4$ at low temperatures. However it should be noted, that this description lacks when the magnetic field angle Φ is changed, since the direction of the AC field cannot be changed simultaneously. Thus the quantity determined is

$$\chi = \frac{\delta M_z(H(\Phi), T)}{\delta H_{\mathrm{AC},z}(\omega)}, \tag{2.1.6}$$

where z denotes the crystalline z-axis. For perfect perpendicular field alignment $\Phi = 0$, both equations (2.1.5) and (2.1.6) are equal.

2.1.2. Experimental Technique

A mutual induction method was used to determine the AC susceptibility. In this method an oscillating magnetic field of a primary induced a voltage in a balanced pair of secondary coils [4, 79]. The induced voltage is described by Faraday's law

$$U_{\text{ind}}^{\text{vac}}(t) = -N_s \frac{\text{d}\Phi}{\text{d}t} = -N_s \frac{\text{d}}{\text{d}t} \int_A \mu_0 \cdot H_{\text{AC}} \cdot \text{d}A = \mu_0 H_0 \omega A N_s \sin(\omega t) \qquad (2.1.7)$$

where N_s is the number of windings of the secondary "pick-up" coil, Φ is the magnetic flux, μ_0 is the magnetic permeability, $H_{\text{AC}} \propto \cos(\omega t)$ is the magnetic field of the primary coil and A the cross-section of the solenoid. Since the pair of secondary coils is balanced $U_{\text{ind},1}^{\text{vac}} = U_{\text{ind},2}^{\text{vac}}$, their combined vacuum signal is zero $U_{\text{ind,tot}}^{\text{vac}} = U_{\text{ind},1}^{\text{vac}} - U_{\text{ind},2}^{\text{vac}} = 0$.

Inserting a sample in one of the secondary coils leads to a net signal proportional to the magnetic AC susceptibility χ.

$$U_{\text{ind}}^{\text{sample}} = U_{\text{ind},1}^{\text{vac}} + U_{\text{ind},1}^{\text{sample}} - U_{\text{ind},2}^{\text{vac}} = \mu_0 H_0 \omega A N_s \sin(\omega t) \chi_{\text{sample}} f_{\text{sample}}, \qquad (2.1.8)$$

where f_{sample} represents the filling factor, i.e. the volume fraction of the secondary coil filled by the sample.

This differential signal of the two secondary coils is recorded with a phase sensitive detector (PSD), which was phase-locked to the current of the primary coil I_p, allowing to record the in-phase and out-of-phase signal. In practice, both signals are recorded simultaneously in a lock-in amplifier [80].

The in-phase signal is the direct response of the sample to the excitation corresponding to the real part of the susceptibility χ', while the out-of-phase signal represents the dissipative or imaginary part χ'' of the susceptibility

$$\chi = \chi' + i\chi'' = \text{Re}(\chi) + i\text{Im}(\chi). \qquad (2.1.9)$$

As part of this study, the real and imaginary part of the transverse susceptibility (2.1.5) were measured using this method. Throughout this thesis the transverse AC susceptibility will denoted by $\chi_\perp = \chi$ unless stated otherwise.

2.2. Experimental Method

The following section describes the experimental methods used for the measurements of the transverse susceptibility of $LiHoF_4$. First the dilution refrigerator will be introduced, which provided access to temperatures between 60 mK and 1.6 K. The vector magnet used to study the angular dependence under magnetic fields up to 5.5 T at angles Φ between $-10°$ and $90°$ will be presented in the second subsection. This is followed by a description of the small susceptometer, similar to the design presented in Refs. [4, 72], used for measurements of the AC susceptibility. The section concludes by presenting the spherical $LiHoF_4$ sample and the procedure used to align the sample with the susceptometer and vector magnet.

2.2.1. Dilution Unit

The experiments in this thesis focused on the temperature regime between ≈ 1.5 K and ≈ 50 mK, of the ferromagnetic phase of $LiHoF_4$. To achieve such low temperatures, a Joule-Thompson (JT) $^3He/^4He$ dilution insert from *Oxford Instruments* was used. A mixture of $^3He/^4He$ gas circulates through the insert as shown in Fig. 2.2.1 (A). A compressor raises the pressure of the gas to 1.5 bar and pushes it through a nitrogen trap. The mixture is pre-cooled in a heat exchanger in the helium bath of the magnet. A Joule-Thomson expansion stage reduces the temperature to $T \approx 1$ K such that the He gas condenses. In the mixing chamber (MC), the mixture separates into ^3He rich and a ^3He poor phase. Additional cooling is achieved by depleting the ^3He poor phase further referred to as *dilution* [4, 81, 82]. This drives a quasi-evaporation of ^3He atoms from the rich to the poor phase which allows cooling down to a few milli-Kelvin. The JT insert used achieved temperatures down to 35 mK, although ohmic-heating limited the base temperature to $T \approx 60$ mK when using the susceptometer.

The susceptometer and heat capacity setup were mounted to the bottom of the mixing chamber as shown in Fig. 2.2.1 (B). Thermometers at the 4 K-heat-exchanger, on the inside of the IVC-seal, at the still and at the MC allowed to monitor and regulate the insert with a Lakeshore LS370 controller via a LabView program [4].
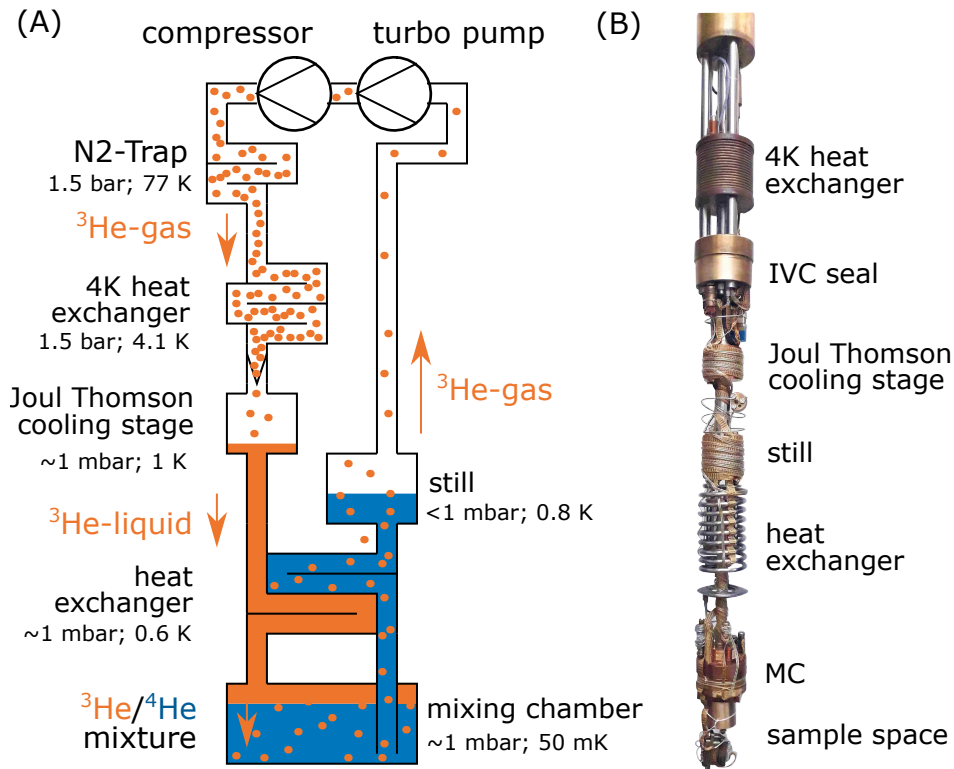
Figure 2.2.1.: The JT dilution unit primarily used in this thesis. (A) A scheme of the layout and flow of ^{3}He (orange) gas through the system. (B) A picture of the insert, the components are described in further detail in the text.

2.2.2. Superconducting Vector Magnet

A superconducting 2D vector magnet from *American Magnetics* was used for this study. The system allowed to generate magnetic fields of ± 9 T along the vertical axis (z) and ± 4.5 T along the horizontal axis (y). Due to technical limitations, it was not possible to drive the horizontal field to full strength, when the vertical field exceeded ± 4.5 T. Therefore any magnetic field with an absolute strength below 4.5 T was accessible within the y-z-plane, but stronger fields were limited to angles closer to the z-axis. The accessible regime in field is shown in Fig. 2.2.2 (A). The magnets power supplies were capable of adjusting angles reproducibly. Above 1 T absolute field, the angle can be adjusted with above 0.001° precision, while being strictly less precise at lower fields, as determined by Ref. [4], cf. Fig. 2.2.2 (B) and (C).

The magnet was capable of ramping as fast as 1.72 T/min along the z-axis and 0.17 T/min along the y-axis. The minimal ramp speed was defined by the precision of the power
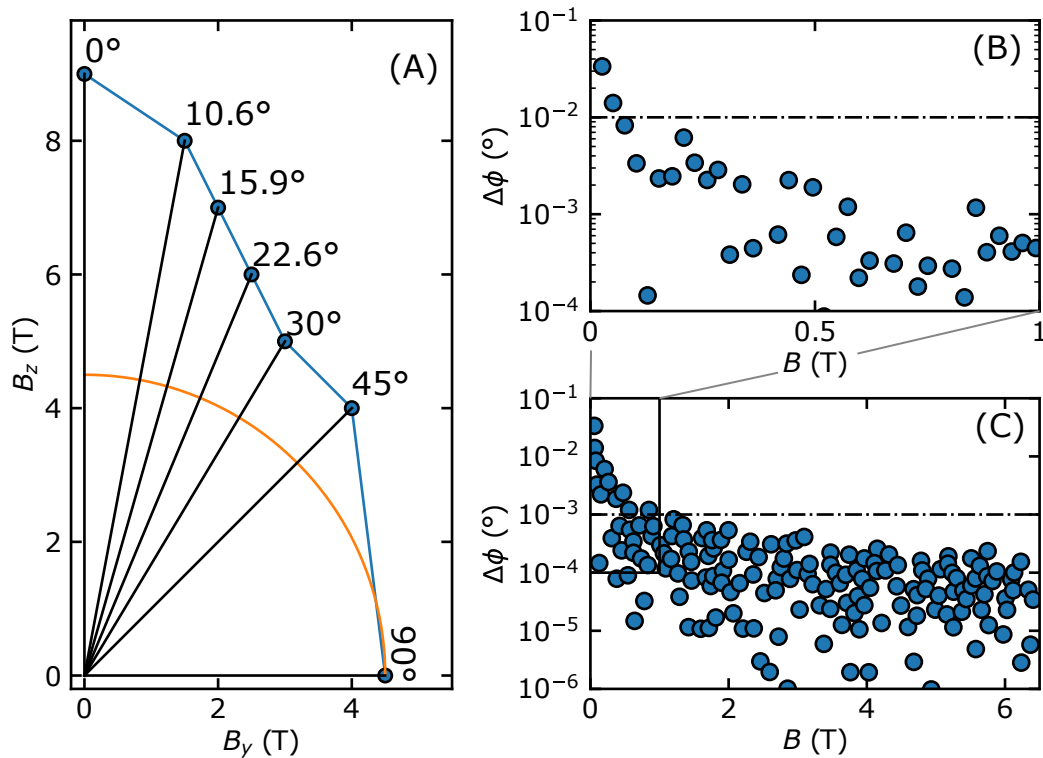
Figure 2.2.2.: Key characteristics of the AMI vector magnet. (A) The accessible fields as taken from the magnet manual and corresponding angles at the given points. These values are taken from the corresponding diagram in the AMI Magnet user manual. (B) At absolute fields below 1 T, the magnet is capable to drive angles better than 0.01°, at larger fields (C) a precision even under 0.001° is achieved. These points are taken from Ref. [4].

supplies for ramping the field at small angles, which was relevant for the magnetocaloric measurements described in Sec. 3.1.3. Each power supply was capable of adjusting the ramp rate at a minimum of $0.001\,\mathrm{A/min} \approx 0.0455\,\mathrm{mT/min}$. This limited the precision of the slower power supply when ramping at an angle. Thus, the minimal ramp-rate was faster at low angles and minimal at 45°. For the magnetocaloric measurements described in Sec. 3.3.2 ramp rates as slow as $15\,\mathrm{mT/min}$ at $\approx 1°$ were used.

2.2.3. Susceptometer

For measurements of the transverse susceptibility a susceptometer originally designed by F. Rucker [4, 72] was used, cf. Fig. 2.2.3 (A). A copper body provided good thermal anchoring to the mixing chamber. The temperature of this body was monitored with a calibrated Ruthenium oxide (ROX) resistor thermometer and recorded with a Lakeshore LS372 resistance bridge. Further details on the thermometer properties are provided in Sec. 3.2.5.

The primary coil, made of $100\,\mu$m thick Cu-wires, was wound on a sapphire cylinder (length: $16\,$mm, diameter: $8\,$mm). It consists of 1525 windings resulting in a resistance of $105\,\Omega$ at room temperature. Two secondary coils (length: $4\,$mm, inner diameter: $3.2\,$mm, outer diameter: $6\,$mm) with 1200 windings and $260\,\Omega$ at room temperature each were attached to the inside of this sapphire cylinder and cast in 2850 Stycast epoxy. One of the secondaries supported the sample, while the other was empty measuring the vacuum background only. The signal of these coils without sample was adjusted so that the measured difference in induction voltage was close to zero. In this configuration the secondaries are referred to as *balanced* and the combined voltage corresponds to the samples response. The balance is achieved by optimizing their position within the sapphire cylinder manually until the difference of the vacuum signal Eq. (2.1.7) is effectively zero. Following this, the position is fixed using GE-varnish. All coils were in good thermal contact with the MC via the sapphire cylinder and the copper body. The sample was mounted on top of a sapphire rod and inserted into one of the two secondaries.

A Keithley K6221 current source provided the AC excitation current of the primary. A Stanford Research SR830 lock-in amplifier detected the signal, recording the difference of the voltage signal of the secondaries, thus the magnetic susceptibility as discussed in Sec. 2.1.2. The electric wiring is illustrated in Fig. 2.2.3 (B).

For the study presented, the susceptibility was calibrated using the low temperature field sweeps from Ref. [4], since the same sample was used. For a comparison of the datasets used, see Fig. 2.3.8.
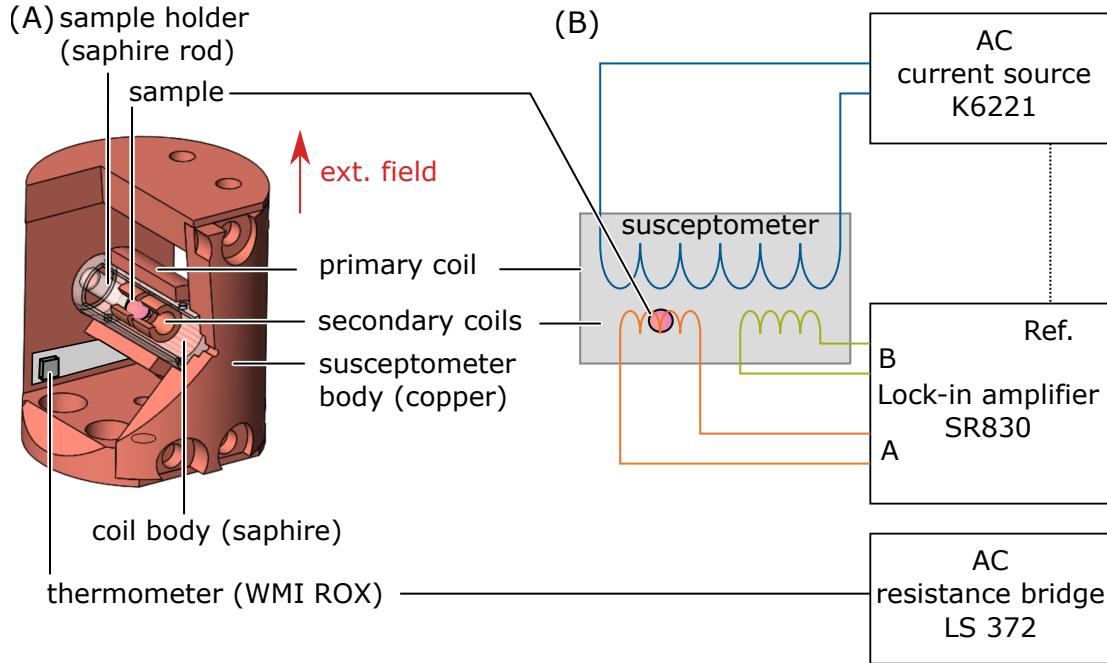
Figure 2.2.3.: Setup used for transverse susceptibility measurements. (A) Schematic depiction of the low temperature susceptometer for studies in transverse field geometry developed by F. Rucker [4]. The body is designed as symmetric as possible to reduce signal background. The primary coil is wound on a sapphire tube whereas the secondary coils are fixed inside it. A sapphire rod centers the sample in one of the secondary coils and couples it thermally to the susceptometer body. (B) Sketch of the electronics used in the experiment. A Keithley K6221 current source drives the primary coil. A Stanford Research SR830 Lock-in Amplifier measures the induced voltage in the two primary coils, using the frequency of the AC current source as a reference. The temperature is determined by a Lakeshore LS372 resistance bridge with a calibrated ROX sensor, see Tab. 3.2.1 for further details.

2.2.4. Spherical LiHoF$_4$ Sample

The sample was purchased from Altechna/AcalBFI Germany with the tracking number #523201216. The single crystal had the shape of a cylinder of 6 mm diameter, with the c-axis pointing along the cylinder axis. A cubic sample was cut by a diamond wire saw in the crystal lab. Afterwards, an external gem-cutter polished it into a spherical shape. The diameter of the sphere was $d \approx 2.8\,\mathrm{mm}$ and the sample mass was $m_{\mathrm{LiHoF_4}} = 54.7 \pm 0.7\,\mathrm{mg}$. The sample is shown in Fig. 2.2.4 (A) on top of the sample holder during the alingment process described below.
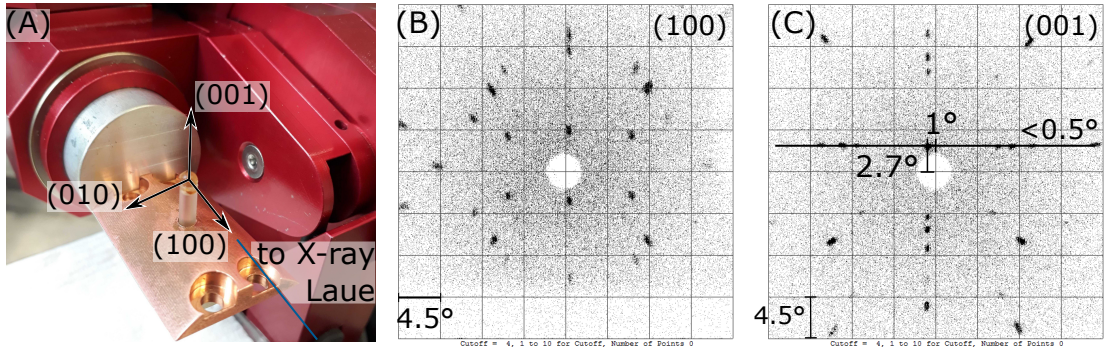
Figure 2.2.4.: Orientation of the sample using X-ray Laue diffraction. (A) The sample on the sapphire rod on the Laue diffractometer. (B) Image of the Laue pattern during initial orientation. (C) Laue pattern along the susceptometer axis after the glue has hardened.

2.2.5. Sample Alignment Process

The exact orientation of the sample within the reference frame of the vector magnet was mandatory for the precise measurement of the angle Φ between the easy axis of LiHoF$_4$ and the magnetic field. In the following, the procedure used for sample alignment with respect to the susceptometer is described, followed by definitions for the various angles, planes and reference frames necessary to understand the multi-step alignment process with respect to the vector magnet.

Alignment in the Susceptometer In the first step, the sample was aligned with its c-axis (001) along the sapphire sample holder in the susceptometer, parallel to the AC field, as shown in Fig. 2.2.4 (A) and (B). GE varnish 7031 is used to glue the sphere to the rod. While the varnish dried the sphere shifted by roughly 2-3°, cf. Fig. 2.2.4 (C).

Alignment in the Vector Magnet In addition to the alignment of sample and susceptometer, the assembly also needs to be aligned in the AMI vector magnet. For the description of this process, the angles and directions are defined, as shown in Fig. 2.2.5. Within the coordinate system (x, y, z) of the vector magnet, the magnetic field points along

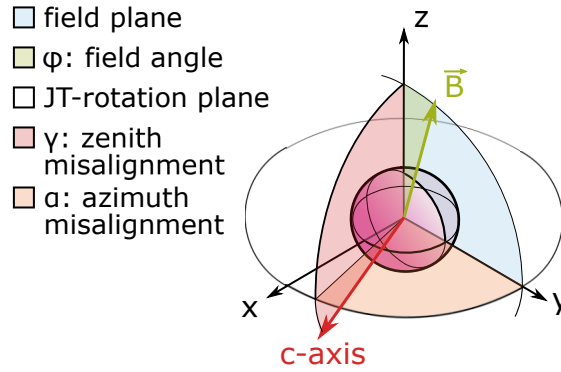$$\vec{B} = B \begin{pmatrix} 0 \\ \sin\phi \\ \cos\phi \end{pmatrix}, \tag{2.2.1}$$

Figure 2.2.5.: The definitions of the angles used in this experiment.

which is depicted as a green arrow in Fig. 2.2.5 together with the field angle ϕ. The crystalline c-axis points along

$$\vec{c} = \begin{pmatrix} \sin(\gamma)\sin(\alpha + \alpha_{\mathrm{JT}}) \\ \sin(\gamma)\cos(\alpha + \alpha_{\mathrm{JT}}) \\ \cos(\gamma) \end{pmatrix}, \tag{2.2.2}$$

where α is the azimuth misalignment angle, α_{JT} is the manual rotation angle of the insert. The zenith angle of the easy axis is γ. The two angles α and γ are highlighted in orange and red respectively in Fig. 2.2.5.

For the experiment this c-axis (red arrow) needs to lie within the y-z-plane (blue) of the vector magnet. In this case, the field angle ϕ describes the angle between $\vec{B}$ and c-axis, apart from a constant offset. For a successful alignment, α and γ were determined and corrected by turning the JT insert and magnetic field.

To define the rotation angle of the JT insert α_{JT}, the AMI magnet was equipped with a scale with a diameter of $727.2\,\mathrm{mm}$ and $0.1°$ steps. A laser on top of the JT insert pointed on the scale and allowed to read its rotation relative to the magnet. The mounting precision of this scale is better than $2\,\mathrm{mm} \approx 0.26°$ and the reading precision is better than $1\,\mathrm{mm} \approx 0.13°$, which gives a combined error of not larger than $\Delta\alpha_{\mathrm{JT}} \approx 0.4°$. The various possible sources of misalignment are summarized in Tab. 2.2.1. Especially the orientation within the azimuthal plane was challenging, since the angle between susceptometer and laser was difficult to determine and the approximate direction of the y-z-field-plane was known only.

Table 2.2.1.: Relevant angles for the alignment process, their definitions and factors influencing their precision.

	angle	error sources	estimate
ϕ	field angle	AMI precision $B > 2\,\mathrm{T}$	$< 0.001°$ (Fig. 2.2.2)
α	azimuth misalignment	orientation on X-ray Laue	$< 3°$
		mounting the suszeptometer on the JT	$< 5°$
		orienting the JT with respect to the magnet	$< 5°$
γ	zenith misalignment	orientation on X-ray Laue	$< 3°$
$\delta\alpha_s$	precision of the scale on top of the magnet	laser point size and scale spacing	$< 0.4°$

To determine α and γ, the JT was positioned in two different orientations, defined by its rotation with respect to the scale α_{JT}. A linear system of equations then allowed to calculate the angles. The three steps are summarized as follows:

Step I: The c-axis was perpendicular to the field plane within precision. The rotation of the insert was $\alpha_{\mathrm{JT}} = 90°$. The misalignment angles α and γ were unknown.

Step II: The c-axis was turned by exactly 90°, thus approximately parallel to the y-axis of the magnet. The rotation of the insert was $\alpha_{\mathrm{JT}} = 0°$; The misalignment angles α and γ were calculated.

Step III: The c-axis was aligned with the field plane. The rotation of the insert α_{JT} was adjusted such that $\alpha = 0°$.

The configuration in every step is depicted in Fig. 2.2.6. At each position, the critical field B_c was determined by a field sweep at the lowest temperature of $T \approx 65\,\mathrm{mK}$ as described later. The sweeps were repeated for different angles ϕ, as shown in Fig. 2.2.7 (A), where the upward triangles mark the critical field.

The optimal field orientation $\vec{B}_{opt}$ is found, when the critical field is maximal. In this configuration, the field is perpendicular to the crystalline c-axis, as highlighted in Fig. 2.2.6. Fig. 2.2.7 (B) shows B_c as a function of the magnet field angle ϕ. As expected, the angular dependence is a lot flatter in the first step, when the c-axis points almost perpendicular to the field plane. A Gaussian fit is used to determine the position of the maximum in each
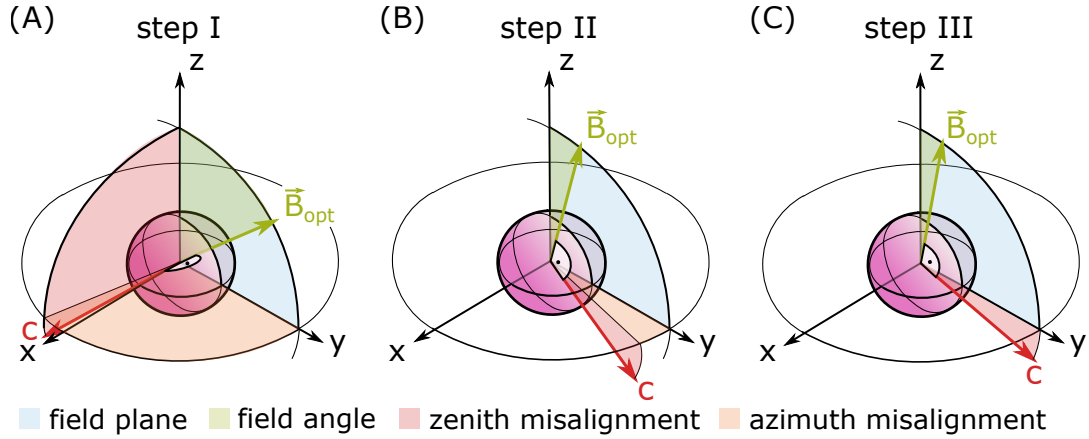
Figure 2.2.6.: Procedure used to align the sample within the vector magnet. (A) The c-axis of the sample points roughly perpendicular to the field plane (blue), along the x-axis. The optimal field $\vec{B}_{\text{opt}}$, where it is perpendicular to the c-axis is determined by scanning the field angle ϕ (green). (B) After turning the insert by 90°, the c-axis points roughly along the y-axis. A different optimal field orientation will be determined. (C) After calculating the zenith and azimuth misalingment angle, the sample is aligned with the field plane (blue) by turning the insert again. The zenith misalignment angle is always measured from the z-axis to the c-axis, as defined in Fig. 2.2.5, but was only drawn from the x-y plane in (B) and (C) for better visibility.

step. The location of the maximum was $\phi_{\text{I}} = 7.07\pm0.18°$ for step I and $\phi_{\text{II}} = -2.21\pm0.028°$ for step II.

With these information, the zenith (γ) and azimuth (α) angle of the c-axis were determined by solving a linear system of equations. The following two expressions were found for

$$\alpha = \arctan \frac{\tan \phi_{\text{II}}}{\tan \phi_{\text{I}}} = -17.36 \pm 0.47° \tag{2.2.3}$$

and

$$\gamma = \arctan \frac{-1}{\tan \phi_{\text{II}} \cos \alpha} = 87.881 \pm 0.023°. \tag{2.2.4}$$

These two misalignment angles were corrected in the third step, confirming that the maximal field now lies at $\phi_{\text{III}} = -2.22° \pm 0.041$, close to the expected $\gamma - 90° = -2.12°$. Uncertainties were inferred from partial derivatives and Gaussian error progression.

After successful orientation, the field angle can be redefined, such that $\Phi = \phi + 2.2°$. For all other parts of this thesis, we refer to the field angle as this corrected value, denoted by capital Φ, whereas the absolute reading of the AMI-magnet is denoted by ϕ.
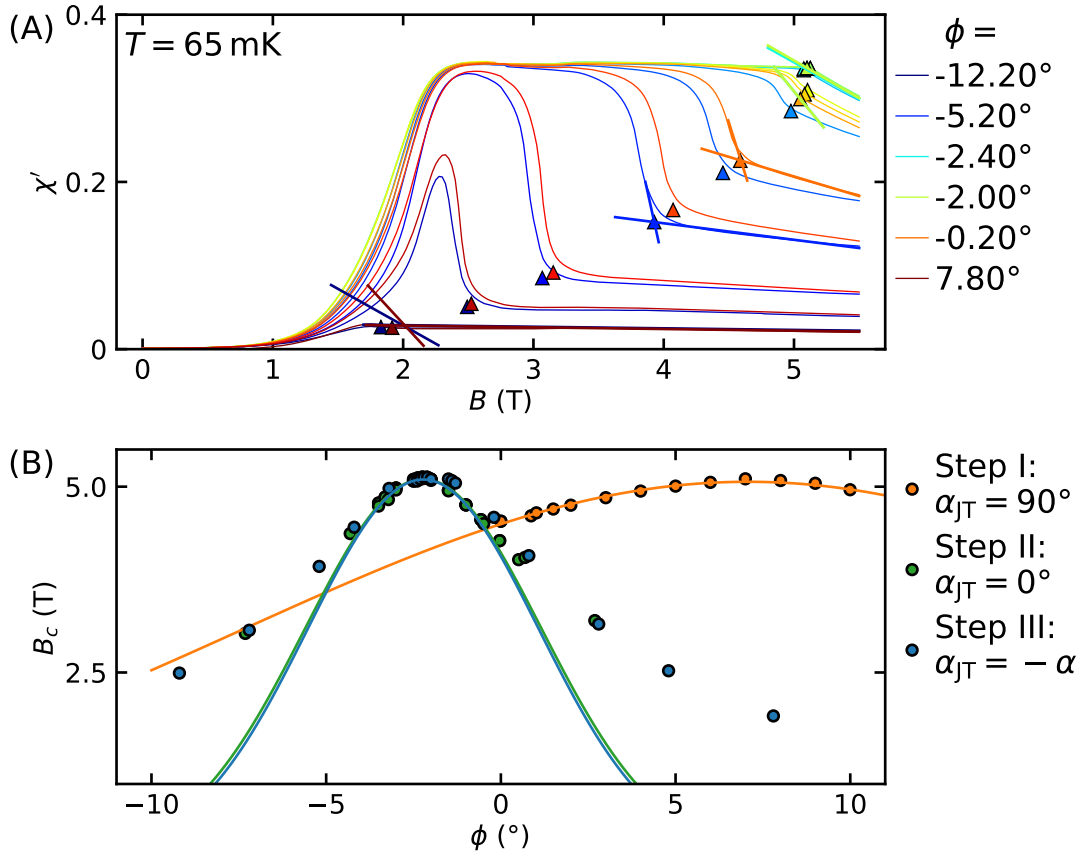
Figure 2.2.7.: Experimental results for the determination of the sample alignment. (A) During each step, data were recorded at $T \approx 65\,\text{mK}$ and various field angles as a function of magnetic field strength. The critical field was determined by the intersection of two lines, shown exemplary for selected curves and is marked by the upward triangle. (B) The maximum critical field B_c as a function of field angle ϕ was determined by Gaussian fits.

Estimates of Angular Uncertainties The uncertainty of the arrangement was estimated based on the error of the scale when turning the JT between step I and II as well as twice the reading error, as summarized in Tab. 2.2.1. $\delta\alpha = 0.46° + 0.26° + 2 \cdot 0.13° = 0.98°$. The alignment of the crystalline a-axis with this plane is the precision of the X-ray Laue orientation $\approx 2\,\text{deg}$. The angle between the field $\vec{B}$ and the c-axis $\vec{c}$ around their perpendicular orientation can be determined with much larger precision since it mostly depends on the precision of the vector magnet, which is better than $\delta\phi < 0.001$ for fields $B > 2\,\text{T}$, cf. Fig. 2.2.2. The influence of the possible misalignment of the various angles was estimated numerically by Monte Carlo methods. Namely, we considered an error of the vector magnet of $\delta\phi = 0.001°$, the uncertainty of the zenith angle $\delta\gamma = 0.024°$, the uncertainty of the azimuth angle $\delta\alpha = 0.98°$ as derived above. A worst case scenario of
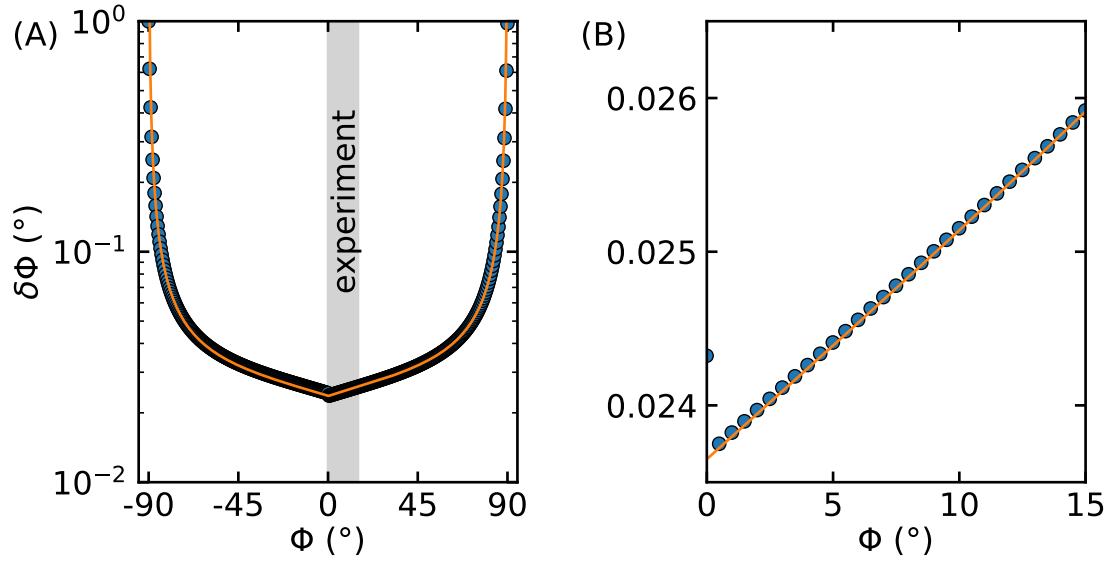
Figure 2.2.8.: The worst case deviation of the field angle Φ from the direction perpendicular to the crystalline c-axis as determined by Monte Carlo methods. (A) The worst case deviation $\delta\Phi$ is shown over the full range $\pm90°$. The experimental window is highlighted in grey. An interpolation is shown in orange. (B) In the experimental regime $\delta\Phi$ is basically linear.

the angular precisions is shown in Fig. 2.2.8. The orange line is an interpolation to this estimate and represents the angular uncertainties used throughout this chapter.

The c-axis of the sample was put within the field plane of the magnet. This means that the uncertainties are dominated by the magnet precision in the regime at low angles, perpendicular to the c-axis, where the phase diagrams were recorded, cf. grey-shaded area in Fig. 2.2.8 (A) and (B). At larger angles, the uncertainties in the JT-rotation α_{JT} and azimuth angle α play a more pronounced role as the field vector is shifting towards the y-axis of the magnet. As will be shown later, the susceptibility is not very sensitive to the field orientation at large angles, hence the precision achieved was sufficient for all results presented.

2.3. Experimental Results

This section covers the results of the measurements of the transverse AC susceptibility $\chi_\perp$ of LiHoF$_4$. First the determination of the critical field and the magnetic phase diagram will be reported for selected examples for constant Φ and the general features of the data will be explained. Following that, specific details will be highlighted, starting at the dependence of the susceptibility on the field angle, followed by the analysis of the critical exponents around the quantum phase transition.

2.3.1. Magnetic Phase Diagram

The magnetic phase diagrams were determined by performing scans at constant temperature or constant field, as shown in Fig. 2.3.1 for a tilt angle of $\Phi = 0°$. The field scans were performed while increasing the field in 25 mT steps from zero to 5.5 T to reduce systematic errors when ramping the magnet continuously. The temperature scans were performed as continuous sweeps at 5 mK/min from 1.4 to 1.6 K using the heater at the MC.

Data were recorded at temperatures between $T = 67$ mK and $T = 1.6$ K for magnetic fields from $B = 0$ to 5.5 T. The susceptibility was measured at an excitation frequency of $f_{\mathrm{AC}} = 511$ Hz and an excitation field $B_{\mathrm{AC}} = 13\,\mu$T, unless stated otherwise.

The resulting phase diagram is shown as a 2D colorplot of the real part of the transverse susceptibility χ' as a function of magnetic field and temperature in Fig. 2.3.1 (A) for $\Phi = 0°$, i.e. perfect transverse orientation. Typical scans of the temperature (B1), (B2) and field (C1), (C2) are shown in the panels, the real part χ' is shown in blue and the imaginary part χ'' in red. The position of the scans is highlighted by grey lines in the colormap (A).

The data of the temperature scans were smoothed with a rolling average to reduce noise in temperature unavoidable when operating the JT insert in this temperature range. The critical temperature and critical field were determined by the intersection of two linear fits. A first line was fitted to the jump in χ', between the two points of inflection (minimum and maximum in the second derivative of χ'). When no jump was visible, as for $\Phi = 0°$
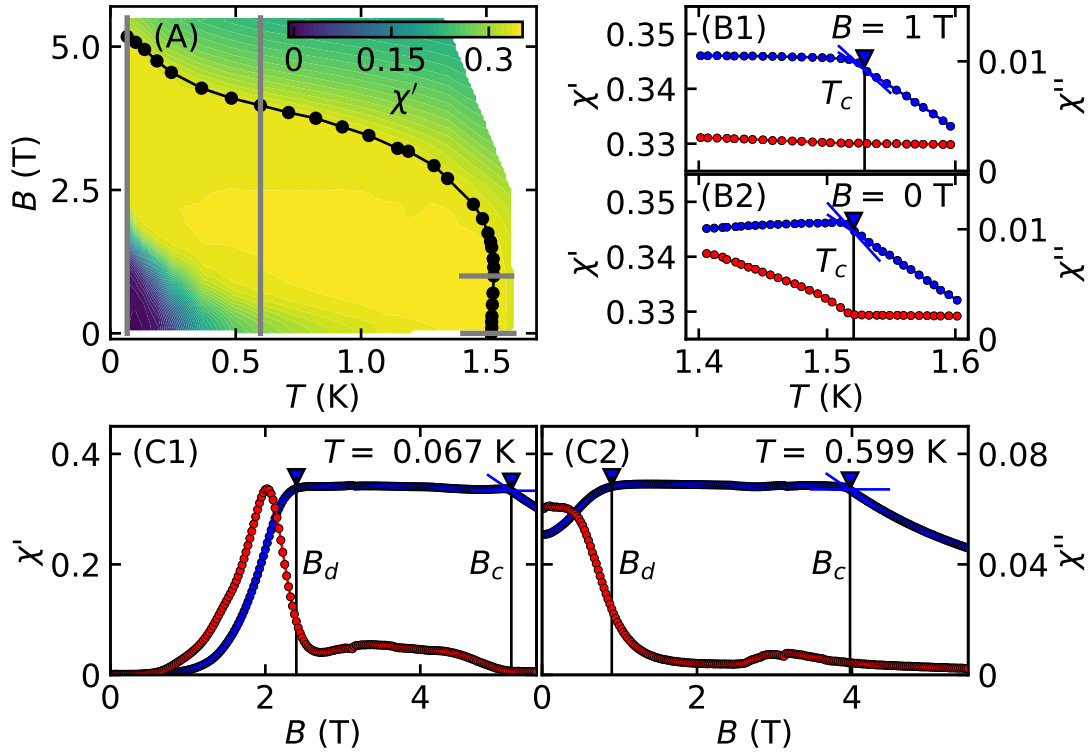
Figure 2.3.1.: Determination of the magnetic phase diagram for $\Phi = 0°$. (A) The data are shown as a colormap, where the phase boundary is shown in black. The grey lines highlight the position of the exemplary slices. (B, C) The real and imaginary parts of the transverse susceptibility are shown in blue and red, respectively. The phase transition is denoted by a triangle and black line. Critical fields B_c and critical temperatures T_c were determined by the linear fits shown as solid lines. (B1, B2) Temperature sweeps were performed at $B = 1\,\mathrm{T}$ and $B = 0$. The number of data points shown is reduced by a factor of 100 for better visibility. (C1, C2) Field step scans were performed at $T = 69\,\mathrm{mK}$ and $T = 0.599\,\mathrm{K}$.

and Fig. 2.3.1, the value of the plateau was used instead to determine a line of intersection. A second line was fitted to the decreasing χ' in the paramagnetic regime above the second point of inflection.

As a function of increasing temperature at $B = 1\,\mathrm{T}$, χ' displays a plateau up to T_c, followed by a linear decrease. For $B = 0\,\mathrm{T}$ the real part of the transverse susceptibility rises slightly up to T_c, after which it decreases slowly, as shown in Fig. 2.3.1 (B2). The imaginary part χ'' shown in red decreases up to the phase transition and is constant and almost zero above. This thermal phase transition was studied in great detail in Refs. [4, 12, 41, 43, 47, 68].

The field scan for the lowest temperature studied, $T = 67\,\text{mK}$, is shown in Fig. 2.3.1 (C1). With increasing field, the real part of the magnetic susceptibility starts at zero and rises rapidly around $B_d \approx 2\,\text{T}$. This region can be attributed to a freezing of domain walls, which follow no longer the AC-field and thus contributes no longer to χ'. Increasing the field further a plateau at $\chi' \approx 0.34$ stabilizes up to the quantum phase transition, observed at a critical field of $B_c = 5.13\,\text{T}$ in excellent agreement with literature [12]. The plateau reflects an infinite susceptibility that is limited by the effects of stray fields [78]. With increasing temperatures B_c as well as B_d decrease, cf. Fig. 2.3.1 (C2), and the susceptibility at low temperatures becomes non-zero. While B_d may be observed with a clear increase or maximum in the imaginary part χ'', B_c is not clearly visible. The signal χ'' around $4\,\text{T}$ cannot be clearly distinguished from the background signal of the susceptometer.

While many features do not change when tilting the magnetic field away from the optimal orientation, some key differences arise. These will be illustrated for $\Phi = 1°$ and $\Phi = 10°$ but can be observed also at all other angles $\Phi \neq 0$. For tilted fields, Landau theory predicts a smooth crossover instead of a well-defined phase transition, because the longitudinal field component breaks the Ising symmetry between up and down states [5, 21] and prevents spontaneous symmetry breaking, as explained in Sec. 1.1. As a crossover of the order parameter, the magnetization, is smooth, one would expect also a smooth behavior of its derivative, the susceptibility.

In stark contrast, we observe, that already at an angle as small as $\Phi = 1°$ the shape of χ' around the phase transition changes significantly, cf. Fig. 2.3.2 (C1). The kink at B_c turns into a drop of χ' characteristic of a well-developed, distinct phase transition. We defined the height of the discontinuous jump by the difference in χ' at the phase transition and the plateau value, representing χ' in the ferromagnetic phase as limited by demagnetization effects.

Additionally, the value of the critical field is reduced in comparison to $\Phi = 0$, and $B_c = 5\,\text{T}$ at $64\,\text{mK}$ and $B_c = 3.9\,\text{T}$ at $599\,\text{mK}$. The behavior at low fields does not change significantly with increasing Φ, indicating that the domain wall freezing is not affected when tilting the field. A small jump of χ' is also visible at the phase transition in the temperature scans in Fig. 2.3.2 (B1, B2), indicating a change of the nature of this transition at finite angles as compared to $\Phi = 0$. The transition temperature T_c is not influenced
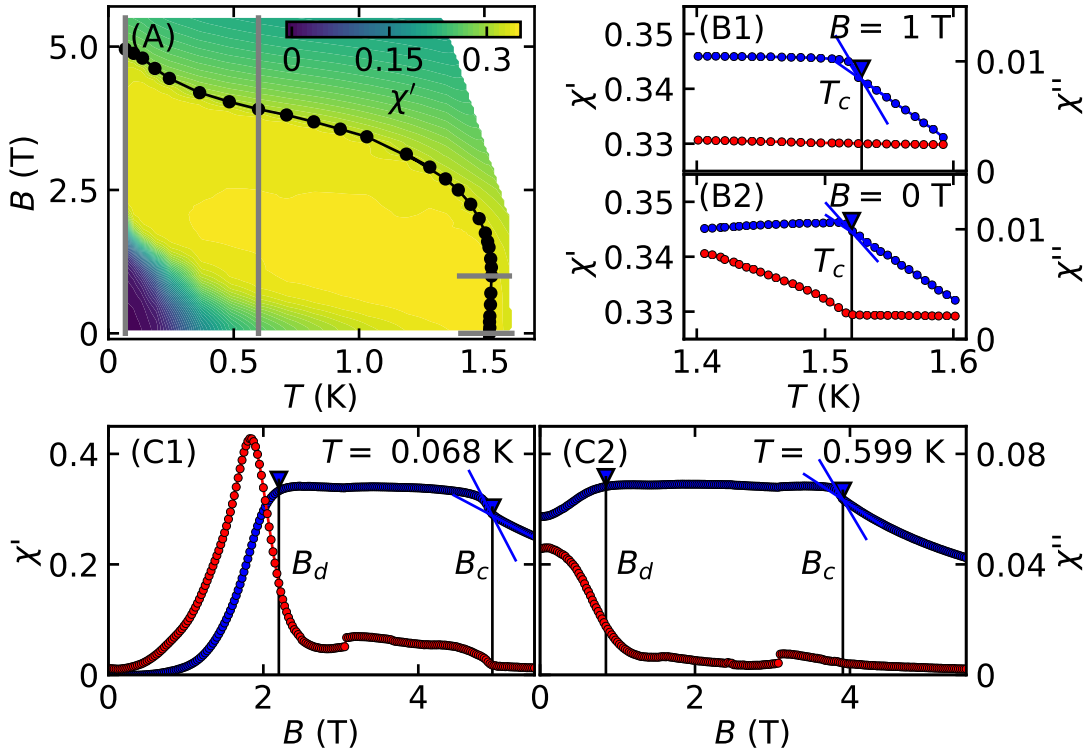
Figure 2.3.2.: Determination of the magnetic phase diagram for $\Phi = 1°$. (A) The data are shown as a colormap, where the phase boundary is shown in black. The grey lines highlight the position of the exemplary slices. (B, C) The real and imaginary parts of the transverse susceptibility are shown in blue and red, respectively. The phase transition is denoted by a triangle and black line. Critical fields B_c and critical temperatures T_c were determined by the linear fits shown as solid lines. (B1, B2) Temperature sweeps were performed at $B = 1\,\mathrm{T}$ and $B = 0$. The number of data points shown is reduced by a factor of 100 for better visibility. (C1, C2) Field step scans were performed at $T = 68\,\mathrm{mK}$ and $T = 0.599\,\mathrm{K}$.

significantly. The imaginary part of the transverse susceptibility χ'' is qualitatively unchanged.

At $\Phi = 10°$, the jump at the phase transition is even more pronounced, both in the temperature scans, cf. Fig. 2.3.3 (B1, B2) and the field scans, cf. Fig. 2.3.3 (C1, C2). The critical field is suppressed further. As shown in Fig. 2.3.3 (C2), the critical field at $T \approx 0.6\,\mathrm{K}$ is $B_c \approx 2\,\mathrm{T}$ as compared to the $4\,\mathrm{T}$ for $\Phi = 0$. For the lowest temperature of $T = 69\,\mathrm{mK}$, the critical field is in the field range of domain wall freezing and is barely visible in χ'. The domain freezing at B_d is not shown in Fig. 2.3.3 (C1), since the regime of the plateau is completely suppressed here. Apart from that, the low-temperature and low-field behavior is unchanged, showing that the domain wall freezing is independent of the field angle.
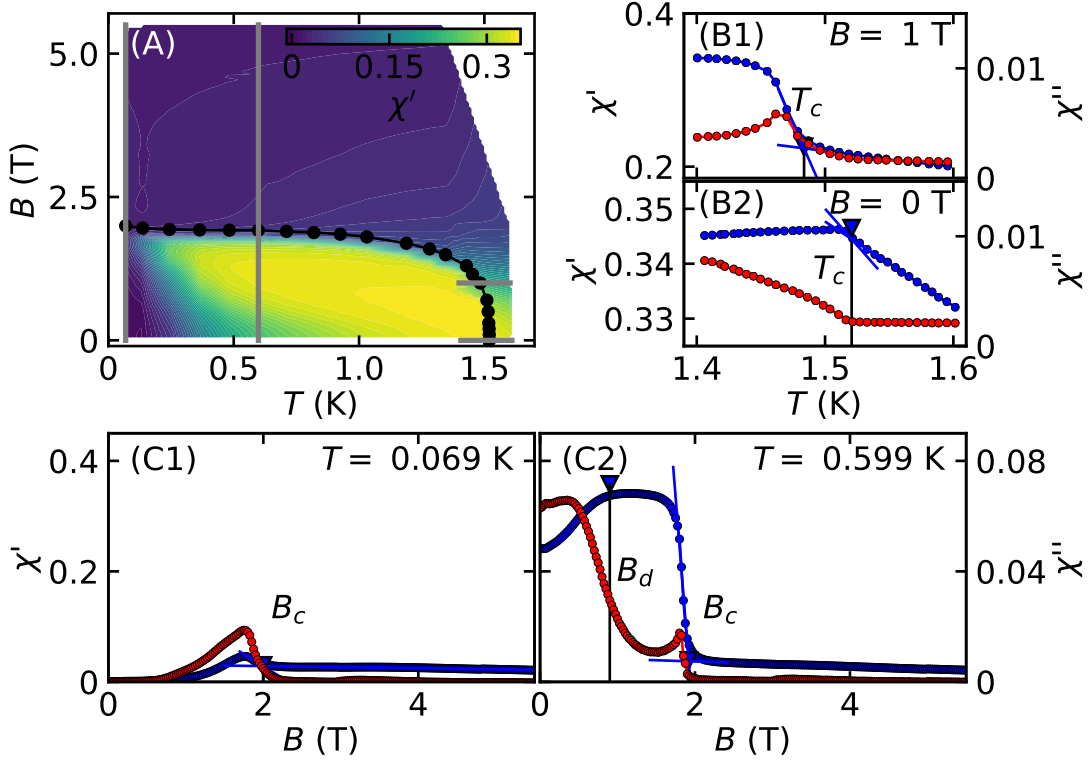
Figure 2.3.3.: Determination of the magnetic phase diagram for $\Phi = 10°$. (A) The data are shown as a colormap, where the phase boundary is shown in black. The grey lines highlight the position of the exemplary slices. (B, C) The real and imaginary parts of the transverse susceptibility are shown in blue and red, respectively. The phase transition is denoted by a triangle and black line. Critical fields B_c and critical temperatures T_c were determined by the linear fits shown as solid lines. (B1, B2) Temperature sweeps were performed at $B = 1\,\mathrm{T}$ and $B = 0$. The number of data points shown is reduced by a factor of 100 for better visibility. (C1, C2) Field step scans were performed at $T = 69\,\mathrm{mK}$ and $T = 0.599\,\mathrm{K}$.

The imaginary part displays peaks at both the thermal and the quantum phase transition for this angle, as shown in Fig. 2.3.3 (B1) and (C2).

These observations may be summarized by taking a look at the complete evolution of the phase diagram with changing field orientation from $\Phi = 0°$ to $\Phi = 15°$. This is shown in Fig. 2.3.4, where the phase boundary as defined by B_c and T_c is shown in red. For comparison, the phase boundary for $\Phi = 0$ is shown in white. The first observation is, that by increasing the field angle from $\Phi = 0°$ in Fig. 2.3.4 (A) to $\Phi = 15°$ in Fig. 2.3.4 (F) the critical field decreases strongly. Second, for $\Phi = 0°$, B_c is enhanced below $T \approx 0.5\,\mathrm{K}$ due to hyperfine interactions, as explained in above and originally observed by Bitko *et al.* [12]. With increasing tilt angle this feature is suppressed and the critical field
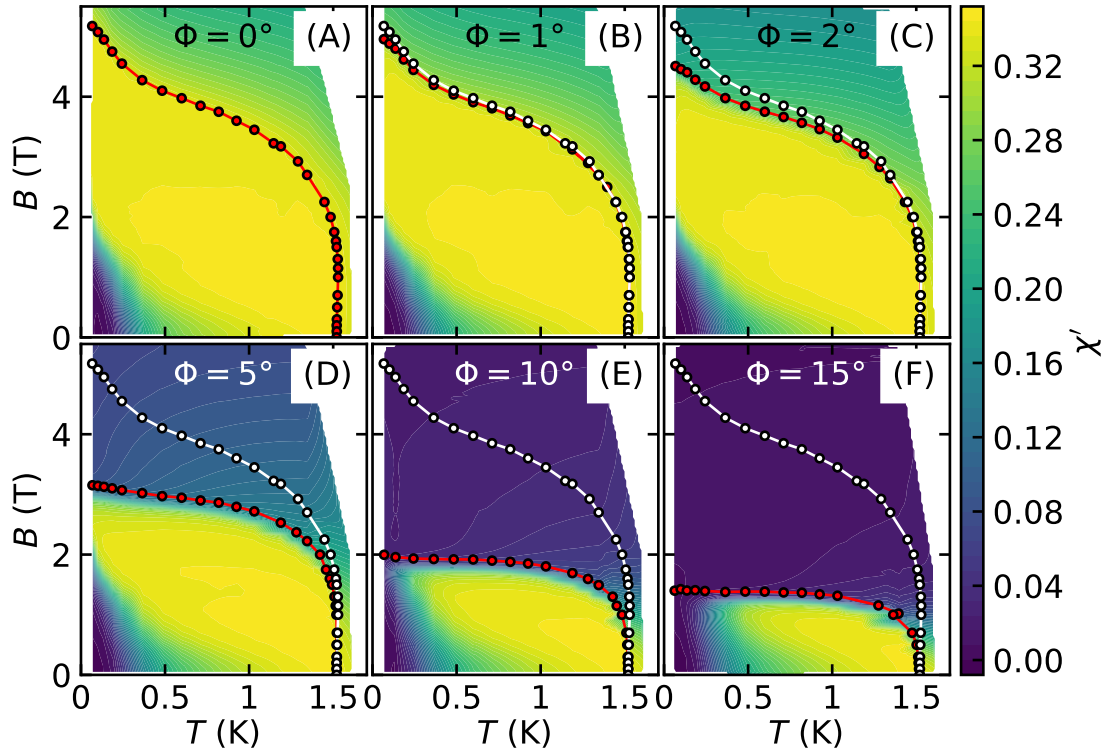
Figure 2.3.4.: Overview over the magnetic phase diagrams by determined from transverse susceptibility. (A-F) The real part of the transverse susceptibility is given as a color map. The phase boundaries are shown in red and the boundary for $\Phi = 0°$ is shown in white.

B_c is constant for $\Phi > 5°$ at temperatures up to $800\,\text{mK}$. Third, the region of low AC susceptibility χ' at low fields and low temperatures is independent of the field orientation Φ, cf. the blue area at $T < 0.5\,\text{K}$ and $B < 2\,\text{T}$ in Fig. 2.3.4 (A-F). Thus the domain wall freezing is not function to the field orientation.

At temperatures $T \approx 1.5\,\text{K}$ a small regime of re-entrant behavior can be observed, cf. Fig. 2.3.7. It will be discussed later in comparison with previous studies in Sec. 2.3.4.

2.3.2. Angular Dependence of Field Sweeps

The behavior of χ' and χ'' was investigated in detail for angles below $\Phi = 15°$, covering the full phase diagram. A specific comparison of field sweeps at $T = 64\,\text{mK}$ is shown in Fig. 2.3.5 (A1,A2). Exemplary also larger field angles $\Phi = 0 - 90°$ were investigated by field sweeps at $T = 1.2\,\text{K}$, shown in Fig. 2.3.5 (B1, B2). The fast decrease of the value of B_c at low field angles Φ slows down significantly with increasing Φ, cf. Fig. 2.3.5 (B1, B2). It reaches a constant value of $B_c \approx 0.5\,\text{T}$ for $\Phi > 50°$ and the shape of the discontinuous jump remains qualitatively unchanged.

The dataset therefore shows a continuous connection of the transition observed at finite angles with the coercitive field in the ferromagnetic $LiHoF_4$, observed in the longitudinal AC susceptibility along the easy axis at $\Phi = 90°$. This suggests that anisotropic ferromagnets may display such characteristics in general and that the picture of mesoscale quantum phase transitions developed in Sec. 2.4 applies to these material class as a whole. The continuous connection to $\Phi = 90°$ also suggests that domains play a key role in this material [21] and this behavior of the phase boundary is in very good agreement with theoretical predictions based on the formation of domain walls presented in Sec. 2.4. The direct connection to the coercive field at large field angles is again discussed later, when this effect is also found in the heat capacity and in comparison to results of Mennenga *et al.* [43], cf. Fig. 3.4.3 in Sec. 3.4.
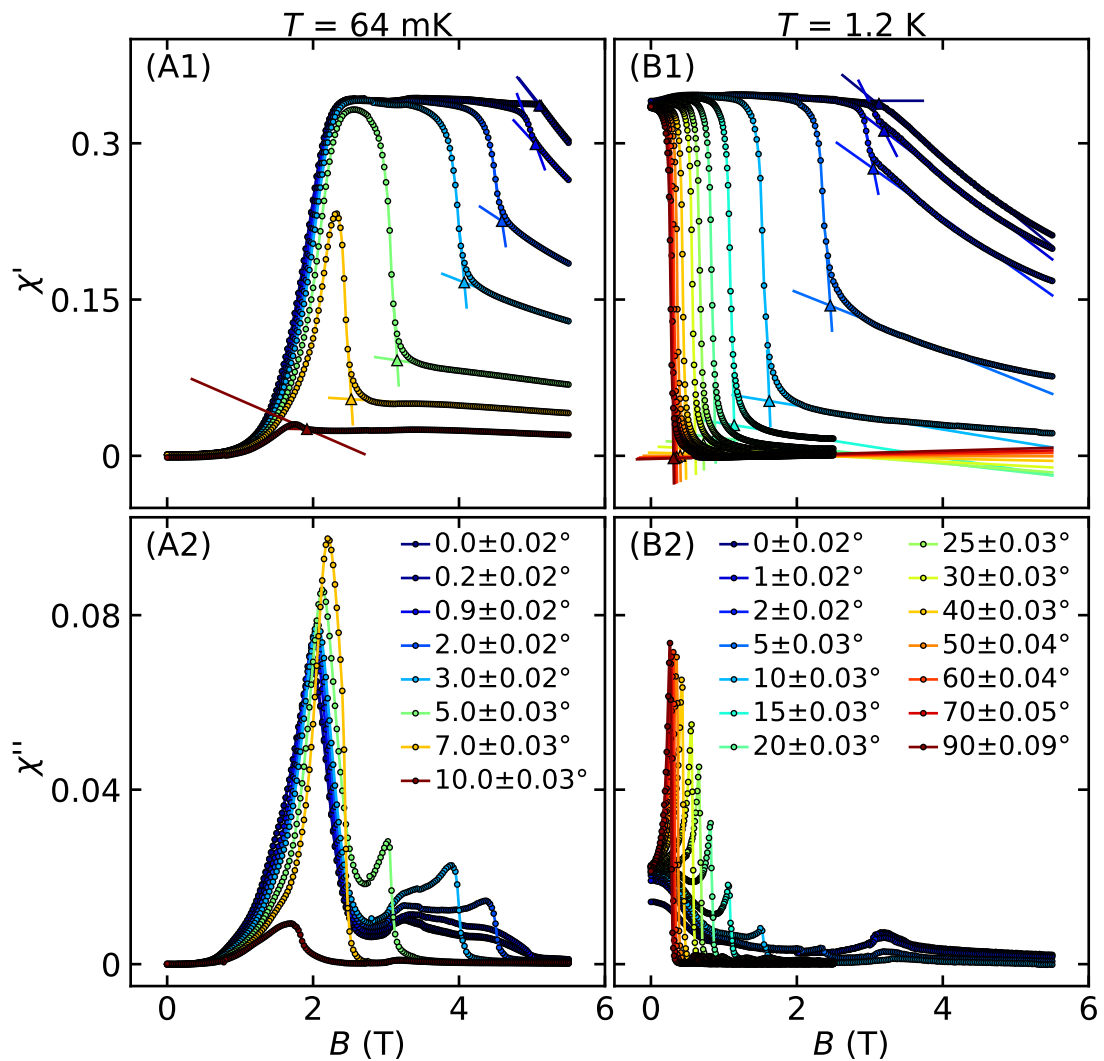
Figure 2.3.5.: Transverse susceptibility as a function of magnetic field for various tilt angles. (A1) The real part of the magnetic susceptibility is shown for $T = 64\,\text{mK}$. Triangles highlight the position of B_c and lines the corresponding linear fits as explained in the text. (A2) The imaginary part of the magnetic susceptibility is shown for the same angles as in (A1). (B1) The real part of the magnetic susceptibility is shown for $T = 1.2\,\text{K}$. (B2) The imaginary part of the magnetic susceptibility is shown for the same angles as in (B1).

2.3.3. Analysis of Critical Exponents

Already in the earliest studies of LiHoF$_4$, the critical mean-field exponent $\gamma = 1$ has been determined and since then has been confirmed in various studies [4, 12, 19]. It may be extracted by fitting a power law to the magnetic susceptibility at the phase transition, as the susceptibility diverges in the ferromagnetic state.

$$\chi \propto (T - T_c)^{-\gamma} \tag{2.3.1}$$

for the case of a thermal phase transition and

$$\chi \propto (B - B_c)^{-\gamma} \tag{2.3.2}$$

for field driven transition, such as at the QCP. In a real experiment however, the susceptibility χ is limited by demagnetization effects and a plateau is observed. To correct this effect Eq. (2.1.4) is rewritten so that the theoretical susceptibility reads

$$\chi'_{\text{th}} = \frac{1}{1/\chi'_{\text{exp}} - N} = \frac{1}{1/\chi'_{\text{exp}} - 1/\chi'_{\text{max}}}, \tag{2.3.3}$$

where $\chi'_{\text{exp}} = \chi'$ is the transverse AC susceptibility measured experimentally, $N = 1/\chi'_{max}$ is the demagnetization factor, which is equal to the inverse of the maximum of the transverse susceptibility in the regime of diverging χ_{th}. Therefore, $\chi'_{max} = 0.335$ is defined as the value at the plateau of the transverse susceptibility in the ferromagnetic state.

Following this, we determined the theoretical susceptibility according to Eq. (2.3.3) and fitted it with a power law dependence

$$\chi'_{th} = a \cdot (B - B_c)^{-\gamma} \tag{2.3.4}$$

for $\Phi = 0$ as shown in Fig. 2.3.6 (A). For all temperatures the results agree with the theoretical prediction of $\gamma = 1$, cf. Fig. 2.3.6 (B). When the theoretically predicted susceptibility χ'_{th} is shown as a function of $(B - B_c)/B_c$ on a logarithmic scale, the power law dependence appears as a straight line with the slope proportional to γ. As shown in Fig. 2.3.6 (C), the curve for $\Phi = 0°$ shows this behavior. For larger Φ however, the curve is non-linear and thus does not permit a description with a critical exponent. Similar to the critical behavior expected from theory (see. Sec. 2.4, Fig. 2.4.7), the susceptibility approaches a constant value at large field angles and fields.
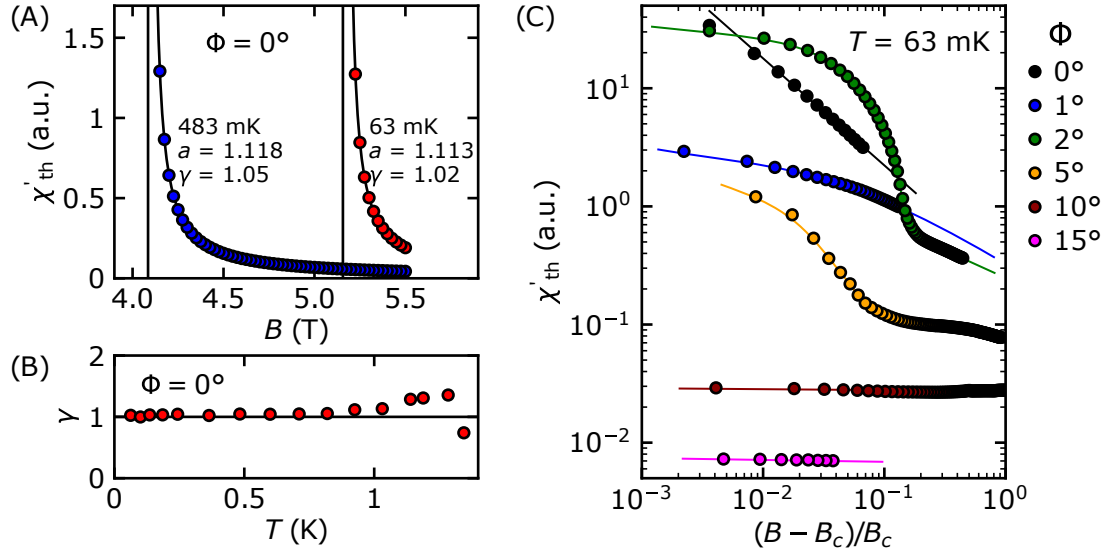
Figure 2.3.6.: Typical data featuring power law dependence and the critical exponent γ at B_c. (A) Normalized transverse susceptibility as a function of transverse field B for two temperatures and $\Phi = 0°$. The circles are data points, the black lines are fits to the data. The vertical lines mark the position of B_c. (B) The results for the fits for all temperatures at $\Phi = 0°$, the line serves as a guide to the eye and represents $\gamma = 1$ predicted theoretically. (C) Data for different Φ at $T = 63\,\text{mK}$ shown on a double-logarithmic scale. Only the data for $\Phi = 0°$ follows a linear dependence and thus shows the power law dependence expected.

2.3.4. Comparison with Previous Studies

The most detailed study of the magnetic susceptibility of $LiHoF_4$ to date was published by Bitko *et al.* [12]. It was also one of the first reporting a detailed investigation of the magnetic phase diagram and discussing the importance of hyperfine interactions. The phase diagram of $LiHoF_4$, reported by Bitko *et al.* is reproduced in Fig. 2.3.7 as light blue squares in comparison to the results obtained in this study, shown as the circles for various field orientations Φ. In 2018, Rucker *et al.* [4, 72] repeated this study and discovered additional details (green squares). They reported an enhancement of the AC susceptibility in the region, where hyperfine interactions play an important role. This region is shown in Fig. 2.3.7 (B). Additionally, a re-entrant behavior at low fields around the thermal transition was reported, cf. Fig. 2.3.7 (C). Further details of previous studies were summarized above.
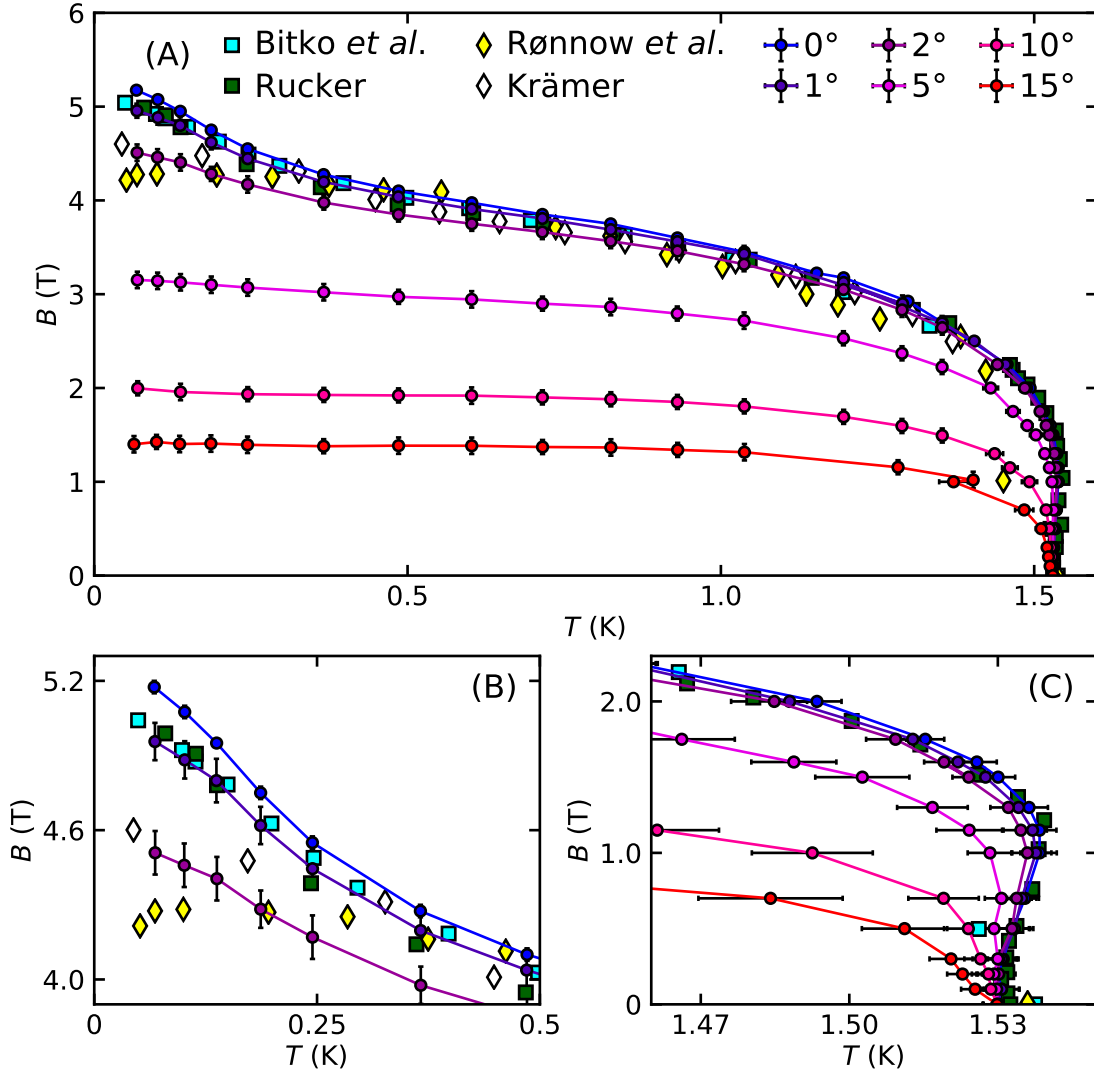
Figure 2.3.7.: Comparison of the phase diagram for various field orientations to with literature. (A) T_c and B_c as determined by the AC susceptibility measurements presented in this study are shown for various angles Φ ($\circ$). Bitko *et al.* [12] and Rucker [4] performed AC susceptibility measurements at $\Phi = 0$ conceptually similar to this study ($\square$). Rønnow *et al.* [14] and Krämer [66] utilized neutron diffraction and neutron triple-axis-spectroscopy to determine the phase boundary at $\Phi = 0$ ($\Diamond$). (B) A detailed view of the high field, low temperature region shows the reduced B_c for the neutron studies [14, 66]. (C) The low field, high temperature regime shows re-entrant behavior around the thermal phase transition.

Another set of experimental phase boundaries was published by Rønnow *et al.* [14] (yellow diamonds) and later by Krämer [66] (white diamonds). They performed extensive neutron scattering studies to determine the electronic mode softening at the QPT. In their studies, however, it was not possible to reproduce the low temperature critical field observed in the transverse susceptibility. As shown in Fig. 2.3.7 (B) the authors attributed this to poor thermal coupling of the sample, which decoupled at 300 mK. While this scenario is plausible, given the comparatively low thermal conductivity of $LiHoF_4$ at low temperatures and the technical challenges of providing a proper thermal connection between sample and bath in such experiments, a comparison with our data also suggests another explanation, namely that there was a slight misalignment of the sample in the order of $\approx 2 \deg$ in the experiments of Rønnow and Krämer.

Fig. 2.3.7 (C) shows the thermal phase transitions with a critical temperature of $T_c = 1.53\,$K at zero field in good agreement with literature [4, 12, 13, 19, 43, 53, 55, 72, 83]. As already observed by Ref. [4], the critical temperature has a maximum around $B = 1.1\,$T, where $T_c = 1.54\,$K. This behaviour is visible even after considering the error margins stemming from the critical field determination process and can be seen directly in the raw data, cf. Fig. A.1.2. It should be mentioned at this point, that the same thermometer was used compared to the study of Ref. [4], so that this comparison is not able to reveal any systematic errors in the temperature determination.

A comparison of the magnetic field dependence of χ' with the results of Ref. [4] is shown in Fig. 2.3.8. Both datasets were recorded at the same frequency of 511 Hz and at $\Phi = 0$. The excitation field of Ref. [4] was significantly larger and 0.16 mT, compared to the 0.013 mT applied in our study. Our lowest temperature studied is also slightly lower with $T = 62\,$mK compared to the $T = 76\,$mK of Ref. [4]. Nonetheless, the data show excellent agreement over a large field range. The biggest difference is the regime between 4 T and 5 T, where Ref. [4] found an enhancement of the susceptibility due to the hyperfine interaction. In our data, this feature is not clearly visible. Since the same parameters and sample were used, this is most likely a result of a small field dependent background signal of the susceptometer. The other features, such as the position of the critical field, the field dependence at high fields and the domain wall freezing at lower temperatures are in excellent agreement. Therefore the present study agrees in all points relevant to the determination of the magnetic phase diagram and the development of the theory discussed in the next section (Sec. 2.4). The significantly lower excitation field chosen in this study might explain the differences as compared to Ref. [4]. As explained below, magnetic
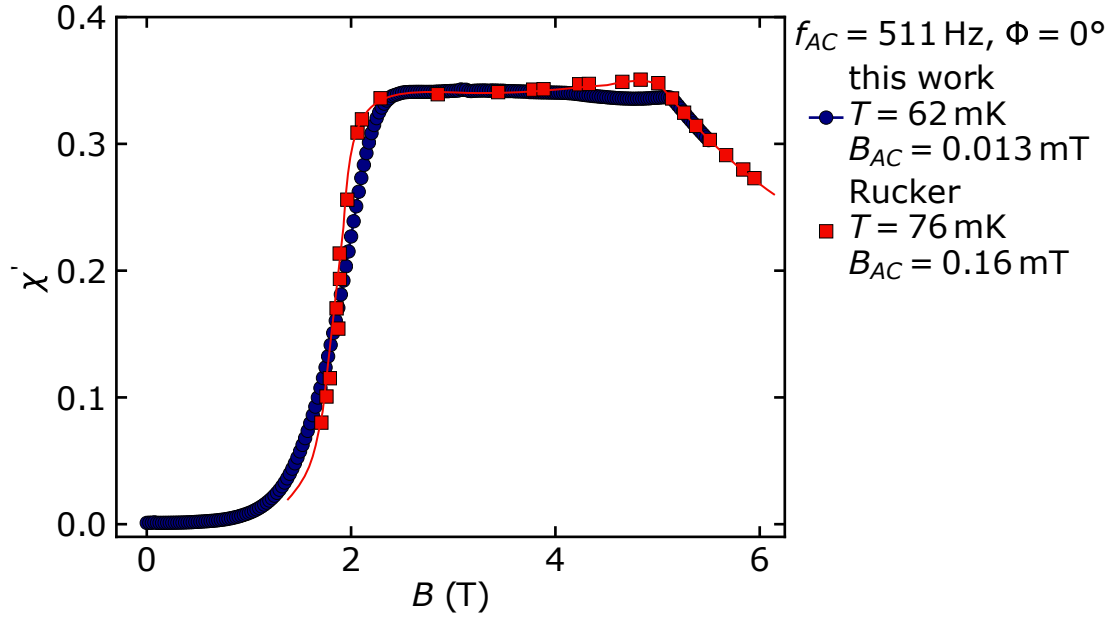
Figure 2.3.8.: Comparison of the real part of the magnetic susceptibility with the results of Rucker [4]. The results for the lowest temperature of $62\,\mathrm{mK}$ and $\Phi = 0$ are shown in blue and compared to the data of Rucker, recorded at $76\,\mathrm{mK}$ shown as red squares. The red line is a guide to the eye.

domains play an important role in the underlying physics of LiHoF$_4$. Domain formation, rearrangement and domain wall movement are sensitive to the excitation strength, thus the difference in B_{AC} may explain the different results.

2.4. Discussion and Comparison with Theory

The key observations in tilted magnetic fields, which need theoretical explanation can be summarized as follows:

1. The onset of magnetic order displays the characteristics of a well-defined phase transition in contrast to the crossover, which is expected from microscopic theory.
2. The transition immediately changes its character when deviating from the transverse field alignment as a jump in χ' develops.
3. Increasing the field angle Φ leads to a rapid decrease of the critical field B_c.
4. The temperature dependence of the phase boundary changes qualitatively, since the enhancement of B_c attributed to hyperfine coupling disappears.

Based on these findings and in a close collaboration with Heike Eisenlohr [5] and Matthias Vojta from the Technical University of Dresden a theoretical interpretation of our data was developed [21]. In summary, a dipolar Ising ferromagnet which forms domains is sufficient to describe all observations listed above. However, several important improvements of the transverse field Ising model compared to previous studies are necessary to describe the system properly and capture all effects.

The following section summarizes the theory. We follow the derivation presented in Refs. [5, 21] permitting detailed comparison with the experiment and highlight the new insights gained through this collaboration. For full details of the derivation of the presented theory, refer to part III of the dissertation of H. Eisenlohr [5].

We begin in Sec. 2.4.1 with a Landau model of the transverse field quantum phase transition under tilted magnetic fields. Following this, we describe the microscopic Hamiltonian for LiHoF$_4$ taking into account the crystalline electric field (CEF), Zeeman terms of the tilted field, hyperfine coupling to nuclear spins and interaction between electronic spins. Afterwards, the mean-field approximation of this model is presented. At this point the pure microscopic model will be reviewed and established, that it is insufficient to describe the experiments and that domain effects need to be included. In Sec. 2.4.2 we proceed with a review of the literature on domains in LiHoF$_4$, in order to motivate our choice of sheet-like domains considered in our model. Finally, we will describe the domain pattern in this model and show how it can be combined with the microscopic mean-field model.

The chapter will be concluded with a direct comparison of the final model and the data to complete the discussion.

2.4.1. Microscopic Model

Landau Theory   A simple phenomenological description of a transverse-field Ising quantum phase transition may be given in terms of a Landau model [5, 21]. The magnetization M acts as a scalar order parameter with Ising symmetry. Its order-parameter mass term is $(h - h_c)$ for perfectly transverse field h ($\Phi = 0°$). Hence, for $h < h_c$ an ordered phase is realized. If we account for tilting of the field by an angle $\Phi \neq 0°$, we find a Landau functional of the form [21]

$$F(M) = \frac{a}{4} M^4 + \frac{1}{2} \left(h \cos \Phi - h_c \right) M^2 + M h \sin \Phi. \qquad (2.4.1)$$

where $h \sin \Phi$ represents a field conjugate to the order parameter. For $\Phi = 0$ the transition at h_c displays mean-field exponents, i.e., $M \propto (h - h_c)^\beta$ and $M^\delta \propto h_c \Phi$.

At finite Φ however, the longitudinal field renders M non-zero for any order-parameter mass and in turn destroys the field-driven phase transition, which turns into a crossover. The location of this crossover can be defined by the maximum of the susceptibility as a function of h. Linear expansion of the free energy F at small angles $\Phi \ll 1$ removes the trigonometric terms and allows to calculate the susceptibility, which yields [5]

$$h_c - h^* \propto \Phi^{2/3}. \qquad (2.4.2)$$

As described in more detail below, our microscopic calculation for LiHoF$_4$ also yields a crossover at $B_c - B^* \propto \Phi^{2/3}$ if domain effects are neglected, see Fig. 2.4.1 (B).

In stark contrast, the experiment provides evidence of a qualitatively different behavior. Instead of a crossover, a sharp transition is observed, with the critical field approximately shifting proportional to Φ^2. The existence of a sharp thermodynamic transition at finite tilt angles is clearly beyond a single-component order-parameter description in the spirit of Landau theory.

Microscopic Model Since the magnetism in LiHoF$_4$ originates in the Holmium ions, the development of a microscopic description starts with the properties of a single Ho^{3+} ion. This Ho-atom is placed in a magnetic field applied under an angle Φ with respect to the hard axis, $\vec{B} = (B\cos\Phi, 0, B\sin\Phi)$. It is subject to the crystal field of S_4 symmetry, which in LiHoF$_4$ is created by the neighboring F$^-$ ions [68] as described in Sec. 1.2.1. The single ion Hamiltonian can be written as

$$H_{\text{ion}} = V_{\text{CF}}(\vec{J}) + A\vec{J}\cdot\vec{I} - \mu_B\vec{B}\cdot(g\vec{J} + g_N\vec{I}) \qquad (2.4.3)$$

with $J = 8$ electronic moments and $I = 7/2$ nuclear moments [5, 21]. The hyperfine coupling to the nuclear spins is assumed to be of Heisenberg type [42]. The associated material-specific strength of the hyperfine coupling for LiHoF$_4$ is $A = 39\,\text{mK}$. The CEF term V_{CF} is described by the common Stevens operators, which describe the orientational dependence, and coefficients fitting to the experimental data provided by Chakraborty *et al.* [41].

From the same Ref. [41], the electronic Landé factor g of a single Ho^{3+} ion is derived from the Wigner-Eckardt theorem to be 5/4. In large crystals, small deviations from this single-ion value are expected [19, 53]. We used $g = 1.1$, i.e., 12% lower than the single-ion value to achieve good agreement with our experimental data. Our results remain qualitatively unchanged without this adjustment, however there is a larger mismatch of B_c/T_c compared to experiment. As will be shown later, the value of g additionally has an influence on the stray-field energies and thus domains. The nuclear Zeeman term with $g_N = 1.5 \times 10^{-3}$ is included for completeness. Since the behavior of the nuclear spins is dominated by the hyperfine coupling, its impact stays relatively small.

The energetic landscape of the crystalline electric field in LiHoF$_4$ was already described in detail in Sec. 1.2.1 and shown in Fig. 1.2.1 (B1). The relevant detail for our model is the low-lying non-Kramers doublet with a large moment along the Ising axis, but non perpendicular to it. As a result of mixing with higher CEF levels, the application of a magnetic field along the hard axis x^1 leads to the corresponding moment scaling as $\langle J^x \rangle \propto B^2$, Fig. 1.2.1 (B2).

---

[1]Note: Here, we stick to the nomenclature established in Ref. [21]. This means, that the easy, crystalline *c*-axis is denoted by z, x is the hard axis within the field plane and y the hard axis perpendicular to the field plane.

In contrast to theoretical work reported in the literature [41, 42, 68] where the ground-state doublet was treated as a pseudospin 1/2, we keep the full 17-dimensional Hilbert space. This way our calculation fully accounts for the non-Kramers physics. This proves to be essential when describing the effects of an applied magnetic field in both the *z and* the *x* direction.

Ferromagnetism in $LiHoF_4$ is driven by interactions between the electronic spins of different Ho^{3+} ions, which involve both long-range dipolar and nearest-neighbor exchange interactions. For simplicity, we model this combination by a nearest-neighbor Heisenberg interaction K [68], recalling that the dominant source of magnetic anisotropy is the CEF term.

Taken together, this leads to a microscopic Hamiltonian of electronic spins $\vec{J}$ and nuclear spins $\vec{I}$ of the form

$$H_{\text{mic}} = -K \sum_{\langle ij \rangle} \vec{J}_i \cdot \vec{J}_j + \sum_i \left[V_{\text{CF}}(\vec{J}_i) + A\vec{J}_i \cdot \vec{I}_i \right] - \mu_B \vec{B} \cdot \sum_i (g\vec{J}_i + g_N \vec{I}_i), \qquad (2.4.4)$$

where $\langle ij \rangle$ runs over pairs of nearest neighbors. At this point the strength of the effective interaction reduces to a fit parameter. For good agreement with the experimental critical temperature T_c we choose $K = 14.5\,\text{mK}$, which is consistent with the order of magnitude of values estimated for the dipolar and exchange couplings in $LiHoF_4$ [42].

Mean-Field Modeling   The effects of fluctuations are suppressed due to the long-ranged nature of the dipolar interaction in $LiHoF_4$ and a mean-field treatment appears justified. Within mean-field approximation, the Hamiltonian in Eq. (2.4.4) reduces to a single-site problem

$$H_{\text{mic}}^{\text{MF}} = -nK(\vec{J} \cdot \vec{\bar{J}} - \frac{\vec{\bar{J}}^2}{2}) + V_{\text{CF}}(\vec{J}) + A\vec{J} \cdot \vec{I} - \mu_B \vec{B} \cdot (g\vec{J} + g_N \vec{I}), \qquad (2.4.5)$$

where $n = 4$ represents the number of nearest neighbors. Solving $H_{\text{mic}}^{\text{MF}}$ amounts to the diagonalization of a 17×8-dimensional matrix, supplemented by the self-consistency condition $\vec{\bar{J}} = \langle \vec{J} \rangle$. All parameters used as well as the details of the derivation can be found in Sec. 9.2 of Ref. [5].
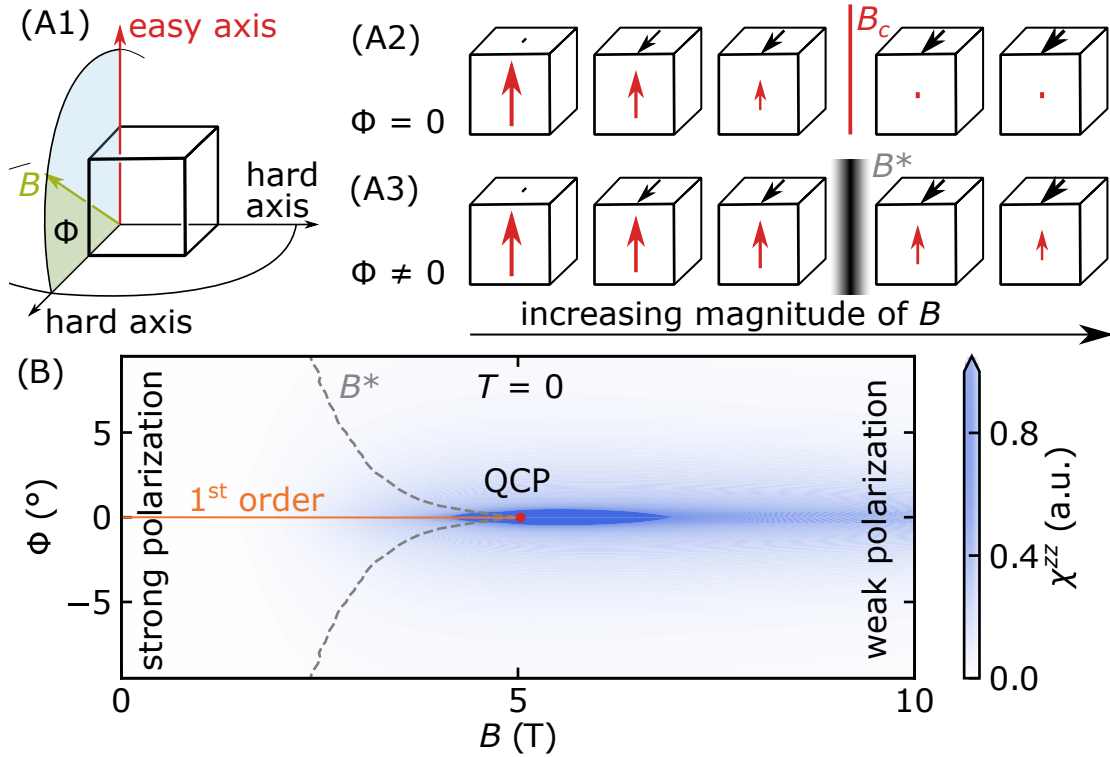
Figure 2.4.1.: Microscopic phase transition without magnetic domains. (A1) The field angle is applied in the plane between one hard axis and the easy axis. (A2) The phase transition is visualized for $\Phi = 0$. The longitudinal (red arrows) and transverse (black arrows) magnetization are visualized on the cube for increasing magnetic field. At the critical field B_c, the longitudinal magnetization vanishes. (A3) For $\Phi \neq 0°$, the transition turns into a crossover with B^*, as the longitudinal magnetization, thus the order parameter, stays finite for all field strengths. (B) The zero-temperature phase diagram is shown as a colormap of the magnetic susceptibility along the easy axis χ^{zz} as a function of B and Φ. From the quantum critical point at $\Phi = 0$ a line of crossovers at field B^* emerges under tilted fields. Figure adapted from Ref. [21].

The resulting zero temperature phase diagram of this purely microscopic (i.e. single-domain) scenario is displayed in Fig. 2.4.1.

Crossover in the Single-Domain Model   To emphasize, why it is important to include magnetic domains into the theory, this single-domain model will be analyzed at this point. It simultaneously acts as a status quo of the microscopic description of LiHoF$_4$ prior to the work carried out as part of this project [21], since it captures the features of Landau theory of a transverse-field Ising quantum phase transition, as described above.

Fig. 2.4.1 illustrates this single-domain model, calculated for $T = 0$. The field is applied within the plane spanned by one hard and the easy axis, cf. Fig. 2.4.1 (A1). The angle Φ measures the deviation of the magnetic field from perfect perpendicular alignment to the easy axis. The situation for perfect transverse field ($\Phi = 0°$) is shown in Fig. 2.4.1 (A2). For zero field, the magnetization is oriented solely along the easy axis. Hence, the easy axis magnetization is maximal (red arrow) and the transverse magnetization is zero (black arrow). Increasing the magnetic field leads to an increase in the transverse magnetization and a decrease in the longitudinal magnetization. Upon reaching the critical field B_c, the longitudinal magnetization is zero and the magnetization is parallel to $\vec{B}$.

For $\Phi \neq 0°$, Fig. 2.4.1 (A3), however, this transition turns into a crossover with a characteristic field B^*, above which the magnetization is parallel to $\vec{B}$, but its longitudinal component is non-zero.

The corresponding phase diagram as a function of magnetic field B and field angle Φ is shown in Fig. 2.4.1 (B). The colormap shows the magnetic susceptibility along the easy axis χ^{zz}. A quantum critical point (red) exists for $\Phi = 0°$ at $B_c = 5.1\,\text{T}$, which evolves into a line of crossover transitions for $\Phi \neq 0°$, as shown in a dashed grey line. The properties of this crossover are consistent with the results from Landau theory as outlined above. Namely, the susceptibility χ_{zB} along the hard axis z with field change in the field direction B displays a maximum as function of applied field at B^*, the location of which is shown in Fig. 2.4.1 (B). At small angles, we find $B_c - B^* \propto \Phi^{2/3}$ as expected.

At $\Phi = 0$, a first order transition occurs, since the easy axis field $B_z = B\sin(\Phi)$ changes sign and $\langle J_z \rangle < 0$ goes to $\langle J_z \rangle > 0$.
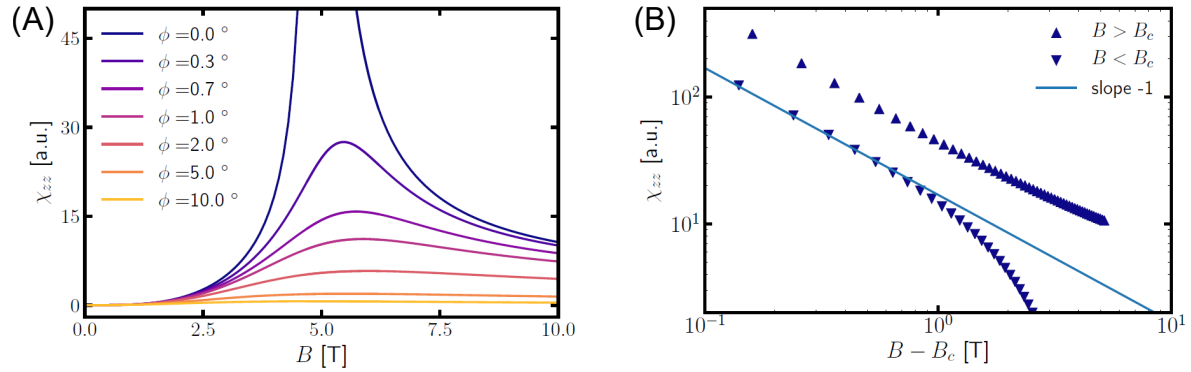
Figure 2.4.2.: Critical behavior of the susceptibility in the single-domain model.   (A) zz-component of the susceptibility, which represents the measured real part of the susceptibility component in the single-domain model. (B) The critical behavior with $\gamma = 1$ is visible at $\Phi = 0°$ and $T = 0$. Figure taken from Ref. [5].

Fig. 2.4.2 shows the magnetic susceptibility χ_{zz} along the easy axis, with field change along the easy axis, for various orientations of the external magnetic field [5]. It corresponds to the real part of the AC susceptibility measured in this thesis. A direct comparison to the data, as in Fig. 2.3.5 (A), reveals significant differences. Not only does the single-domain model lack a jump of χ' at the phase transition, but also is for $\Phi \neq 0°$ no clear transition visible in this choice of components of the susceptibility (zz).

For $\Phi = 0°$ however, the expected critical behavior with $\gamma = 1$ is found, see Fig. 2.4.2 (B). This is observed for measurements with $\Phi = 0$ as well, see Sec. 2.3.3. It thus follows that the purely microscopic model is sufficient to describe experiments at $\Phi = 0°$. Since all susceptibility data published so far [4, 12] used perfect sample alignment, it becomes clear, why our study was necessary to trigger further development of the theory. Only under tilted fields $\Phi \neq 0°$ appear new features asking for more theoretical insights.

In the next section we will proceed with the importance of magnetic domains in the LiHoF$_4$ system and show how they improve the model.

2.4.2. Mesoscopic Model

Magnetic Domains in LiHoF$_4$ It is well-known, that ferromagnets exhibit magnetic domains. As presented in Sec. 1.2.2, the formation of domains in LiHoF$_4$ has been known since the 1970s [53] and has since been the object of several experimental studies [53–57] as well as theoretical work [41, 52, 84].

Magnetic domains form due to the stray-field energy, also referred to as demagnetization energy. The magnetization of a sample creates a magnetic field around it. If the net magnetization is large, the energy of the stray-field is large as well. The formation of domains, areas with homogeneous magnetization pointing in different directions, allows to minimize this energy significantly. Since it also costs energy to create the domain walls, the border between two domains where the magnetic moments are not aligned in parallel, the stray field effect is counteracted and domains typically have a finite size significantly larger than the crystal lattice. The size of the domain walls is usually much thicker than the lattice spacing and the magnetization changes gradually between domains.

Due to this interplay, the optimal domain pattern of a sample tends to be complex in principle. Microscopic interactions and anisotropies influence the structure of domain walls and the form of the domains. Hence, changes in T and B often directly impact the domain pattern as the underlying mechanics changes. Defects in the lattice can pin domain walls and stop their movement. Additionally, the sample geometry has a significant impact on the domain shape, domains interact with the surface, for example in the form of branching [58, 85]. The complexity of domain forms is captured in experimental images of LiHoF$_4$ as presented in Sec. 1.2.2, cf. Fig. 1.2.2.

Theoretical studies of LiHoF$_4$ addressing the long-ranged dipolar interaction employed an Ewald summation [86] or the reaction-field method [87]. The latter incorporates the presence of domains by considering an imaginary microscopic sphere in an effective field of surface charges [41], which breaks down to the use of a demagnetization factor. The former naturally leads to domain formation in Monte Carlo simulations with a large enough unit cell and appropriate boundary conditions [52]. In the study by Biltmo *et al.* [52] a domain pattern of parallel sheets was found to be favorable at zero temperature for an effective spin-1/2 model. The study however only focused on the zero field case.

Domain Model   As the simplest possible geometry, we assume an alternating domain pattern as shown in Fig. 2.4.4 (A), where up and down domains are stacked along the hard axis, with no field component along the stacking. This configuration has the lowest energy in zero field, according to Ref. [52]. Ref. [5] notes, that a pattern with stacking along the other hard axis is unfavorable due to charged domain walls.

The sample in this calculation is cubic, with a base length of $L = 5\,\mathrm{mm}$, about twice the size of the experimental sample, as shown in Fig. 2.4.3 (A). N domains of each type (up and down) are considered. To represent the approximate size of microns of real domains in $\mathrm{LiHoF_4}$, a number of $N = 200$ domain pairs is chosen. Since the number of domains is fixed, the variational parameter in this model is the volume ratio of the domains, called shortly *domain ratio*. It is defined as

$$v = \frac{D_2}{D_1 + D_2}, \tag{2.4.6}$$

with $D_{1,2}$ the thickness of the up and down domain respectively, so that $L = N \cdot (D_1 + D_2)$. The optimum of v is determined by energy mimimization and varies as a factor of magnetic field and temperature [5, 21], cf. Fig. 2.4.3 (B, C). The details of the energy optimization are beyond the scope of this thesis, for more information we refer to Refs. [5, 21].

The model assumes a homogeneous magnetization throughout all domains of each type. While this idealization is not true for a cubic sample, where demagnetization effects are present at the surface and edges of the sample, it is a good assumption, when a spherical sample is used, such as the one in the experiment which is homogeneously magnetized. This magnetization density can be related to the microscopic spins by $\vec{m}_{1,2} = g\mu_b \vec{J}_{1,2} M/V$ with the electronic g-factor g, the Bohr magneton μ_B, the number of lattice sites M and the sample volume V. Nuclear spins are neglected, since they are suppressed by their significantly smaller g-factor.

The domain energy terms are quadratic in the magnetization, thus also in spin and can therefore be seen as effective interactions between the microscopic moments $\vec{J}$. Hence, the domain energy can be written as [21]

$$E_{\mathrm{dom}} = M \sum_\alpha \left(c_1^\alpha \bar{J}_1^\alpha \bar{J}_1^\alpha + c_2^\alpha \bar{J}_2^\alpha \bar{J}_2^\alpha + c_{12}^\alpha \bar{J}_1^\alpha \bar{J}_2^\alpha \right), \tag{2.4.7}$$

with the coupling parameters c^α containing the domain wall energies as well as the potential energy contributions of the surface charges by the magnetization along $\alpha = x, y, z$.
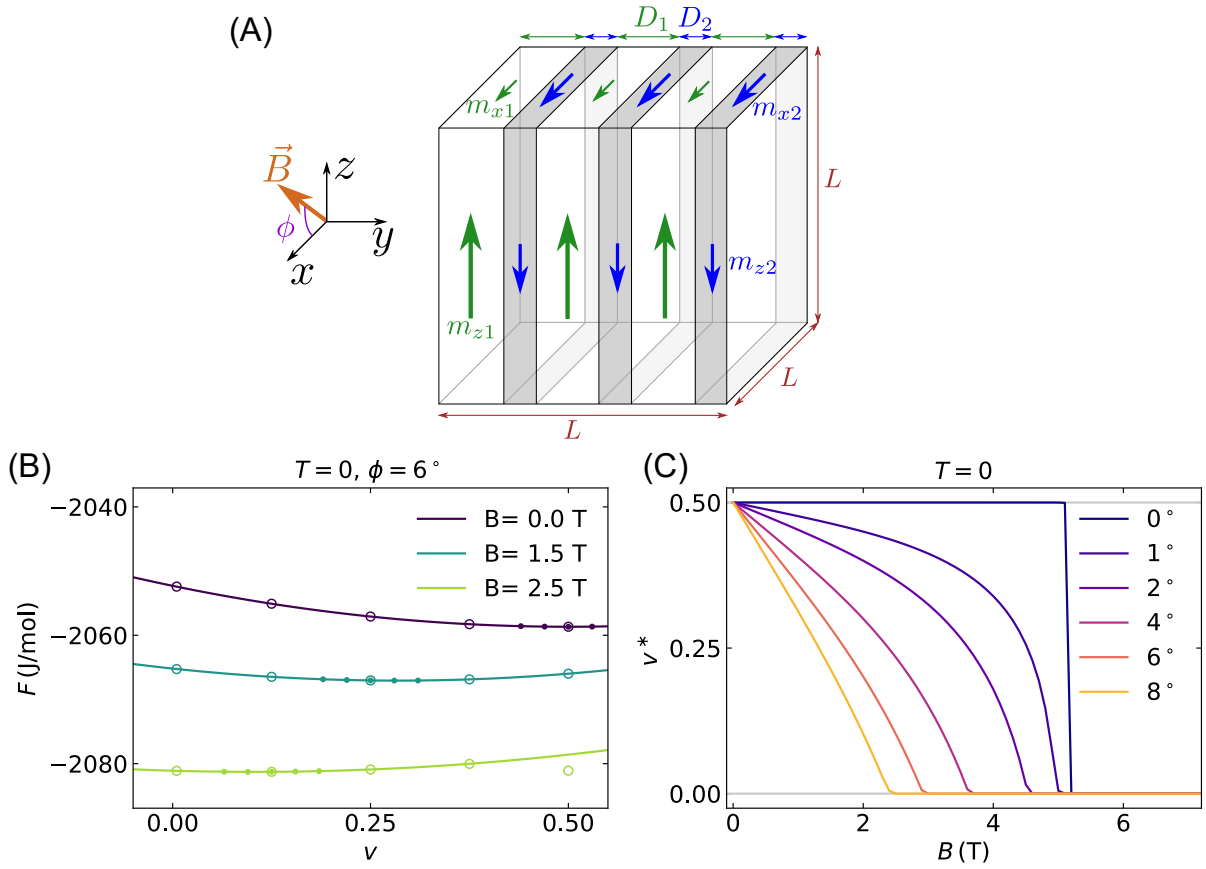
Figure 2.4.3.: The domain model used in the theory. (A) Sheet like arrangement of the magnetic domains stacked along one easy axis. The magnetic field is applied in the plane of the sheets. (B) Free energy as a function of domain ratio for $T = 0$, $\Phi = 6°$ and various fields. The optimal domain ratio v^* is found at the minimum of the free energy. (C) v^* as a function of field B for various field angles Φ. Figure taken from Ref. [21].

The above mentioned energy minimization determines these parameters, which are used in the combined mean-field model.

Combined Mean-Field Hamiltonian The microscopic Hamiltonian Eq. (2.4.5) as well as the domain energies Eq. (2.4.7) may at this point be combined in a final model. By introducing domain independent mean-fields $\vec{\bar{J}}_{1,2}$ as well as neglecting the microscopic interactions across domain walls, the microscopic Hamiltonian H_{mic} is translated in two independent mean-field problems for each domain, Eq. (2.4.8) and (2.4.9). Interactions between the domains are turned into effective mean-field interactions. The two coupled mean-field Hamiltonians are [21]

$$
\begin{aligned}
H_1^{\text{MF}} &= \left(-\frac{n}{2}K + \frac{c_1^x}{1-v}\right)\left(2\bar{J}_1^x J_1^x - (\bar{J}_1^x)^2\right) \\
&+ \frac{c_{12}^x}{1-v}\left(\bar{J}_2^x J_1^x - \frac{1}{2}\bar{J}_1^x \bar{J}_2^x\right) \\
&+ \left(-\frac{n}{2}K + \frac{c_1^z}{1-v}\right)\left(2\bar{J}_1^z J_1^z - (\bar{J}_1^z)^2\right) \\
&+ \frac{c_{12}^z}{1-v}\left(\bar{J}_2^z J_1^z - \frac{1}{2}\bar{J}_1^z \bar{J}_2^z\right) \\
&- \frac{n}{2}K\left(2\bar{J}_1^y J_1^y - (\bar{J}_1^y)^2\right) + H_{\text{ion}}(\vec{\hat{J}}_1),
\end{aligned}
\tag{2.4.8}
$$

and

$$
\begin{aligned}
H_2^{\text{MF}} &= \left(-\frac{n}{2}K + \frac{c_2^x}{v}\right)\left(2\bar{J}_2^x J_2^x - (\bar{J}_2^x)^2\right) \\
&+ \frac{c_3^x}{v}\left(\bar{J}_1^x J_2^x - \frac{1}{2}\bar{J}_1^x \bar{J}_2^x\right) \\
&+ \left(-\frac{n}{2}K + \frac{c_2^z}{v}\right)\left(2\bar{J}_2^z J_2^z - (\bar{J}_2^z)^2\right) \\
&+ \frac{c_{12}^z}{v}\left(\bar{J}_1^z J_2^z - \frac{1}{2}\bar{J}_1^z \bar{J}_2^z\right) \\
&- \frac{n}{2}K\left(2\bar{J}_2^y J_2^y - (\bar{J}_2^y)^2\right) + H_{\text{ion}}(\vec{\hat{J}}_2),
\end{aligned}
\tag{2.4.9}
$$

with the self-consistency conditions

$$
\vec{\bar{J}}_n = \langle \vec{\bar{J}}_n \rangle,
\tag{2.4.10}
$$

which are solved iteratively and where the expectation value is taken with respect to H_n^{MF}. This is equivalent to promoting E_{dom} Eq. (2.4.7) to a bilinear Hamiltonian and using mean-field notation to decouple its interaction terms, thus producing terms of the form $\bar{J}_1^\alpha J_1^\alpha$ etc. The total energy then may be written as

$$
E_{\text{tot}}^{\text{MF}} = M(1-v)\langle H_1^{\text{MF}}\rangle + Mv\langle H_2^{\text{MF}}\rangle.
\tag{2.4.11}
$$

The optimum domain ratio v^* is then obtained for each set of parameters (B, T, ϕ) by minimizing the free energy $F(v)$. Taken together, Eqs. (2.4.8-2.4.10) form the model, which combines and consistently describes the domain energy term, microscopic interactions as well as the interplay of stray-field effects with the microscopic expectation values.

Mesoscopic Model in Tilted Fields After this overview of the mesoscopic (multi-domain) model, we want to present its behavior in tilted magnetic fields to emphasize the improvements compared to the purely microscopic (single-domain) model.

As described in Sec. 2.4.1, the magnetic field is applied in the plane spanned by one hard axis and the easy axis. The field angle Φ is defined to be zero, when perfectly perpendicular to the hard axis, representing the experimental configuration, cf. Fig. 2.4.4 (A1).

Within the ferromagnetic phase, at fields below B_c, it is favorable for the system to create a domain pattern with up and down domains stacked along one hard axis, with the easy-axis magnetization alternating, as discussed above and shown in Fig. 2.4.4 (A2). For perfect field alignment, $\Phi = 0°$, the transition from the ferromagnetic multi-domain to the field polarized single-domain state coincides with the microscopic ordering transition at B_c. As seen in Fig. 2.4.5 (A2), the magnetization along the easy axis approaches zero simultaneously for both domains and the volume ratio v of both domains stays the same at $v = 0.5$. This is shown quantitatively in Fig. 2.4.5 (A1), where the magnetization of the up and down domains along the easy z-axis is displayed in cyan and the domain ratio v is shown in brown.

Under tilted magnetic fields, $\Phi \neq 0°$, the volume fraction of the minority domains decreases continuously with increasing field, characterizing a second-order phase transition at B_c, where v reaches zero. As shown quantitatively in Fig. 2.4.5 (A2) and depicted in Fig. 2.4.4 (A3), the domain ratio decreases monotonously. This decrease is linear close to the phase transition [5] and for larger angles the linear regime expands towards $B = 0$ T. Again, the magnetization along the hard axis increases with field and the magnetization of both domains along the easy axis decreases. Above B_c the magnetization in the single domain polarized state points along the field direction. Looking into the magnetization in detail, cf. Fig. 2.4.5 (A1, A2), reveals that the magnetization in each domain behaves the same for $\Phi = 0°$ and $\Phi = 3°$. But only for the optimal orientation, the microscopic transition, where J^z reaches zero coincides with the vanishing of the minority domains.
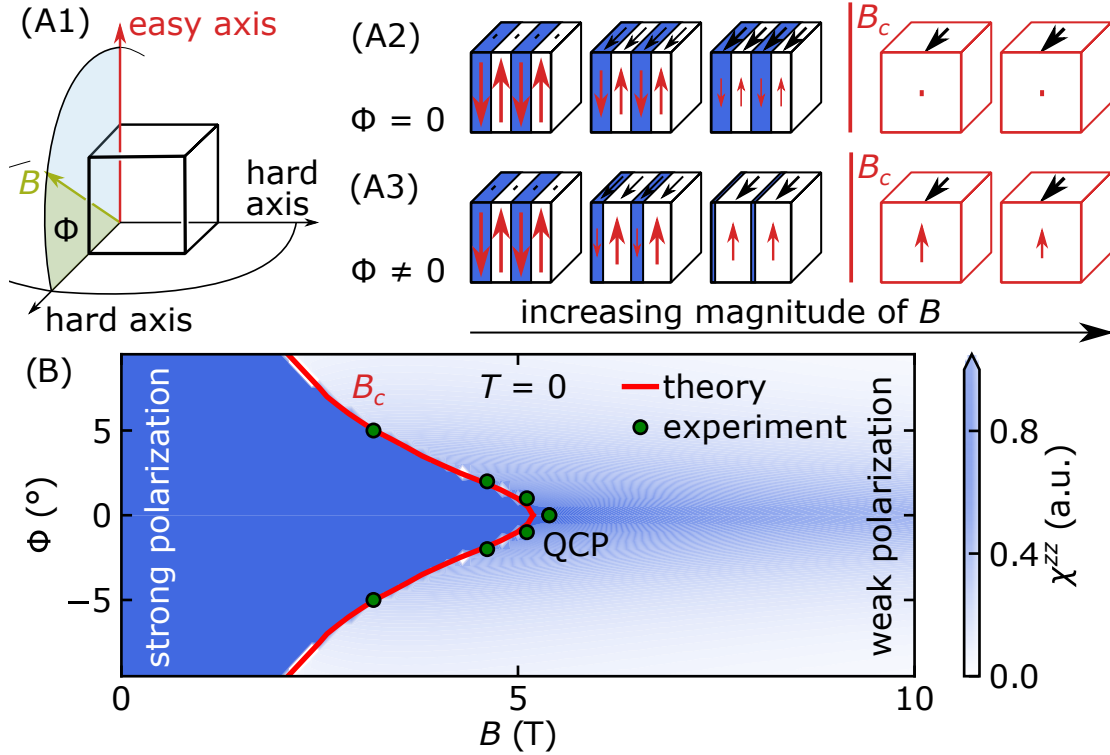
Figure 2.4.4.: The multi-domain model of transverse field QPT and mesoscale QPT. (A1) The field angle is applied in the plane between one hard axis and the easy axis. (A2) The transverse field QPT is visualized for $\Phi = 0$. The longitudinal (red arrows) and transverse (black arrows) magnetization are visualized on the cube for increasing magnetic field. The minority domains are shown in blue and majority domains in white, respectively. At the critical field B_c, the longitudinal magnetization vanishes in both domain types simultaneously. The domain ratio v is constant up to the critical field. (A3) For $\Phi \neq 0°$, both the longitudinal magnetization in the domains as well as the volume fraction of the minority domains v decreases with increasing field. At the critical field, v vanishes. (B) The zero-temperature phase diagram is shown as a colormap of the magnetic susceptibility along the easy axis χ^{zz} as a function of B and Φ. From the transverse field quantum critical point at $\Phi = 0$ a line of quantum critical points emerge under tilted fields. The experimental datapoints for the critical field at $T = 67\,\mathrm{mK}$ (green circles) are in good agreement with this theory. Figure adapted from Ref. [21].

For tilted fields, the minority domains vanish much earlier and the average magnetization approaches the magnetization of the majority domains at the transition.

Based on this, an alternative order parameter can be defined, in terms of the difference of the easy axis magnetization of the majority domain and the average magnetization in that direction [5], which shows critical behavior $\beta = 1/2$ only for $\Phi = 0°$ and $\beta = 1$ otherwise.

These observations are summarized in the B-Φ-phase-diagram shown in Fig. 2.4.4 (B). In very good agreement with our experimental data (green circles), a line of sharp second-order phase transitions (red line) expands from the quantum critical point. The strong polarization along the easy axis is suppressed by application of the magnetic field. The magnetic susceptibility is large within the ferromagnetic multi-domain state and only limited by the demagnetization factor of the sphere.

2.4.3. Comparison of Experiment and Theory

Magnetization along specific directions and domain ratios are difficult to evaluate experimentally. Therefore the magnetization along the field direction is shown in Fig. 2.4.5 (B1). It shows a kink at the phase transition, highlighted by an arrow. In comparison to the AC susceptibility, this feature is significantly less pronounced and makes the determination of B_c difficult from this quantity alone [44].

The phase transition is characterized by a jump in the magnetic susceptibility along the easy axis, as shown in Fig. 2.4.5 (B2). Both experimental results for $T = 67\,\mathrm{mK}$ (solid lines) and theoretical results for $T = 0\,\mathrm{K}$ (dashed lines) are in very good agreement in the field polarized state at high fields. While the theoretical results show a sharp jump at B_c, the experimental data are rounded in this regime. Nonetheless, the definition of the location of B_c as the point, where χ' deviates from the high field behavior[2] is confirmed as a good choice, since this point is very similar in both theory and experiment. The rounding effect in the experiment is expected, since the theory assumes ideal homogeneous stray fields. In the real sample, however, these stray fields are likely inhomogeneous and the domains vanish at different external fields, depending on their position within the sample. Imperfections in the spherical sample shape enhance this effect. This further highlights

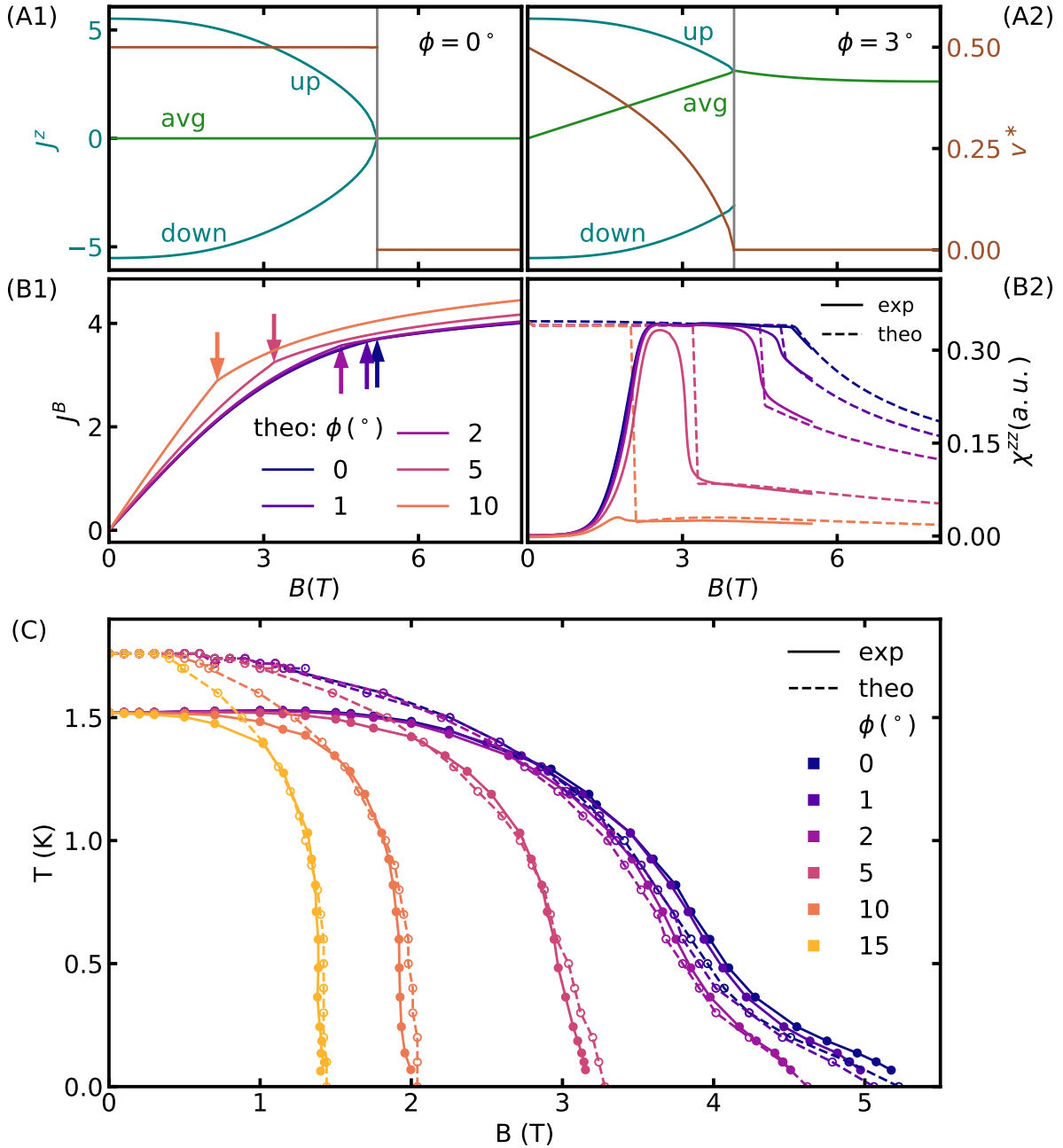---

[2]See Sec. 2.2.5 and Fig. 2.2.7 for the exact definition.

Figure 2.4.5.: Results of the magnetization and susceptibility from the multi-domain model. (A1) For $\Phi = 0°$, the domain ratio (brown) is constant up until the phase transition, where it jumps to zero. The magnetization along the easy axis J^z for the up and down domains (cyan) goes continuously to zero at the phase transition. (A2) For $\Phi = 3°$ the domain ratio decreases continuously and reaches zero at the phase transition. J^z is finite over the whole field range. (B1) The magnetization along the field direction J^B displays a small kink at the phase transition. (B2) In the experimental (solid lines) and theoretical (dashed lines) data of the transverse susceptibility, the transition is clearly visible as a jump. (C) The phase boundaries from theory (dashed lines) and experiment (solid lines) are compared in the B-T-phase-diagram. Figure taken from Ref. [21].

the importance to use a spherical sample compared to cuboids, where this effect will be even more pronounced.

Decreasing the field below B_c leads to the formation of a plateau in both experiment and theory, before χ' goes to zero for $B < 2\,\mathrm{T}$ in the experiment. In the data for the imaginary part χ'' is a peak visible at this drop. As explained earlier, this is a sign of a dissipative process, previously identified with the freezing of domain wall motion. Dynamic and dissipative effects however are beyond the current modelling, which assumes a static susceptibility $\chi_{zz}(f = 0)$ and therefore cannot replicate such effects [5]. It should be noted at this point, that the AC susceptibility measured at $f = 511\,\mathrm{Hz}$ can be considered quasi-static for the comparison with theory, since the electronic energy scales are significantly larger, and the crystal field energies in the range of several Kelvin translate into the GHz frequencies.

While it is shown here only for $T = 0\,\mathrm{K}$, the qualitative theoretical findings are basically unchanged for finite temperatures [5, 21]. The corresponding results are shown in the magnetic phase diagram in Fig. 2.4.5 (C). Theory and experiment agree over a wide temperature and field range.

Especially the surprising sensitivity of the transition field B_c to small tilt angles and the disappearance of the inflection point in the phase boundary as a function of temperature for $\Phi > 5°$ is captured by the theory very well. Both effects can only be replicated by including the interplay of non-Kramers physics and strong hyperfine coupling [21], as depicted in Fig. 2.4.6.

Due to the crystal field environment the magnitude of the magnetic moment $|J|$ is not constant as a function of B, cf. Fig. 2.4.6 (B1). While the easy axis component decreases slowly, the field induced hard axis component increases quadratically, since its formation requires a interaction of the non-Kramers doublet states with higher CEF states [21]. As a result, $|J|$ has a minimum at B_c. With increasing angle Φ this minimum gets less pronounced, cf. Fig. 2.4.6 (B1). Since the hyperfine coupling A energetically prefers large electronic moments $|J|$, it stabilizes the ferromagnetic with respect to the paramagnetic phase for temperatures $T < 0.5\,\mathrm{K}$ as more hyperfine energy can be gained by anti-alignment of nuclear spins if $|J|$ is larger, cf. Fig. 2.4.6 (A1). This leads to the low-temperature "nose" feature in the phase boundary [12], see Fig. 2.4.5 (C). As the variation of $|J|$ gets less pronounced with increasing tilt angle Φ, the energy gain of the ordered
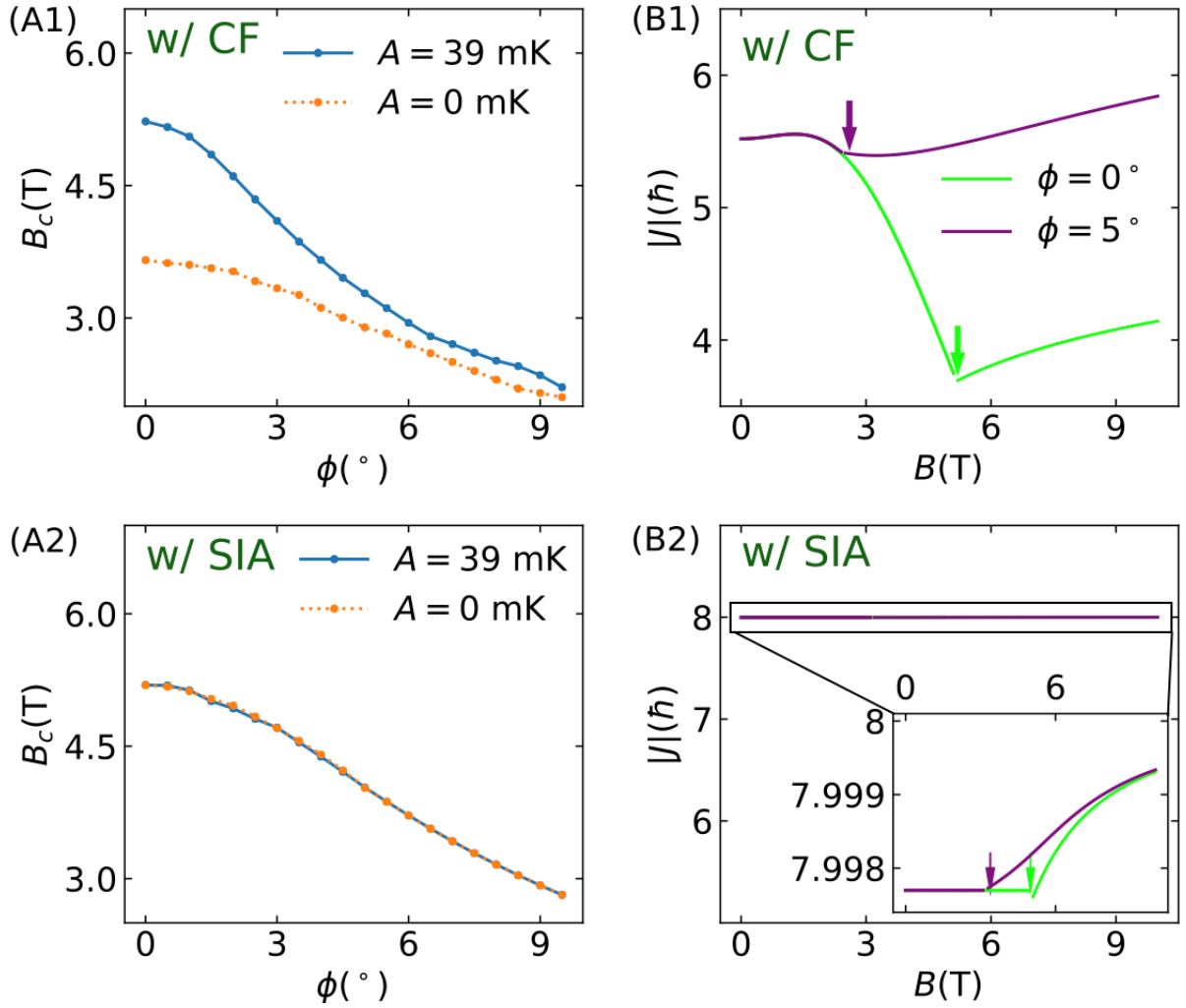
Figure 2.4.6.: Interplay of hyperfine coupling with the non-Kramers ground state at zero temperature. Treatment of the Ising anisotropy in terms of the non-Kramers full crystal field terms is denoted (CF). Treatment of the Ising anisotropy in terms of a simple single-ion anisotropy acting on a Kramers moment is denoted (SIA). (A1) Calculated critical field, B_c, as a function of Φ, with and without hyperfine coupling A, while the full crystal-field Hamiltonian is taken into account. B_c exhibits a strong dependence on Φ, when hyperfine coupling is included. (A2) B_c as a function of Φ with and without hyperfine coupling A, where the Ising character is accounted for by a SIA acting on a Kramers moment. The critical field does not exhibit a substantial dependence on the hyperfine coupling and the sensitivity of B_c to changes of ϕ is much reduced. (B1) The electronic moment of the Ho ion, $|J| = \sqrt{\langle J^{x2} + J^{y2} + J^{z2} \rangle}$, as a function of field. Within the ordered phase it is significantly enhanced. (B2) $|J|$ is essentially field-independent. The tiny variation of $|J|$ under these conditions, highlighted in the inset, reflects the hyperfine-induced entanglement of the electronic moment with the nuclear spin. Figure taken from Ref. [21].

phase is only slightly enhanced by the hyperfine interaction. This explains both the absence of the "nose" of the phase-boundary for $\Phi > 5°$ and the strong variation of B_c for $\Phi < 5°$ as shown in Fig. 2.4.5 (C), Fig. 2.3.7 (A), and Fig. 2.3.5. In short, tilted fields rapidly eliminate the non-Kramers variation of $|J|$ and hence the hyperfine-induced enhancement of B_c. If only a simple single ion anisotropy is considered instead of the full CF scheme, B_c is less sensitive to the tilt angle and the hyperfine coupling A has no impact, cf. Fig. 2.4.6 (A2). This is due to $|J|$ being basically independent of the magnetic field B as shown in Fig. 2.4.6 (B2). For a more detailed analysis of the non-Kramers physics refer to the Supplementary Information of Ref. [21] and Cha. 10.5 of Ref. [5].

The largest discrepancies are found around the thermal phase transition, which is common for theoretical work and also observed in Refs. [41, 68]. A good match of both T_c and B_c strongly depends on the g-factor. Our work uses $g = 1.1$, 12% below the literature value of $g = 1.25$ found with various techniques [19, 22, 43]. Mean field models, such as the presented multi-domain model tend to overestimate order, thus it is not surprising that T_c is larger in the theory. Moreover, we found a re-entrant behavior near the thermal transition, shown in Fig. 2.3.7 (C). This feature is not replicated by the calculations. Taken together with the mismatch of T_c, this suggests, that additional mechanism might be present, which suppress magnetic order at elevated temperatures, which are not part of the current model.

Earlier, in Sec. 2.3.3, it was shown that the experimental AC susceptibility χ' displays a critical behavior with $\gamma = 1$ for perfect transverse field, i.e. $\Phi = 0°$. For $\Phi \neq 0°$ however the critical power law cannot be observed, rather χ' is constant at large angles. Similarly, an analysis of the order parameter susceptibility in Ref. [5] reveals that within the multi-domain state only for $\Phi = 0°$ a mean field exponent of $\gamma = 1$ is observed. For tilted fields, the order parameter susceptibility approaches a constant at the phase transition ($\gamma = 0$), as shown in Fig. 2.4.7 (A). This is closely connected to the domain ratio v, which mirrors this behavior (B). For $\Phi = 0$, the domain ratio is constant and thus all domains have the same size near the phase transition. In this regime, microscopical criticality is observed, characterized by an increasing correlation length [5]. In tilted fields however the correlation length is constant and the domain ratio goes to zero. The position of the crossover between the regime of domain-driven criticality and microscopical criticality could not be determined exactly by the model, since computation near the phase transition and at smallest angles is numerically difficult [5].
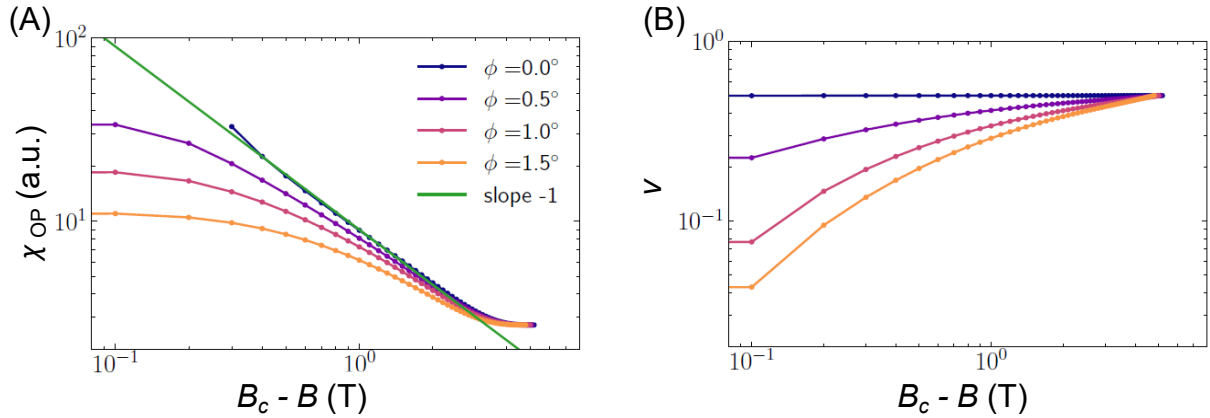
Figure 2.4.7.: The order parameter susceptibility χ_{OP} in the ordered phase diverges with the mean-field exponent $\gamma = 1$ in transverse field and approaches a constant ($\gamma = 0$) in tilted fields (A). This change of the critical exponent mirrors the deviation of the optimal domain ratio from its $\Phi = 0$ value $v = 0.5$ (B) and thus separates microscopic and domain-driven criticality. Figure taken from [5], with updated labels to adjust the notation.

It needs to be noted, that the calculation shown here is valid within the multi-domain state and is thus not directly comparable to the analysis presented in Sec. 2.3.3, which was done above B_c in the field polarized state. Nonetheless gives this comparison insight in the sensitivity of the transition to the field angle and the aspects of the domain-driven transition.

2.5. Summary and Outlook

In this chapter, the transverse susceptibility of the dipolar Ising ferromagnet LiHoF$_4$ was investigated as a function of field, temperature and field angle. In the first part the technique of AC susceptibility was introduced, followed by a detailed description of the experimental setup. Special attention was brought to the sample alignment and corresponding error estimates, since a good angular precision proved crucial for this study.

In the third section, an overview of the data collected was given. We determined the magnetic phase diagram as a function of field and temperature for fields perfectly perpendicular to the easy c-axis and for tilt angles $\Phi = 1°$, $2°$, $5°$, $10°$ and $15°$. As a main result, we observed a strong dependence of the critical field on the field orientation as well as a disappearance of the hyperfine enhanced ferromagnetic regime at low temperatures and high fields. Already tilt angles as small as $1°$ change the form of the AC susceptibility signal significantly, as the kink in χ' at the phase transition observed at perfectly transverse field develops into a jump of χ'.

The regime at low fields $B < 2\,\text{T}$ and temperatures $T < 0.4\,\text{K}$, where freezing of the domain wall motion suppresses the AC susceptibility signal was found to be independent of the field orientation. This is consistent with the picture of domain walls pinning to crystalline defects, since those are intrinsic to the material and not influenced by the direction of the applied magnetic field.

In agreement with the findings of Ref. [4], we observe discrepancies to the published mean-field behavior around T_c. Not only is the measured critical temperature lower than the calculated value, but more importantly we find that T_c is slightly enhanced around $B = 1\,\text{T}$ compared to zero field. Future efforts of the theoretical modeling might concentrate on this aspect, which suggests additional underlying interactions. This feature appears to be independent of the field angle and only disappears, when the critical field is reduced significantly due to tilted field.

Field sweeps of the AC susceptibility for various field angles revealed, that a clear phase transition with a sharp jump of χ' is observed at finite angles. As a result the form of the transition changes significantly and the critical behavior with $\gamma = 1$ at $\Phi = 0°$ can no longer be identified in tilted fields.

Since the transition observed in tilted fields is in stark contrast to the expected crossover from Landau theory, an advanced theoretical description was developed [5, 21] by including a mesoscopic model of the magnetic domains and considering the non-Kramers physics of the CEF instead of treating the system as spin 1/2. These two new aspects go beyond previous modeling [12, 14, 41, 42] and prove do be key to understand the experimental observations.

3. Caloric Properties under Transverse Magnetic Fields

As part of this thesis, two caloric properties were investigated, namely the specific heat and the magnetocaloric effect. By combining the two observables, the entropy of LiHoF$_4$ can be studied. This chapter provides an overview of the experimental principles and setup, followed by a presentation of the results and their discussion in the context of the theory described in the previous chapter.

3.1. Experimental Techniques

3.1.1. Theoretical Foundations

For the experiments reported in this thesis, the entropy S, heat capacity C and thermal conductance k play an important role and will be described in this section.

Entropy In statistical physics, the entropy is defined as

$$S = k_B \ln \Omega, \tag{3.1.1}$$

where k_B is the Boltzmann constant and Ω is the accessible phase-space, typically described by the systems particle number, energy, volume and pressure. In a quantum mechanical sense it is the number of accessible states in the microcanonical ensemble. Therefore, the entropy is a measure of the systems degrees of freedom and highly ordered systems have smaller entropy.

73

A system of N independent particles in an external magnetic field $\vec{B}$ may also be described by its internal energy U, the total differential of which reads

$$dU = TdS - pdV - V\vec{M} \cdot d\vec{B}. \tag{3.1.2}$$

Here, T is the temperature, S the entropy, p the pressure, V the volume, $\vec{M}$ the magnetization and $\vec{B}$ the applied magnetic field. The first term $TdS = \delta Q$ is the applied heat, which leads to the second law of thermodynamics

$$dS \geq \frac{\delta Q}{T}, \tag{3.1.3}$$

stating that in any process in a closed system, the entropy never decreases. In Eq. (3.1.3) the equality holds for reversible processes in closed systems or quasi-static processes if the system is not closed. Furthermore, the third law of thermodynamics states that the entropy approaches zero at zero temperature.

Heat Capacity The heat capacity of a system is defined as

$$C = \frac{\delta Q}{dT} = T\frac{\delta S}{\delta T} \tag{3.1.4}$$

the heat change in a system per temperature change. It is therefore a measure of the energy content of a material, directly related to the entropy. The term *specific heat* describes the heat capacity per particle number or mass of material.

In the context of this thesis the heat capacity per Ho-ion will be reported. It proves to be helpful to compare the molar heat capacity to the universal gas constant $R = N_A k_B \approx$ 8.314 J/mol K, where N_A is Avogadro's number. C/R therefore gives the specific heat per Ho-ion in units of k_B.

There are several contributions to the heat capacity of a system. The phononic contribution was described by Debye [88]. In an isotropic (cubic) system at temperatures significantly below the Debye temperature $T \ll \Theta_D$, the phononic heat capacity can be written as [89]

$$C_{\text{ph}} = 12/5\pi^4 N_A k_B \left(\frac{T}{\Theta_D}\right)^3. \tag{3.1.5}$$

The experiments in this thesis were performed at temperatures below $T < 4\,\mathrm{K}$, well below the Debye temperature of LiHoF$_4$ $\Theta_D \approx 600\,\mathrm{K}$ [37]. At such low temperatures, the lattic contribution to the heat capacity played a minor role.

In addition to the lattice vibrations, the conduction electrons in metals also contribute to the heat capacity. Since electrons are Fermions they obey the Pauli principle. Therefore the electrons fill energy states up to the Fermi energy $E_\mathrm{F} = k_B T_\mathrm{F}$, with T_F the Fermi temperature. The electronic specific heat is given by

$$C_\mathrm{e} = \pi^2/2 N_A k_B \frac{T}{T_\mathrm{F}} = \gamma T, \tag{3.1.6}$$

where γ is the Sommerfeld constant tabulated for most metals [89]. While LiHoF$_4$ is an insulator, the electronic heat capacity plays an important role for the low temperature contribution to the specific heat of the sample support, which was made of silver.

A very important contribution at low temperatures originates in the energy levels of a magnetic system. Crystalline electric field levels are one prominent example of special relevance to LiHoF$_4$. The canonical ensemble of such a system is described by its partition function

$$Z = \sum_i \exp(-E_i/k_B T), \tag{3.1.7}$$

with the energy levels E_i. The occupation of a single level is given by

$$P(E_i) = \exp(-E_i/k_B T)/Z. \tag{3.1.8}$$

The internal energy of the system then reads

$$U = \sum_i P(E_i) E_i. \tag{3.1.9}$$

The specific heat can be derived from this energy as [43]

$$C/R = \frac{1}{N}\frac{\delta E}{\delta T} \tag{3.1.10}$$

resulting in

$$C/R = \frac{1}{(k_B T)^2}\frac{\sum_{ij}(E_i^2 - E_i E_j)\exp(-(E_i + E_j)/k_B T)}{\sum_{ij}\exp(-(E_i + E_j)/k_B T)}. \tag{3.1.11}$$

The specific heat therefore shows a maximum depending on the distribution of the energy levels. Such a maximum is referred to as a *Schottky anomaly*. For a simple two level system

with $E_0 = 0$ and $E_1 = \Delta E$, one finds the location of the maximum with $0.42\Delta E \approx k_B T$. Below, the maximum the specific heat rises exponentially, while it falls off with $1/T^2$ above the maximum. For a magnetic system, the value of the maximum $C_{\max}/R$ as well as its position rise with increasing spin or nuclear moment.

LiHoF$_4$ also displays a Schottky anomaly at low temperatures, originating from the hyperfine interaction of the Ho-ions ($I = 7/2$) [43] described in detail in Ref. [5] and introduced in Eq. (2.4.4). From these hyperfine levels, one expects a peak at $T \approx 0.2\,\mathrm{K}$ with a value of $C_{max}/R \approx 0.9$ [43]. At larger temperatures, additional peaks are expected originating from the CEF levels, depicted in Fig. 1.2.1.

For the investigation of phase transitions, the following characteristics of the heat capacity are helpful. At a first order phase transition, latent heat and a discontinuity in the entropy is observed, resulting in diverging heat capacity. At a second order phase transition, the change of entropy is continuous, but the heat capacity shows a discontinuity.

Thermal Conductance   The thermal conductance describes the rate of heat flow under a temperature gradient. While not a primary observable of the experiments presented in this thesis, the absolute thermal conductance

$$k = \frac{\dot{Q}}{\Delta T} \tag{3.1.12}$$

is important for the design of the experimental setup. Since the heat flow depends on the cross section A and the length l of the material, where the heat is transported through, the specific thermal conductivity is defined as

$$\kappa = k \cdot l/A. \tag{3.1.13}$$

The transport of heat in non-magnetic materials, such as the experimental setup, has two major sources, electrons and phonons. The lattice thermal conductivity is given by

$$\kappa_{\mathrm{ph}} = \frac{1}{3}\frac{C_{\mathrm{ph}}}{V_{\mathrm{m}}}v_s\lambda_{\mathrm{ph}}, \tag{3.1.14}$$

with the factor 1/3 due to three dimensions, C_{ph} the phononic heat capacity, λ_{ph} the phonon mean free path and v_s the speed of sound [89]. At low temperatures, it is proportional to the phononic specific heat as well as the phonon mean free path and thus

$$\kappa_{\mathrm{ph}} \propto T^3 \lambda_{\mathrm{ph}}, \text{ at } T \leq \Theta_D/10. \tag{3.1.15}$$

At even lower temperatures, the phonon density is low and phonon-phonon scattering unlikely, thus the phonon mean free path is constant. Therefore at very low temperatures, as in the experiments presented below, the thermal conductivity is only proportional to [89]

$$\kappa_{\mathrm{ph}} \propto T^3, \text{ at } T \ll \Theta_D. \tag{3.1.16}$$

As a result of the absence of phonon-phonon scattering, defects and impurities play a important role for the heat transport at low temperatures. Hence, pure materials have a better thermal conductivity. These effects are rather complex and will not be discussed in detail. In literature the following contributions are reported [89]:

$$\begin{aligned} \lambda_{\mathrm{ph}} &= \text{const.} && \text{phonon-grain boundary scattering} \\ \lambda_{\mathrm{ph}} &\propto T^{-1} && \text{phonon-dislocation scattering} \\ \lambda_{\mathrm{ph}} &\propto T^{-4} && \text{phonon-point defect scattering} \end{aligned} \tag{3.1.17}$$

Heat transport originating from conduction electrons in metals is described by

$$\kappa_{\mathrm{e}} = \frac{1}{3}\frac{C_{\mathrm{e}}}{V_{\mathrm{m}}} v_{\mathrm{F}} \lambda_{\mathrm{e}}, \tag{3.1.18}$$

with v_{F} the Fermi velocity, C_{e} the electronic heat capacity and λ_{e} the electronic mean free path [89]. In typical metals, the Fermi velocity is much larger than the velocity of sound $v_{\mathrm{s}} \ll v_{\mathrm{F}}$. In turn, the electronic thermal conductivity is significantly larger than the phonon contribution. As for phonons, the electronic mean free path at low temperatures is constant and thus the thermal conductivity tracks the temperature dependence of the electronic heat capacity

$$\kappa_{\mathrm{e}} \propto C_{\mathrm{e}} \propto T. \tag{3.1.19}$$

All these mechanisms play an important role for the design of the heat capacity setup for measurements in the mK-regime, presented in Sec. 3.2.
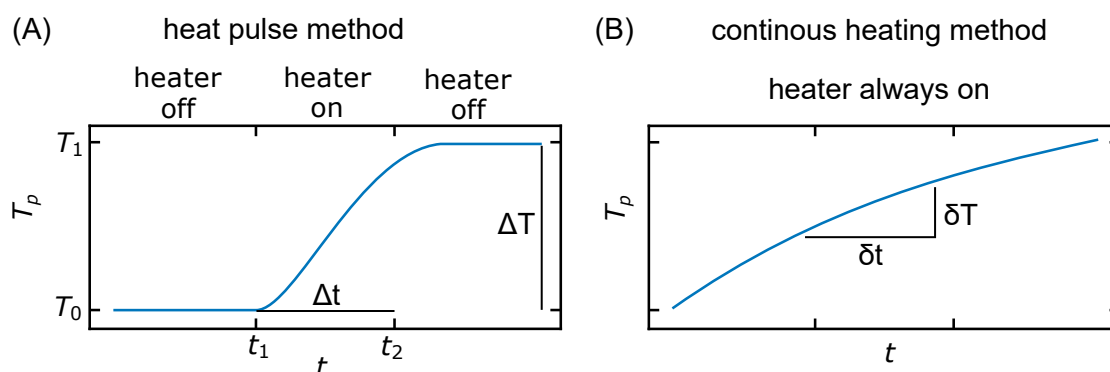
Figure 3.1.1.: Signal shape for the two most common adiabatic heat capacity techniques. (A) The heat pulse method (HPM) relies on a well defined heat pulse of length Δt, that raises the temperature by ΔT. (B) In the continuous heating method (CHM), the heater is on during the whole measurement and the slope of the temperature $\delta T/\delta t$ is measured.

3.1.2. Specific Heat Measurements

Since the pioneering work by Eucken and Nernst [90, 91], several experimental methods were developed to determine the heat capacity of materials at low temperatures. A review of those methods can be found in Refs. [92, 93]. Two classes of experiments can be distinguished in terms of the thermal coupling between the sample and a heat bath. Typical adiabatic and non-adiabatic methods with their benefits and challenges will be presented to motivate the choice for the non-adiabatic thermal relaxation method in this study followed by a detailed description of this method.

Adiabatic Methods   aim to decouple sample and setup thermally from the surroundings. Important examples are the heat pulse method (HPM) as well as the continuous heating method (CHM). In the HPM [43, 94, 95] the relation $C = \lim_{\Delta T \to 0}(\frac{\Delta Q}{\Delta T})$ is used to infer the heat capacity of the sample by applying a well defined heat pulse $\Delta Q = P \cdot \Delta t$ and measuring the resulting temperature difference ΔT. A schematic heating curve is shown in Fig. 3.1.1 (A). As may be seen, the system needs some time to equilibrate after the heater is turned off.

At low temperatures, the study of small samples is limited by the contribution of the electrical wiring to the thermal conductance to the bath. These cannot be avoided and lead to considerable heat loss. On the other hand, when large samples are studied heat

switches are required for cooling the sample in the first place, adding technical complexity to the setup. The HPM is widely used, for instance, in measurements of the specific heat of low temperature antiferromagnetic samples in magnetic fields [96, 97]. By waiting for platform and sample to equilibrate this method avoids complications originating from poor thermal coupling between sample and platform. These so called τ_2-effects will be discussed in greater detail below when presenting the thermal relaxation method and the setup used in this work.

The CHM [98, 99] exploits the relation $C = \frac{\delta Q}{\delta T} = \frac{\dot{Q}}{\dot{T}}$. Thus the heat capacity is inferred from the slope of the temperature $\delta T/\delta t$, while a constant power $P = \delta Q/\delta t = \dot{Q}$ is applied to the platform, as shown in Fig. 3.1.1 (B). Due to the small thermal link, the heat flow from the sample to the bath is minimal and the sample temperature rises continuously. Only changes of the heat capacity can be extracted from the slope of the curve. As a consequence it is necessary to determine the absolute specific heat at the start of the measurement using another method. The great strength of this technique lies in the fast measurement times as data are acquired during a temperature scan. Furthermore, changes in the heat capacity, e.g. at thermal phase transitions, may be resolved with such improved resolution. This method is challenging to implement for measurements spanning the 0.1 K to 10 K regime, since both the specific heat and thermal conductivity change drastically in this temperature range.

Similar to the CHM is the large pulse method, used in the Quantum Design PPMS systems [100, 101], which is also based on the derivative of the temperature trace. However, it is effectively a non-adiabatic method due to the much stronger thermal coupling between platform and bath.

Non-Adiabatic Methods determine the heat capacity, while the sample is thermally coupled to the heat bath in a non-negligible strength. The correct choice of this heat link defines the time constant τ_1 characterizing the relaxation to thermal equilibrium between platform and heat bath. Two main techniques fall in this category, the AC method (ACM) and the thermal relaxation method (TRM), the latter was used in this thesis and will be introduce in more detail below.

The ACM, first described by Sullivan and Seidel [102], employs a sinusoidal AC heating power to determine the heat capacity from the temperature oscillation, permitting data can be recorded also while changing other external parameters such as magnetic field. A
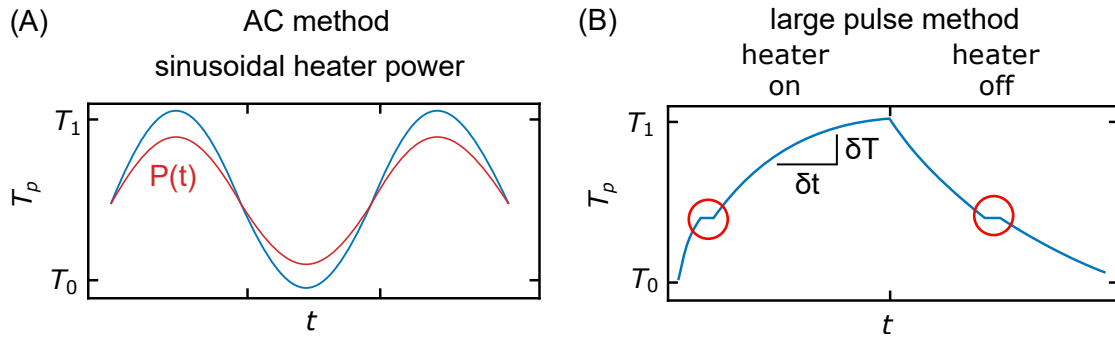
Figure 3.1.2.: Signal shape for the two non-adiabatic heat capacity measurement techniques. (A) The AC method measures the temperature response to a sinusoidal heater power. (B) The large pulse method determines $\delta T/\delta t$, similar to the CHM. Changes in the heat capacity, e.g. at phase transitions, are visible as kinks (red circles).

schematic temperature signal of this technique is shown in Fig. 3.1.2 (A). Due to the strong thermal link, no heat switch is necessary to cool even large samples to low temperatures. A correct choice of the frequency with respect to the relaxation times of sample and addenda is crucial. Compared to the TRM presented below, the ACM is inaccurate if the sample has a low thermal conductance. Furthermore, the technique is most reliable when measuring relative changes of the heat capacity in the presence of a large addenda [93]. Therefore, this method can be limited at lowest temperatures compared to the TRM or needs to be complimented with TRM to obtain a precise starting point of the heat capacity from which relative changes are tracked. A recent example of this technique is the AC setup reported by Rost *et al.* [103] which is capable of withstanding the mechanical forces generated at the metamagnetic transition of $Sr_3Ru_2O_7$.

More exotic methods involve the measurement of the thermal conductivity and heat capacity at the same time, by observing the heat flow through a sample with a heater at one side and the bath on the other [104].

As mentioned above, by knowing the thermal conductance between bath and platform the heat capacity can be inferred from the relation $C = \frac{dQ}{dT} = \frac{\dot{Q}}{\dot{T}}$ under non-adiabatic conditions as well. The large pulse method [105, 106] measures the slope of the temperature during long and large heating pulses, where the temperature of the sample changes by typically 10-30%. Fig. 3.1.2 (B) visualizes a typical signal, kinks in the temperature curve indicate large changes in the heat capacity, for example at phase transitions.
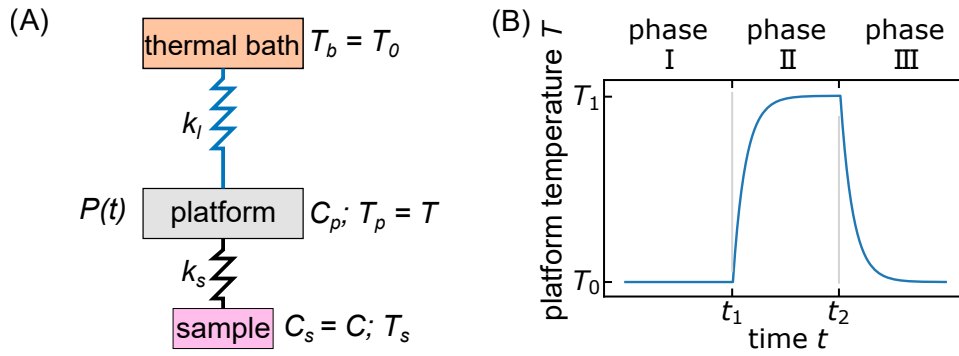
Figure 3.1.3.: The relaxation time method for heat capacity measurements. (A) Schematic setup and key variables. (B) Idealized heat pulse comprising three phases.

The Thermal Relaxation Method (TRM) first reported by Bachmann *et al.* [107] in 1972 was chosen for the work presented in this thesis. It exploits the characteristic exponential relaxation of the platform temperature towards the bath temperature after a heat pulse. The heat capacity is then extracted from the characteristic time scale τ_1. The data analysis is based on the algorithm presented by Hwang *et al.* [108], which is rather sophisticated and especially designed for this kind of experimental setup. The initial focus of this technique lied on small sample sizes [107, 109] and the usage in the mK-regime [110], where the TRM performs better as compared to the adiabatic methods, due to the reliable cooldown through the thermal link. Additionally, automation and data analysis tools [108, 111] were developed.

Fig. 3.1.3 (A) depicts the minimal experimental setup needed for this method. It consists of a thermal bath with a constant temperature T_b. Connected to the bath via a thermal link with thermal conductance k_l is a platform with heat capacity C_p and temperature T_p. Applying the power $P(t)$ heats the platform. A sample with heat capacity C_s and temperature T_s is connected to the platform and the corresponding thermal conductance is k_s.

To measure the heat capacity of the sample $C = C_s$ at a given temperature T and magnetic field B, a certain measurement protocol is used, resulting in a heat pulse. A typical curve is shown for an idealized experiment ($k_s = \infty; C_p = 0$) in Fig. 3.1.3 (B). Each heat pulse may be separated in three phases. In phase I the heater is off and the sample is in thermal equilibrium with the platform and the bath. If both are not in equilibrium due to changes in B, T before the measurement, this phase is extended until thermal equilibrium between bath and platform is reached. The sample temperature is constant

at the temperature of the bath $T = T_0$, the *base temperature*. In phase II, the heater is turned on, leading to a rise of the platform temperature. It reaches a constant value, when a balance between the heater power and the heat flux to the bath $\dot{Q} = k(T - T_0)$ is reached and the sample and platform are warmed up. The heating curve follows a characteristic exponential dependence

$$T(t) = T_1 + (T_0 - T_1)e^{-\frac{k}{C}(t-t_1)} = T_1 + (T_0 - T_1)e^{-\frac{(t-t_1)}{\tau}}. \qquad (3.1.20)$$

Phase III begins, when the heater is turned off and the platform temperature relaxes back to the base temperature T_0

$$T(t) = T_0 + (T_1 - T_0)e^{-\frac{k}{C}(t-t_2)} = T_0 + (T_1 - T_0)e^{-\frac{(t-t_2)}{\tau}}. \qquad (3.1.21)$$

Here, $C = C_s$ is the sample heat capacity and $k = k_l$ is the thermal conductance of the link. It can be determined in the steady state with the heater turned on, at the end of phase II from the applied power and temperature difference $k = \frac{\dot{Q}}{T_1 - T_0}$. Above, we have also introduced the relaxation time

$$\tau = \frac{C}{k} \qquad (3.1.22)$$

as the time constant of the exponential time dependence. A typical heat pulse recorded at $T = 210\,\text{mK}$, $B = 5.1\,\text{T}$ and $\Phi = 0°$ and the associated fit using the algorithm of Hwang *et al.* [108] described below is shown in Fig. 3.1.4. The pulse is shown as the temperature difference $\Delta T = T - T_0$ compared to the baseline in percent as a function of time t in seconds. At $t = 0$, the heater is turned on and a jump ΔT_2 of the temperature is recorded. The experimental heat pulse differs from the idealized pulse described above. It allows to illustrate the challenges of the TRM and non-adiabatic methods in general.

The most important difference is the jump ΔT_2, when the heater is turned on and off. It may be attributed to the so-called τ_2-effect, which originates from the heat capacity of the platform C_p and the thermal link between sample and platform k_s neglected so far. For a finite heat capacity of the addenda and a finite thermal conductance between platform and sample, a second relaxation time τ_2 is observed. In this regime the thermometer, heater and platform heat up much faster than the sample, since these components have a much smaller specific heat. Therefore, the τ_2-effect effect appears as a jump in Fig. 3.1.4, as $\tau_2 \approx 10^{-2}\,\tau_1$ in the experiments presented in this thesis.

The analysis and reduction of this effect was in the focus of the development of the TRM [107, 109, 111, 112]. A good summary of the τ_2-effect may be found in Ref. [113]. To
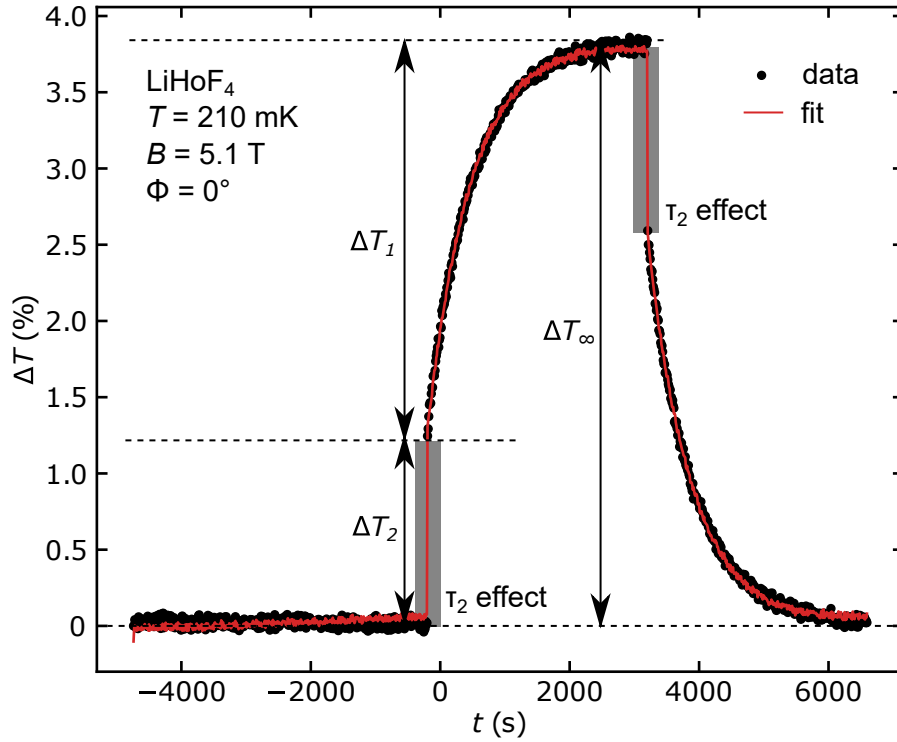
Figure 3.1.4.: Typical heat pulse at a base temperature of $T = 210\,\mathrm{mK}$, a magnetic field of $B = 5.1\,\mathrm{T}$ and $\Phi = 0°$. Only every tenth data point is shown, representing a spacing of 1 second between two points. See text for details on the temperature differences ΔT_∞, ΔT_1 and ΔT_2 as well as the τ_2 effect.

understand the phenomena in this thesis it is sufficient to know that the relaxation time of the addenda is proportional to the heat capacity of the addenda $\tau_2 \propto C_{\mathrm{addenda}}$, representing the whole setup (platform, heater, thermometer, etc.) combined. Furthermore, also the height of the jump ΔT_2, or more accurately the ratio of ΔT_1 to ΔT_2, depends on the ratio of k_l to k_s. The larger k_s is as compared to k_l, the smaller ΔT_2. This is due to the fact, that a smaller temperature gradient between sample and platform is needed to achieve the same heat flow, if k_s is large.

The Curve Fitting Method   (CFM) provides a practical solution to the τ_2-effect by including it in the fitting algorithm developed by Hwang *et al.* [108]. This algorithm was used to fit the data presented in this thesis. Hwang *et al.* developed a fitting routine, which takes the full response of a calorimeter into account and makes it applicable for all heat pulse based methods, ranging from TRM to HPM type setups. This allows to extend the temperature range of measurements as the choice of the thermal link becomes less important and the τ_2-effect is treated correctly. As a result, the choice of τ_1 is a lot more flexible such that the sample size may be chosen more flexibly. As the CFM works for both adiabatic and non-adiabatic conditions, significant changes in the thermal coupling with the same setup are tolerable. These properties make the CFM the method of choice for research presented in this thesis, since the whole operation range of the JT-insert (40 mK - 5 K) can be covered, where a large variation of the thermal conductance of the link may be expected.

The CFM is based on a set of differential equations that describes the system. The heat flux in and out of the platform are in equilibrium

$$P(t) = C_p \frac{dT_p}{dt} + k_s(T_p - T_s) + k_l(T_p - T_0). \tag{3.1.23}$$

When P is the power applied by the heater, C_p the heat capacity of the platform, T_s and T_p the temperature of the sample and platform, respectively, and k_s and k_l the thermal conductance between platform and sample and platform and thermal bath, respectively. The heat flux to the sample may be described by

$$C_s \frac{dT_s}{dt} = k_s(T_p - T_s). \tag{3.1.24}$$

The following assumptions are important, when deriving this framework:

- The heater and the thermometer are firmly attached to the platform with a large thermal conductance, thus C_p describes the whole addenda, without differentiating between different components.
- The internal thermal conductance of sample and platform are significantly larger than k_s and k_l. Note that the TRM actually works up to a ratio of $k_s \approx k_l$, while the ACM would not be able to provide meaningful results under these conditions [93, 107].

- C_s, C_p, k_l and k_s are temperature independent within the small temperature window of a single heat pulse.

To fit these differential equations to an experimental heat pulse, equations 3.1.23 and 3.1.24 are combined and written in the form

$$T(t) - T(0) = h \cdot H(t) + q \cdot Q(t) + s \cdot S(t), \tag{3.1.25}$$

as derived in Ref. [108]. Where the characteristic functions are defined as

$$H(t) = \quad P(t) - C_p V(t) \tag{3.1.26}$$

$$V(t) = \quad \frac{dT}{dt'}\big|_0^t \tag{3.1.27}$$

$$Q(t) = \quad \int_0^t P(t')\mathrm{d}t' \tag{3.1.28}$$

$$S(t) = \quad \int_0^t T(t')\mathrm{d}t', \tag{3.1.29}$$

and $P(t)$ is the heater power applied. These functions can be easily determined from the data recorded by means of numerical integration and differentiation using Python. Eq. (3.1.25) is then fitted using least squares methods. From the parameters h, q and s, the heat capacity C_s, the thermal conductances k_l and k_s as well as the relaxation times τ_1 and τ_2 can be calculated as described in Ref. [108].

Since the measurement protocol is the same as for the TRM and the signal follows the characteristic exponential shape, thermal relaxation (TRM) and curve fitting method (CFM) will be used as interchangeable terms throughout this thesis, especially, since CFM is a term solely used by Hwang *et al.* [108].

3.1.3. Magnetocaloric Measurements

The *magnetocaloric effect* describes a change in entropy in a material that originates from a change of applied magnetic field. Today this effect is often used for demagnetization refrigeration, which allows cooling to mK-temperatures without using liquid helium [89, 114, 115]. In contrast to the specific heat measurements, where the temperature is varied for constant magnetic field, a magnetocaloric measurement is a magnetic field sweep at constant temperature. The quantity of interest is the isothermal entropy change

$$\left. \frac{\delta S}{\delta H} \right|_T . \tag{3.1.30}$$

The magnetocaloric effect is linked to the magnetic Grüneisen parameter

$$\Gamma_H = \frac{1}{T} \left. \frac{\delta T}{\delta H} \right|_S , \tag{3.1.31}$$

for which Zhu, Garst and Rosch [116, 117] showed divergent behavior close to quantum critical points. Moreover, they showed that the Grüneisen parameter and magnetocaloric effect change sign near generic quantum critical points.

The entropy as a function of magnetic field can be calculated from the heat capacity

$$\begin{aligned} S(H_1, T) - S(H_0, T) &= \int_0^T \left(\frac{\delta S(H_1, T')}{\delta T'} - \frac{\delta S(H_0, T')}{\delta T'} \right) dT' \\ &= \int_0^T \left(\frac{C(H_1, T')}{T'} - \frac{C(H_0, T')}{T'} \right) dT'. \end{aligned} \tag{3.1.32}$$

Thus it is in principle possible to reconstruct the entropy of a system by only measuring the heat capacity. In reality however, the heat capacity cannot be measured to zero temperature and therefore interpolations are necessary. In turn, this also implies that such reconstructions can only be applied reliably in well understood systems. The magnetocaloric sweeps presented here provide experimental access to the entropy change as a function of field, without prior knowledge of the heat capacity down to zero temperature. The technique described here follows the procedure described by Rost *et al.* [103, 118, 119].

In the following, the method will be described for the data recorded at $T \approx 0.2\,\mathrm{K}$ at a ramp rate of $\dot{B} = 15\,\mathrm{mT/min}$. Fig. 3.1.5 (A) shows the temperature reading of the

bath in blue and the sample platform in black. The dashed lines show the temperature readings, without correction of the magnetoresistance of the temperature sensor, which are performed as described in Sec. 3.2.6 below. Following this calibration, the curves with the solid lines are obtained. The bath temperature is not constant due to the magnetoresistance of the mixing chamber thermometer, which is not compensated for the combination of JT insert and AMI magnet.

The temperature difference $\Delta T = T_s - T_0$ between platform and bath, shown in 3.1.5 (B) originates from heating and cooling effects in the sample due to the magentocaloric effect. As the magnetic field B is increased from $B = 0$ to $6.5\,\mathrm{T}$, the temperature drops monotonically by about $5\,\mathrm{mK}$ and reaches a minimum at the phase transition at $B_c = 4.6\,\mathrm{T}$. Increasing the field above the phase boundary, heat is released and the sample warms up. This temperature profile as well as its derivative were used to extract the derivative of the entropy with respect to the magnetic field, which can be written as [119]

$$\left.\frac{\delta S}{\delta B}\right|_T = -\frac{k}{T_s}\Delta T \frac{1}{\dot{B}} - \frac{C}{T_s}\frac{\mathrm{d}T_s}{\mathrm{d}B}. \tag{3.1.33}$$

Here, T_s is the sample/platform temperature, T_0 the bath temperature, $\dot{B}$ the derivative of the magnetic field with respect to time. C is the heat capacity of the sample and k the thermal conductance between platform and bath.

While magnetocaloric measurements offer additional information on the entropy landscape, they cannot be performed without additional relaxation time measurements of the heat capacity, since the parameters k and C must be determined independently. Fortunately, both can be extracted directly from the heat pulses. To make use of them in Eq. (3.1.33), C was interpolated over the whole T-B-region of the magnetocaloric measurements as shown in Fig. 3.4.6. The link $k = k_l$ was independent of B and Φ, where the relevant data are shown in Fig. 3.3.2 (E).

The results following data reduction are shown in Fig. 3.1.5 (C). For further analysis, these can be integrated as a function of magnetic field B to obtain the change in entropy

$$\Delta S(B^*, T) = S(B^*, T) - S(0, T) = \int_0^{B^*} \left.\frac{\delta S}{\delta B}\right|_T \mathrm{d}B, \tag{3.1.34}$$

which is shown in Fig. 3.1.5 (D).
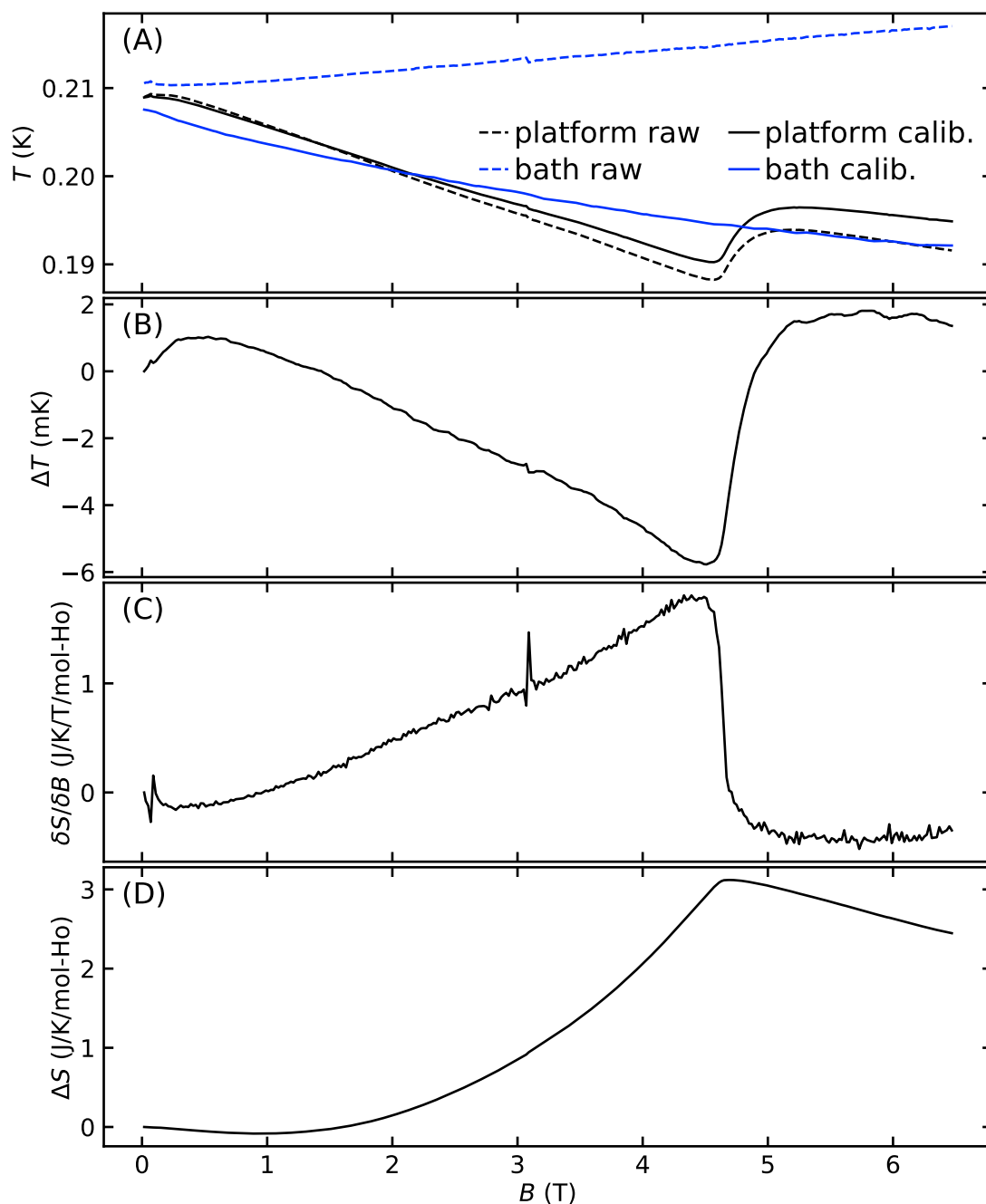
Figure 3.1.5.: Data reduction process for magnetocaloric sweeps. (A) The raw data consist of two temperature readings, the platform thermometer and the sample thermometer (dashed lines). To correct for the magneto-resistance of the temperature sensor, these are field calibrated (solid lines), as described in Sec. 3.2.6. The slope of the calibrated thermometers follows the control thermometer at the mixing chamber of the JT insert. (B) The difference of the calibrated temperature readings is used to calculate $\frac{\delta S}{\delta B}$ (C) using Eq. (3.1.33). (D) These results can be integrated as a function of magnetic field to obtain ΔS.

While the data analysis takes equation Eq. (3.1.33) fully into account, the measurements were performed in the non-adiabatic limit, where the thermal link k is large as compared to the ramp rate $\dot{B}$ and the first term dominates.

$$\left.\frac{\delta S}{\delta B}\right|_{T} \approx -\frac{k}{T_s}(T_s - T_0)\frac{1}{\dot{B}} \qquad (3.1.35)$$

If a faster ramp rate is chosen, the heat capacity of the sample introduces significant delay of the heating and cooling effects with respect to the true value of the magnetic field. This effect is highlighted in Fig. 3.1.6 (A), where ΔT is shown as a function of B. Ramping the field down from $B = 6.5\,\mathrm{T}$ to $B = 0$ at $15\,\mathrm{mT/min}$, a small kink in the temperature can be seen at the critical field, after which the temperature rises to a maximum around $4\,\mathrm{T}$. Increasing the ramp rate leaves the field of the kink unchanged, while the maximum shifts to lower temperatures, approaching $3\,\mathrm{T}$ for $100\,\mathrm{mT/min}$. This can be explained by the heat capacity of the sample, which delays the heating of the sample. Due to the higher ramp rate, the field at which the maximum is observed is lowered. In addition, the heating effects are stronger at larger sweep rates, consistent with expectation.

Ignoring the effects of the heat capacity and the second term of Eq. (3.1.33), the behavior shown in Fig. 3.1.6 (B) is obtained. The shift in the maximum is clearly visible, while the amplitudes are corrected for the sweep rate.

Including the heat capacity and using the full Eq. (3.1.33) the behavior shown in Fig. 3.1.6 (C) is obtained, where the derivative of the entropy as a function of field is independent of the ramp rate, consistent with expectation. While the same results are obtained using both formulas, the measurements were performed at slow ramp rates to be as close to the non-adiabatic limit as possible. Only in this limit are the effects of the heat capacity are negligible, reducing errors due to imperfect interpolation of the heat capacity. In practice however the ramp rate is limited by the available measurement time and the precision of the thermometers, as lower ramp rates yield smaller signals.
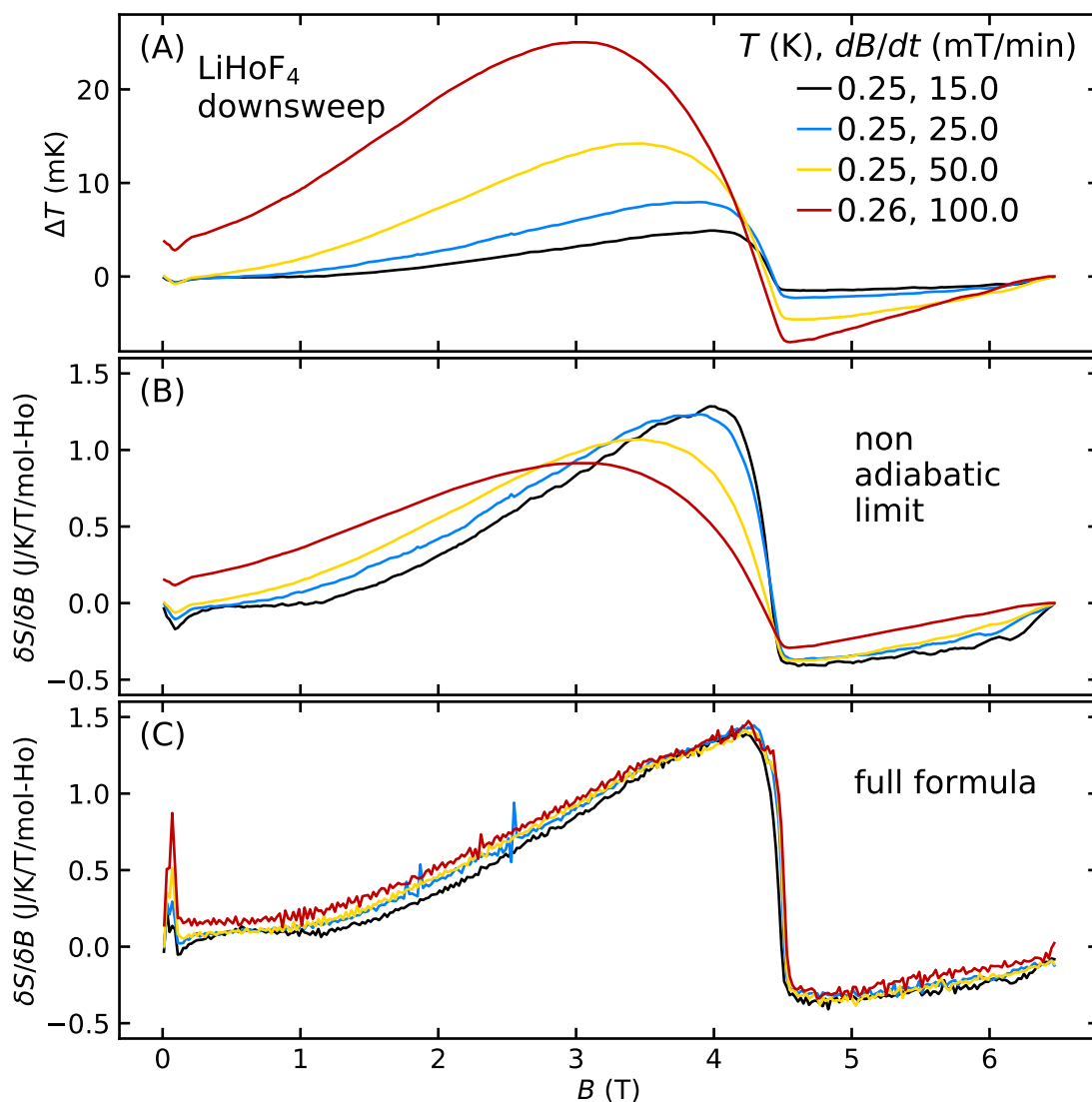
Figure 3.1.6.: Influence of the sweep rate of the magnetic field in magneto-caloric measurements. (A) Temperature difference between platform and bath as a function of field for various ramp rates. At higher ramp rates, the heat capacity leads to significant rounding of the curves. (B) $\frac{\delta S}{\delta B}$ using Eq. (3.1.35) for the adiabatic limit, which neglects the effects of the heat capacity and keeps the rounding. (C) When correcting for the heat capacity and using Eq. (3.1.33), the curves are found to be independent of the ramp rate.

3.2. Experimental Setup

In this section, we will focus on the experimental setup developed for this project and its design criteria, temperature calibration and sample alignment.

3.2.1. Design Criteria

The fundamentals of the experimental techniques described above impose several requirements on the experimental setup that will be summarized in the following.

Mechanical Stability Since LiHoF$_4$ carries a large magnetic moment with a strong anisotropy, the setup needs to be designed to withstand a large force due to the magnetic torque.

Good Temperature Stability of the Bath Due to the large sample heat capacity, measurement times at lowest temperatures may be as long as several hours. The mixing chamber temperature needs to be stable over the whole period.

Large Thermal Coupling of the Sample To reduce the τ_2-effect, the thermal coupling k_s between sample and platform needs to be large.

Small Heat Capacity of the Addenda In comparison to the specific heat of the sample, the heat capacity of heater, thermometer and platform needs to be small to reduce the τ_2-effect. A small C_{addenda} results in short relaxation times of τ_2 and thus allow an easier correction of this effect.

Thermal Link to the Bath To obtain reasonable measurement times, k_l needs to be tuned according to $\tau = C/k_l$. The last two points will be achieved by separating the mechanical support, thermal link and electrical connections into separate components to have maximum freedom to optimize for a specific application. A first attempt of this
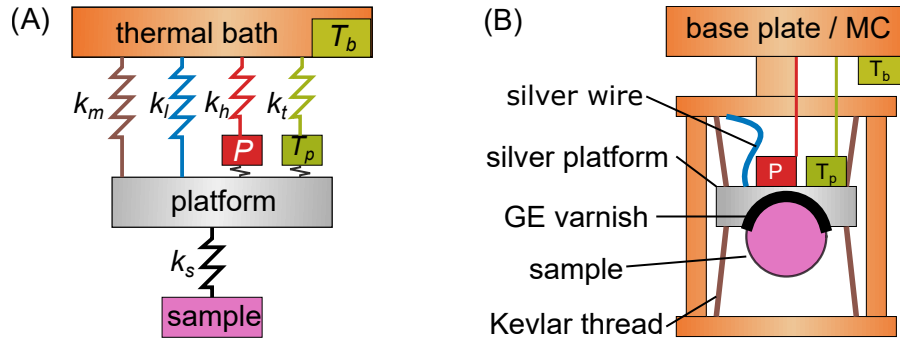
Figure 3.2.1.: Qualitative depiction of the setup used for heat capacity measurements and magnetocaloric sweeps. (A) Several thermal conductances contribute to the setup. The indices correspond to the various components as defined in the text. (B) A simplified sketch of the experimental setup.

concept was presented by Nives Bonačić [101]. The design presented in this thesis was optimized for the use at mK-temperatures and found to be satisfactory.

Thermometry and Heater   A well defined power $P(t)$ needs to be applied to the platform and the temperature of both platform and bath need to be measured with sufficient resolution as well as a fast readout rate. Noise and a low number of data-points especially influence the precision of the derivatives negatively, which are crucial to the specific heat fits and magnetocaloric data-reduction.

The components of the experimental setup are shown in Fig. 3.2.1 (A) and (B). The thermal bath is realized by the copper base plate and the mixing chamber, a thermometer measures T_b. The mechanical connection of the platform to the support is realized by Kevlar threads with thermal conductance k_m denote in brown shading. A silver wire (blue) acts as the thermal link k_l, which may be modified. Heater (red) and thermometer (green) are connected to the platform via GE varnish (black), as is the LiHoF$_4$ sample (pink).

Fig. 3.2.2 shows pictures of the setup, which is mounted on the bottom of the mixing chamber of the JT dilution insert described in Sec. 2.2.1 right in the field center of the AMI vector magnet described in Sec. 2.2.2 using a heat shield. The temperature of the bath was controlled with the mixing chamber (MC) thermometer. A silver platform supports the sample in a half-spherical mold attached using GE varnish 7031. The sample is additionally secured against the magnetic torque in the experiment by a woven basket
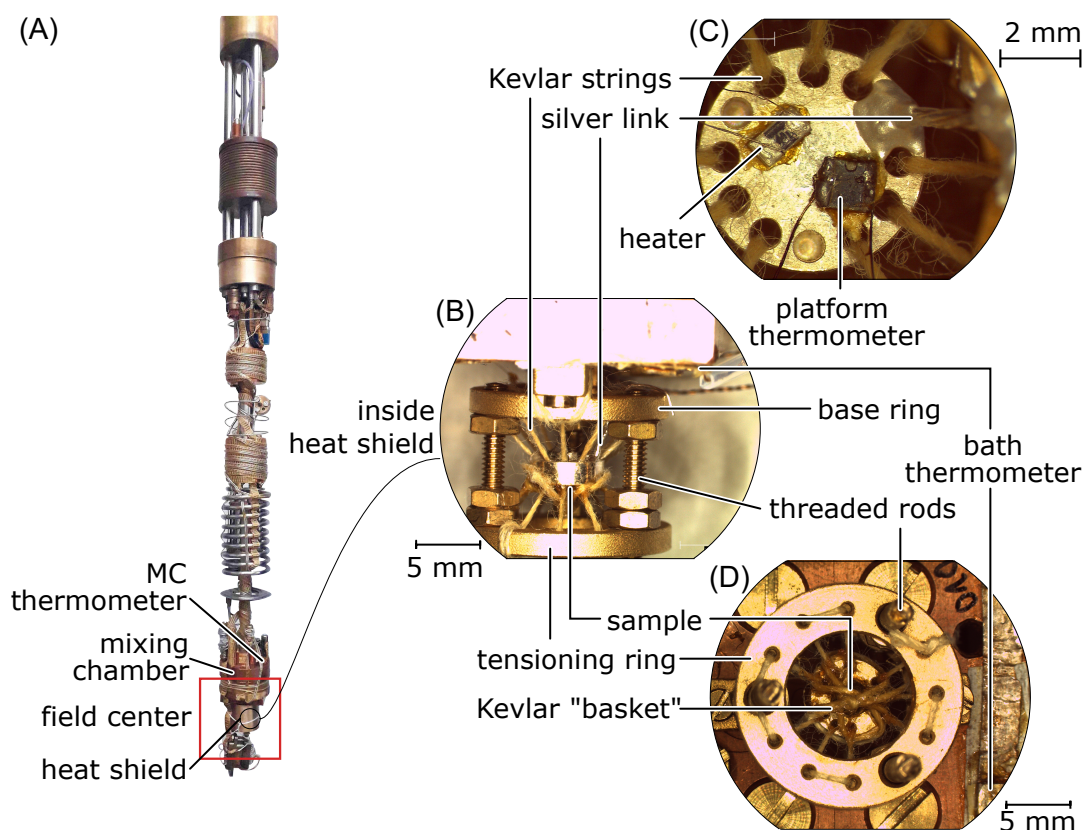
Figure 3.2.2.: The experimental setup used for heat capacity and magnetocaloric measurements. (A) The JT dilution insert with the setup covered by a heat shield. The red square depicts the central region of the field of the AMI vector magnet. (B) A side view of the setup provides an overview of the components inside the heat shield. (C) Backside of the sample platform, facing the mixing chamber. (D) Front of the platform with the sample fixed under a weave of Kevlar strings.

made of Kevlar strings. The silver platform was held in place by one Kevlar string, which was woven through nine holes in the platform to connect it with two copper rings above and below the platform. These in total 18 connections can be tightened by separating the two rings using nuts on threaded rods. A $250\,\mu$m thick silver link, glued to both platform and ring using a silver epoxy[1], connected the platform thermally with bath. Both thermometer and heater were connected to the back of the silver disk using GE varnish.

---

[1]EPO-TEK EJ2018

3.2.2. Mechanical Stability

LiHoF$_4$ under an applied magnetic field experiences a strong magnetic torque. For the sample used, a magnetic moment up to $\vec{m} = 0.01$ J/T may be expected based on the easy axis magnetization measurements by Stefan Legl [44, 69] and the number of Ho-ions of $N_{\text{Ho}} = 0.22$ milli-mol in the sample. Under the assumption that the magnetic moment is constant and aligned parallel to the easy axis, a magnetic torque of $\vec{\tau} = 0.08$ Nm may be expected for the largest field of 9 T of the AMI vector magnet.

This force is too strong for a conventional setup like the one in a Quantum Design PPMS [120], where the sample platform is supported by the electrical wiring only. Kevlar[2] was chosen due to its low thermal conductivity - to minimize k_m - combined with high strength, cf. Fig. 3.2.1 and Fig. 3.2.2 (B,D).

In the literature, designs have been discussed that put enormous effort on counteracting the effects of the thermal expansion of Kevlar [119], which has a negative linear thermal expansion coefficient of $\alpha_{L,Kevlar} = -2 \cdot 10^{-6}$ K^{-1} [121]. While negative, this is also quite small compared to most other materials, notably copper which has a coefficient of $\alpha_{L,Cu} = 17 \cdot 10^{-6}$ K^{-1} [122] the material used mostly in the setup. Since the Kevlar strings used are short, their change of length under cooling will not be a major factor and not weaken the setup. Technical solutions to correct this effect such as additional springs, which tighten under cooling [119], were discarded, since they are impractical to use for the large number of Kevlar strands. Instead the strings were pre-tensioned manually by separating the base- and the tensioning-ring via threaded rods, cf. Fig. 3.2.2 (B).

---

[2]The used Kevlar threads are tex-80 provided by kiutra. [115]

3.2.3. Thermal Conductance

The thermal conductance of the mechanical support and the electrical connections was designed to be as low as possible to allow tuning of the thermal coupling between platform and bath with an additional silver wire, shown in blue in Fig. 3.2.1 and in Fig. 3.2.2 (B, C). For our preliminary calculations, we used the values for silver given in Ref. [89]

$$\kappa_{\text{Ag}}(T) = 10^{-1}T\,\text{W}\,\text{cm}^{-1}\,\text{K}^{-1}. \tag{3.2.1}$$

With a diameter of the wire $d_{\text{Ag}} = 250\,\mu\text{m}$ and a length of $l_{\text{Ag}} = 4\,\text{mm}$ the black line shown in Fig. 3.2.3 (A) is obtained.

The fitting routine [108] allowed to determine the true value of the thermal conductance as shown in Fig. 3.2.3 (A). The thermal conductance k_l is independent of magnetic field. While the temperature dependence develops as expected, the measured thermal conductance is up to five times smaller than calculated. Impurities reduce the thermal conductivity of metals significantly [89, 123] and are the most likely explanation for the observed reduction. Furthermore, the silver wire is connected to both the platform and the bath using a silver epoxy[3] typically used for microelectronics manufacturing. While this epoxy mixed with small silver particles provides good electrical and thermal connection, it is likely that it also reduces the thermal conductance of the link, especially at $T < 1\,\text{K}$. To minimize this effect, the silver wire was completely engulfed by silver epoxy in a bore-hole with a diameter of $0.75\,\text{mm}$ to fit three intertwined $0.25\,\text{mm}$ silver wires, cf. Fig. 3.2.2 (C).

Later, the strand of three silver wires shown in cf. Fig. 3.2.2 (C) was replaced by a single $0.25\,\text{mm}$ silver wire, since the larger link required too much heating for a good signal to noise ratio and influenced the bath-stability negatively. This smaller thermal link led to longer measurement times, which could only be counteracted by a smaller sample.

---

[3]EPO-TEK EJ2018; A similar epoxy - EPO-TEK H20S - used by N. Bonačić [101] proved that it provides good thermal conductivity at low temperatures, where these products are not specified. EJ2018 was used over H20S due to its better thermal conductivity within the specified range and easier treatment after consultation with the manufacturer.

Both electrical wiring made of Manganin and Kevlar strings have far lower thermal conductance, cf. Fig. 3.2.3 (A), which allows to describe the system by only considering the silver heat link. For Kevlar, the expression for thermal conductivity from Ref. [124]

$$\kappa_{\text{Kevlar}}(T) = 3.9 \cdot 10^{-5} \, T^{1.17} \, \text{W/cmK} \tag{3.2.2}$$

was used. For the setup this yields a thermal conductance of $k_m = \kappa_{\text{Kevlar}} \cdot A/l = 6.59 \cdot 10^{-8} \, \text{W/K}$ at 100 mK, for 18 strings with a total cross section of $A = 0.55 \, \text{mm}^2$ and length of $l = 4 \, \text{mm}$ each. For the four Manganin wires with a length of $l_{\text{Manganin}} = 2 \, \text{cm}$ eacj and a diameter of $d_{\text{Manganin}} = 30 \, \mu\text{m}$ each used for the electrical connections the relation [89, 101]

$$\kappa_{\text{Manganin}}(T) = 9.5 \cdot 10^{-4} \, T^{1.19} \, \text{W/cmK}, \tag{3.2.3}$$

lead to the green curve shown in Fig. 3.2.3 (A).

3.2.4. Heat Capacities

As described above, for an easy correction of the τ_2-effect, the heat capacity of the addenda needs to be significantly smaller, than the heat capacity of the sample $C_{\text{addenda}} < C$. The various contributions to the addenda are shown in Fig. 3.2.3 (B) in comparison to the measured absolute zero field heat capacity of LiHoF$_4$.

The largest part of the mechanical setup is the silver platform with its mass of 360 mg. As the temperatures studied are far below the Fermi and Debye temperature of silver, the specific heat can be estimated to be the dominant part of the addenda due to the electronic specific heat following the Sommerfeld approximation

$$C_p = C_{\text{Ag}} = \gamma_{\text{Ag}} T + \beta_{\text{Ag}} T^3, \tag{3.2.4}$$

where $\gamma_{\text{Ag}} = 0.64 \, \text{mJ/g/K}^2$ and $\beta_{\text{Ag}} = 0.167 \, \text{mJ/g/K}^4$ from the Debye temperature $\Theta_D = 227.3 \, \text{K}$ [93]. With a mass of 360 mg one obtains the blue curve in Fig. 3.2.3 (B). At lowest temperatures the term linear in temperature dominates and above 2 K the T^3-term increases. Eq. (3.2.4) was used to calculate the addenda for the fitting algorithm.

The electrical wiring consisted of $30 \, \mu\text{m}$ thick Manganin as described above. As depicted in Ref. [89], this material has a very low specific heat, but shows an increase below $\approx 0.5 \, \text{K}$
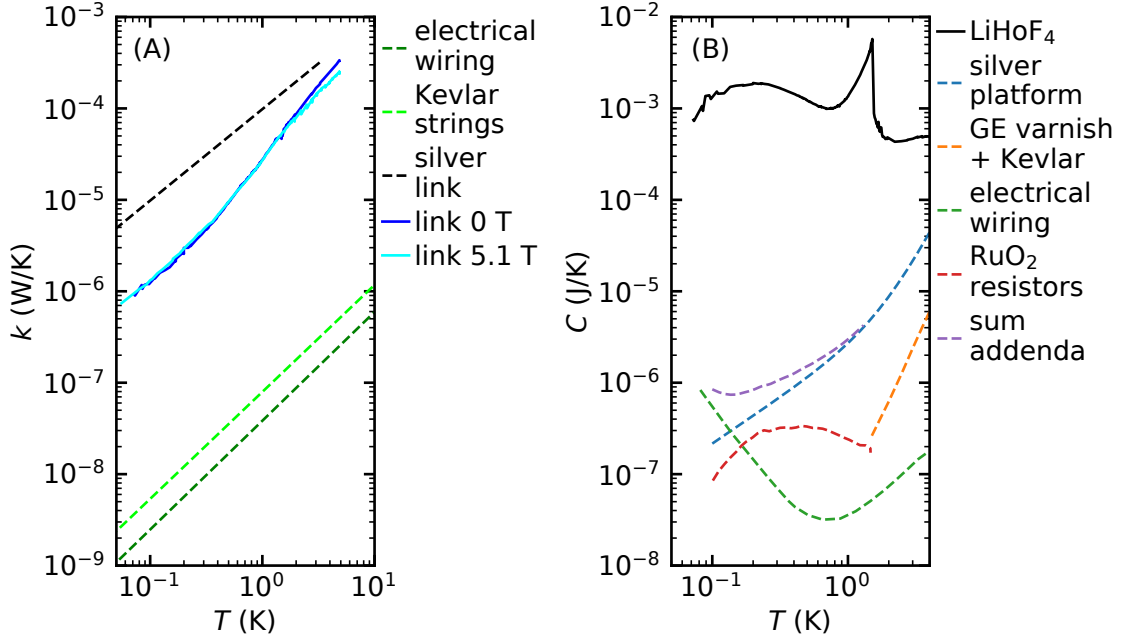
Figure 3.2.3.: Preliminary calculations of caloric properties for the configuration of the setup. (A) Comparison of theoretical and experimental thermal conductances of components in the setup. Dashed lines describe calculations for ideal components as described in the text. Solid lines show measurement results of the real components. The electrical wiring made from Manganin was described as by Bonačić[101]. Kevlar was described by Eq. (3.2.3) derived by Ref. [124]. Values for the silver link were taken from Ref. [89]. The link between bath and platform was determined in the measurement and does not change with magnetic field. (B) Estimates (dashed) of the zero field heat capacities of various components of the addenda compared with experimental results (solid) for the heat capacity of LiHoF$_4$. The total addenda is comprised of the electronic heat capacity of silver described by Eq. (3.2.4) with values from Ref. [93], GE varnish (5 mg)[125], Manganin wires [89] and RuO$_2$ chips based on Ref. [126] and scaled as described in the text.

due to a Schottky anomaly. Manganin, however, exhibits a minimal magnetoresistance only, which is helpful for measurements under magnetic fields [127]. Manganin was used in other low-temperature heat capacity setups reported, e.g., in Refs. [101, 103, 119]. Its contribution to the total addenda is reduced due to its low thermal conductivity, *i.e.* only the part close to the platform contributes effectively. Yet, in future versions of the setup, designed to study much smaller samples, Pt/W-wiring should be used instead, as it exhibits a Schottky anomaly below 50 mK only [89, 128], well below the practical measuring range of interest of most studies.

Sample, heater and thermometer were attached to the silver platform using GE varnish 7031. The contribution of this component as well as the Kevlar strings to the heat capacity are minimal due to their T^3-dependence and low mass of $m_{\text{GE}} \leqslant 5\,\text{mg}$. An estimate for their contribution is given in Fig. 3.2.3 (B) based on the addenda reported in Ref. [125].

As heater and thermometer Ruthenium oxide (ROX) resistors were used, which also show a broad Schottky anomaly at $T \approx 400\,\text{mK}$ [126]. While the pure compound RuO_2 shows no such peak [126], the Al_2O_3 substrate displays this behavior at low temperatures [104]. Based on the extensive data reported by Volokitin *et al.* [126] the characteristics of a sensor close to the chips used in our setup was chosen and its heat capacity scaled by a factor of five to match the mass of the chips in our setup. The result is presented in Fig. 3.2.3 (B).

Taken together, all contributions to the specific heat of the addenda are more than two orders of magnitude smaller than the specific heat of $LiHoF_4$ and therefore allow precise measurements with manageable τ_2-effect.

3.2.5. Thermometry

As stated at the beginning of this chapter, precise and fast temperature measurements that can resolve the shape of a heat pulse as depicted in Fig. 3.1.4 are crucial for the relaxation time technique. ROX chips were used, as the resistance increases with decreasing temperature, cf. Fig. 3.2.5. The resistance of the thermometers was recorded with a Lakeshore resistance bridge, as shown in Fig. 3.2.4 (A). These bridges also provide directly the temperature by comparing the measured resistance with a calibration file. Unfortunately, this coarse method of calibration is only suitable for temperature control and better precision is needed for the measurements. Therefore, the resistance was measured and converted to the temperature using the procedure described below. Tab. 3.2.1 lists all thermometers, their location, calibration range and their respective functions. The locations of the chips are shown in Fig. 3.2.4 (B) schematically and in (E) in the picture of the HC platform. The JT MC ROX (i) chip was located at the mixing chamber. It was used for temperature control, using the Labview software [4]. The WMI ROX[4] (ii) was a thermometer calibrated over a wide range of magnetic fields and thus used for calibration and monitoring the bath stability T_b. The E51 ROX BR3 was a small 1.5 x 1.5 mm bare

---

[4]Provided by Dr. Neumaier from the WMI; field calibrated by Rucker [4]

sensor	function	location	B range	T range
JT MC ROX	temperature regulation	on the top of the mixing chamber	0 T	0.01 - 150 K
WMI ROX	bath thermometer	on the base plate attached to the MC	0 T 0-9 T	0.1 - 5 K 0.18 - 2 K
E51-ROX BR3	platform thermometer	on the back of the sample platform	0 T	0.02 - 5.5 K

Table 3.2.1.: Thermometers used during this thesis.
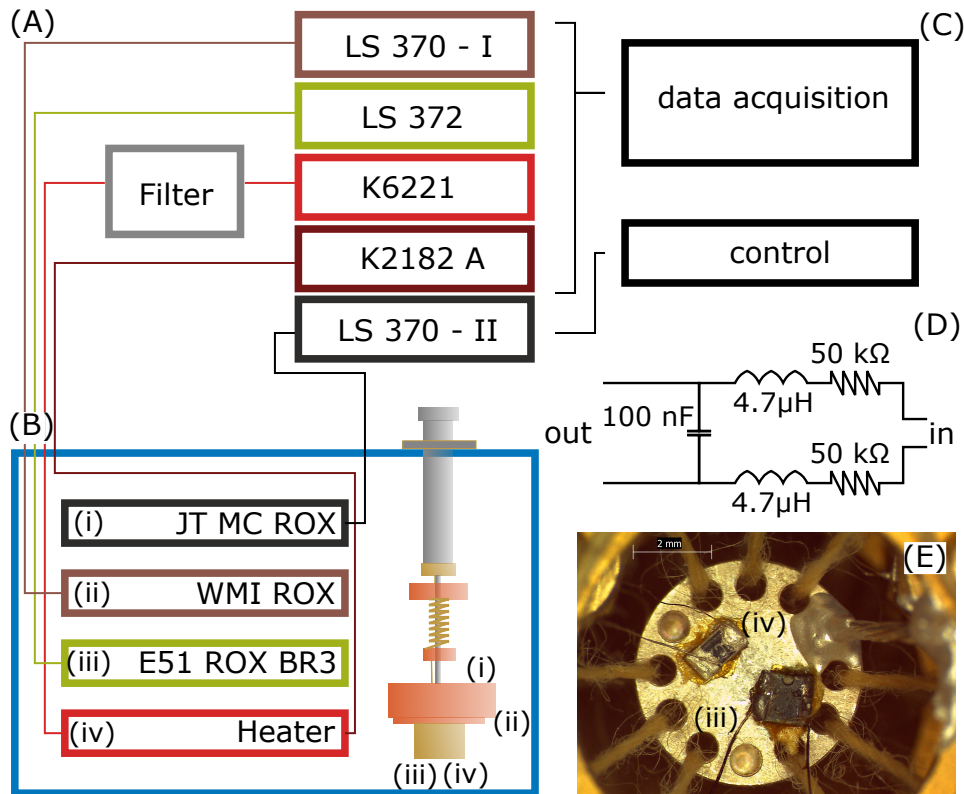
Figure 3.2.4.: The electrical wiring of the heat capacity setup. (A) Schematic depiction of the instruments used for measurement, control and input. The connected sensors are highlighted by connections and color. (B) Chips installed on the experimental setup with a schematic depiction of their location. (C) Depiction of the usage of the devices in the software. The data acquisition was separated from the control to enhance the readout time. (D) Diagram of the custom built low-pass filter for usage with the K6221 current source. (E) Photograph of the sample platform with the heater and E51 ROX BR3 chip.

ROX chip purchased from Lakeshore. It was glued to the back of the silver platform to determine the platform temperature T_p. Platform and bath thermometer were read by two separate Lakeshore resistance bridges, using different sampling frequencies of their internal Lock-in amplifiers to minimize cross-talk and noise. All Lakeshore resistance bridges used the Lakeshore scanner module, since it provided proper signal shielding for the devices.

The heater (iv) was a 1kΩ SMD 0603 resistor as depicted in Fig. 3.2.4 (E) directly connected to the back of the platform. It was driven by a Keithley K6221 current source in DC mode. To reduce parasitic heating effects due high frequency noise coupling into the resistor, the output was fed through a bespoke low-pass filter as recommended in the Keithley manual Appendix E [129] with the specifications shown in (D). Since the voltage drop over the heater was measured by a Keithley K2182A Nanovoltmeter, the power $P(t)$ could be calculated using Ohm's law.

To ensure a fast data acquisition rate, the equipment readout was completely decoupled from the control program. With this setup, it was possible to record roughly 10 datapoints every second, which was the limit of the Lakeshore instruments and proved to be sufficient for the time constants between 10 s and 1 h achieved in the measurements.

3.2.6. Temperature Calibration

As mentioned above, the resistance values measured need to be converted to a precise temperature reading when analyzing the heat pulses. The following section provides the relevant steps for temperature calibration for the heat capacity and the magnetocaloric measurements.

Heat Capacity Measurements   The ROX sensors used showed a strong magnetoresistance, which had to be taken into account to obtain a correct temperature and thus correct specific heat readings. The first step of the calibration process was to record the resistance of the platform sensor R_p (E51 ROX BR3) in the regime of thermal equilibrium between bath and platform. Thus for each heat pulse the average before the heating phase was taken. The temperature was determined by simultaneously recording the resistance of the bath thermometer R_b (WMI), calibrated as summarized in Tab. 3.2.1 [4]. From this

followed the resistance-temperature relation for the platform thermometer, as shown in Fig. 3.2.5 (A) and (C).

Different models for the T_p versus R_p relation were tested to describe the $B = \text{const}$ behavior. Spline interpolation provided the best results, cf. Fig. 3.2.5 (B) where the deviation of the interpolation from the data points is shown. For each constant field B, the spline was determined, cf. Fig. 3.2.5 (C). For increasing magnetic field, the resistance increases, as shown in Fig. 3.2.5 (D). Since this effect depends on the temperature, an individual correction for each heat pulse was carried out.

Kinks in these splines provide another problem. Kinks, jumps and oscillations like in the blue curve in Fig. 3.2.5 (D) lead to errors in the temperature derivative and thus significant errors in the heat capacity fits. Chebycheb polynomials have the same issue and were discarded after testing for this reason.

Therefore, all heat pulses were calibrated in the same way. First, the mean temperature of the heat pulse was determined. The resistance data of the pulse were divided by the value shown in Fig. 3.2.5 (D) at the given T and B. This way the resistance values were obtained, equivalent to the resistance values if this heat pulse was measured at zero-field. As the heat pulses were only a few percent in amplitude, this simplification is valid, since the magnetoresistance does not change significantly during the pulse. The zero-field equivalent resistance data R_p were all calibrated using the same Lakeshore calibration dataset, obtaining the smooth platform temperature T_p.

Magnetocaloric measurements While the calibration for the heat capacity measurements required a smooth definition of the resistance-temperature relation for a constant field only, magnetocaloric measurements required to cover the whole B-T-space. Due to the different spacing of datapoints, notably twelve values as a function of field but close to fifty values as a function of temperature, a 2D-interpolation using typical methods appeared to be too complicated. Furthermore, finding a sufficiently precise expression in 2D was not possible. The data were therefore calibrated using a mixed method of fitting and interpolation.

Taking the data from Fig. 3.2.5 (D), a curve was fit at constant temperature. The expression

$$R = a + b \cdot B^{1/2} + c \cdot B + d \cdot B^2 \tag{3.2.5}$$

101
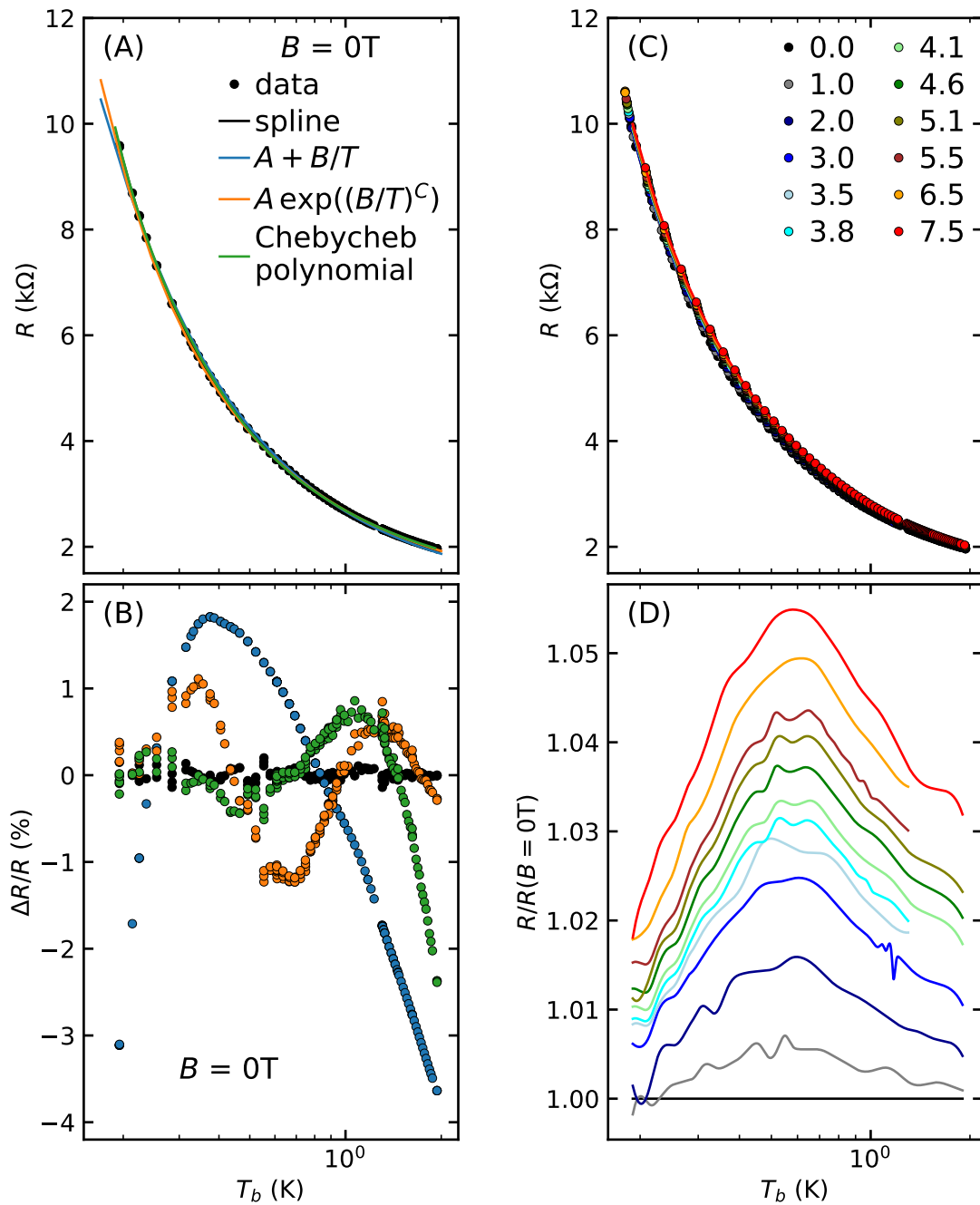
Figure 3.2.5.: Calibration of the ROX-BR3 thermometer. (A) For a given magnetic field, the restistance of the the thermometer is plotted against the temperature of the calibrated Bath thermometer. The data were interpolated with cubic splines, the relation $R = A + B/T$, $R = A \exp\left((B/T)^C\right)$ as well as Chebycheb polynomials. Both equations fail to describe the R-T-relation in parts of the temperature range, as shown in (B) where the difference between interpolation and measured resistivity is shown exemplary for zero field. (C) The resistivity rises with increasing field. This is clearly visible when dividing the spline interpolation for each field by the zero field value as shown in (D).
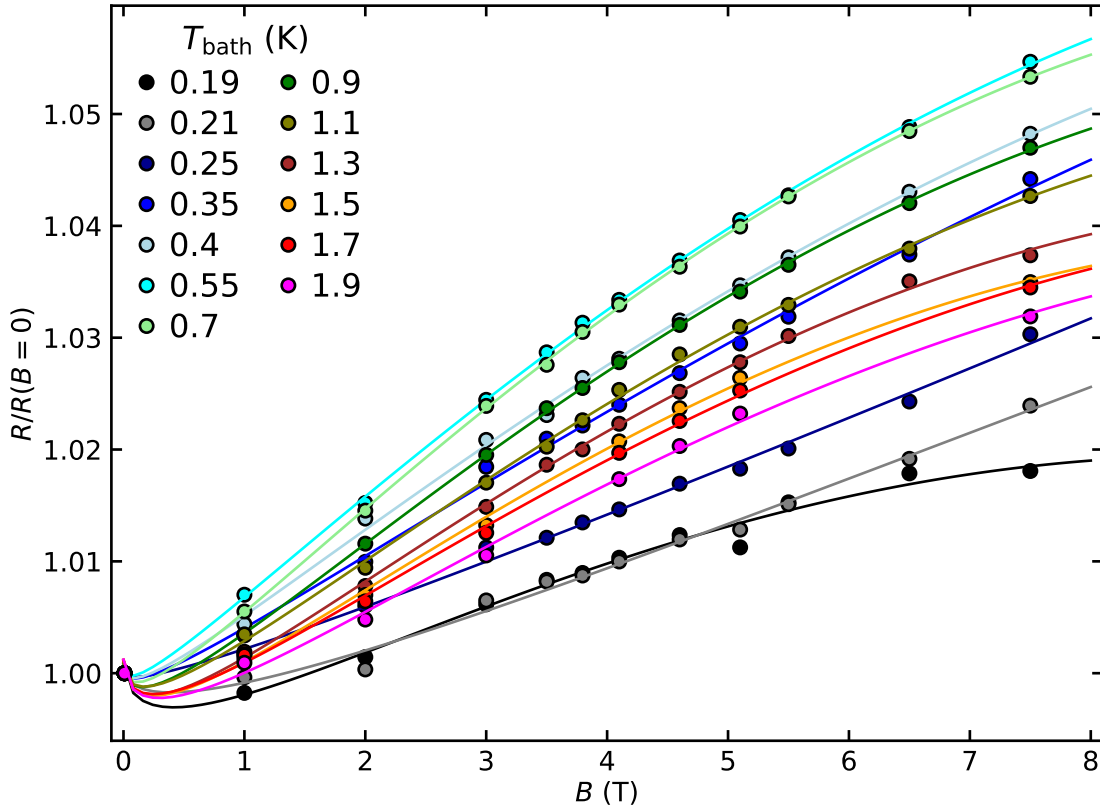
Figure 3.2.6.: Exemplary slices through the spline dataset from Fig. 3.2.5 (d) fitted using (3.2.5). The qualitative behavior, especially the minimum below 1 K for low temperatures is in agreement with the study of Goodrich *et al.* [130].

was used to describe the data, following by the findings of Rost and Goodrich *et al.* [119, 130]. In the high field data, the square root behavior dominated, but the linear and cubic term were necessary to describe the minimum between 0.5 and 1 T at low temperatures, which is typical for ROX chips as a direct comparison with Goodrich *et al.* [130] shows. The behavior together with the corresponding fit is shown in Fig. 3.2.6 for various cuts of constant temperature. The $R - T - B$ dataset was cut in 1 mK wide slices and each slice was fitted as shown in Fig. 3.2.6. Full details are shown in App. A.2. These results were stored in a lookup table. For each magneto-caloric sweep, the mean bath temperature T_b was used to select the appropriate parameters, which were then used to calculate the resistance R_p according to Eq. (3.2.5). These calibrated resistances were used to determine the temperature according to the zero-field calibration.

(A) sample orientation

(B) gluing the sample to the platform
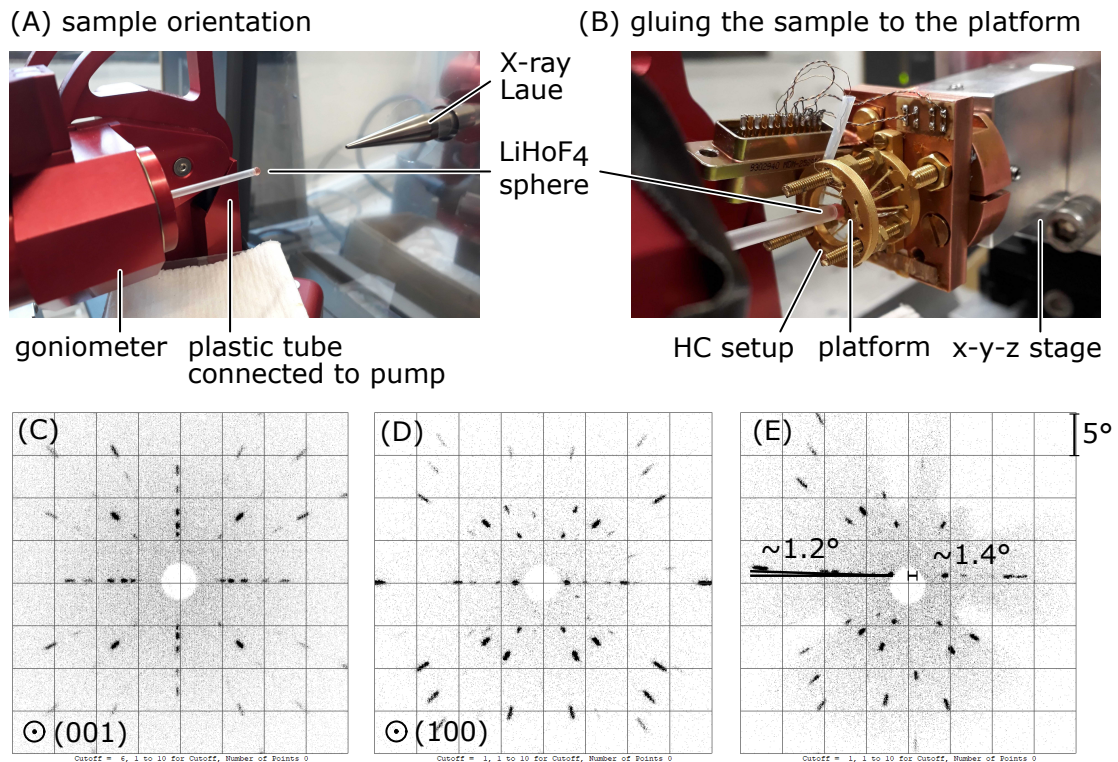
Figure 3.2.7.: Process of orienting and attaching the sample to the HC platform using X-ray Laue diffraction. (A) The spherical LiHoF$_4$ sample is sucked to a small plastic tube using a vacuum pump connected to the tube. Rotating the goniometer allows to orient the sample. (B) The oriented sample is kept in a fixed position. The heat capacity setup is moved in position with a x-y-z translation stage. (C) Looking along the easy axis (001) the typical four fold pattern can be observed. Mounted in the cryostat, this is the direction of the y-axis of the vector magnet. Rotating the sample to the right by 90° reveals the (100) direction as shown in (D), which is along the z-axis of the magnet. The goniometer allows to orient the sample with a precision $< 0.1°$. (E) After gluing the sample to the platform, only small deviations $< 1.5°$ from the optimal orientation are observed. The screws of the setup cover parts of the X-ray detector, leading to areas without reflections.

3.2.7. Sample Alignment Procedure

As established in Sec. 2.2.5, a good alignment of the sample with respect to the transverse magnetic field is crucial for the studies pursued in this thesis. The spherical LiHoF$_4$ sample with a diameter of 2.8 mm was aligned using X-ray Laue diffraction.

As shown in Fig. 3.2.7 (A), the sphere was oriented using the goniometer at the Laue diffractometer. A small plastic tube was connected to a vacuum pump, which sucked
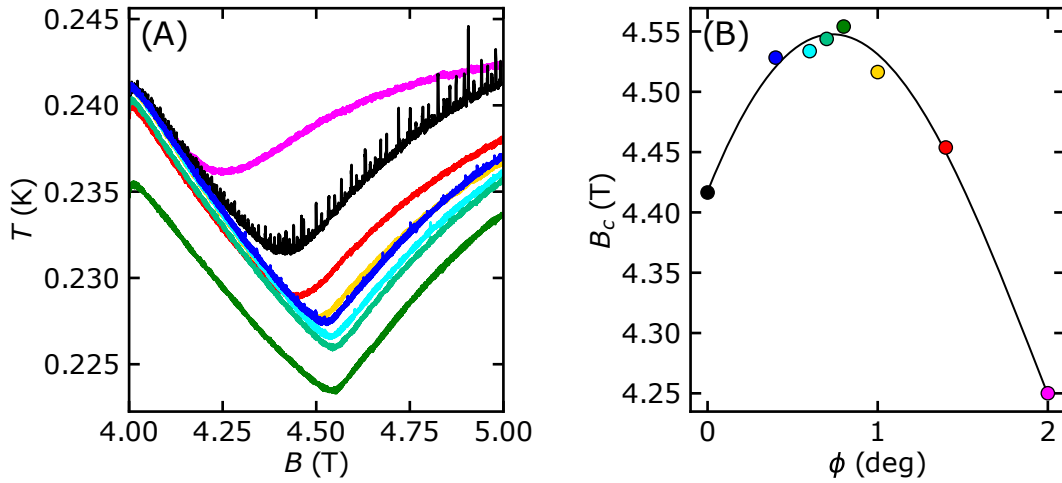
Figure 3.2.8.: Sample orientation inferred from magnetocaloric sweeps. (A) The critical field is visible as a clear kink of the platform temperature when ramping the magnetic field at a constant angle ϕ. (B) A maximum is observed around $\approx 0.7°$. The colors of the curves in (A) correspond to the datapoints in (B). The line represents a guide to the eye.

the sphere in a fixed position. This allowed to put the sample in the desired orientation with respect to the diffractometer, as shown in Fig. 3.2.7 (C) and (D). Next the heat capacity setup was aligned with the optical table of the Laue diffractometer and the sample was glued to the platform using the x-y-z translation mount to move the HC setup, cf. Fig. 3.2.7 (B). After the GE varnish had dried, the vacuum pump was turned off. A scattering pattern was recorded, as shown in Fig. 3.2.7 (E). The alignment was confirmed to be better than $\approx 1.5°$ along both rotational directions.

After inserting the JT in the AMI vector magnet, the sample alignment with the magnet was determined similar to Sec. 2.2.5. Since heat capacity measurements take a very long time, magnetocaloric sweeps were used to determine the critical field B_c as a function of angle Φ. B_c is visible as a kink in the platform temperature, cf. Fig. 3.2.8 (A). An optimal field angle $\phi \approx 1.2°$ was determined after the initial cooldown of the sample. Ramping the field to its maximum value it was observed that the sample shifted. Another set of MC sweeps determined the optimum angle $\phi \approx 0.7°$ afterwards, as shown in Fig. 3.2.8 (B). In analogy to Sec. 2.2.5, the field angle was then defined as $\Phi = \phi - 1.2°/0.7°$.

3.3. Experimental Results

Using the measurement setup described in the last section, the experimental results recorded will be presented in the following. First, the results of the specific heat measurements using the relaxation time method will be described in Sec. 3.1.2. The heat pulses will be discussed, followed by a detailed overview of the fit results as a function of angle Φ, field B and temperature T. Second, following the same strategy, the magnetocaloric sweeps will be presented and analyzed in Sec. 3.3.2.

3.3.1. Specific Heat

Data were recorded using the JT dilution refrigerator insert described in Sec. 2.2.1 in combination with the AMI vector magnet described in Sec. 2.2.2. Heat pulses were measured after setting the magnetic field B at angle Φ and the platform temperature at T, following the procedure described in Sec. 3.1.2.

Heat Pulses Fig. 3.3.1 shows typical heat pulses for various B, Φ and T. Similar baseline temperatures in the range of $T \approx 200\,\mathrm{mK}$, $470\,\mathrm{mK}$, $900\,\mathrm{mK}$ and $1.35\,\mathrm{K}$ are shown in Fig. 3.3.1 (A-D), respectively. Since the heat pulses were set manually, they range between 1 and 4% in height. With increasing temperature T, the time constants τ and thus pulse times decrease significantly. Simultaneously, the τ_2-effect with the distinct jump at $200\,\mathrm{mK}$ decreases in size. This suggests, that the thermal coupling of the sample as compared to the silver link improves with increasing temperature. Given that the thermal conductivity of GE 7031 varnish strongly depends on the temperature, consistent with expectation.

Increasing the magnetic field B and angle Φ, the τ_2-effect was found to become more pronounced, suggesting that there are additional effects influencing the heat flow. Large differences in the pulse shape between zero field and $B = 5.1\,\mathrm{T}$ can be observed at $T > 0.9\,\mathrm{K}$. They may be attributed to the precise location in the ferromagnetic and the field polarized phases of LiHoF$_4$, respectively.

A noteworthy observation can be made at $T = 210, 480\,\mathrm{mK}$, $B = 5.1\,\mathrm{T}$. The shapes of the pulses at 0°, cf. Fig. 3.3.1 (A2,B2), and 5°, cf. Fig. 3.3.1 (A3,B3), differ significantly,
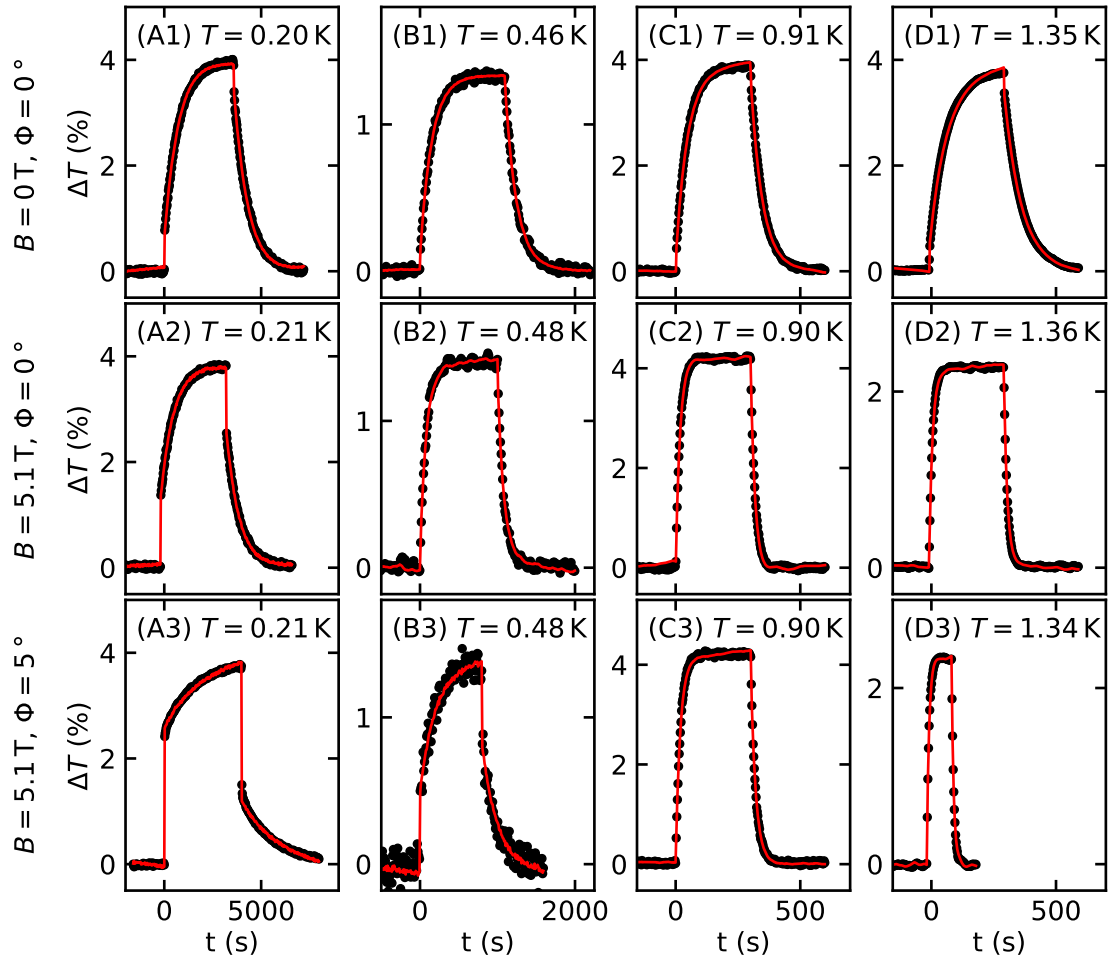
Figure 3.3.1.: Exemplary heat pulses for various field angles Φ, magnetic fields B and platform baseline temperatures $T \approx 200\,\mathrm{mK}$ (A), $470\,\mathrm{mK}$ (B), $900\,\mathrm{mK}$ (C) and $1.35\,\mathrm{K}$ (D). The pulse amplitude ΔT is given in percent of the baseline temperature. Only every 250th, 100th, 25th and 25th point is shown for clarity. (A1-D1) Zero field heat pulses. (A2-D2) Pulses at $B = 5.1\,\mathrm{T}$ and $\Phi = 0°$. (A3-D3) Pulses at $B = 5.1\,\mathrm{T}$ and $\Phi = 5°$.

although both are located in the field polarized regime at the same temperature and field. It appears that the thermal conductivity varies in this regime, since both the relaxation time and the τ_2 effect are influenced here. We have no explanation for this effect.

Fit Results   Fig. 3.3.2 shows the fit results of the specific heat as well as the other fit parameters as a function of temperature for several transverse fields B at $\Phi = 0°$. These parameters were fitted as explained above using Eq. (3.1.25) [108]. The specific heat C/R is shown in Fig. 3.3.2 (A). In zero field, with increasing temperature a broad peak is observed around $T \approx 200\,\text{mK}$ after which C/R displays a minimum around 800 mK. Following this the heat capacity increases again monotonically until the critical temperature T_c is reached, where it sharply falls by one order of magnitude and then starts to rise slowly afterwards.

The maximum at low T bears the characteristics of a Schottky anomaly and can be attributed to the hyperfine interaction [43]. Increasing the magnetic field B shifts its position to lower temperatures. Below 150 mK C/R is enhanced at larger fields, especially around the critical field $B = 5.1\,\text{T}$. Above 5.1 T the hyperfine peak starts to shift towards higher temperatures. The minimum above the hyperfine peak deepens and shifts to larger temperatures with increasing field reaching $\approx 1\,\text{K}$ at 7.5 T.

The increase of C/R approaching the phase transition is identical for all fields, the sharp drop appears earlier as T_c shifts to lower temperatures with increasing field. Additionally, a broader peak evolves above $B = 2\,\text{T}$, appearing beneath the sharp transition and shifting to higher temperatures with increasing field. This feature can be attributed to the crystal field splitting of the ground state doublet under magnetic field.

Fig. 3.3.2 (B) shows the fitted relaxation time of the sample τ_s, which is maximal at low temperatures, where the heat capacity of the sample is large as compared to the thermal link. It shows a local maximum at the phase transition, where the specific heat has a maximum.

The relaxation time of the addenda τ_l is shown in Fig. 3.3.2 (C). Since this property depends strongly on the shape of the jump of the τ_2-effect it displays a large spread in the data points, also because only a few data points contribute to this fit parameter. It is inversely correlated to the thermal conductance of the sample k_s shown in Fig. 3.3.2 (D), which reduces the height of the τ_2 effect. Above 500 mK the initial jump is not very
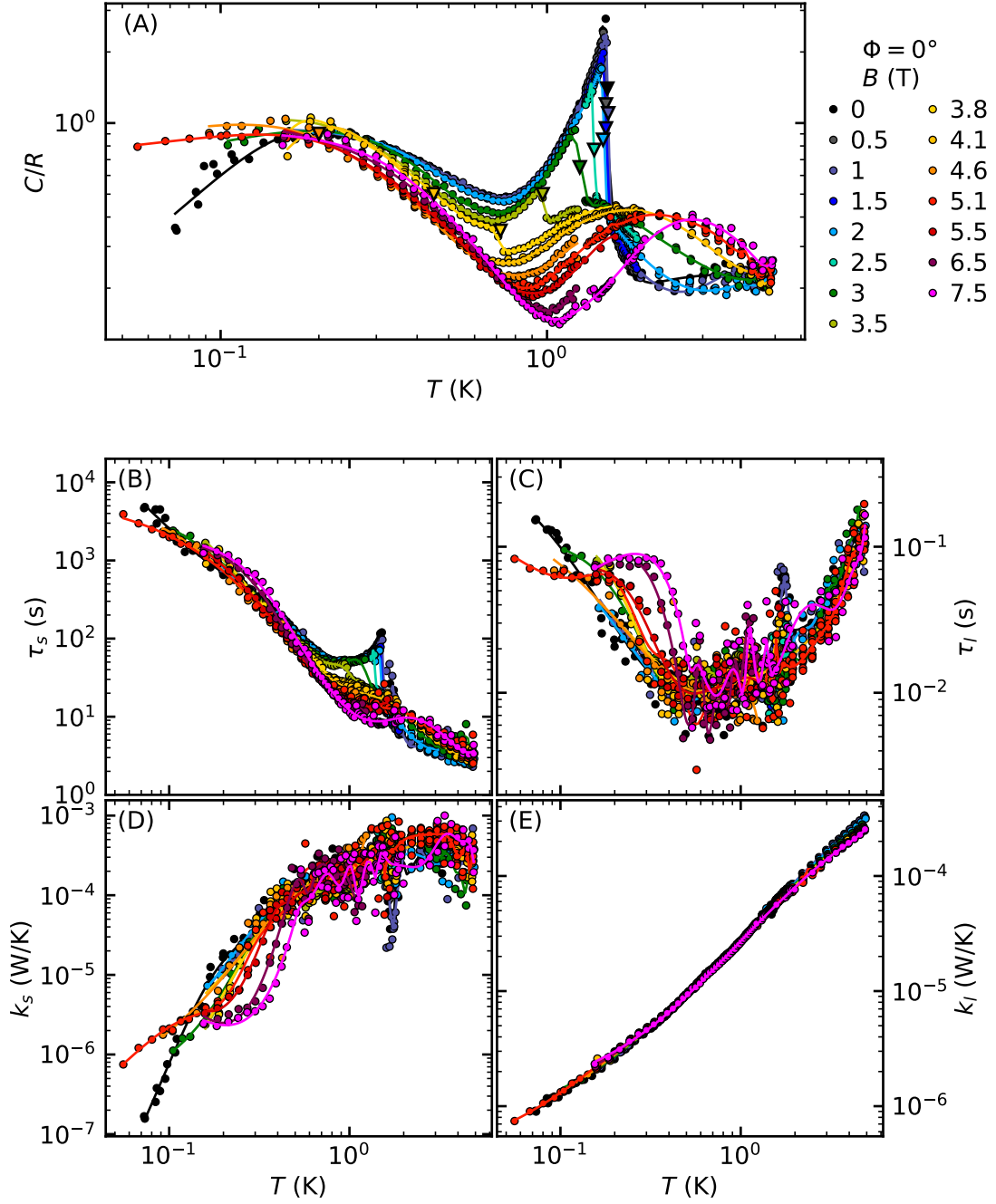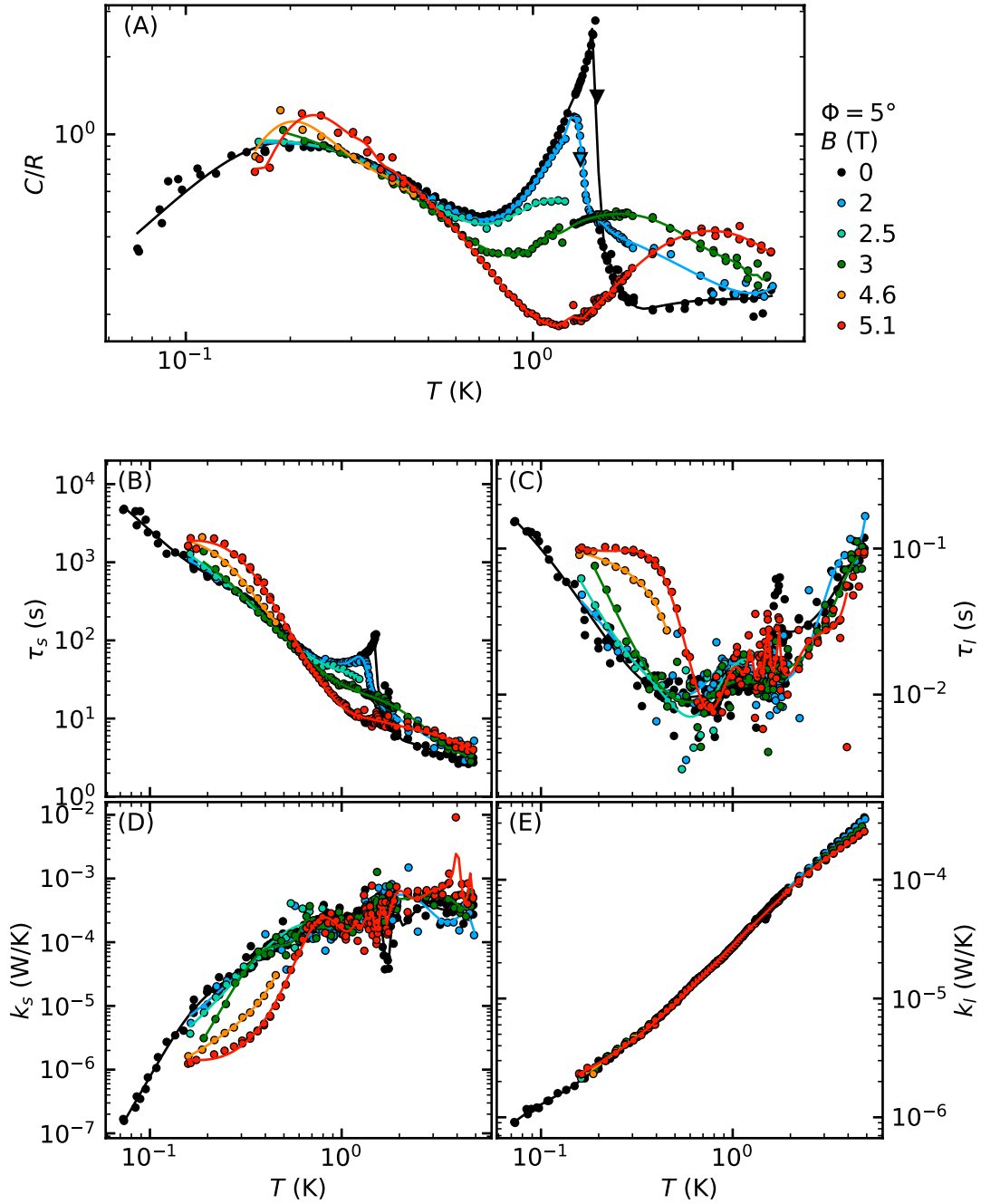
Figure 3.3.2.: Specific heat fit results for a angle of $\Phi = 0°$. (A) The specific heat C/R as a function of temperature. The triangles mark the position of the phase transition to the ferromagnetic state. (B) The relaxation time of the sample τ_s is directly correlated to the specific heat. (C) The relaxation time of the addenda τ_l is several orders of magnitude faster as compared to the sample. (D) The thermal conductance between sample and platform k_s. (E) The thermal conductance between platform and bath k_l is independent of magnetic field and is dominated by the thermal conductance of the silver wire.

pronounced and a large spread of this parameter is observed. In stark contrast, the thermal conductance of the link k_l shows almost no variation, cf. Fig. 3.3.2 (E), since it can be directly derived from the amplitude of the heat pulses which are known precisely.

At a finite angle of $\Phi = 5°$, the peak at the ferromagnetic transition T_c is unchanged in form, but is cut off at lower fields, since the ferromagnetic phase is suppressed at a lower temperature. As depicted in Fig. 3.3.3 (A), already at 2.5 T no transition may be discerned in C/R. The broad peak, which evolves under the transition peak around 1.5 K at 2.5 T shifts to higher temperatures with increasing field even faster than for $\Phi = 0°$, reaching a maximum at 5.1 T at 3 K.

In the peak of the hyperfine contribution, the data above 4.6 T stand out, since they have a larger spread and are higher compared to the data recorded in low fields in the region of 150 mK to 400 mK. As discussed above, the pulse shape in this regime differs significantly from the shapes at lower fields and other angles. The relaxation time τ_s is especially large in this area, cf. Fig. 3.3.3 (B). This made measurements very demanding as longer wait times were required to reach equilibrium. Simultaneously, the relaxation time of the addenda shown in Fig. 3.3.3 (C) is also enhanced and the thermal conductance of the sample k_s is reduced significantly. Possible explanations for this effect will be discussed below. Apart from this anomaly, τ_s, τ_l, k_s and k_l at $\Phi = 5°$ follow the behavior of $\Phi = 0°$.

At an even larger angle of $\Phi = 10°$, the heat capacity data shows no transition as a function of temperature for $B \geq 2$ T, as these fields are outside the ferromagnetic phase; see Fig. 3.3.4 (A). The increase of the shift of the high temperature maximum is even more pronounced, with the maximum at 5.1 T being located at 4 K.

The results of the fits of the relaxation times and thermal conductance (Fig. 3.3.4 (B)-(E)) show no anomalies at this angle and follow the trends observed at $\Phi = 0°$. The changes with field angle were investigated in more depth for $B = 2$ T, 3 T and 5.1 T. Fig. 3.3.5 (A) shows the evolution of the specific heat C/R with increasing field angle for a constant field of $B = 2$ T. The hyperfine peak is independent of Φ as the specific heat C/R is the same for all angles up to 600 mK, where differences are due to the thermal phase transition. For $\Phi = 0°$ and $B = 2$ T, the transition occurs at $T_c \approx 1.5$ K. The transition shifts towards lower temperatures with increasing angle Φ and reaches $T_c \approx 1.1$ K at $\Phi = 6.6°$. At higher angles only a broad peak is visible, which shifts to higher temperature with increasing angle.

Figure 3.3.3.: Specific heat fit results for a angle of $\Phi = 5°$. (A) The specific heat C/R as a function of temperature. The triangles mark the position of the phase transition to the ferromagnetic state. (B) The relaxation time of the sample τ_s is directly correlated to the specific heat. (C) The relaxation time of the addenda τ_l is several orders of magnitude faster as compared to the sample. (D) The thermal conductance between sample and platform k_s. (E) The thermal conductance between platform and bath k_l is independent of magnetic field and is dominated by the thermal conductance of the silver wire.
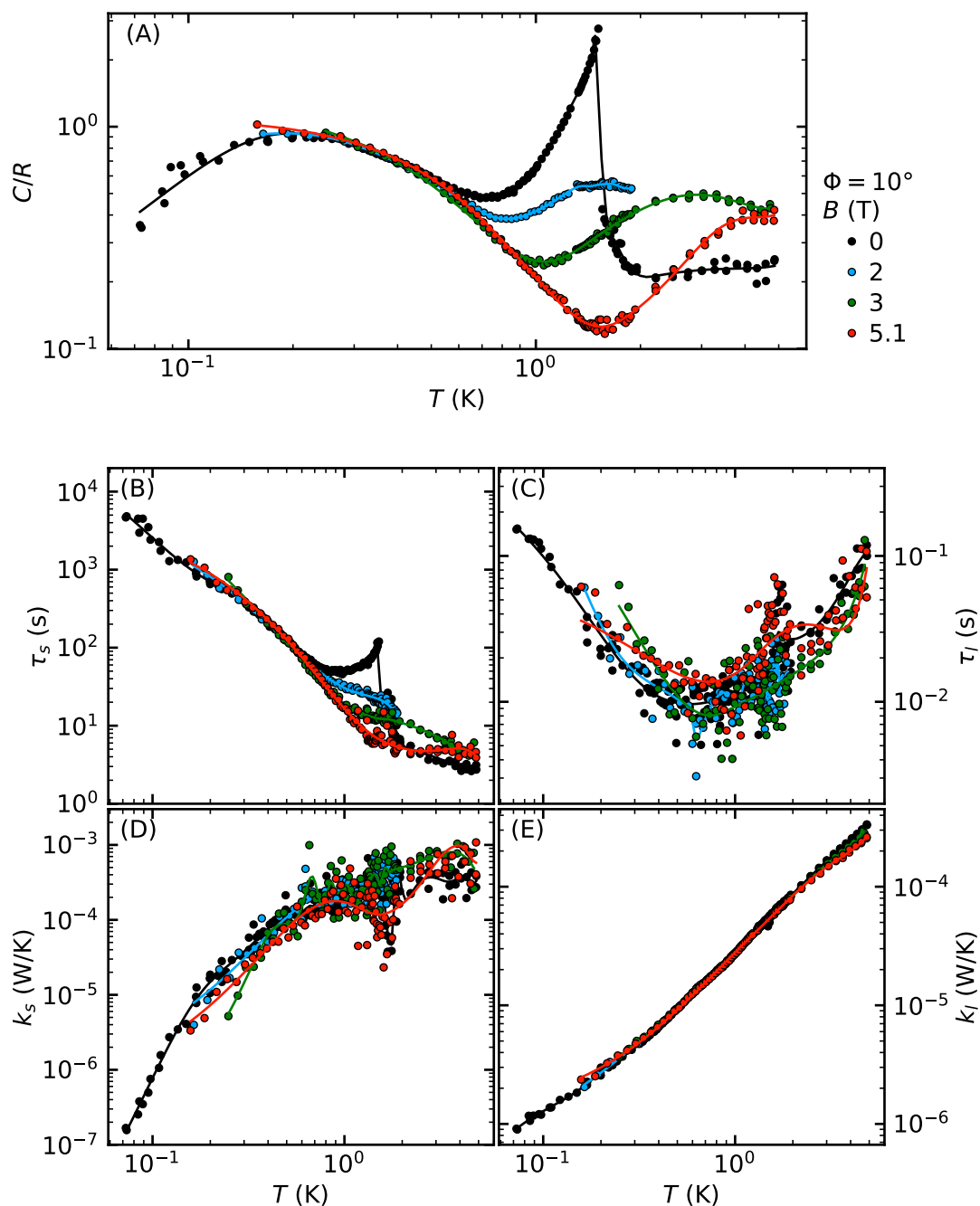
Figure 3.3.4.: Specific heat fit results for a angle of $\Phi = 10°$. (A) The specific heat C/R as a function of temperature. The triangles mark the position of the phase transition to the ferromagnetic state. (B) The relaxation time of the sample τ_s is directly correlated to the specific heat. (C) The relaxation time of the addenda τ_l is several orders of magnitude faster as compared to the sample. (D) The thermal conductance between sample and platform k_s. (E) The thermal conductance between platform and bath k_l is independent of magnetic field and is dominated by the thermal conductance of the silver wire.

The other fit parameters τ_s, τ_l, k_s and k_l show no unexpected trends or anomalies and follow the general behavior described above. The associated data are shown in App. A.3 for the three fields presented in Fig. 3.3.5.

For $\Phi \leq 6.6°$ the specific heat follows the same form quantitatively up to the phase transition, whereas at larger angles the curves start to deviate from one another around $T \approx 600\,\mathrm{mK}$. While the peak amplitude decreases with increasing angle, it stays almost constant at $C/R \approx 0.6$ for $\Phi \geq 7.5°$. In summary, while the ferromagnetic phase is characterized by essentially the same specific heat independent of the angle ϕ, the paramagnetic or field polarized is phase are characterized by maxima shifting towards larger temperatures with increasing Φ.

The same behavior is found at $B = 3\,\mathrm{T}$, as shown in Fig. 3.3.5 (B). For this field, also a sweep at an angle of $\Phi = 90°$, thus along the easy c-axis was performed. As may be seen, the curve shifts drastically to larger temperatures. As shown in App. A.3, the other fit parameters τ and k also diverge from the lower angles, indicating that the setup performs differently at such large angles, explaining also the larger scatter of the data points of this curve.

At a constant field of $B = 5.1\,\mathrm{T}$ all measurements apart from $\Phi = 0$ at the lowest temperatures were performed in the field polarized regime, cf. Fig. 3.3.5 (B). The hyperfine peak of the specific heat shifts to larger temperatures with increasing angle. While $\Phi = 0°$ the specific heat starts do decrease around $200\,\mathrm{mK}$, this drop shifts to over $300\,\mathrm{mK}$ in the case of $10°$. The same behavior is also observed for the high temperature peak, which shifts from $T \approx 2\,\mathrm{K}$ to $T \approx 5\,\mathrm{K}$ respectively.

In this dataset, the $B = 5.1\,\mathrm{T}$ and $\Phi = 5°$ stands out, since they show the anomalously high hyperfine peak described above, which is also visible as a large deviation in the other parameters, cf. Fig. A.3.3 (B-E). As discussed above, the thermal conductance seems to be reduced here. Whether this originates from the experimental setup or is related to the internal thermal conductivity of LiHoF$_4$ is beyond the scope of the work presented here.
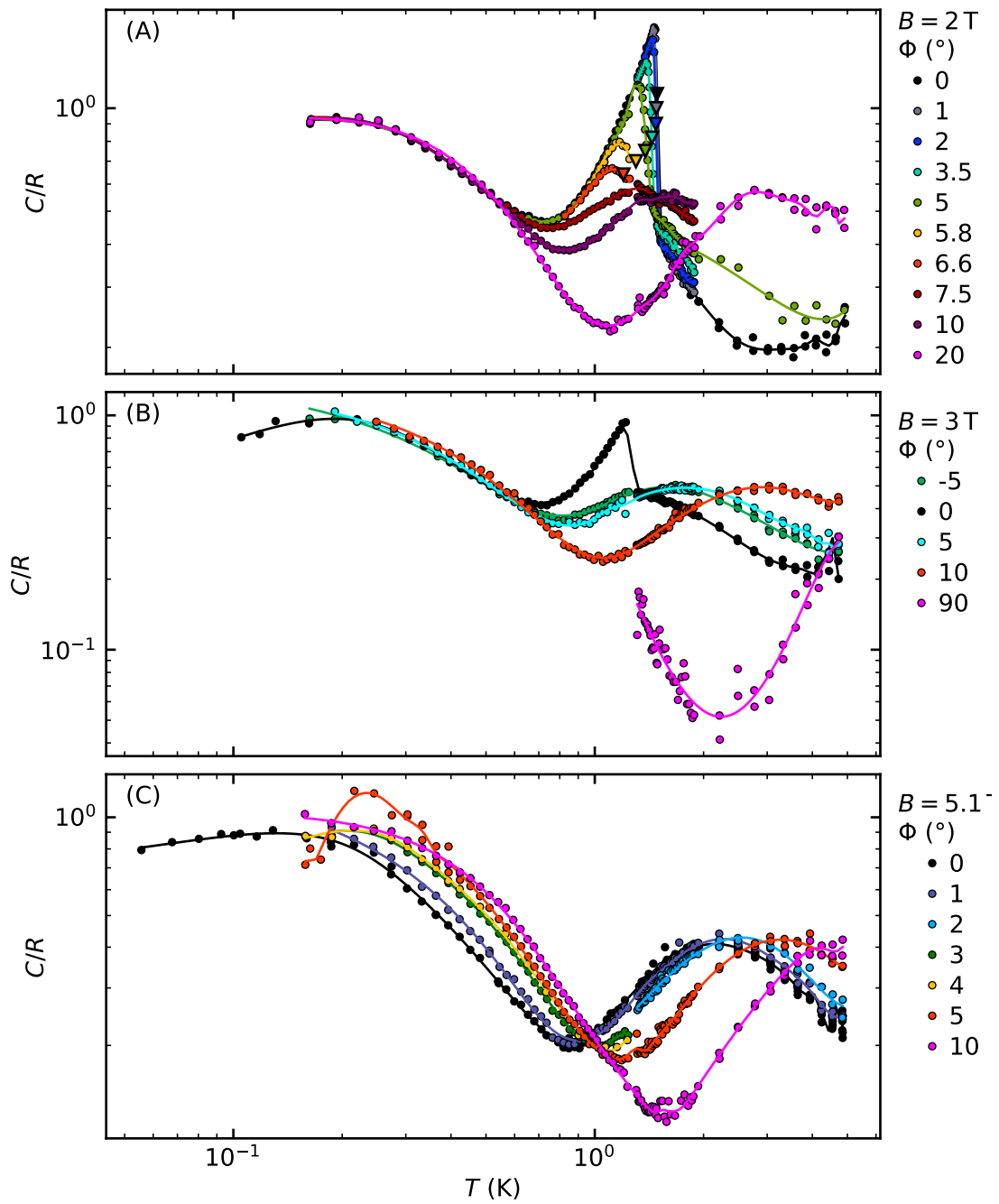
Figure 3.3.5.: Specific heat C/R as a function of temperature for various angles and fields. (A) Experimental results for $B = 2\,\mathrm{T}$. The triangles mark the position of the phase transition. (B) Experimental results for $B = 3\,\mathrm{T}$. (C) Experimental results for $B = 5.1\,\mathrm{T}$.

3.3.2. Magnetocaloric Field Sweeps

Using the same experimental setup, the magnetocaloric effect was measured in LiHoF$_4$. As explained in Sec. 3.1.3, the derivative of the entropy Eq. (3.1.33) may be determined by scanning the magnetic field at a constant rate and recording the sample temperature. The experiments were performed in the non-adiabatic limit, cf. Eq. (3.1.35), in order to reduce errors due to the heat capacity of the material. Since in practice the ramp-rate represented a compromise between measurement time, signal-to-noise and errors, cf. Eq. (3.1.35), the ramp rates were adjusted manually for each temperature. Due to the lower thermal conductance $k = k_l$ of the link, the ramp rate was slower at low temperatures.

The results at $\Phi = 0°$ are shown in Fig. 3.3.6. Each sweep shows three distinct features. First, with increasing field, $\delta S/\delta B$ rises linearly as the field approaches the phase transition from the ferromagnetic to the field polarized state at B_c. Generally, this slope is steeper for lower temperatures and the maximum reached at the phase transition is higher. For $T \geq 1.3$ K this initial slope shows an additional feature. Below $B = 0.5$ T a distinct maximum in the up- and a minimum in the down-sweep can be observed. This feature likely does not originate from the magnetocaloric effect, since the platform was heated in both cases and an inversion of heating/cooling between up- and down-sweep would be expected from the magnetocaloric effect instead. Moreover, this feature is also present in a field sweep at $T = 1.82$ K, a temperature above the ferromagnetic phase. An systematic or instrumental effect seems most plausible for this. At the lowest temperature of $T = 0.2$ K up- and down-sweep show a different shape approaching the jump of $\delta S/\delta B$ at $B \approx 4$ T, which is likely due to a violation of the non-adiabatic condition Eq. (3.1.35).

Second, at the phase transition, marked in Fig. 3.3.6 using triangles pointing down, the derivative $\delta S/\delta B$ drops significantly. This jump is larger in regimes, where the specific heat is also large, such as the hyperfine peak at 0.2 K or between 1.3 and 1.5 K. At $T = 1.82$ K, no drop is visible, since the field sweep was outside of the ferromagnetic phase. Third, above the phase transition, the slope of $\delta S/\delta B$ is almost horizontal for temperatures up to 0.6 K. With rising temperature the slope increases and reaches a maximum at 1.5 K.

All previous descriptions correspond to the up-sweeps shown in Fig. 3.3.6 (A). Due to the definition of the temperature difference ΔT in the sweeps, all curves start at zero at $B = 0$ T. Therefore, distortions are not represented equally in up- and down-sweeps,
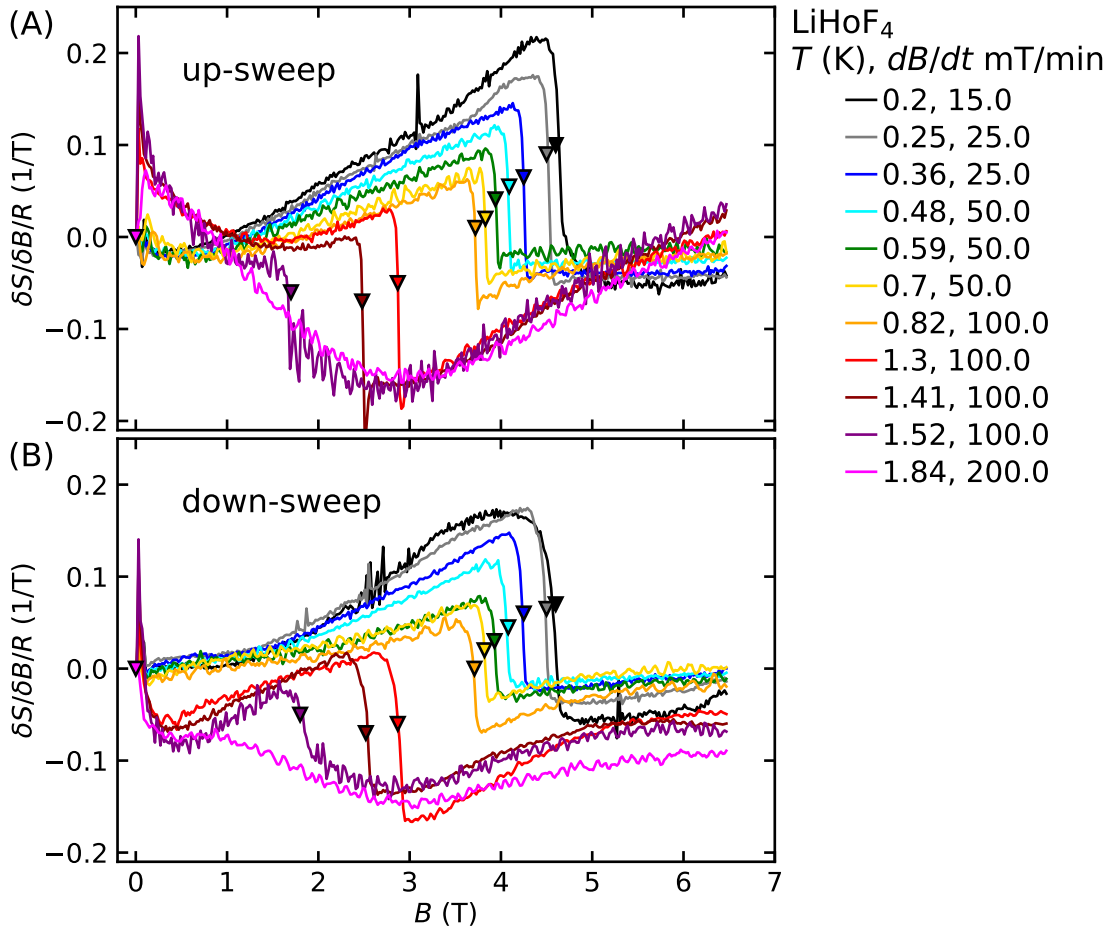
Figure 3.3.6.: Magnetocaloric sweeps. The derivative of the entropy with respect to magnetic field after Eq. (3.1.33) is shown as a function of the magnetic field B for the up-sweeps (A) and the down-sweeps (B). Data were recorded at different ramp-rates to accommodate for the effects of the heat capacity as discussed in Sec. 3.1.3.

cf. Fig. 3.3.6 (A) vs. (B). These differences arise from the heat capacity and the spike in temperature, which occurs immediately after the magnet ramping was started while it takes time to establish an equilibrium between heat flow and Eddy current heating. These are especially significant above 1.3 K, where larger ramp rates lead to stronger Eddy current heating. Nevertheless, both sweep directions result in the same critical fields B_c and allow to describe the phase diagram qualitatively.

In the next step, $\delta S/\delta B$ can be integrated to obtain $\Delta S = S(B) - S(B = 0\,\text{T})$. The result is shown in Fig. 3.3.7. To account for the differences between up- and down-sweep in the analysis, both are shown as dotted and dashed lines respectively, while the mean is shown as a solid line. Starting from zero, for all temperatures $\Delta S/R$ is basically constant as a
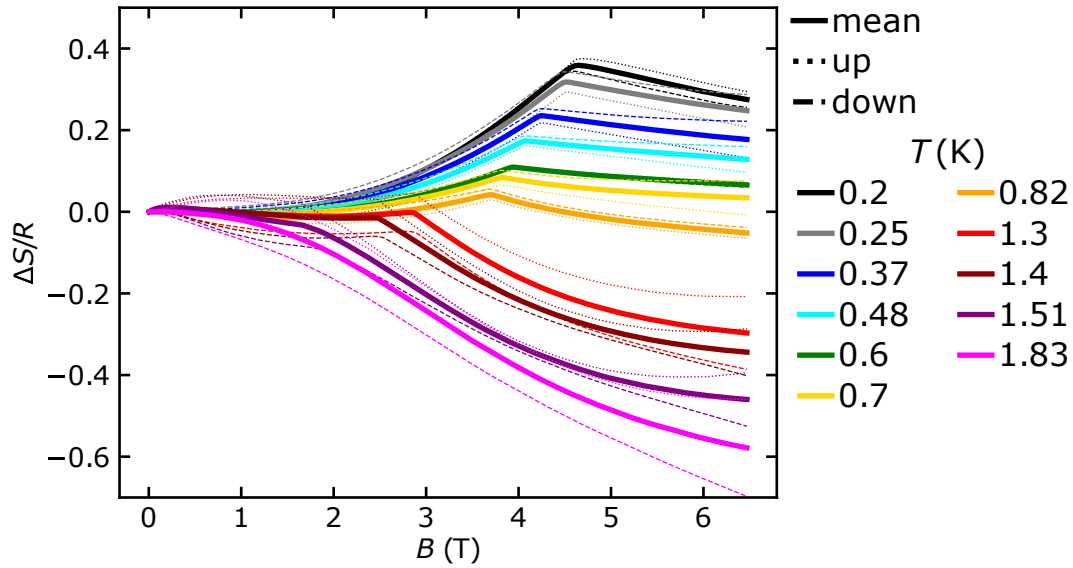
Figure 3.3.7.: Entropy as a function of magnetic field for various temperatures. The results from the up- (dotted line) and down (dashed line) are combined to a mean (solid line). The phase transition is visible as a kink in the curve up to $1.5\,\mathrm{K}$.

function of field up to $B \approx 2\,\mathrm{T}$. Above this field, it rises up to the phase transition, where a kink at the maximum can be observed. This maximum shifts from $\Delta S/R = 0.39$ at $T = 0.2\,\mathrm{K}$ to $\Delta S/R \approx 0$ at $T = 1.51\,\mathrm{K}$. Similarly, the position of the transition decreases with temperature, as already observed in susceptibility and heat capacity measurements. Notably, the increase approaching the transition also becomes flatter with temperature and the decrease after the maximum deeper. This entropy landscape will be compared below to the theoretical predictions.

3.4. Comparison with Literature and Theory

In this section the experimental results described above will be discussed in comparison to other experimental work and the theoretical model developed above. The discussion focuses first on the specific heat followed by the magnetocaloric sweeps.

Specific Heat in the Literature   The first measurements of the specific heat in LiHoF$_4$ were reported by Mennenga *et al.* [43, 83]. This study reported the most sophisticated analysis of the low temperature heat capacity in this material so far. Therefore, it is natural to compare the results presented above with this study, as shown in Fig. 3.4.1. Over a wide temperature range, both studies are in perfect agreement, both the hyperfine peak at $\approx 200\,\mathrm{mK}$ and the thermal phase transition at $T = 1.53\,\mathrm{K}$ coincide quantitatively. Only the data above the phase transition display a smaller specific heat in our study. This discrepancy may be related to account of the addenda, since the heat capacity of any setup typically increases with T^3. In the heat pulse technique of Ref. [43] based on Ref. [94], the addenda is quite extensive and the corresponding subtraction not described, making an assessment difficult.
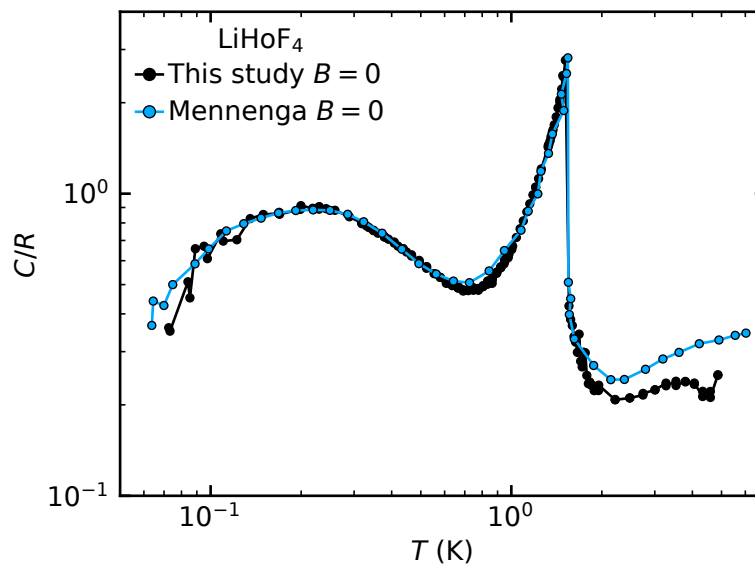
Figure 3.4.1.: Comparison of zero-field heat capacity data with the data reported by Mennenga *et al.* [43].
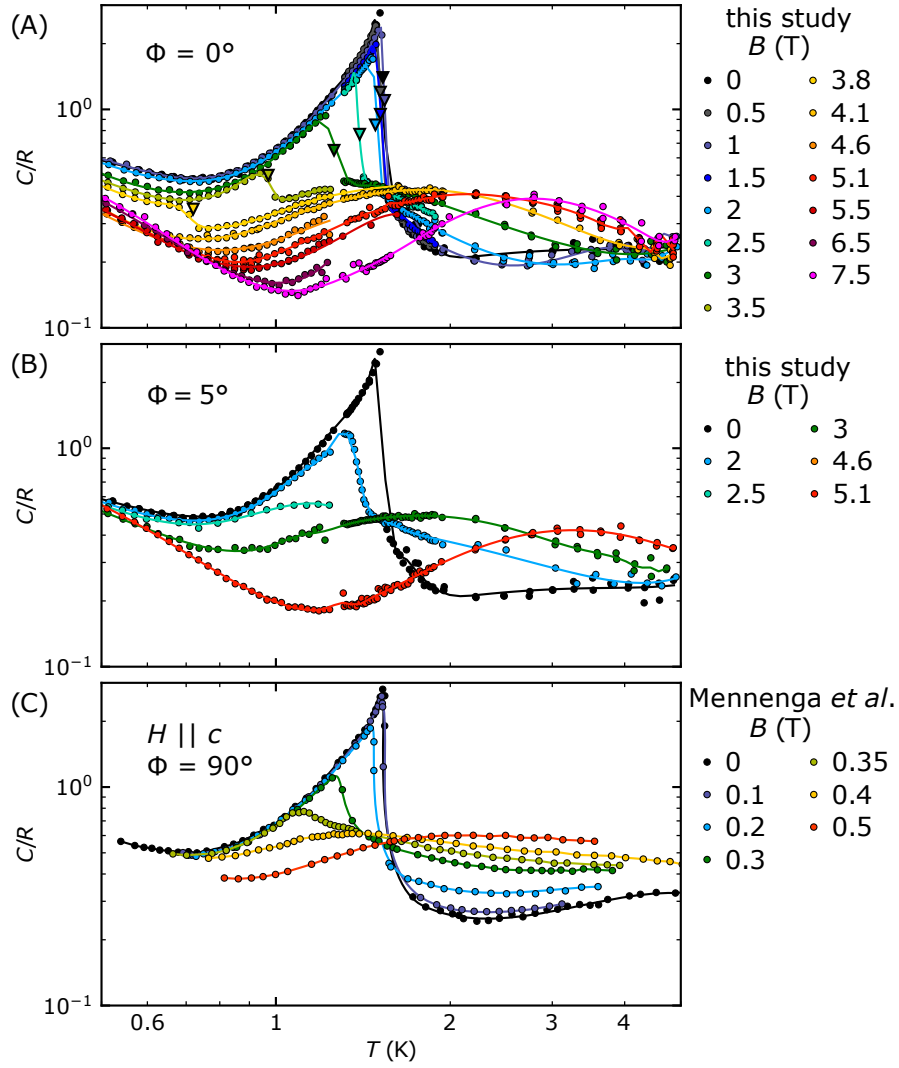
Figure 3.4.2.: The evolution of the shape of the heat capacity around the phase transition for varying field and various field angles. (A) Experimental results for $\Phi = 0°$. (B) Experimental results for $\Phi = 5°$. (C) Results from Ref. [43] with magnetic field applied parallel to the easy axis ($\Phi = 90°$).

Mennenga *et al.* furthermore recorded data applying the magnetic field parallel to the *c*-axis of their spherical LiHoF$_4$ sample, cf. Fig. 3.4.2 (C). They oriented the sample by applying a magnetic field at $T = 4.2$ K, leading to a rotation of the sample due to the Ising anisotropy [43]. Comparing the longitudinal data reported by Mennenga *et al.* , shown in Fig. 3.4.2 (C), with our results obtained under transverse magnetic field (A and B) one finds a very similar qualitative evolution of the curve shape around the phase transition. In both cases, the low-temperature side slope of the peak is independent of field and the drop marking the phase transition occurs at a lower temperature with increasing field. However, while Mennenga's data appear almost field independent for $T < 1$ K, our results show pronounced changes. Furthermore, the phase transition is also visible here as a drop, which appears sharper between 1 and 1.3 K, cf. 3, 3.5 T in (A) vs. 0.3, 0.35 T in (C).

The total field values that are necessary to suppress the transition are a factor of ≈ 10 smaller under longitudinal fields as compared to the transverse fields. A direct comparison of the phase boundary inferred from the transition temperatures is shown in Fig. 3.4.3 in good agreement with our results from transverse susceptibility measurements.

Phase Diagram from Different Methods Fig. 3.4.3 shows a comparison of the phase boundaries obtained by various methods and at various angles. The results inferred from the transverse susceptibility are shown as circles and for angles of $\Phi = 0, 1, 5, 10°$. In direct comparison are the results inferred from the heat capacity measurements shown as squares. Both methods observed the same phase boundary. At low temperatures the boundary could not be determined in the specific heat, since it is too flat with respect to temperature scans performed during heat capacity measurements. The points at the lowest temperatures for their respective angle, for $\Phi = 0°$ at 0.2 K and $\Phi = 5°$ at 1.4 K, show a lower critical field as expected in the susceptibility. This may be an indication for a slight misalignment of the sample not affecting the comparison with theory.

At low temperature, the magnetocaloric sweeps were used to determine the phase boundary and they are in agreement with the results obtained by the AC susceptibility measurements. No MC sweeps were recorded at larger angles and only data for $\Phi = 0°$ and 1° are available. As another direct comparison, the results of Mennenga *et al.* [43] obtained from specific heat and Bitko *et al.* [12] obtained from AC susceptibility are depicted as "+"- and "x"-symbols respectively. The transverse susceptibility results of Bitko are in good agreement with our results for $\Phi = 0$. The longitudinal heat capacity results of Mennenga
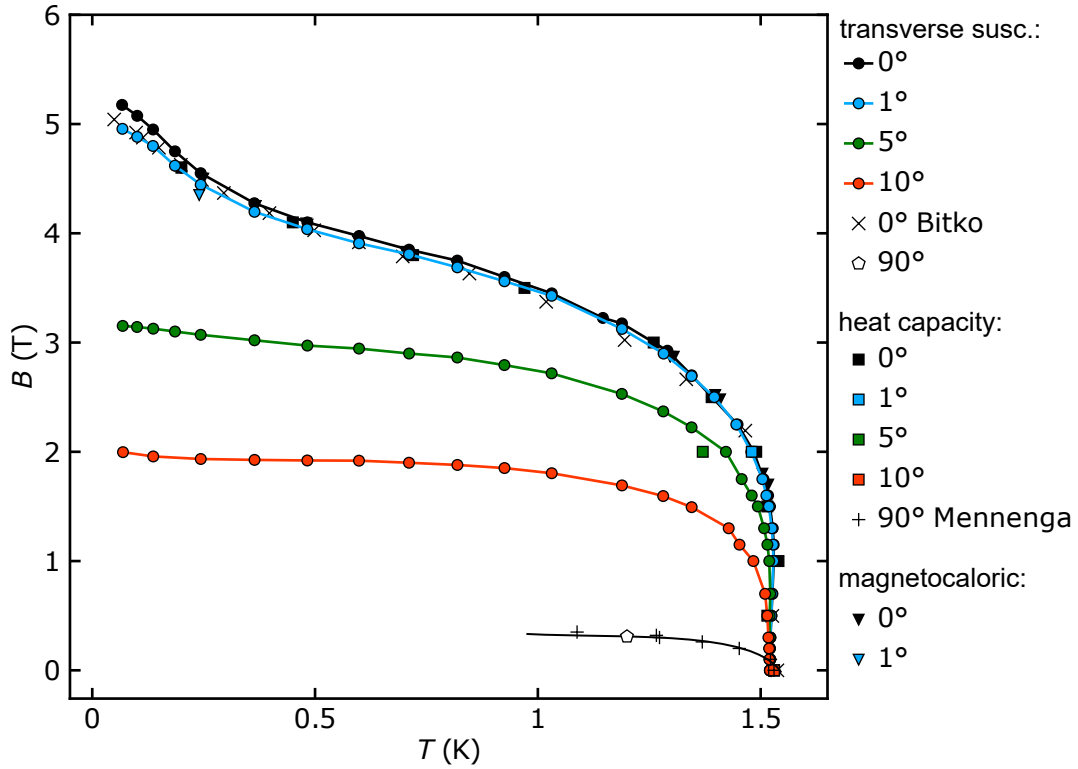
Figure 3.4.3.: The magnetic phase boundary for various angles Φ obtained from different methods. Results from transverse susceptibility (∘) are taken from Cha. 2. One scan of the transverse susceptibility at $\Phi = 90°$ only provided one point and is therefore shown separately. The results of Bitko *et al.* [12] (x) are provided as comparison. The experimental results of the heat capacity (□) are compared to the study by Mennenga *et al.* [43] (+), who measured with field applied along the easy axis. The experimental results of the magnetocaloric sweeps (∇) compare well with the other methods. Lines are guides to the eye.

are consistent with our findings of the AC susceptibility measured under $\Phi = 90°$. This shows that the phase diagram evolves smoothly from the transverse to the longitudinal configuration confirming that the domain-driven phase transition connects to the coercive field.
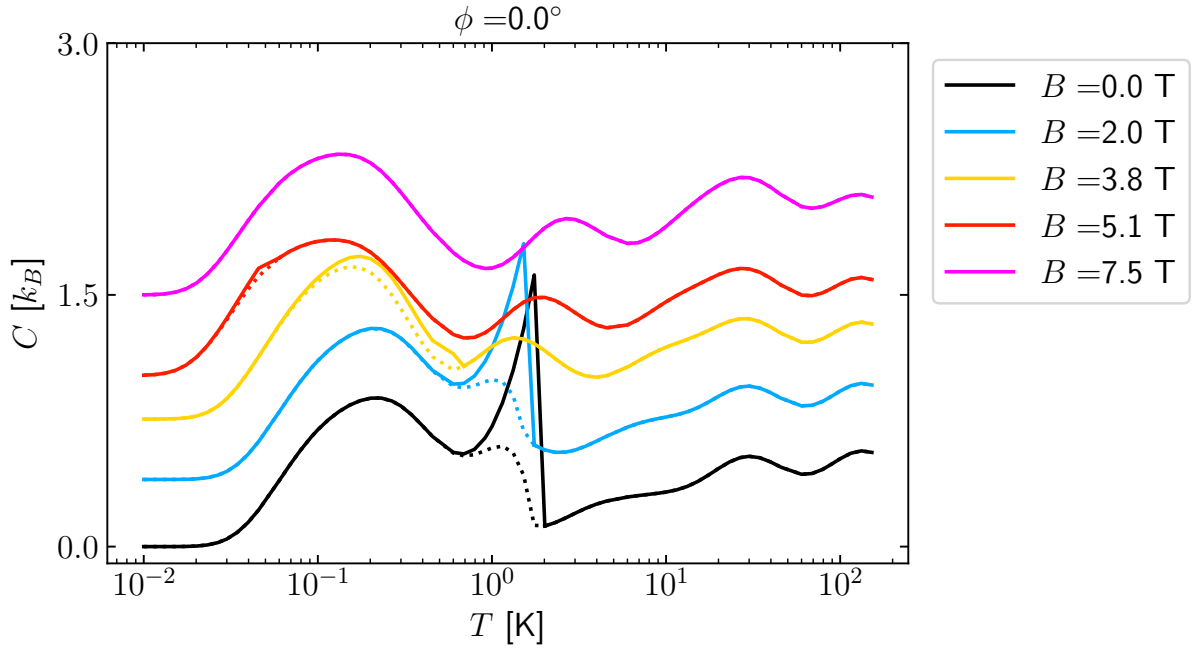
Figure 3.4.4.: Theoretical prediction of the specific heat of LiHoF$_4$ in units of k_B. The curves are shifted proportional to the magnetic field for better visibility. Figure taken from [5].

Theoretical Results of the Specific Heat   After this comparison with other results, follows a direct comparison with the theory presented in Sec. 2.4. The theoretical model described in Sec. 2.4.2 permits to calculate the specific heat and entropy. Three contributions enter the calculated heat capacity. The occupation of the energy levels is temperature dependent and leads to the well known formula $C_0 = k_B \beta^2 (\langle E^2 \rangle - \langle E \rangle^2)$ of the heat capacity for a simple temperature independent Hamiltonian [5]. Furthermore, the energy levels themselves are temperature dependent due to the mean fields. The corresponding terms were evaluated by H. Eisenlohr in terms of derivatives of the form $\langle E \cdot \delta_T E \rangle - \langle E \rangle \langle \delta_T \rangle$ and $\langle \delta_T^2 E \rangle$ [5]. In addition, also the domain ratio $v(T)$ is temperature dependent. If the up- and down-domain have different free energies, a shift in the domain pattern will also lead to an energy change.

The results of this calculation are shown in Fig. 3.4.4 over the temperature range of 10 mk to 150 K. With increasing temperature, a broad peak is observed around 100-200 mK, which may be identified as the hyperfine peak stemming from the contribution of nuclear excitations. Its maximum shifts as a function of magnetic field, reaching a minimum at $B = 5.1$ T. This is consistent with the picture of the nuclear modes closing the gap at the quantum phase transition at $B \approx 5.1$ T. At higher temperatures $T > 5$ K, above the
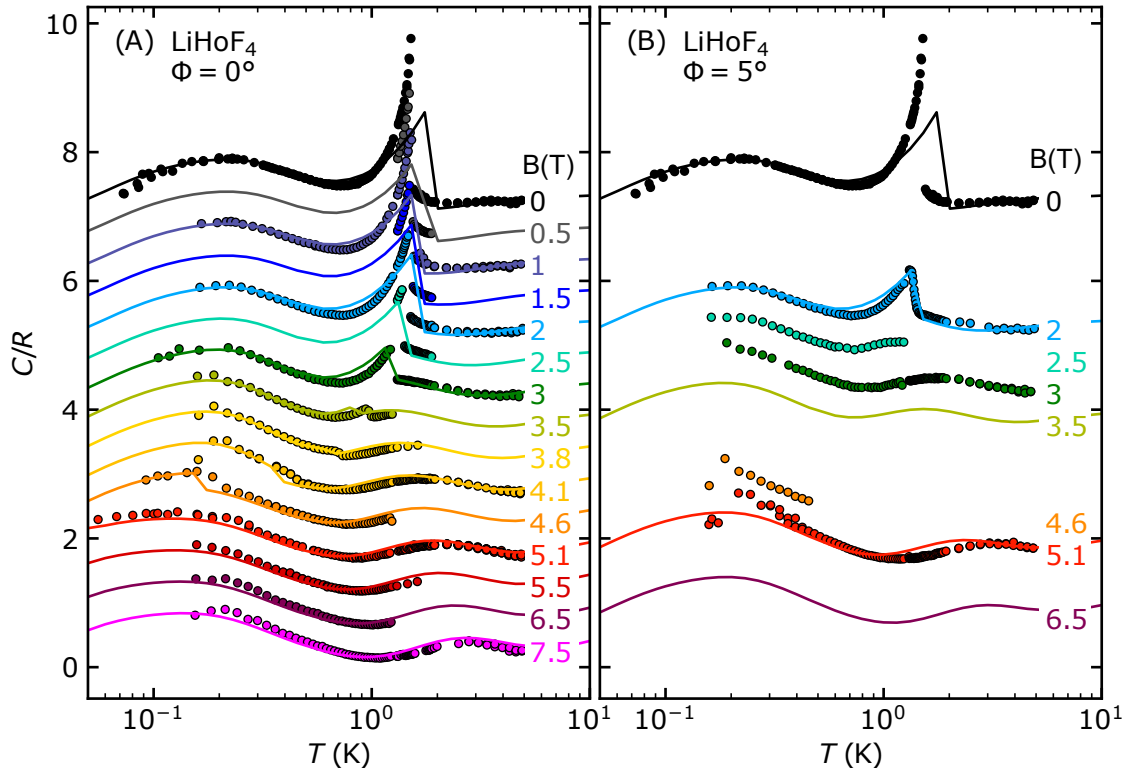
Figure 3.4.5.: Comparison of the specific heat results from heat capacity measurements (points) and the theory (lines). (A) Results for $\Phi = 0°$ at various magnetic fields. (B) Results for $\Phi = 5°$. The datasets were shifted by $C/R = 0.5$ each for clarity.

range of measured data, several flat peaks may be discerned that correspond to crystal field levels at higher energies. The corresponding crystal field spectrum may be seen in Fig. 1.2.1. Another maximum is located at 1-2 K, which is the most prominent feature of the heat capacity data, resembling the anomaly at the phase transition. It is visible in the calculations for $0\,\text{T}$ and $2\,\text{T}$ and then replaced at larger fields with a broad maximum that shifts to larger temperatures with increasing fields. The dotted lines mark the results for C_0, if the temperature dependent energy level and domain ratio terms are neglected. As it may be seen, in this case, the sharp peaks at the phase transition disappear.

The results of these theoretical calculations may be compared with the data in Fig. 3.4.5. Fig. 3.4.5 (A) shows the results for $\Phi = 0°$, where good agreement between experiment and theory both qualitatively and quantitatively is observed. The height and location of the hyperfine peak as well as its shift to lower temperatures at $5.1\,\text{T}$ are in remarkable agreement. Also the development of the broad maximum from the thermal phase transition matches the experimental observations well.

The thermal transition itself however differs between experiment and theory, as observed in the transverse susceptibility. Within the model, the peak position is located at slightly larger temperatures for low fields, as the mean-field modeling over-estimates the stability of the ordered phase. Furthermore, the anomaly is not as high in the theory as critical fluctuations are not included in the theory. At fields, $B > 2\,\mathrm{T}$, the maximum and location match better.

In Fig. 3.4.5 (B) with results for $\Phi = 5°$, only some of the calculations were performed at parameters matching the data [5]. In the case of comparable parameters however, good agreement is observed. Especially the thermal phase transition at $B = 2\,\mathrm{T}$ (blue) matches the experiment both in terms of height and location. This parameter set is especially important, since Ref. [5] does not find the transition at $B = 2\,\mathrm{T}$ and $\Phi = 5°$, when a model without domains is investigated, further emphasizing the importance of magnetic domains in this system. The anomalously large heat capacity observed at the hyperfine peak of the $B = 5\,\mathrm{T}$, $\Phi = 5°$ data-set (red) is not accounted for in the theory. The calculations do find, however, that the hyperfine peak shifts to lower temperatures, at the domain driven quantum phase transition at $B \approx 3\,\mathrm{T}$.

Another depiction of this behavior may be found in Fig. 3.4.6, where the experimental results and the theoretical calculations of the specific heat C/R for $\Phi = 0°$ are shown as colormaps. Fig. 3.4.6 (A) shows the positions of the measured data points in B-T-space as black dots. The color map shows a cubic interpolation on a triangular grid between these points. Using the same interpolation scheme, the model is shown in Fig. 3.4.6 (B). Both panels also show the phase boundary as a black line, with the exact position of the phase transition observed in the measurements highlighted with black triangles.

Several features may be discerned in this representation. First, the position of the hyperfine peak resides at the lowest temperature in the field range of the quantum phase transition. This is consistent with the expected mode softening around the QCP. Second, the peak of the thermal phase transition does not shift, but is cut off at T_c. Its falling flank is independent of temperature. Furthermore, another peak develops from underneath the thermal phase transition peak and shifts towards higher temperatures with increasing field. This is visible as the green band in the high-T and high-B region of the graphs and may be explained in terms of the Zeeman splitting of the crystal fields.
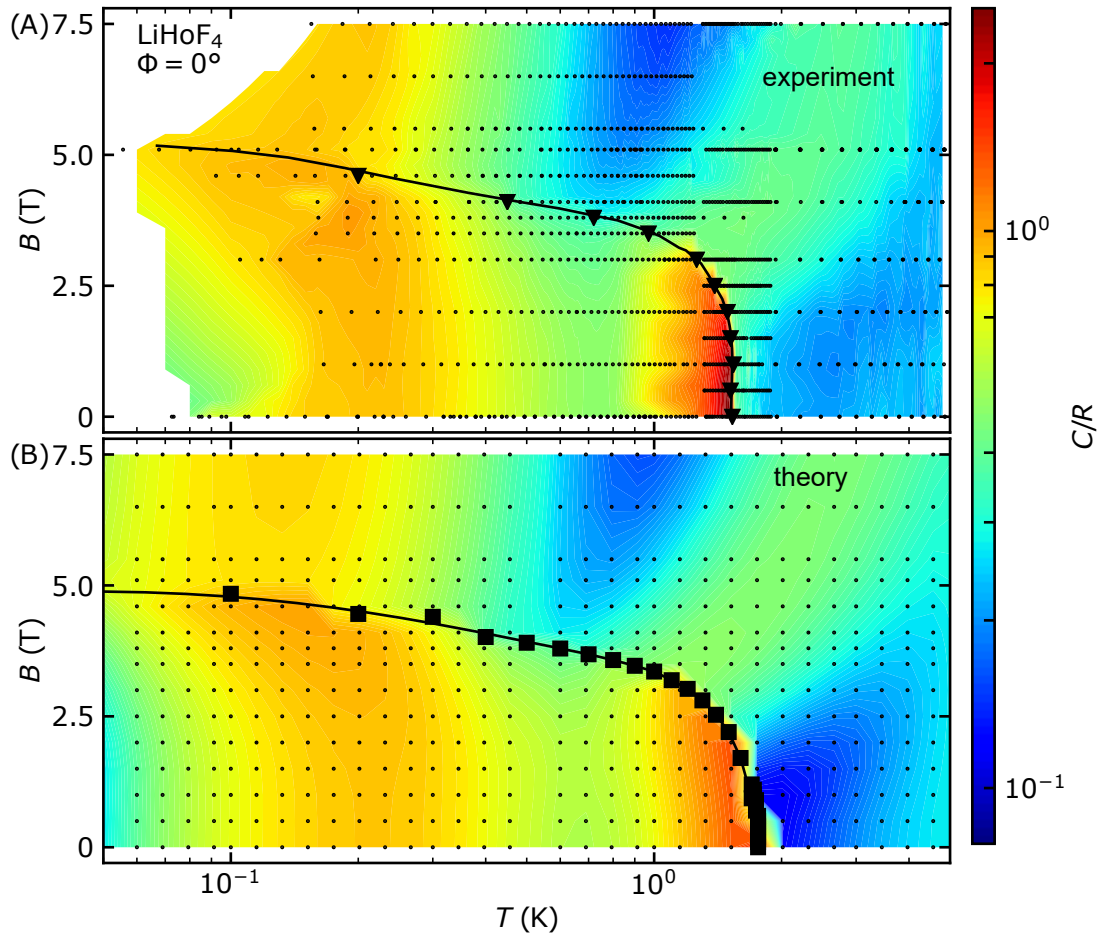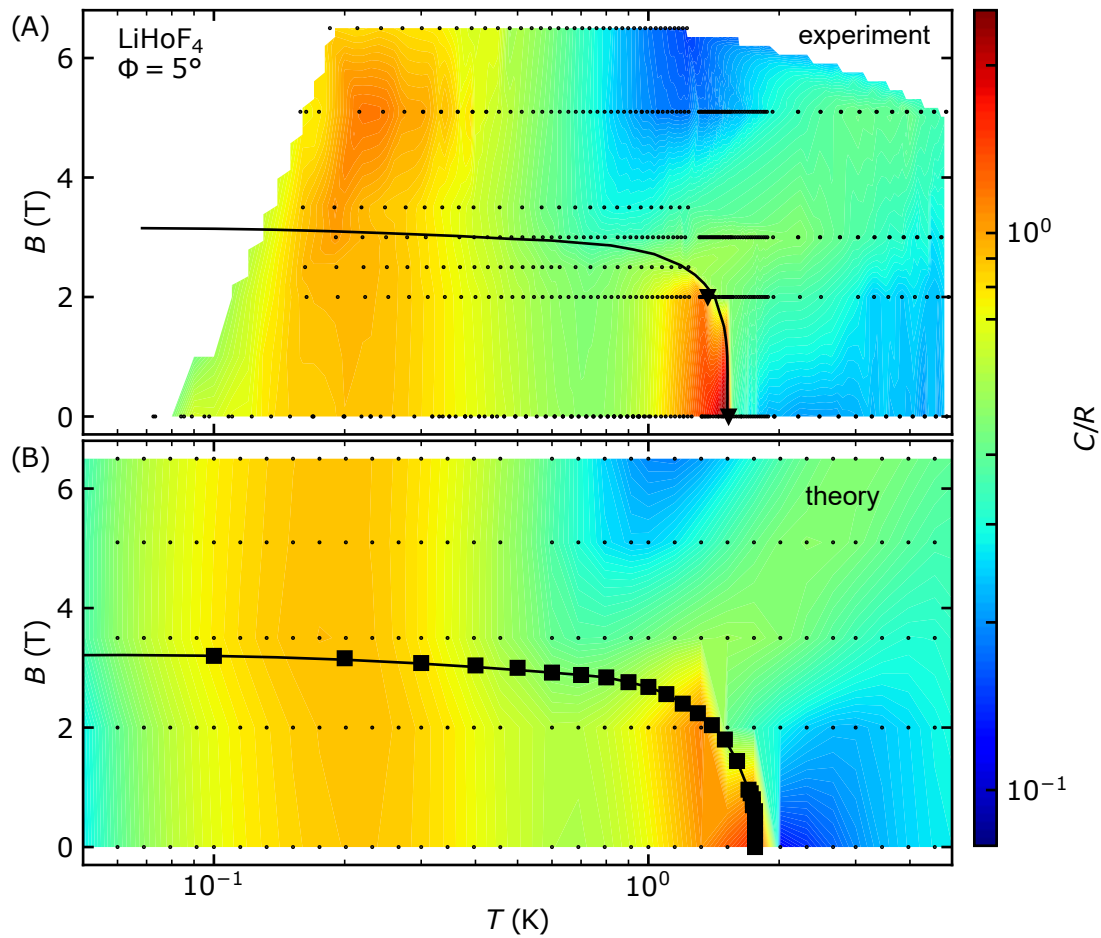
Figure 3.4.6.: Colormaps of the specific heat C/R measured experimentally and calculated theoretically as a function of magnetic field B and temperature T for a perfect alignment of $\Phi = 0°$. (A) The color map of the experimental data was created using a cubic grid interpolation. Positions of data-points used for the interpolation are marked as dots. The black line represents the experimental phase boundary inferred from the transverse susceptibility, cf. Sec. 2.3.1. The phase boundary inferred from the experimental results of the specific heat as shown in Fig. 3.3.2 is depicted as triangles. (B) Color map of the theoretically calculated specific heat. Dots represent the calculated datapoints used for the cubic grid interpolation. The phase boundary inferred from theoretical calculations of the transverse susceptibility, cf. Sec. 2.4.2, depicted as squares. The line is a guide to the eye.

Figure 3.4.7.: Colormaps of the specific heat C/R measured experimentally and calculated theoretically as a function of magnetic field B and temperature T for a perfect alignment of $\Phi = 5°$. (A) The color map of the experimental data was created using a cubic grid interpolation. Positions of data-points used for the interpolation are marked as dots. The black line represents the experimental phase boundary inferred from the transverse susceptibility, cf. Sec. 2.3.1. The phase boundary inferred from the experimental results of the specific heat as shown in Fig. 3.3.3 is depicted as triangles. (B) Color map of the theoretically calculated specific heat. Dots represent the calculated datapoints used for the cubic grid interpolation. The phase boundary inferred from theoretical calculations of the transverse susceptibility, cf. Sec. 2.4.2, depicted as squares. The line is a guide to the eye.
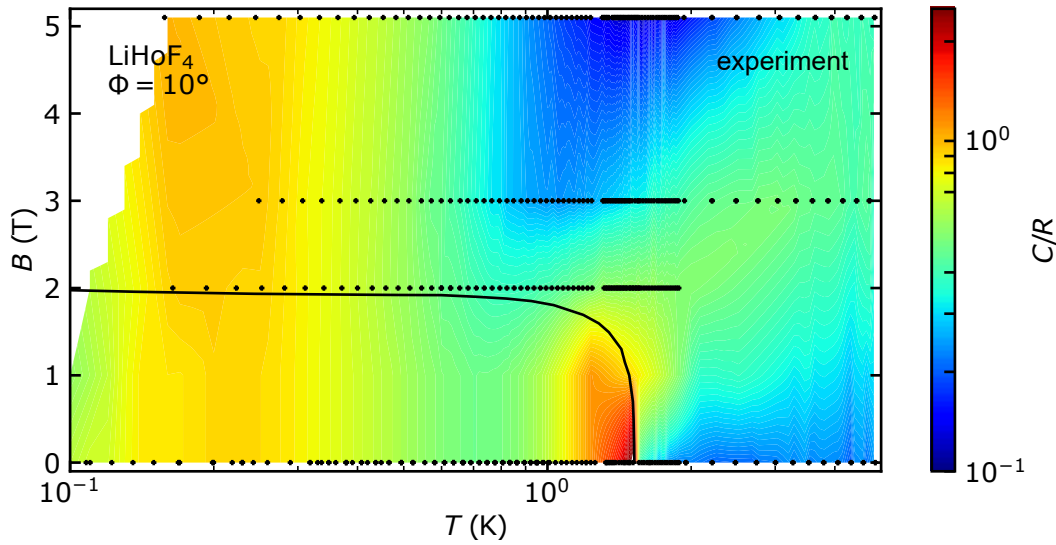
Figure 3.4.8.: Colormap of the experimental specific heat C/R as a function of magnetic field B and temperature T for an angle of $\Phi = 10°$. Positions of data-points used for the interpolation are marked as dots. The location of the phase transition determined by AC susceptibility is shown as a black line.

Looking at the same representation for $\Phi = 5°$ in Fig. 3.4.7, the same features may be observed. The measurements, cf. Fig. 3.4.7 (A), do not reach low enough temperatures to observe the minimum of the hyperfine peak at the domain driven phase transition, as it is predicted in the theory. Here, theory predicts that this dip is weaker as compared to $\Phi = 0°$, cf. Fig. 3.4.7 (B). Again, the evolution of the high-T, high-B peak is tracked both in the experimental data and calculation.

An interpolation of the experimental data at $\Phi = 10°$ is shown in Fig. 3.4.8. Unfortunately no calculations were performed for this angle. The hyperfine peak is now independent of B. No significant changes of its position are observed around the domain driven phase transition, marked by the black line in Fig. 3.4.8, which represents the phase boundary determined by AC susceptibility. At $\Phi = 10°$, the peak, which emanates from the thermal phase transition with increasing field shifts to higher temperatures faster as compared to $\Phi = 0°$ and $5°$.

While the theory [5] covers the contribution at high temperatures accurately on a quantitative level, a simple model is helpful to highlight the underlying physics in a more

approachable way. One of the simplest accounts for peaks in the heat capacity is a simple two level model

$$C/R \propto (\Delta/T)^2 \frac{e^{\Delta/T}}{1 + e^{\Delta/T}}, \tag{3.4.1}$$

where Δ is the energy gap between the two levels. This simple model was fitted to the peak evolving from the thermal phase transition, as shown in Fig. 3.4.9. Each panel shows the data for one field angle $\Phi = 0, 5, 10°$. The data points, which contribute to the fit are highlighted as circles, while the other data are depicted by smaller rectangles. Since the peak is visible above the thermal phase transition, only fields above $B = 3, 2.5, 2\,\text{T}$ were investigated for $\Phi = 0, 5, 10°$, respectively, and only data above the transition temperature were considered. The fits are shown as lines. The peak shifts towards higher temperatures with increasing field. The increase is faster at larger field angles. This behavior is also shown in Fig. 3.4.10, where the energy gap Δ of the two level model is shown as a function of magnetic field B. Thus the peak may be attributed to the two lowest lying crystalline electric field (CEF) levels, cf. Fig. 1.2.1 (B), whose splitting is shown as a dotted line. The agreement between the fit results for $\Phi = 0°$ and the CEF splitting is very good, emphasizing that the single ion effects set an important energy scale in the paramagnetic phase. Within the ferromagnetic phase however the peak is not visible, suggesting that the spin degrees of freedom and their ordering are the dominant scale.

The accelerated shifting of the peak for $\Phi = 5°$ and $10°$ shown in Fig. 3.4.10, suggests that the tilted magnetic field does not only control the magnetic domain formation, but also the crystalline electric fields. The theoretical calculations also display a stronger field dependence of Δ for the case of tilted fields $\Phi = 10°$, cf. Fig. 3.4.10. The theory based on the crystal field parameters from Ref. [41] expects a flatter dependency when compared to the experiment [5]. Further investigation is necessary to determine if subtle changes in the crystal field environment can explain this behavior. Nonetheless, this highlights, why the model presented in Sec. 2.4.2 is so important, incorporating the full CEF Hamiltonian and properly treating tilted field angles.

In addition, the hyperfine peak is also dependent on the magnetic field for small field angles. Interestingly, the effect becomes less pronounced, with increasing field angle. This emphasizes the relevance of the interaction between nuclear and electron spins included in the model. As explained in Sec. 2.4.2, the non-Kramers doublet CEF states of the Ho ions display an interesting interplay with the hyperfine coupling. The non-Kramers nature leads to a minimum of $|J|$ near B_c. Since the hyperfine interactions favor large
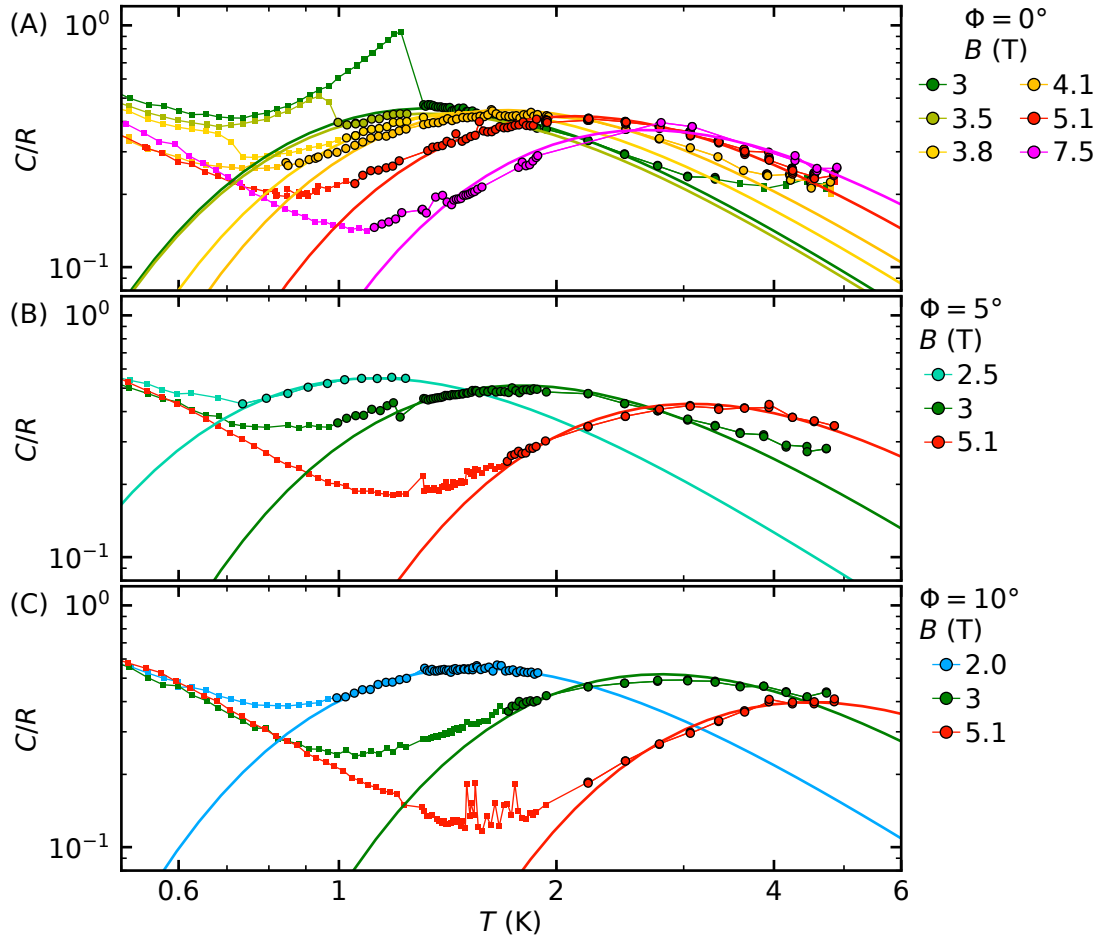
Figure 3.4.9.: The evolution and fit of the specific heat peak above 1 K for various fields and field angles. (A) Experimental data of the specific heat as a function of temperature for $\Phi = 0$. Lines represent fits to the data in the form of a simple two level model Eq. (3.4.1). Data points that contribute to the fit are highlighted as larger circles. (B) Experimental results for C/R and corresponding fits for $\Phi = 5°$. (C) Results and fits for $\Phi = 10°$.
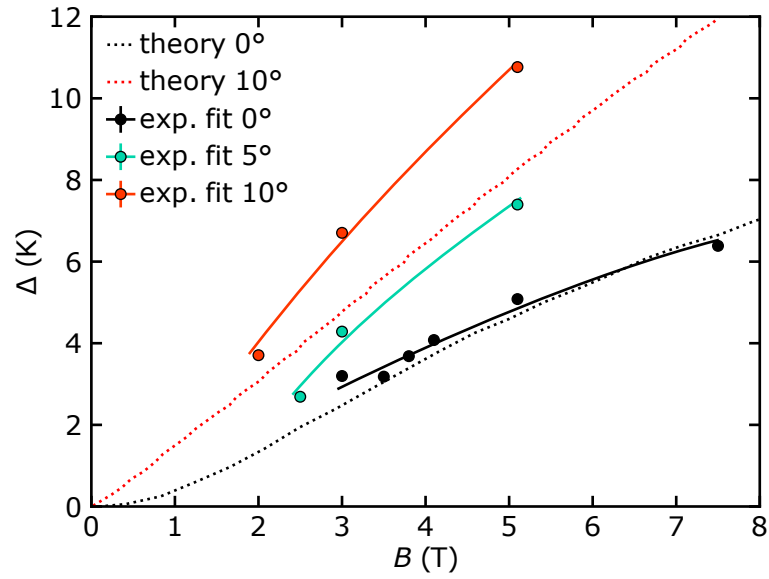
Figure 3.4.10.: The energy gap Δ of the two level model as a function of field for $\Phi = 0, 5, 10 \deg$. Solid lines represent guides to the eye. For comparison, the splitting of the two lowest CEF levels are shown as a dotted line for $\Phi = 0$ and $10°$. The theoretical line for $\Phi = 0$ corresponds to the line in Fig. 1.2.1 (B2).

moments $|J|$ they stabilize the ferromagnetic phase, increasing B_c for small field angles. As Φ increases, the minimum in $|J|$ becomes less pronounced and the effect vanishes.
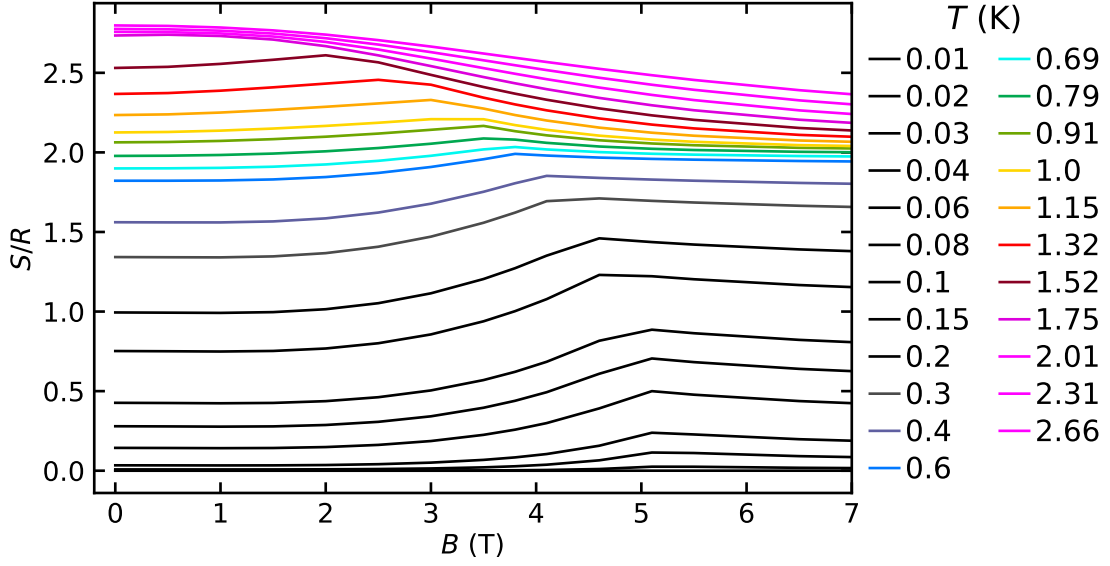
Figure 3.4.11.: Theoretical calculations of the specific entropy S/R of LiHoF$_4$ as a function of magnetic field B at various temperatures. Values are taken from calculations by H. Eisenlohr [5].

Theory of Magneto-Caloric Sweeps Comparing the specific heat results to the literature and theory, the results of the magneto-caloric sweeps will now be addressed as compared to the theoretical model describe above. It allows to calculate the free energy of the system [5]. Starting from the free energy the entropy may be calculated as

$$S = -\frac{\delta F}{\delta T} \approx -\frac{F(T + \Delta T) - F(T)}{\Delta T}, \tag{3.4.2}$$

where in a numeric evaluation with $\Delta T = 10^{-3}$ K was chosen. Ref. [5] then proceeded to calculate the derivative with respect to field as

$$\frac{\delta S}{\delta B} \approx \frac{F(T + \Delta T, B + \Delta B) - F(T + \Delta T, B) - F(T, B + \Delta B) + F(T, B)}{\Delta T \cdot \Delta B}, \tag{3.4.3}$$

with $\Delta T = 10^{-3}$ K and $\Delta B = 5 \cdot 10^{-5}$ T.

The results of the specific entropy S/R are shown in Fig. 3.4.11 as a function of magnetic field for various temperatures between $10\,\text{mK}$ and $2.66\,\text{K}$. At the lowest temperature, the entropy is close to zero as expected and increases with temperature. In addition, the entropy also increases with magnetic field and develops a maximum at the critical field $B_c = 5.1\,\text{T}$, which shifts to lower fields with increasing temperature. This peak disappears above the critical temperature. To compare these results to the measurements, the entropy
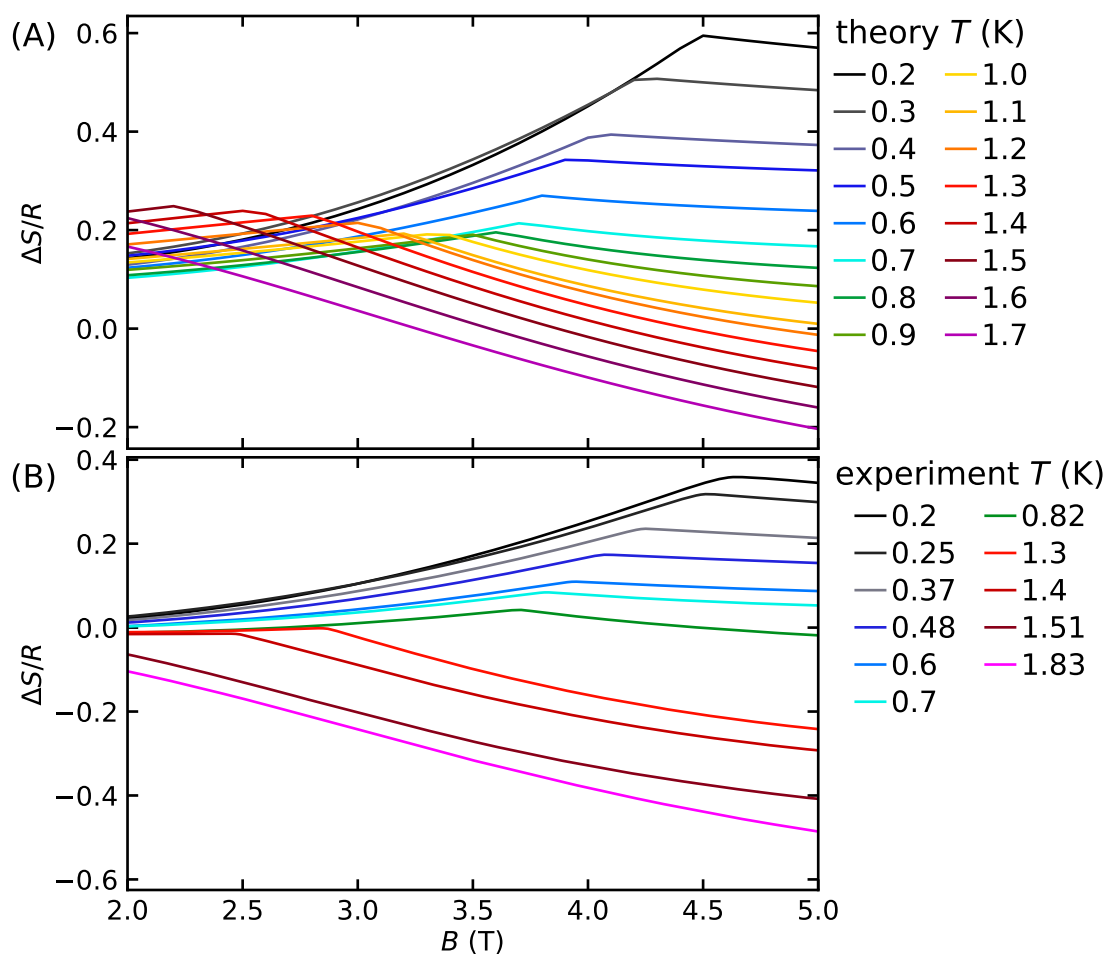
Figure 3.4.12.: The change of the specific entropy $\Delta S/R = S(B)/R - S(B = 0\,\mathrm{T})/R$ of LiHoF$_4$ as a function of the magnetic field B at various temperatures. (A) Results of the theoretical calculations performed by H. Eisenlohr [5]. (B) Experimental data.

change with field $\Delta S/R = S(B)/R - S(B = 0\,\mathrm{T})/R$ needs to be investigated, since the magneto-caloric sweeps can only measure $\delta S/\delta B/R$, and thus ΔS after integration.

Therefore, the entropy was evaluated numerically in detail around the phase transition. Subtracting the zero field values, Fig. 3.4.12 is obtained. Fig. 3.4.12 (A) shows $\Delta S/R$ from the theoretical calculations and Fig. 3.4.12 (B) shows the mean of up and down sweeps from Fig. 3.3.7. Both data and theory show the same general behavior, with a steady increase up until the maximum at the phase transition. The theory however predicts a maximum 50% larger than experiment. Furthermore, in the experimental data the height of the maximum decreases steadily with increasing temperature. In the theory however, the peak value is minimal around $0.8\,\mathrm{K}$, where also the specific heat has its local minimum, and increases again towards higher temperatures. In addition, a decrease at larger fields
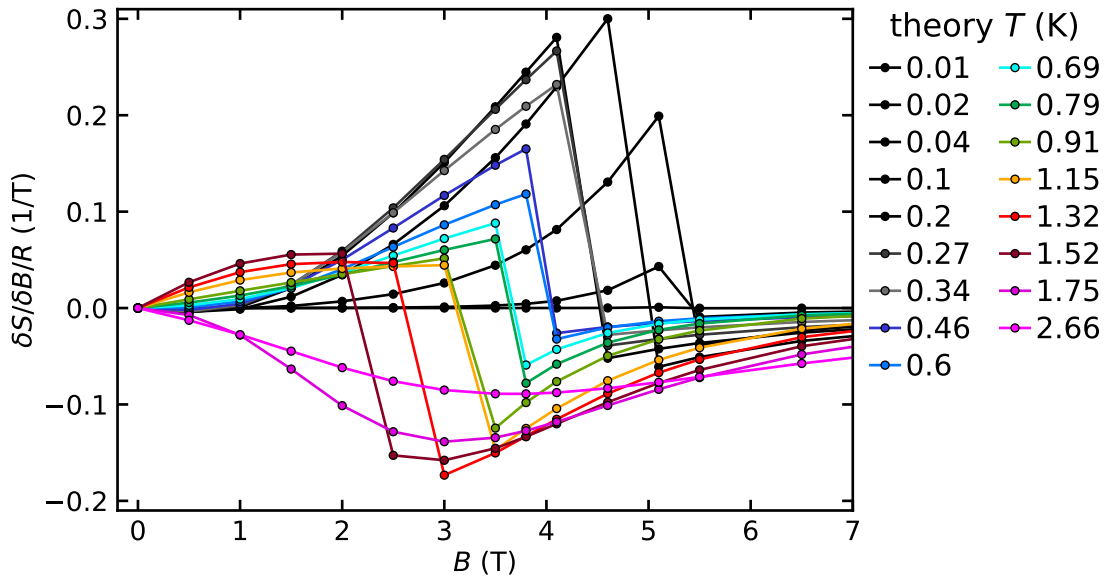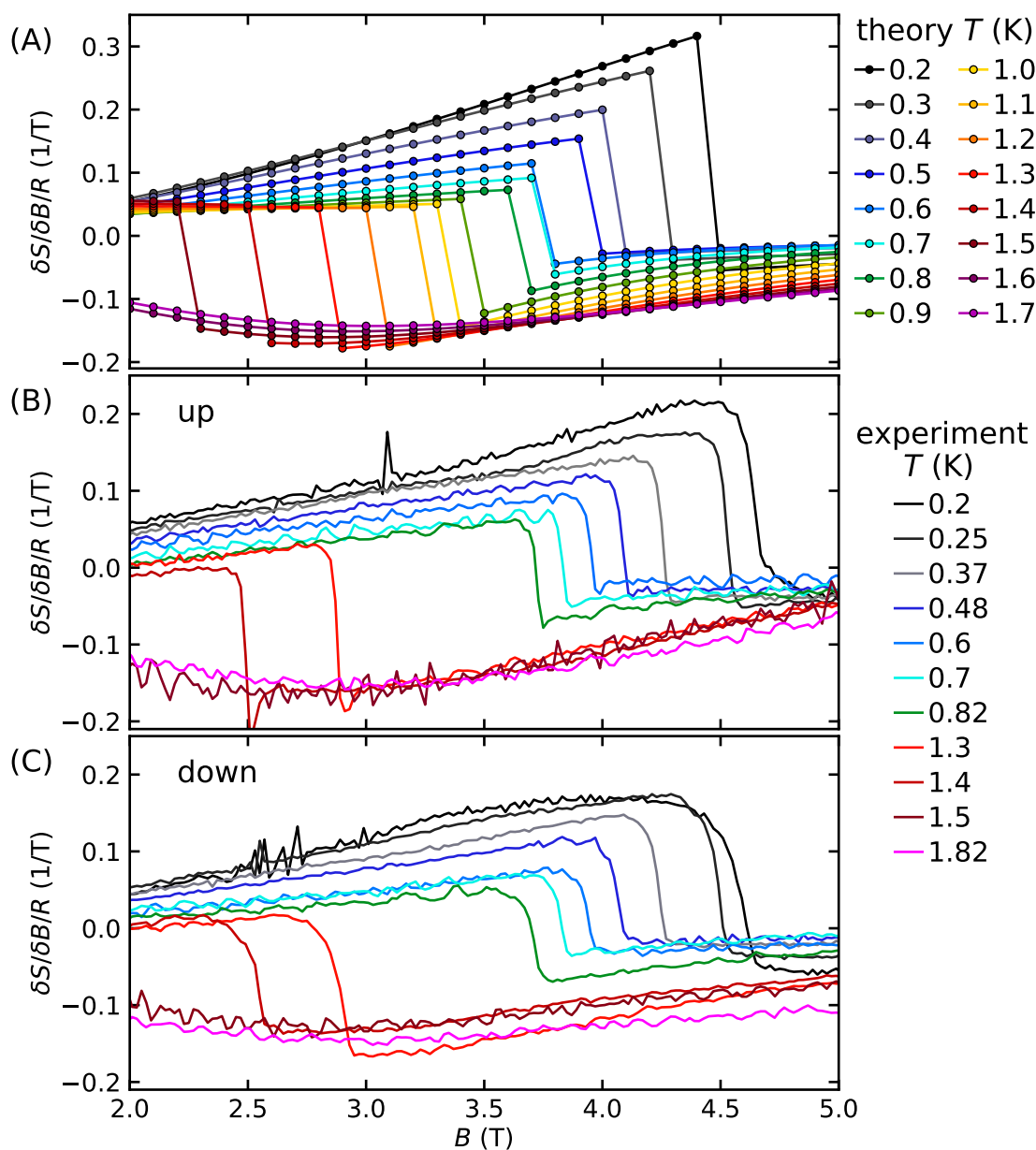
Figure 3.4.13.: Derivative of the specific entropy with respect to magnetic field $\delta S/\delta B/R$ of LiHoF$_4$ as a function of the magnetic field B at various temperatures. Values are taken from calculations performed by H. Eisenlohr [5].

is expected in shape and magnitude and the difference between $0.2\,\mathrm{K}$ and $1.5\,\mathrm{K}$ at the larges field of $B = 5\,\mathrm{T}$ is similar in both theory and experiment.

As the next step, the derivative $\delta S/\delta B/R$ was calculated according to Eq. (3.4.3) and plotted in Fig. 3.4.13. As may be seen, the derivative is zero at the lowest temperature of $10\,\mathrm{mK}$. With increasing temperature, a sharp maximum with a rapid drop develops around the critical field B_c. This maximum is largest for $0.1\,\mathrm{K}$ and decreases with temperature to reach a minimum at $1.15\,\mathrm{K}$. Similarly, the jump height is minimal at $1.15\,\mathrm{K}$. The jump disappears above the thermal phase transition where it merges into a broad minimum.

To explain the behavior around the critical field in further detail, $\delta S/\delta B/R$ was calculated with a smaller step size between 2 and $5\,\mathrm{T}$ for temperatures between $0.2\,\mathrm{K}$ and $1.7\,\mathrm{K}$. The results ares shown in Fig. 3.4.14 (A). For comparison the experimental results are displayed in Fig. 3.4.14 (B) and (C) for the up- and down-sweep, respectively. Again, the absolute values are approximately 50% larger in the calculation, as compared to experiment. The location and relative height of the maximum at the phase transition as well as the shape of the curves in the paramagnetic regime agrees very well. The drop is sharper in the calculation, which is likely due to the fact, that the heat capacity effects and sample inhomogeneities smear out the transition in the experiment.

Figure 3.4.14.: Derivative of the specific entropy with respect to magnetic field $\delta S/\delta B/R$ of LiHoF$_4$ as a function of the magnetic field B at various temperatures in the vicinity of the field driven phase transition. (A) Results of the theoretical calculations by H. Eisenlohr [5]. (B) Experimental data obtained from the up-sweep. (C) Experimental results from the down-sweep.

When comparing up- and down-sweep, the up-sweeps seem to represent the calculation better. Likely reasons for this behavior may be the imperfect thermalization of the sample when switching from up to down sweep. In the experiments, this effect was counteracted by giving the sample time to equilibrate between both sweeps. Another option is that the numeric process of correcting the effects of sample heat capacity did not work as well for the down sweeps as the features appear more rounded. While the reason for such a behavior is unclear, it is possible that the tiny effects of hysteresis observed in the AC susceptibility play also a role here. Such effects would not be visible in the heat capacity data, since they were measured in temperature sweeps. Thus the correction method cannot take them into account.

3.5. Conclusions

In this section, we have described the development of a new experiemental setup that allows measurements of the specific heat and magnetocaloric effect at mK-temperatures on a LiHoF$_4$ sample with large magnetic anisotropy. For the first time, measurements under transverse field and as a function of field angle were conducted.

Several findings can be concluded from these measurements and their comparison to the theory. The first and most important observation is that the model for a mesoscale quantum phase transition introduced in Sec. 2.4.2 qualitatively accounts for the caloric properties determined in this chapter. Moreover, the quantitative agreement is excellent as well, apart from a linear offsets in $\delta S / \delta B / R$, resulting from critical fluctuations which are neglected in the theory at this point. This proves, that the model introduced based on the AC susceptibility describes the energy landscape of LiHoF$_4$ very well, validating the ansatz of magnetic domains and the corresponding minimization of the domain wall energy.

These measurements furthermore allow a direct observation of the mode softening around the QCP at $B = 5.1\,\mathrm{T}$, as the specific heat is very high even at lowest temperatures $T < 60\,\mathrm{mK}$. The calculations suggest, that this softening is also present in a less pronounced fashion even if the field is applied at an angle of $\Phi = 5°$. This supports the notion of a new kind of quantum phase transition, associated with mesoscale magnetic domains only. Unfortunately, at $\Phi > 0°$ it was not possible to collect data down to sufficiently low temperatures of $T < 100\,\mathrm{mK}$, to fully verify this observation as shown in Fig. 3.4.7.

Measurements of the specific heat, magnetocaloric effect and AC susceptibility in combination with the theory show that the mesoscale quantum phase transitions play a key role to understanding the LiHoF$_4$ system, especially for $\Phi \neq 0$. The strong sensitivity to changes of the field angle is visible in the jump of the transverse susceptibility and shift of the critical field B_c and can only be explained by including magnetic domains. Similarly, the evolution of the anomaly at the thermal phase transition with magnetic field for finite Φ is better explained by the full mesoscale model [5]. Moreover, the methods combined establish for $\Phi = 0$ a transverse field QPT with mean field character due to the long-range dipolar interactions. The critical exponents for this transition are $\alpha = 0$ describing the jump of the heat capacity when crossing the transition by increasing the magnetic field, cf. Fig. 3.4.6, $\beta = 1/2$ describing the vanishing of the longitudinal magnetization, which is

the order parameter in this case, cf. Fig. 2.4.5 (A1) and $\gamma = 1$ as established in Sec. 2.3.3. For $\Phi > 0$ however our studies showed that the continuous suppression of the minority domains drives the mesoscale QPT. Here we find again $\alpha = 0$ due to the jump of the heat capacity, $\beta = 1$ due to the linear behavior of the domain ratio v at the transition and $\gamma = 0$ due to the flat order susceptibility approaching the jump of the AC susceptibility [5].

Future measurements might be conducted to focus on this regime as well as to reproduce the increase in heat capacity C and reduction of the thermal conductance k_s of the sample around $T = 200\,\text{mK}$, $B = 5.1\,\text{T}$ and $\Phi = 5°$. Such measurements could be accompanied by direct measurements of the thermal conductivity of LiHoF_4 under the same conditions.

In addition, spectroscopic measurements of the critical modes using neutron TAS [131, 132] should be conducted, since new insights were gained since the experiments by Rønnov and Krämer *et al.* [13, 14, 66]. Our studies emphasize the importance of the sample alignment with respect to the magnetic field. Additional studies under varying field angle promise to shed new light on these results and the importance of either domain driven mesoscale QPT or transverse-field QPT. Furthermore, MIEZE spectroscopy [75, 133–135] might be employed to analyze the very low energy excitations around the QCP. These promise additional information as a function of wave vector adding to the studies of McKenzie, Stamp and Libersky *et al.* [42, 67].

Another direction of future research are fluctuations, beyond the modeling in this thesis, which must be anticipated in several regions of the phase diagram, for example, when the thickness of the minority domains approaches microscopic distances near B_c or around the re-entrant phase boundary, cf. Fig. 2.3.7 (C). Furthermore, the mesoscale QPT continuously connect the TF-QCP with the coercive field, cf. Fig. 2.3.5 (B1), suggesting the search for mesoscale QPT in other anisotropic ferromagnets.

The experimental setup developed as part of this thesis opens up the opportunity to investigate the mK-heat capacity in magnetic fields in a variety of materials with strong magnetic anisotropy.

A. Appendix

A.1. Transverse Susceptibility: Additional Data

This section gives an overview of all transverse susceptibility data, which were recorded and discussed above. As shown in Fig. A.1.1, the transverse susceptibility was recorded as a function of temperature by performing a step sweep. The color represents the corresponding temperature going from cold (blue) to hot (red) the up-sweeps are depicted as dashed lines, whereas the down-sweeps are depicted as solid lines.

Fig. A.1.2 shows the temperature sweeps, where the color represents the field strength, going from $B = 0$ (blue) to maximum field (red).

The parameters of every measurement shown in these figures are summarized in Tab. A.1.1.
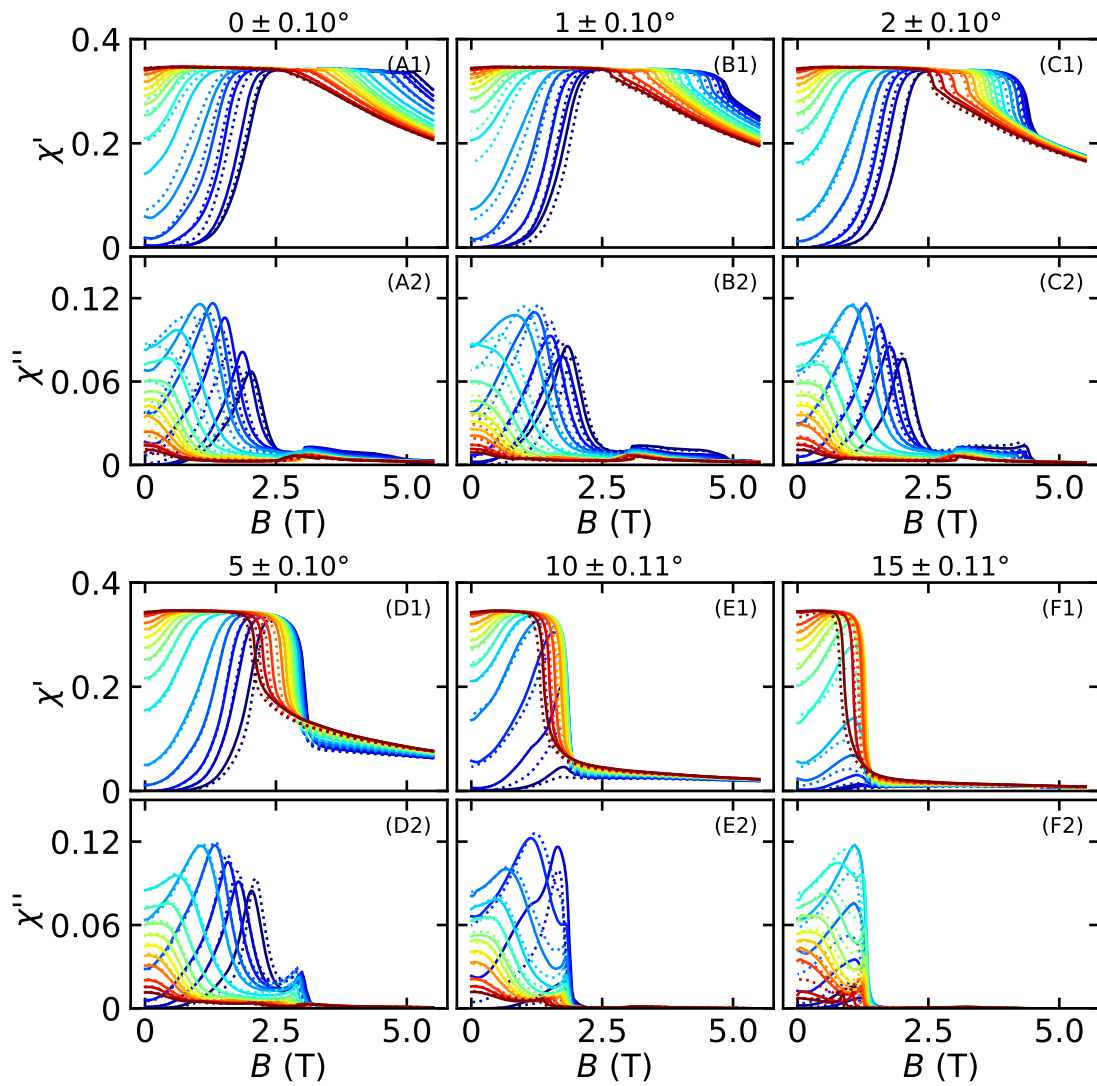
Figure A.1.1.: Overview of transverse susceptibility field sweeps for various angles. The up sweep is shown as a dashed the down sweep as a solid line.
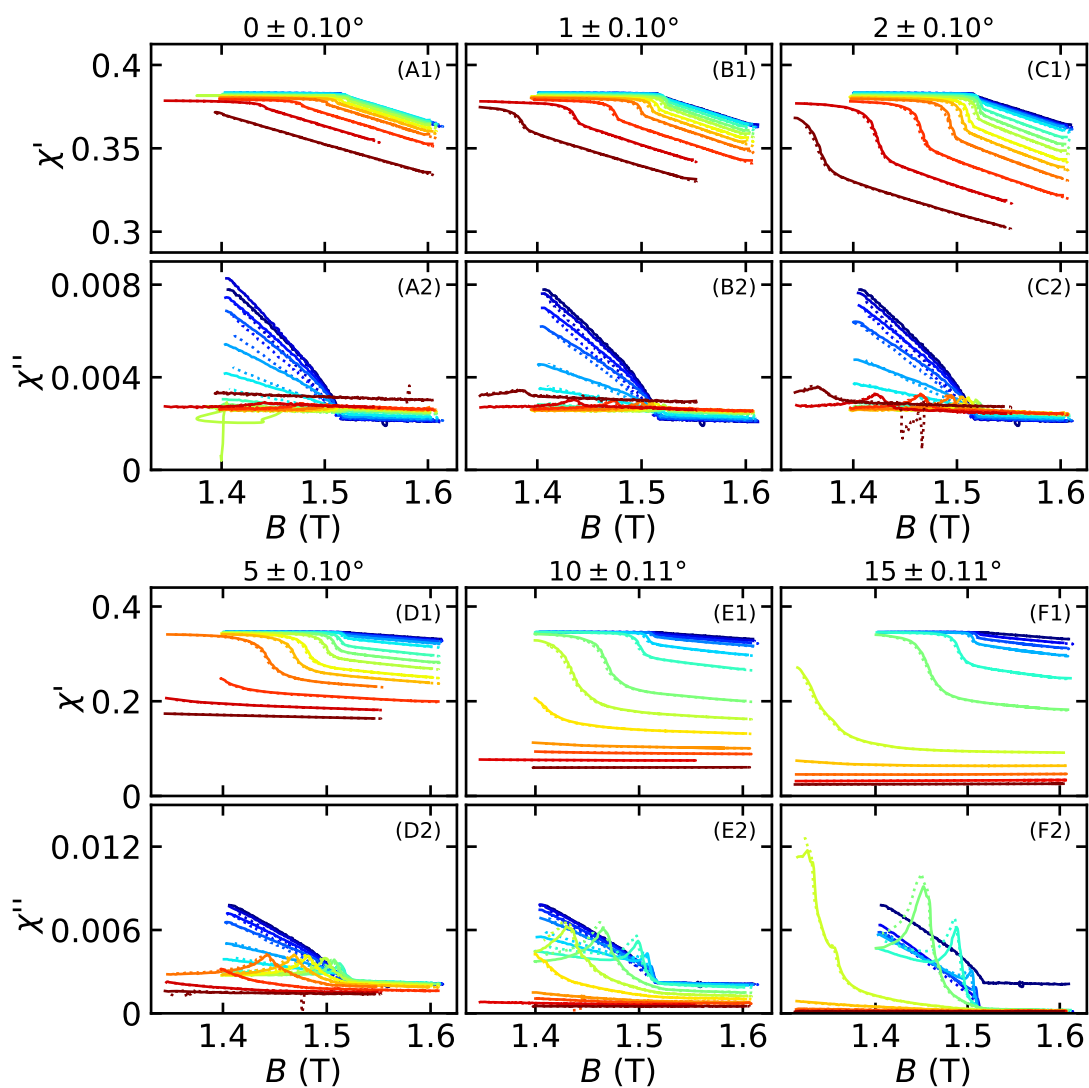
Figure A.1.2.: Overview of transverse susceptibility temperature sweeps for various angles. The up sweep is shown as a dashed the down sweep as a solid line.

B-Scans		0 - 5.5 T
Fig. A.1.1	$\Phi\,(°)$	$T\,(\text{mK})$ blue - red
(A1, A2)	0	67, 101, 136, 186, 243, 364, 483, 599, 711, 819, 925
		1031, 1146, 1189, 1291, 1345
(B1, B2)	1	68, 101, 136, 186, 243, 364, 482, 599, 711, 819, 925
		1031, 1189, 1282, 1345
(C1, C2)	2	68, 100, 137, 186, 243, 364, 483, 599, 711, 819, 925
		1031, 1189, 1281, 1345
(D1, D2)	5	68, 101, 137, 186, 243, 364, 483, 599, 711, 819, 925
		1031, 1188, 1281, 1345
(E1, E2)	10	69, 137, 244, 364, 483, 599, 711, 819, 925, 1031
		1189, 1281, 1345
(F1, F2)	15	63, 99, 135, 185, 243, 364, 483, 599, 711, 820, 925
		1031, 1275, 1394
T-Scans		1.35 - 1.6 K
Fig. A.1.2	$\Phi\,(°)$	$B\,(\text{T})$ blue - red
(A1, A2)	0	0, 0.1, 0.2, 0.3, 0.5, 0.7, 1.0, 1.15, 1.3, 1.5, 1.6, 1.75, 2.0, 2.25, 2.5
(B1, B2)	1	0, 0.1, 0.2, 0.3, 0.5, 0.7, 1.0, 1.15, 1.3, 1.5, 1.6, 1.75, 2.0, 2.25, 2.5
(C1, C2)	2	0, 0.1, 0.2, 0.3, 0.5, 0.7, 1.0, 1.15, 1.3, 1.5, 1.6, 1.75, 2.0, 2.25, 2.5
(D1, D2)	5	0, 0.1, 0.2, 0.3, 0.5, 0.7, 1.0, 1.15, 1.3, 1.5, 1.6, 1.75, 2.0, 2.25, 2.5
(E1, E2)	10	0, 0.1, 0.2, 0.3, 0.5, 0.7, 1.0, 1.15, 1.3, 1.5, 1.6, 1.75, 2.0
(F1, F2)	15	0, 0.1, 0.2, 0.3, 0.5, 0.7, 1.0, 1.15, 1.3, 1.5, 1.75

Table A.1.1.: Parameters for measurements shown in Figs. A.1.1 and A.1.2.

A.2. Magnetocaloric Measurements: Resistance Interpolation

For the magnetocaloric measurements described in Sec. 3.1.3, it was established in Sec. 3.2.6 that a proper calibration of the sensors is necessary to compensate for the magneto-resistance. To allow magnetocaloric sweeps as a function of field at various temperatures, an interpolation of the resistance was determined, by using the field-calibrated WMI-ROX sensor as a reference as described in Sec. 3.2.6.

Fig. A.2.1 shows the whole interpolated regime as a color map of $R/R(B = 0)$ of the ROX-BR3 thermometer as a function of field and temperature.
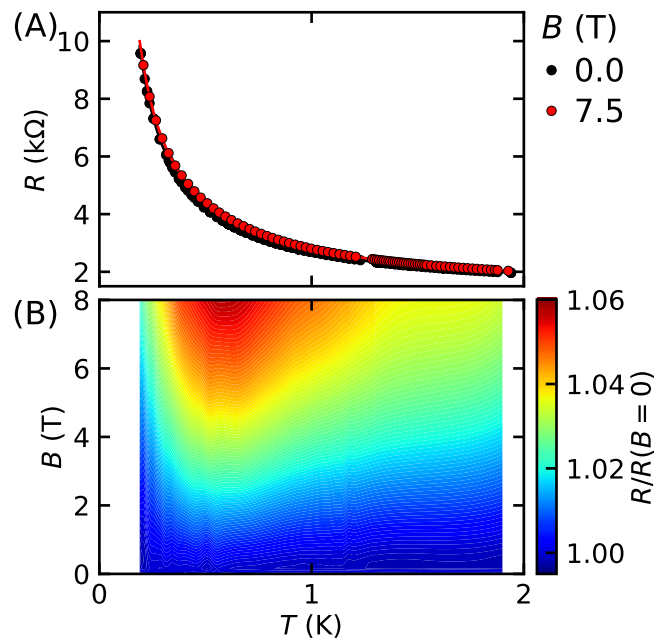
Figure A.2.1.: Interpolation of the resistance R as a function of field and temperature for calibration of the ROX-BR3 thermometer.

A.3. Specific Heat: Additional Data

The heat capacity data were described in Sec. 3.3.1 and discussed in full detail in the corresponding figures. For completeness the data will be presented here covering additional angles Φ at $B = 2, 3, 5.1\,\mathrm{T}$.

A.3.1 (A) shows the specific heat C/R as a function of temperature for various angles between $\Phi = 0°$ and $20°$. The hyperfine peak below $800\,\mathrm{mK}$ is identical for all field orientations. The anomaly at the thermal phase transition is cut off at lower temperatures with increasing angle. For large angles, a broad maximum emerges at elevated temperatures, which shifts towards higher temperatures with increasing Φ.

The sample relaxation time τ_s displays no anomalies and correlates with the specific heat, as shown in Fig. A.3.1 (B). The relaxation time of the addenda shows a broad minimum around $T = 1\,\mathrm{K}$, cf. Fig. A.3.1 (C). The sample thermal conductance k_s increases monotonically and shows no significant dependence on Φ, cf. Fig. A.3.1 (D). As in all datasets, the thermal conductance of the addenda is independent of the angle, cf. Fig. A.3.1 (E).

Fig. A.3.2 (A) shows the specific heat C/R as a function of temperature for various angles between $\Phi = -5°$ and $90°$. The hyperfine peak below $800\,\mathrm{mK}$ exhibits a small angular dependence shifting to higher temperatures at $\Phi = 10°$. For large angles, a broad maximum emerges at elevated temperatures, which shifts towards higher temperatures with increasing Φ, as already observed for the other fields.

The sample relaxation time τ_s displays an unusual increase for the $\Phi = 90°$ curve with decreasing temperature approaching $T = 1.3\,\mathrm{K}$, cf. Fig. A.3.2 (B). The relaxation time of the addenda shows a broad minimum around $T = 1\,\mathrm{K}$, cf. Fig. A.3.2 (C). Only the data at $\Phi = 90°$ deviate significantly putatively suggesting that the thermal conductance of the platform to the bath is angle dependent. An analogous anomaly may be seen in the sample thermal conductance k_s, which is significantly reduced in the case of $\Phi = 90°$, cf. Fig. A.3.2 (D). As in all datasets, the thermal conductance of the addenda is independent of the angle, cf. Fig. A.3.2 (E).

Fig. A.3.3 (A) shows the specific heat C/R as a function of temperature for various angles between $\Phi = 0°$ and $10°$. The hyperfine contribution displays a strong angular dependence, shifting towards higher temperatues with increasing field angle Φ.

The sample relaxation time τ_s lies above the other curves for $\Phi = 5°$, as shown in Fig. A.3.3 (B). Together with the increased τ_l, Fig. A.3.3 (C), and decreased k_s, cf. Fig. A.3.3 (D) it supports the notion that the thermal conductance of the sample, or from the sample to the platform is reduced at this angle. As in all datasets, the thermal conductance of the addenda is independent of Φ, cf. Fig. A.3.3 (E).
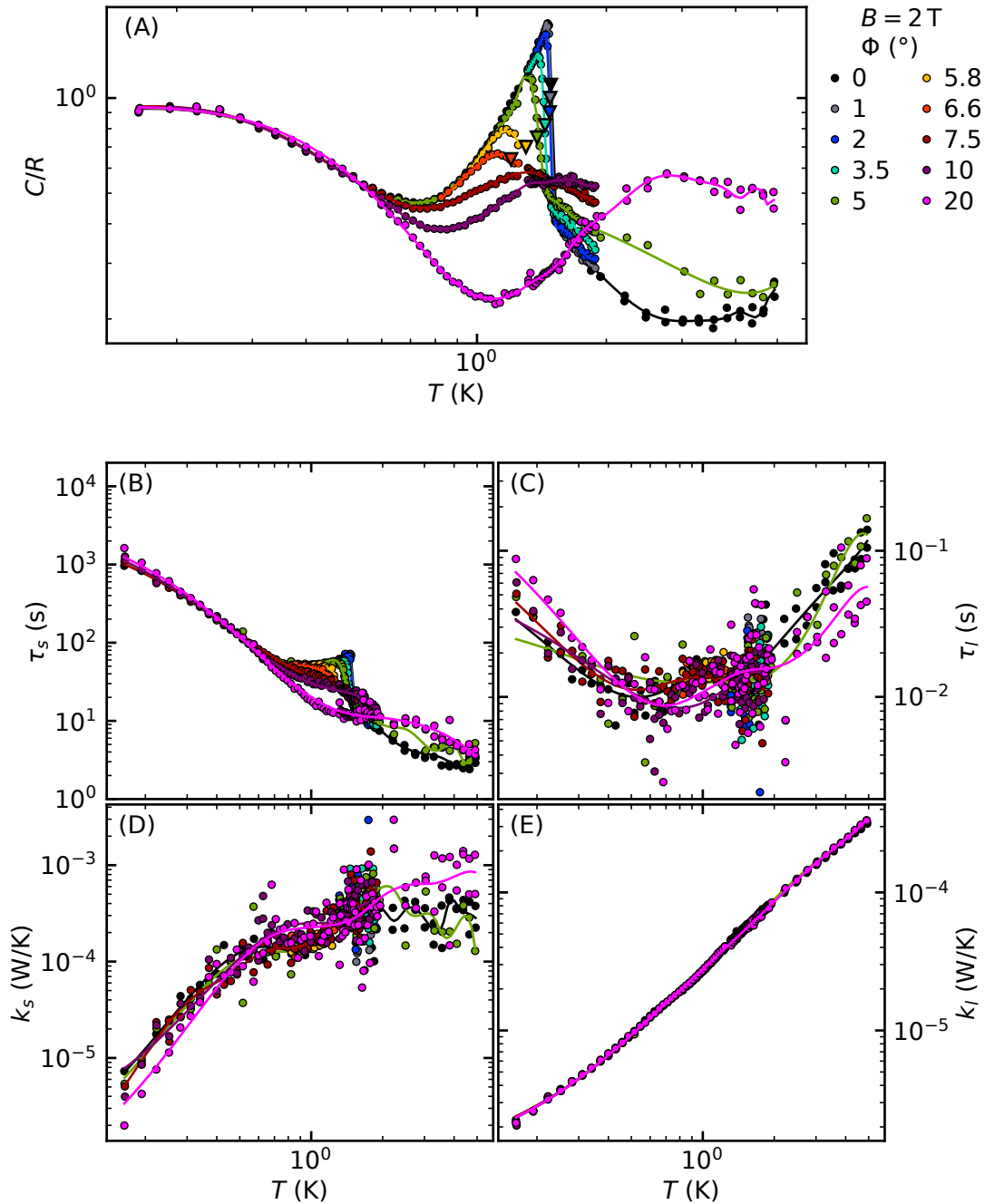
Figure A.3.1.: Specific heat fit results for $B = 2\,\mathrm{T}$ and various angles Φ. (A) The specific heat C/R as a function of temperature. The triangles mark the position of the phase transition to the ferromagnetic state. (B) The relaxation time of the sample τ_s is directly correlated to the specific heat. (C) The relaxation time of the addenda τ_l is several orders of magnitude faster as compared to the sample. (D) The thermal conductance between sample and platform k_s. (E) The thermal conductance between platform and bath k_l is independent of magnetic field and is dominated by the thermal conductance of the silver wire.
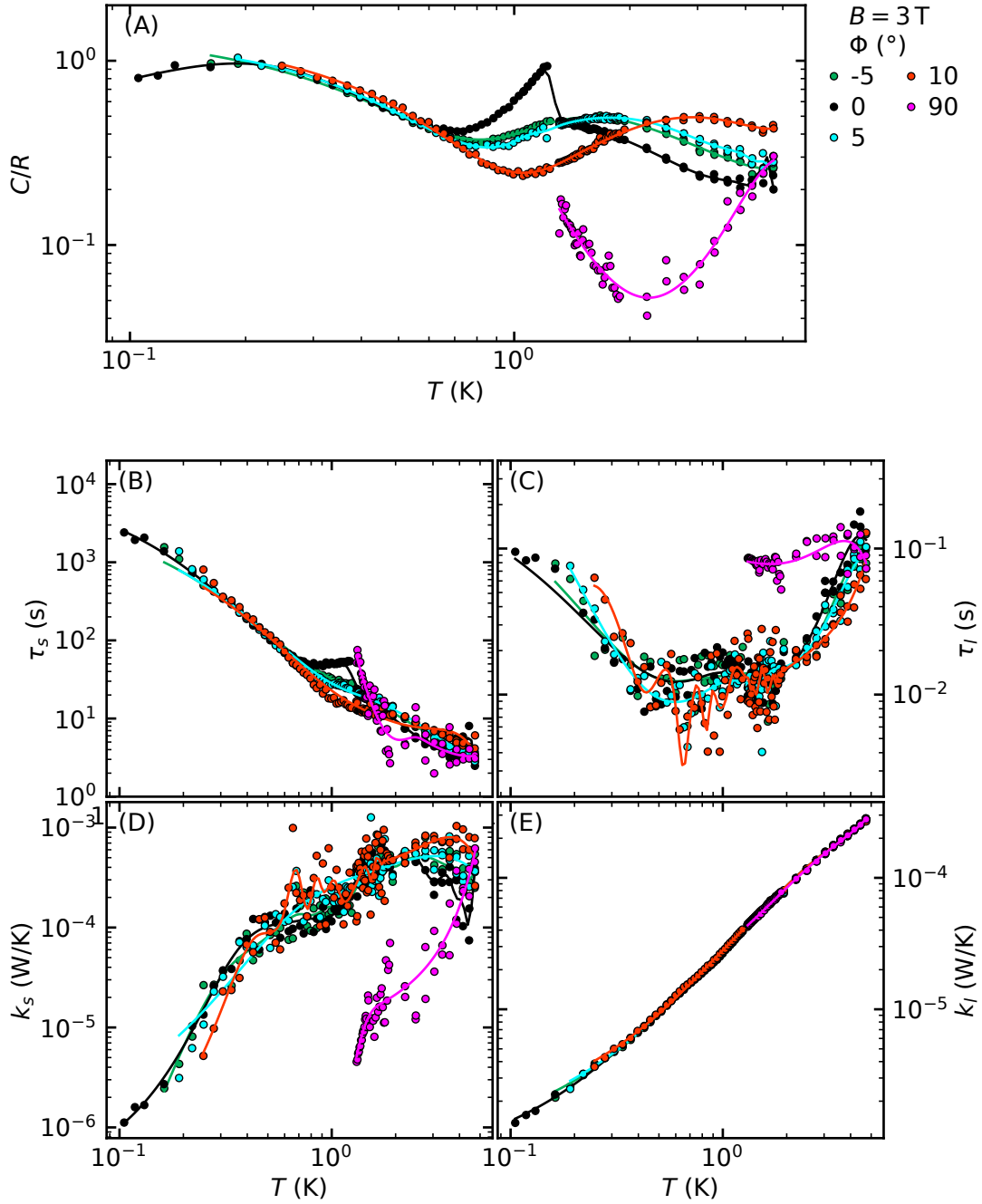
Figure A.3.2.: Specific heat fit results for $B = 3\,\mathrm{T}$ and various angles Φ. (A) The specific heat C/R as a function of temperature. The triangles mark the position of the phase transition to the ferromagnetic state. (B) The relaxation time of the sample τ_s is directly correlated to the specific heat. (C) The relaxation time of the addenda τ_l is several orders of magnitude faster as compared to the sample. (D) The thermal conductance between sample and platform k_s. (E) The thermal conductance between platform and bath k_l is independent of magnetic field and is dominated by the thermal conductance of the silver wire.
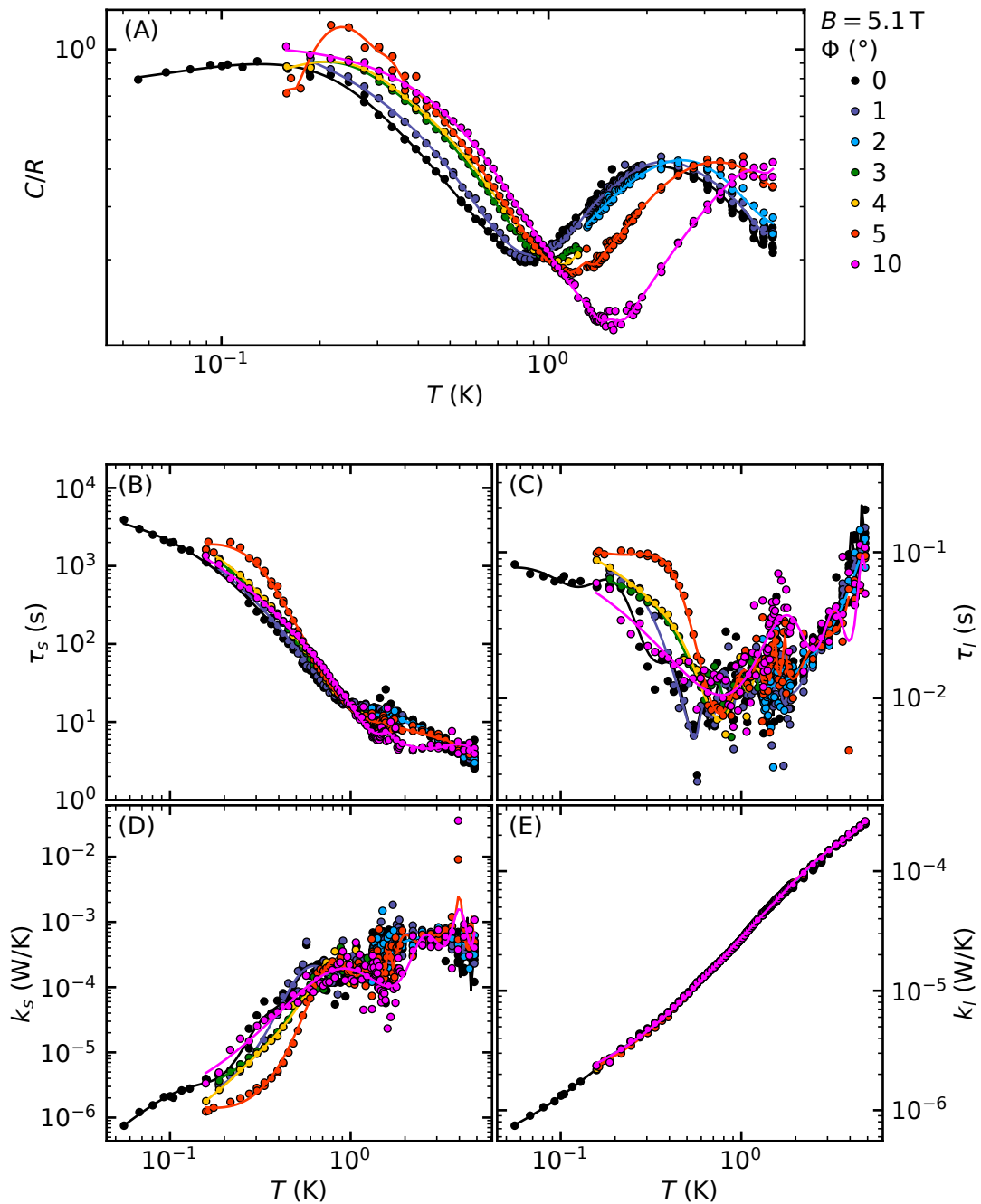
Figure A.3.3.: Specific heat fit results for $B = 5.1\,\text{T}$ and various angles Φ. (A) The specific heat C/R as a function of temperature. The triangles mark the position of the phase transition to the ferromagnetic state. (B) The relaxation time of the sample τ_s is directly correlated to the specific heat. (C) The relaxation time of the addenda τ_l is several orders of magnitude faster as compared to the sample. (D) The thermal conductance between sample and platform k_s. (E) The thermal conductance between platform and bath k_l is independent of magnetic field and is dominated by the thermal conductance of the silver wire.

Bibliography

[1] S. Sachdev, "Quantum phase transitions," *Physics World*, vol. 12, p. 33, 1999.

[2] M. Vojta, "Quantum phase transitions," *Reports on Progress in Physics*, vol. 66, p. 2069, 2003.

[3] S. Sachdev and B. Keimer, "Quantum Criticality," *Physics Today*, vol. 64, p. 29, 2011.

[4] F. Rucker, *Transverse Susceptibility of Complex Magnetic Textures*. PhD thesis, Technical University Munich, 2018.

[5] H. Eisenlohr, *Frontiers of quantum criticality: Mott transition, nuclear spins, and domain-driven transitions*. PhD thesis, 2021.

[6] H. Nishimori and G. Ortiz, *Elements of Phase Transitions and Critical Phenomena*. Oxford University Press, 2010.

[7] A. Kopp and S. Chakravarty, "Criticality in correlated quantum matter," *Nature Physics*, vol. 1, p. 53, 2005.

[8] H. v. Löhneysen, A. Rosch, M. Vojta, and P. Wölfle, "Fermi-liquid instabilities at magnetic quantum phase transitions," *Reviews of Modern Physics*, vol. 79, p. 1015, 2007.

[9] S. Sachdev, *Quantum Phase Transitions*. Cambridge University Press, 2011.

[10] R. L. Greene, P. R. Mandal, N. R. Poniatowski, and T. Sarkar, "The Strange Metal State of the Electron-Doped Cuprates," *Annual Review of Condensed Matter Physics*, vol. 11, p. 213, 2020.

[11] S. Suzuki, J.-i. Inoue, and B. K. Chakrabarti, *Quantum Ising Phases and Transitions in Transverse Ising Models*. Springer, 2012.

[12] D. Bitko, T. F. Rosenbaum, and G. Aeppli, "Quantum critical behavior for a model magnet," *Physical Review Letters*, vol. 77, p. 940, 1996.

[13] H. M. Rønnow, R. Parthasarathy, J. Jensen, G. Aeppli, T. F. Rosenbaum, and D. F. McMorrow, "Quantum phase transition of a magnet in a spin bath," *Science*, vol. 308, p. 389, 2005.

[14] H. M. Rønnow, J. Jensen, R. Parthasarathy, G. Aeppli, T. F. Rosenbaum, D. F. McMorrow, and C. Kraemer, "Magnetic excitations near the quantum phase transition in the Ising ferromagnet LiHoF$_4$," *Physical Review B*, vol. 75, p. 054426, 2007.

[15] H. Xie, L. Tian, Q. Chen, H. Sun, X. Gao, Z. Li, Z. Mo, and J. Shen, "Giant and reversible low field magnetocaloric effect in LiHoF$_4$ compound," *Dalton Transactions*, 2021.

[16] P. J. Walker, "Melt growth of LiHoF$_4$," *Journal of Crystal Growth*, vol. 49, p. 77, 1980.

[17] C. Keller and H. Schmutz, "Die Reaktion von Lithiumfluorid mit den Trifluoriden der Lanthaniden und einiger Actiniden," *Journal of Inorganic and Nuclear Chemistry*, vol. 27, p. 900, 1965.

[18] K. W. H. Stevens, "Matrix elements and operator equivalents connected with the magnetic properties of rare earth ions," vol. 65, p. 209, 1952.

[19] A. H. Cooke, D. A. Jones, J. F. A. Silva, and M. R. Wells, "Ferromagnetism in lithium holmium fluoride - LiHoF$_4$. I. Magnetic measurements," *Journal of Physics C: Solid State Physics*, vol. 8, p. 4083, 1975.

[20] P. E. Hansen, T. Johansson, and R. Nevald, "Magnetic properties of lithium rare-earth fluorides: Ferromagnetism in LiErF$_4$ and LiHoF$_4$ and crystal-field parameters at the rare-earth and Li sites," *Physical Review B*, vol. 12, p. 5315, 1975.

[21] A. Wendl, H. Eisenlohr, F. Rucker, C. Duvinage, M. Kleinhans, M. Vojta, and C. Pfleiderer, "Emergence of mesoscale quantum phase transitions in a ferromagnet," *Nature*, vol. 609, p. 65, 2022.

[22] J. Magariño, J. Tuchendler, P. Beauvillain, and I. Laursen, "EPR experiments in LiTbF$_4$, LiHoF$_4$, and LiErF$_4$ at submillimeter frequencies," *Physical Review B*, vol. 21, p. 18, 1980.

[23] J. H. Page, J. T. Folinsbee, D. R. Taylor, and D. Zobin, "Transverse susceptibility of the uniaxial ferromagnets $LiHoF_4$ and $LiTbF_4$ by dielectric measurements," *Physica B+C*, vol. 107, p. 85, 1981.

[24] D. H. Reich, B. Ellman, J. Yang, T. F. Rosenbaum, G. Aeppli, and D. P. Belanger, "Dipolar magnets and glasses: Neutron-scattering, dynamical, and calorimetric studies of randomly distributed Ising spins," *Physical Review B*, vol. 42, p. 4631, 1990.

[25] P. Babkevich, A. Finco, M. Jeong, B. Dalla Piazza, I. Kovacevic, G. Klughertz, K. W. Krämer, C. Kraemer, D. T. Adroja, E. Goremychkin, T. Unruh, T. Strässle, A. Di Lieto, J. Jensen, and H. M. Rønnow, "Neutron spectroscopic study of crystal-field excitations and the effect of the crystal field on dipolar magnetism in $LiRF_4$ (R = Gd , Ho, Er, Tm, and Yb)," *Physical Review B*, vol. 92, 2015.

[26] A. Beckert, R. I. Hermans, M. Grimm, J. R. Freeman, E. H. Linfield, A. G. Davies, M. Müller, H. Sigg, S. Gerber, G. Matmon, and G. Aeppli, "Precise determination of low energy electronuclear Hamiltonian for $LiY_{1-x}Ho_xF_4$," *arXiv:2012.09233 [cond-mat, physics:physics, physics:quant-ph]*, 2020.

[27] J. Brooke, D. Bitko, T. F, Rosenbaum, and G. Aeppli, "Quantum annealing of a disordered magnet," *Science*, vol. 284, p. 779, 1999.

[28] J. Brooke, T. F. Rosenbaum, and G. Aeppli, "Tunable quantum tunnelling of magnetic domain walls," *Nature*, vol. 413, p. 610, 2001.

[29] S. Ghosh, "Coherent spin oscillations in a disordered magnet," *Science*, vol. 296, p. 2195, 2002.

[30] S. Ghosh, T. F. Rosenbaum, G. Aeppli, and S. N. Coppersmith, "Entangled quantum state of magnetic dipoles," *Nature*, vol. 425, p. 48, 2003.

[31] P. E. Jönsson, R. Mathieu, W. Wernsdorfer, A. M. Tkachuk, and B. Barbara, "Absence of conventional spin-glass transition in the Ising dipolar system $LiHo_xY_{1-x}F_4$," *Physical Review Letters*, vol. 98, p. 256403, 2007.

[32] J. A. Quilliam, S. Meng, C. G. A. Mugford, and J. B. Kycia, "Evidence of spin glass dynamics in dilute $LiHo_xY_{1-x}F_4$," *Physical Review Letters*, vol. 101, p. 187204, 2008.

[33] K.-M. Tam and M. J. P. Gingras, "Spin-glass transition at nonzero temperature in a disordered dipolar Ising system: The case of $LiHo_xY_{1-x}F_4$," *Physical Review Letters*, vol. 103, p. 087202, 2009.

[34] M. J. P. Gingras and P. Henelius, "Collective phenomena in the LiHo$_x$Y$_{1-x}$F$_4$ quantum Ising magnet: Recent progress and open questions," vol. 320, p. 012001, 2011.

[35] M. A. Schmidt, D. M. Silevitch, G. Aeppli, and T. F. Rosenbaum, "Using thermal boundary conditions to engineer the quantum state of a bulk magnet," *Proceedings of the National Academy of Sciences*, vol. 111, p. 3689, 2014.

[36] D. M. Silevitch, C. Tang, G. Aeppli, and T. F. Rosenbaum, "Tuning high-Q nonlinear dynamics in a disordered quantum magnet," *Nature Communications*, vol. 10, p. 4001, 2019.

[37] M. Buchhold, C. S. Tang, D. M. Silevitch, T. F. Rosenbaum, and G. Refael, "Quantum dynamics in strongly driven random dipolar magnets," *Physical Review B*, vol. 101, p. 214201, 2020.

[38] S. Säubert, C. L. Sarkis, F. Ye, G. Luke, and K. A. Ross, "Microscopics of quantum annealing in the disordered dipolar Ising ferromagnet LiHo$_x$Y$_{1-x}$F$_4$," *arXiv:2105.03408 [cond-mat]*, 2021.

[39] H. P. Christensen, "Spectroscopic analysis of LiHoF$_4$ and LiErF$_4$," *Physical Review B*, vol. 19, p. 6564, 1979.

[40] G. S. Shakurov, M. V. Vanyunin, B. Z. Malkin, B. Barbara, R. Y. Abdulsabirov, and S. L. Korableva, "Direct measurements of anticrossings of the electron-nuclear energy levels in LiYF$_4$:Ho3+ with submillimeter EPR spectroscopy," *Applied Magnetic Resonance*, vol. 28, p. 251, 2005.

[41] P. B. Chakraborty, P. Henelius, H. Kjønsberg, A. W. Sandvik, and S. M. Girvin, "Theory of the magnetic phase diagram of LiHoF$_4$," *Physical Review B*, vol. 70, p. 144411, 2004.

[42] R. D. McKenzie and P. C. E. Stamp, "Thermodynamics of a quantum Ising system coupled to a spin bath," *Physical Review B*, vol. 97, p. 214430, 2018.

[43] G. Mennenga, L. de Jongh, and W. Huiskamp, "Field dependent specific heat study of the dipolar Ising ferromagnet LiHoF$_4$," *Journal of Magnetism and Magnetic Materials*, vol. 44, p. 59, 1984.

[44] S. Legl, *Entwicklung eines Spulen-Vibrationsmagnetometers zur Untersuchung korrelierter Elektronensysteme bei ultratiefen Temperaturen.* PhD thesis, Technische Universität München, 2010.

[45] A. Aharony, "Critical behavior of magnets with dipolar interactions. v. uniaxial magnets in d dimensions," *Physical Review B*, vol. 8, p. 3363, 1973.

[46] E. Brézin and J. Zinn-Justin, "Critical behavior of uniaxial systems with strong dipolar interactions," *Physical Review B*, vol. 13, p. 251, 1976.

[47] P. Beauvillain, J. P. Renard, I. Laursen, and P. J. Walker, "Critical behavior of the magnetic susceptibility of the uniaxial ferromagnet $LiHoF_4$," *Physical Review B*, vol. 18, p. 3360, 1978.

[48] J. A. Griffin, M. Huster, and R. J. Folweiler, "Critical behavior of the spontaneous magnetization at marginal dimensionality in $LiHoF_4$," *Physical Review B*, vol. 22, p. 4370, 1980.

[49] L. M. Holmes, F. Hulliger, H. J. Guggenheim, and J. P. Maita, "Specific heat of a dipolar-coupled Ising ferromagnet $LiTbF_4$," *Physics Letters A*, vol. 50, p. 163, 1974.

[50] G. Ahlers, A. Kornblit, and H. J. Guggenheim, "Logarithmic corrections to the landau specific heat near the Curie temperature of the dipolar Ising ferromagnet $LiTbF_4$," *Physical Review Letters*, vol. 34, p. 1227, 1975.

[51] J. Nikkel and B. Ellman, "Testing renormalization group theory at the critical dimension in $LiHoF_4$," *Physical Review B*, vol. 64, p. 214420, 2001.

[52] A. Biltmo and P. Henelius, "The ferromagnetic transition and domain structure in $LiHoF_4$," *EPL (Europhysics Letters)*, vol. 87, p. 27007, 2009.

[53] J. E. Battison, A. Kasten, M. J. M. Leask, J. B. Lowry, and B. M. Wanklyn, "Ferromagnetism in lithium holmium fluoride - $LiHoF_4$. II. Optical and spectroscopic measurements," *Journal of Physics C: Solid State Physics*, vol. 8, p. 4089, 1975.

[54] Ö. Karcı, J. O. Piatek, P. Jorba, M. Dede, H. M. Rønnow, and A. Oral, "An ultra-low temperature scanning Hall probe microscope for magnetic imaging below 40 mK," *Review of Scientific Instruments*, vol. 85, p. 103703, 2014.

[55] J. Pommier, P. Meyer, J. Ferré, and I. Laursen, "(H, T) phase diagram of a uniaxial dipolar ferromagnet: $LiHoF_4$," *Le Journal de Physique Colloques*, vol. 49, p. C8, 1988.

[56] P. Meyer, J. Pommier, and J. Ferre, "Magnetooptic observation of domains at low temperature in the transparent ferromagnet $LiHoF_4$," in *Electro-Optic and Magneto-Optic Materials and Applications* (J.-P. Castera, ed.), vol. 1126, p. 93, SPIE, 1989.

[57] P. Jorba, "SHPM imaging of LiHoF$_4$ at ultra low temperatures," Master's thesis, 2014.

[58] M. Gabay and T. Garel, "Properties of the branched state of an Ising dipolar magnet," *Journal de Physique Lettres*, vol. 45, p. 989, 1984.

[59] J. Kötzler, M. Grahl, I. Sessler, and J. Ferré, "Size and fluctuation effects on the dynamics of linear domain walls in an Ising ferromagnet," *Physical Review Letters*, vol. 64, p. 2446, 1990.

[60] R. Choksi, R. V. Kohn, and F. Otto, "Domain branching in uniaxial ferromagnets: A scaling law for the minimum energy," *Communications in Mathematical Physics*, vol. 201, p. 61, 1999.

[61] D. Bitko, *Order and Disorder in a Model Quantum Magnet.* PhD thesis, University of Chicago, 1997.

[62] R. J. Elliott, P. Pfeuty, and C. Wood, "Ising model with a transverse field," *Physical Review Letters*, vol. 25, p. 443, 1970.

[63] P. G. de Gennes, "Collective motions of hydrogen bonds," *Solid State Communications*, vol. 1, p. 132, 1963.

[64] J. A. Hertz, "Quantum critical phenomena," *Physical Review B*, vol. 14, p. 1165, 1975.

[65] M. Suzuki, "Relationship between d-dimensional quantal spin systems and (d+1)-dimensional Ising systems: Equivalence, critical exponents and systematic approximants of the partition function and spin correlations," *Progress of Theoretical Physics*, vol. 56, p. 1454, 1976.

[66] C. Krämer, *Quantum Phase Transitions in a Magnetic Model System.* PhD thesis, ETH Zurich, 2009.

[67] M. Libersky, R. D. McKenzie, D. M. Silevitch, P. C. E. Stamp, and T. F. Rosenbaum, "Direct observation of collective electronuclear modes about a quantum critical point," *Physical Review Letters*, vol. 127, p. 207202, 2021.

[68] S. M. A. Tabei, M. J. P. Gingras, Y.-J. Kao, and T. Yavors'kii, "Perturbative quantum Monte Carlo study of LiHoF$_4$ in a transverse magnetic field," *Physical Review B*, vol. 78, p. 184408, 2008.

[69] S. Legl, C. Pfleiderer, and K. Krämer, "Vibrating coil magnetometer for milli-Kelvin temperatures," *Review of Scientific Instruments*, vol. 81, p. 043911, 2010.

[70] S. Eisenhardt, *Investigation of Quantum Phase Transitions in Ising-like Systems, by Torque Magnetometry and Neutron Scattering.* MSc, Copenhagen University, 2010.

[71] C. Duvinage, "Private communications / PhD thesis in preparation."

[72] F. Rucker and C. Pfleiderer, "Compact susceptometer for studies under transverse field geometries at very low temperatures," *Review of Scientific Instruments*, vol. 90, p. 073903, 2019.

[73] S. Mühlbauer, B. Binz, F. Jonietz, C. Pfleiderer, A. Rosch, A. Neubauer, R. Georgii, and P. Böni, "Skyrmion lattice in a chiral magnet," *Science*, vol. 323, p. 915, 2009.

[74] S. T. Bramwell, "Spin ice state in frustrated magnetic pyrochlore materials," *Science*, vol. 294, p. 1495, 2001.

[75] A. Wendl, "Neutron spin echo spectroscopy on geometrically frustrated magnets," Master's thesis, Technical University of Munich, 2018.

[76] S. Blundell, *Magnetism in Condensed Matter.* Oxford University Press, 2001.

[77] M. Twengström, L. Bovo, O. A. Petrenko, S. T. Bramwell, and P. Henelius, "LiHoF$_4$: Cuboidal demagnetizing factor in an Ising ferromagnet," *Physical Review B*, vol. 102, p. 144426, 2020.

[78] M. Twengström, L. Bovo, O. A. Petrenko, S. T. Bramwell, and P. Henelius, "LiHoF$_4$: Cuboidal demagnetizing factor in an Ising ferromagnet," *arXiv:2006.10090 [cond-mat]*, 2020.

[79] C. Pfleiderer, "Miniature AC susceptometers for use inside clamp type pressure cells," *Rev. Sci. Instrum.*, vol. 68, p. 5, 1997.

[80] Stanford-Research-Systems, "MODEL SR830 DSP Lock-In Amplifier - Manual," 2011.

[81] H. London, G. R. Clarke, and E. Mendoza, "Osmotic pressure of He^3 in liquid He^4, with proposals for a refrigerator to work below 1°K," *Physical Review*, vol. 128, p. 1992, 1962.

[82] D. S. Betts, *Refrigeration and Thermometry Below One Kelvin.* Sussex University Press, 1976.

[83] G. Mennenga, *A Study of Magnetic Ordering Phenomena in Pure and Diluted 3d and 4f Ionic Compounds at Low Temperatures.* PhD thesis, Rijksuniversiteit te Leiden, 1983.

[84] G. I. Mias and S. M. Girvin, "Absence of domain wall roughening in a transverse-field Ising model with long-range interactions," *Physical Review B*, vol. 72, p. 064411, 2005.

[85] M. Gabay and T. Garel, "Phase transitions and size effects in the Ising dipolar magnet," *Journal de Physique*, vol. 46, p. 5, 1985.

[86] P. P. Ewald, "Die Berechnung optischer und elektrostatischer Gitterpotentiale," *Annalen der Physik*, vol. 369, p. 253, 1921.

[87] J. Barker and R. Watts, "Monte Carlo studies of the dielectric properties of water-like models," *Molecular Physics*, vol. 26, p. 789, 1973.

[88] P. Debye, "Zur Theorie der spezifischen Wärmen," *Annalen der Physik*, vol. 344, p. 789, 1912.

[89] F. Pobell, *Matter and Methods at Low Temperatures.* Springer-Verlag, 2nd ed ed., 1996.

[90] A. Eucken, "über die Bestimmung spezifischer Wärmen bei tiefen Temperaturen," *Physikalische Zeitschrift*, vol. 10, p. 586, 1909.

[91] W. Nernst, "Sitzungsbericht königlich preussische Akademie der Wissenschaften," *königlich preussische Akademie der Wissenschaften*, vol. 12, p. 216, 1910.

[92] E. Gmelin, "Modern low-temperature calorimetry," *Thermochimica Acta*, vol. 29, p. 1, 1979.

[93] G. R. Stewart, "Measurement of low-temperature specific heat," *Review of Scientific Instruments*, vol. 54, p. 1, 1983.

[94] H. A. Algra, L. J. de Jongh, W. J. Huiskamp, and R. L. Carlin, "Magnetic behavior of $[(CH_3)_3NH]\,CuCl_3 \cdot 2H_2O$. Evidence for lattice-dimensionality crossovers in a quasi one-dimensional ferromagnet," *Physica B+C*, vol. 92, p. 187, 1977.

[95] Y. Ogata, K. Kobayashi, T. Matsuo, and H. Suga, "An adiabatic low-temperature calorimeter for small samples," *Journal of Physics E: Scientific Instruments*, vol. 17, p. 1054, 1984.

[96] R. A. Fisher, P. Radhakrishna, N. E. Phillips, J. V. Badding, and A. M. Stacy, "Low-temperature specific heat of antiferromagnetic $EuNi_5P_3$ and mixed-valent $EuNi_2P_2$ in magnetic fields to 7 T," *Physical Review B*, vol. 52, p. 13519, 1995.

[97] H. Wilhelm, T. Lühmann, T. Rus, and F. Steglich, "A compensated heat-pulse calorimeter for low temperatures," *Review of Scientific Instruments*, vol. 75, p. 2700, 2004.

[98] J. F. Cochran, C. A. Shiffman, and J. E. Neighbor, "Specific heat measurements in 1–10°K range using continuous warming method," *Review of Scientific Instruments*, vol. 37, p. 499, 1966.

[99] J. Pinel and C. Lebeau, "An apparatus for the measurement of heat capacity at low temperatures," *Journal of Physics E: Scientific Instruments*, vol. 5, p. 688, 1972.

[100] A. Bauer, *Investigation of Itinerant Antiferromagnets and Cubic Chiral Helimagnets.* PhD thesis, Technische Universität München, 2014.

[101] N. Bonacic, *Measurements of Heat Capacity of Systems with Complex Magnetic Phase Diagrams for Magnetic Field along Hard Magnetisation Axes.* MSc, University of Zagreb, 2016.

[102] P. F. Sullivan and G. Seidel, "Steady-state, AC-temperature calorimetry," *Physical Review*, vol. 173, p. 679, 1968.

[103] A. W. Rost, R. S. Perry, J.-F. Mercure, A. P. Mackenzie, and S. A. Grigera, "Entropy landscape of phase formation associated with quantum criticality in $Sr_3Ru_2O_7$," *Science*, vol. 325, p. 1360, 2009.

[104] S. Alterovitz, G. Deutscher, and M. Gershenson, "Heat capacity and thermal conductivity of sintered Al_2O_3 at low temperatures by the heat pulse technique," *Journal of Applied Physics*, vol. 46, p. 3637, 1975.

[105] H. Suzuki, A. Inaba, and C. Meingast, "Accurate heat capacity data at phase transitions from relaxation calorimetry," *Cryogenics*, vol. 50, p. 693, 2010.

[106] A. Scheie, "LongHCPulse: Long-pulse heat capacity on a Quantum Design PPMS," *Journal of Low Temperature Physics*, vol. 193, p. 60, 2018.

[107] R. Bachmann, F. J. DiSalvo, T. H. Geballe, R. L. Greene, R. E. Howard, C. N. King, H. C. Kirsch, K. N. Lee, R. E. Schwall, H.-U. Thomas, and R. B. Zubeck, "Heat capacity measurements on small samples at low temperatures," *Review of Scientific Instruments*, vol. 43, p. 205, 1972.

[108] J. S. Hwang, K. J. Lin, and C. Tien, "Measurement of heat capacity by fitting the whole temperature response of a heat-pulse calorimeter," *Review of Scientific Instruments*, vol. 68, p. 94, 1997.

[109] M. Regelsberger, R. Wernhardt, and M. Rosenberg, "Fully automated calorimeter for small samples with improved sensitivity," *Journal of Physics E: Scientific Instruments*, vol. 19, p. 525, 1986.

[110] R. J. Schutz, "Thermal relaxation calorimetry below 1 K," *Review of Scientific Instruments*, vol. 45, p. 548, 1974.

[111] R. E. Schwall, R. E. Howard, and G. R. Stewart, "Automated small sample calorimeter," *Review of Scientific Instruments*, vol. 46, p. 1054, 1975.

[112] J. P. Shepherd, "Analysis of the lumped τ_2 effect in relaxation calorimetry," *Review of Scientific Instruments*, vol. 56, p. 273, 1985.

[113] M. Brando, "Development of a relaxation calorimeter for temperatures between 0.05 and 4 K," *Review of Scientific Instruments*, vol. 80, p. 095112, 2009.

[114] E. Brück, "Developments in magnetocaloric refrigeration," *Journal of Physics D: Applied Physics*, vol. 38, p. R381, 2005.

[115] "Kiutra - Your partner for cryogen-free research. — Magnetic Refrigeration for Science and Industry." https://kiutra.com/.

[116] L. Zhu, M. Garst, A. Rosch, and Q. Si, "Universally diverging Grüneisen parameter and the magnetocaloric effect close to quantum critical points," *Physical Review Letters*, vol. 91, p. 066404, 2003.

[117] M. Garst and A. Rosch, "Sign change of the Grüneisen parameter and magnetocaloric effect near quantum critical points," *Physical Review B*, vol. 72, 2005.

[118] A. W. Rost, R. S. Perry, J.-F. Mercure, A. P. Mackenzie, and S. A. Grigera, "Supporting online material for - Entropy landscape of phase formation associated with quantum criticality in $Sr_3Ru_2O_7$," *Science*, vol. 325, p. 1360, 2009.

[119] A. W. Rost, *Magnetothermal Properties near Quantum Criticality in the Itinerant Metamagnet $Sr_3Ru_2O_7$*. PhD thesis, Springer Berlin Heidelberg, 2010.

[120] "Physical Property Measurement System Heat Capacity Option User's Manual."

[121] "Goodfellow Technical Information - Polyaramid." http://www.goodfellow.com, 2019.

[122] "Goodfellow Technical Information - Copper." http://www.goodfellow.com, 2019.

[123] D. R. Smith and F. R. Fickett, "Low-temperature properties of silver," *Journal of Research of the National Institute of Standards and Technology*, vol. 100, p. 119, 1995.

[124] G. Ventura, M. Barucci, E. Gottardi, and I. Peroni, "Low temperature thermal conductivity of Kevlar," *Cryogenics*, vol. 40, p. 489, 2000.

[125] N. E. Phillips, "Heat capacity of aluminum between 0.1°K and 4.0°K," *Physical Review*, vol. 114, p. 676, 1959.

[126] Y. E. Volokitin, R. C. Thiel, and L. J. de Jongh, "Heat capacity of thick-film resistor thermometers and pure RuO_2 at low temperatures," *Cryogenics*, vol. 34, p. 771, 1994.

[127] M. Abrecht, A. Adare, and J. J. W. Ekin, "Magnetization and magnetoresistance of common alloy wires used in cryogenic instrumentation," *Review of Scientific Instruments*, vol. 78, p. 046104, 2007.

[128] J. C. Ho and N. E. Phillips, "Tungsten-platinum alloy for heater wire in calorimetry below 0.1°K," *Review of Scientific Instruments*, vol. 36, p. 1382, 1965.

[129] Keithley-Instruments-Inc, "Model 6220 DC Current Source; Model 6221 AC and DC Current Source Reference Manual," 2005.

[130] R. Goodrich, D. Hall, E. Palm, and T. Murphy, "Magnetoresistance below 1 K and temperature cycling of ruthenium oxid-bismuth ruthenate cryogenic thermometers," *Cryogenics*, vol. 38, p. 221, 1998.

[131] R. Georgii and K. Seemann, "MIRA: Dual wavelength band instrument," *Journal of large-scale research facilities JLSRF*, vol. 1, p. 3, 2015.

[132] A. Schneidewind and P. Čermák, "PANDA: Cold three axes spectrometer," *Journal of large-scale research facilities JLSRF*, vol. 1, p. 12, 2015.

[133] T. Keller, R. Golub, and R. Gähler, "Neutron spin echo—a technique for high-resolution neutron scattering," in *Scattering*, p. 1264, Elsevier, 2002.

[134] W. Besenböck, R. Gähler, P. Hank, R. Kahn, M. Köppe, C. H. De Novion, W. Petry, and J. Wuttke, "First scattering experiment on MIEZE: A fourier transform time-of-flight spectrometer using resonance coils," *Journal of Neutron Research*, vol. 7, p. 65, 1998.

[135] C. Franz, O. Soltwedel, C. Fuchs, S. Säubert, F. Haslbeck, A. Wendl, J. K. Jochum, P. Böni, and C. Pfleiderer, "The longitudinal neutron resonant spin echo spectrometer RESEDA," *Nuclear Instruments and Methods in Physics Research Section A: Accelerators, Spectrometers, Detectors and Associated Equipment*, vol. 939, p. 22, 2019.

List of Publications

- **Emergence of mesoscale quantum phase transitions in a ferromagnet**
  <u>A Wendl</u>, H Eisenlohr, F Rucker, C Duvinage, M Kleinhans, M Vojta, C Pfleiderer
  Nature, **609**, 65-70, 2022

- **Optimized signal deduction procedure for the MIEZE spectroscopy technique**
  JK Jochum, L Spitz, C Franz, <u>A Wendl</u> , JC Leiner, C Pfleiderer, O Soltwedel
  Journal of Applied Crystallography, **55**, 1, 2022

- **Longitudinal Neutron Resonance Spin Echo Spectroscopy under Large Energy Transfers**
  C Franz, O Soltwedel, S Säubert, <u>A Wendl</u>, W Gottwald, F Haslbeck, L Spitz, C Pfleiderer
  Journal of Physics: Conference Series, **1316**, 1, 012005, 2019

- **Mieze neutron spin-echo spectroscopy of strongly correlated electron systems**
  C Franz, S Säubert, <u>A Wendl</u>, FX Haslbeck, O Soltwedel, JK Jochum, L Spitz, J Kindervater, A Bauer, P Böni, C Pfleiderer
  Journal of the Physical Society of Japan, **88**, 8, 081002, 2019

- **The longitudinal neutron resonant spin echo spectrometer RESEDA**
  C Franz, O Soltwedel, C Fuchs, S Säubert, FX Haslbeck, <u>A Wendl</u>, JK Jochum, P Böni, C Pfleiderer
  Nuclear Instruments and Methods in Physics Research Section A: Accelerators, Spectrometers, Detectors and Associated Equipment, **939**, 22-29, 2019

- **The software package MIEZEPY for the reduction of MIEZE data**
  A Schober, <u>A Wendl</u>, FX Haslbeck, JK Jochum, L Spitz, C Franz
  Journal of physics communications, **3**, 10, 103001, 2019

- **Neutron MIEZE spectroscopy with focal length tuning**
  JK Jochum, <u>A Wendl</u>, T Keller, C Franz
  Measurement Science and Technology, 31, 3, 035902, 2019

Acknowledgments/Danksagungen

Im Laufe der letzten Jahre haben mich viele Menschen unterstützt und dabei geholfen, diese Arbeit zu einem Erfolg werden zu lassen. Mein besonderer Dank gilt

- Christian Pfleiderer für die sehr direkte und unkomplizierte Betreuung, für Rat und Tat mit der du mir seit meiner Master Arbeit zur Seite stehst und die mir diese Promotion erst ermöglicht haben. Darüber hinaus für die wunderbare Atmosphäre am Lehrstuhl, die Hilfsbereitschaft und guten Arbeitsbedingungen.
- Heike Eisenlohr und Matthias Vojta für die exzellente theoretische Arbeit sowie die stundenlangen erhellenden Diskussionen, die hinter der Interpretation der Daten in dieser Arbeit stecken.
- meinen wissenschaftlichen Vorgängern: Felix Rucker, Christopher Duvinage und Jan Spallek für alle Erklärungen und Einweisungen zu JT, AMI, $LiHoF_4$, Wärmekapazität und vielem mehr. Ohne euch wäre mir der Einstieg nicht so leicht gefallen.
- den Kollegen am RESEDA Christian Franz, Johanna Jochum, Steffen Säubert, Franz Haslbeck, Christian Fuchs, Olaf Soldwedel und Jonathan Leiner, sowie am MIRA Robert Georgii, Markos Skoulatos, Jonathan Frank und Tobias Weber für die Unterstützung bei den verschiedenen Neutronenstreuexperiementen am FRM2, die es leider nicht in diese Arbeit geschafft haben. Meine Ursprünge am FRM2 haben erst meine Begeisterung für diese Arbeit geweckt.
- Andreas Bauer für das "Bauern" von Präsentationen und Plots, die so manchen wissenschaftlichen Vortrag verbessert haben.
- Marc Wilde für all die Kniffe der Tieftemperaturphysik und dem Betrieb von Kryostaten und Magneten die du an mich weitergegeben hast.
- Herbert Hetzl und Marc Wilde für die kontinuierliche Versorgung mit flüssigem Stickstoff und Helium, auch über die Weihnachtsfeiertage.